Analysis and Design of Terahertz Wireless Communication Integrated with Access, IoT, and Cell-Free Networks

THESIS

Submitted in partial fulfillment of the requirements for the degree of

DOCTOR OF PHILOSOPHY

by

Pranay Bhardwaj

Under the Supervision of

Prof. Syed Mohammad Zafaruddin

BITS Pilani
Pilani | Dubai | Goa | Hyderabad

BIRLA INSTITUTE OF TECHNOLOGY AND SCIENCE, PILANI

2024

BIRLA INSTITUTE OF TECHNOLOGY AND SCIENCE, PILANI

Certificate

This is to certify that the thesis entitled **'Analysis and Design of Terahertz Wireless Communication Integrated with Access, IoT, and Cell-Free Networks'** submitted by **Pranay Bhardwaj**, ID.No. **2020PHXF0026P** for award of Ph.D. of the Institute embodies original work done by him under my supervision.

Signature of the Supervisor :
Name: : **Prof. SYED MOHAMMAD ZAFARUDDIN**
Designation : Associate Professor, EEE Department, BITS Pilani, Pilani Campus
Date :

Declaration by the Candidate

I hereby declare that the work presented in the thesis entitled, **'Analysis and Design of Terahertz Wireless Communication Integrated with Access, IoT, and Cell-Free Networks'** in partial fulfillment of the requirements for the award of the Degree of **Doctor of Philosophy** and submitted in the Department of Electrical and Electronics Engineering of the Birla Institute of Technology and Science, Pilani is an authentic record of my own work carried out during a period from November 2020 to March 2024 under the supervision of **Prof. Syed Mohammad Zafaruddin**, Department of Electrical and Electronics Engineering of the Birla Institute of Technology and Science, Pilani.

Signature of the student	:
Name of the student	: **Pranay Bhardwaj**
ID number of the student	: **2020PHXF0026P**
Date	:

Abstract

Fifth-generation (5G) wireless communication is rapidly transitioning from concept to global deployment. The fundamental technologies that facilitate 5G are millimeter wave propagation, a massive multiple-input multiple-output (mMIMO) antenna array system, and the deployment of ultra-dense networks. The forthcoming 6G wireless technology aims to increase data rates, reaching an impressive 1Tbps with improved reliability and reduced latency to support emerging applications such as holographic communications, tactile and haptic internet, and fully autonomous driving. The potential technologies for 6G under consideration are holographic MIMO, reconfigurable intelligent surface (RIS), artificial intelligence-assisted network management, and terahertz (THz) spectrum for wireless communications.

THz spectrum is the next frontier in wireless communications, providing tremendously higher contiguous bandwidth than mmWave propagation for data transmissions. THz wireless can be a potential alternative to free-space optics (FSO) and mmWave technology for backhaul/fronthaul terrestrial connectivity and last-mile access for the next-generation networks. The THz band for wireless communications has appealing characteristics, such as contiguous higher channel bandwidth in the license-free spectrum and robustness to atmospheric turbulence due to the scattering effect. Although the THz band has been widely used for spectroscopy, imaging, and several other applications, its use for wireless communication is still nascent. It is desirable to investigate statistical performance characterization and physical layer algorithms for THz wireless communication as a proof of concept for the next-generation wireless systems. Further, integrating existing wireless technologies and infrastructure seamlessly with THz communication is also essential to ensure a smooth transition and coexistence with previous generations of communication systems.

THz propagation characteristics for wireless applications are challenging, which includes higher path-loss due to molecular absorption, antenna misalignment errors, intricate signal fading, and transceiver hardware impairments. This thesis provides a detailed statistical characterization and performance analysis of the THz band for wireless communication and develops algorithms for integrating the THz wireless system with access, IoT, and cell-free network links, considering the unique characteristics of THz propagation.

The thesis starts with an overview of THz wireless communication, emphasizing spectrum allocation, potential applications, and channel characterizations. Next, a general analysis for multihop transmission is presented to extend the coverage range for the THz wireless

backhaul. The effect of dynamic shadowing due to human movement between transmitter and receiver is also considered in the last link for a better performance assessment specific to the THz propagation. Further, a comprehensive statistical performance for the integrated THz-RF link are presented, demonstrating that existing RF access networks can be integrated with the core network using the THz wireless backhaul as a potential alternative to the wireline fiber. A distributed algorithm for aggregate node (AN) selection is presented for data collection from an Internet-of-Things (IoT) network to an unmanned aerial vehicle (UAV). A triple technology wireless backhaul consisting of mmWave, FSO, and THz is proposed to transfer collected data to the core network. Leveraging unique characteristics of THz propagation, low-complexity algorithms are proposed for cell-free wireless networks. Random access protocols are developed ensuring successful transmission for multiple users with limited delay and energy loss, exploiting the combined effect of random atmospheric absorption, non-linearity of fading, hardware impairments, and antenna misalignment errors.

In summary, this dissertation provides a comprehensive performance evaluation and algorithm design for THz wireless communication under diverse propagation environments to efficiently deploy THz systems for 6G wireless communication integrated with the existing network infrastructure. The proposed research investigates more exclusively the THz band for wireless communications as a high-speed link and wireless backhaul support for access, IoT, and cell-free networks.

Acknowledgments

I would like to express my sincere and heartily gratitude to my supervisor, Prof. Syed Mohammad Zafaruddin, Associate Professor, Department of Electrical and Electronics Engineering, BITS Pilani, Pilani Campus, for his precious guidance, prompting, and constant encouragement during planning, development and completion of this research work. This thesis would not have been possible without his continuous support and encouragement. I am deeply indebted to him for the timely completion of the thesis and for fostering a collaborative and enriching work culture that made this research journey both productive and fulfilling.

I am also very thankful and highly obliged to my doctoral advisory committee members Prof. V. K. Chaubey and Prof. Vinay Chamola for their continuous comments and recommendations during departmental presentations, which not only helped me stay aligned with my research objectives but also significantly enhanced the quality of my work. I am also indebted to them for their valuable input during the initial review of my Ph.D. thesis.

I thank the Departmental Research Committee (DRC) convener Prof. Praveen Kumar A. V. and all DRC members for their continuous support. I want to thank Prof. Navneet Gupta, Head of the EEE Department, for motivating me throughout my degree program. I want to pay my sincere gratitude and thanks to all senior professors Prof. Chandra Shekhar, Prof. Anu Gupta, Prof. H. D. Mathur, Prof. Hari Om Bansal, Prof. Dheerendra Singh, and Prof. K. K. Gupta for their guidance and continuous motivation. Thank them for sharing their knowledge with me, which remains very useful in shaping my ideas and research.

I sincerely express my sincere gratitude and thanks to Prof. Ramgopal Rao, Vice-Chancellor, BITS Pilani to provide me with the opportunity to carry out my Doctoral studies at BITS Pilani. I sincerely thank Prof. Sudhirkumar Barai, Director BITS Pilani, Pilani Campus. I also express my profound gratitude to Prof. S. K. Verma, Dean, Administration, BITS Pilani, Pilani Campus, and Prof. Shamik Chakraborty, Associate Dean, Academic Graduate Studies and Research (Ph.D. Program) Division, for providing valuable support throughout the program.

I wish to heartily acknowledge my lab-mates Vinay Kumar Chapala and Prem Sai Regalla, for their unwavering support and encouragement throughout my research journey. I am deeply thankful to all the research scholars within the department, whose collective assistance and motivation have been invaluable to the progress of my work. I would like to convey my sincere

appreciation to my friends, Jai Prakash Kushvah, Nikhil Pachauri, Amresh Kumar and Shailendra Tripathi, as well as all others whose contributions, both direct and indirect, have played a significant role in helping me navigate challenging situations.

I am also very thankful to all the anonymous reviewers of my research publications. Their comments and suggestions were constructive in shaping my research work.

I would like to dedicate this thesis to my parents, my sisters and my wife. Your endless encouragement, sacrifices, and belief in my abilities have been the foundation upon which my academic pursuits have been built. Your endless support has given me the strength to overcome challenges and pursue my dreams. Your belief in my capabilities has been a source of motivation throughout this journey.

To my wife, Ameesha, your boundless love, understanding, and sacrifices have been my greatest source of strength. Your continuous support, even in the face of countless late nights and missed moments, has been the driving force behind my perseverance. You are my rock, and I am eternally grateful for your presence in my life.

Pranay Bhardwaj
March 2024

Contents

Abstract **iv**

Acknowledgements **v**

List of Figures **xii**

List of Tables **xv**

List of Symbols **xvii**

List of Acronyms/Abbreviations **xix**

1 Introduction **1**

1.1 Literature Survey 3

1.2 Motivation and Objective 8

1.3 Contributions 10

2 Overview of THz Wireless Communications **12**

2.1 Deterministic Path-Loss Model 13

2.2 Antenna Misalignment Errors Model 14

2.3 Short-term Fading Models for THz Link 16

2.3.1 α-μ Model 16

2.3.2 FTR Model 17

2.3.3 Generalized-K Model 17

2.3.4 α-η-κ-μ Model 18

2.3.5 Gaussian Mixture Model 19

2.4 Transceiver Hardware Impairment Model for THz Link 20

2.5 Performance Metrics 20

2.5.1 Average SNR 21

2.5.2 Outage probability 21

2.5.3 Ergodic capacity 21

2.5.4 Average BER 21

2.6 Meijer's-G/Fox's H-function . . . 22
2.7 Chapter Summary . . . 23

3 THz Wireless Communication for Extended Coverage: A General Analysis for Multihop Transmission 24
3.1 Introduction . . . 24
3.2 Motivation and Contribution . . . 25
3.3 System Model . . . 26
3.4 Multihop Terahertz Transmission for Backhaul Link . . . 29
3.4.1 Statistical Results . . . 29
3.4.2 Performance Analysis for CA-multihop and FG-multihop Backhaul Transmission . . . 34
3.5 Performance Analysis of Multihop Backhaul Mixed with Access Link . . . 36
3.5.1 Uplink Transmissions . . . 37
3.5.2 Downlink Transmission . . . 39
3.6 Simulation and Numerical Analysis . . . 42
3.6.1 Multihop Backhaul Transmission . . . 43
3.6.2 Uplink and Downlink Transmission for Mixed Backhaul-Access Link . . . 44
3.7 Chapter Summary . . . 47
3.8 Appendix . . . 48
3.8.1 Appendix 3.1: Proof of Theorem 3.1 . . . 48
3.8.2 Appendix 3.2: Proof of Theorem 3.2 . . . 49
3.8.3 Appendix 3.3: Proof of Proposition 3.2 . . . 49
3.8.4 Appendix 3.4: Proof of Theorem 3.3 . . . 50

4 THz Backhaul Transmission Integrated with Access Network 51
4.1 Introduction . . . 51
4.2 Motivation and Contribution . . . 52
4.3 Integrated THz-RF Wireless Link . . . 54
4.3.1 System Model . . . 54
4.3.2 Cumulative Distribution Function of THz Link . . . 57
4.3.3 Statistical Analysis of SNR . . . 59
4.3.4 Ergodic Capacity . . . 62
4.3.5 Average Bit Error Rate . . . 65
4.4 Simulation and Numerical Results . . . 67
4.5 Integrated THz-RF Wireless Link: Generalized Antenna Misalignment Errors . . . 72
4.5.1 Density and Distribution Functions . . . 74
4.5.2 Outage Probability . . . 76
4.5.3 Simulation and Numerical Results . . . 76

4.6 Integrated THz-RF Wireless Link: Multi-antenna Systems 78
4.7 Performance of SC-RF and THz 81
4.7.1 Outage Probability 82
4.8 Performance of MRC-RF and THz 83
4.9 Simulation Analysis 86
4.10 Chapter Summary 88
4.11 Appendices 89
4.11.1 Appendix 4.1: Proof of Theorem 4.2 89
4.11.2 Appendix 4.2: Proof of Lemma 4.1 89
4.11.3 Appendix 4.3: Proof of Lemma 4.2 90
4.11.4 Appendix 4.4: Proof of Theorem 4.3 92
4.11.5 Appendix 4.5: Proof of Theorem 4.4 93
4.11.6 Appendix 4.6: Proof of Theorem 4.5 93
4.11.7 Appendix 4.7: Proof of Theorem 4.6 95

5 THz-Assisted Backhaul for Data Collection from IoT Network: Distributed Protocol and Performance Analysis 97
5.1 Introduction 97
5.2 Motivation and Contributions 98
5.3 System Description and Channel Models 99
5.4 Protocol Description for Aggregate-Node Selection 102
5.5 Statistical Results for Triple Technology 104
5.6 Data Collection Performance 106
5.6.1 Outage Probability 107
5.6.2 Average BER 108
5.7 Simulation and Numerical Results 109
5.8 Chapter Summary 115
5.9 Appendix 115
5.9.1 Appendix 5.1: Proof of Lemma 5.1 115
5.9.2 Appendix 5.2: Proof of Theorem 5.1 116
5.9.3 Appendix 5.3: Proof of Lemma 5.3 118

6 Low Complexity Algorithms for Multi-User Cell-Free Wireless Networks Exploiting THz Channel Characteristics 120
6.1 Introduction 120
6.2 Motivation and Contributions 121
6.3 System Model 122
6.4 A Generalized Channel Model for THz Transmission 125
6.4.1 Exact Statistical Derivation of α-η-κ-μ Model 125

6.4.2 Statistical Model for Atmospheric Absorption 126
6.4.3 A General THz Model with Combined Channel Effects 127
6.5 Random Access Protocols for multiuser THz transmission 129
6.5.1 Description of the Protocol 129
6.5.2 Performance Analysis for Delay and Scaling Laws 130
6.5.3 Analysis for Energy Consumption Performance 133
6.5.4 Outage Performance for ATP and FTP Protocols 135
6.6 Simulation and Numerical Analysis 136
6.6.1 Generalized Channel Model for THz Transmission with Random Path Loss 136
6.6.2 Random Access Protocols for Cell-Free Network 138
6.7 Chapter Summary 140

7 Conclusions and Future Directions **145**

Appendix **148**

Bibliography **149**

Supervisor Biography **166**

Scholar Biography **168**

List of Publications **170**

List of Figures

2.1 Spectrum allocation for different wireless services. 13
2.2 THz Applications. 14

3.1 Multihop relay-assisted backhaul transmissions integrated with shadowed access link. 27
3.2 Performance of multihop THz backhaul link with 100 m. 43
3.3 Outage probability of the mixed dual-hop relaying system with $m_g = 1$, $\phi_i = 37$, $d_{\mathrm{MH}} = 20$ m, and $d_A = 20$ m. 44
3.4 Outage probability of the mixed multihop relaying system with $m_g = 1$, $\phi_i = 37$, $d_{\mathrm{MH}} = 50$ m and $d_A = 20$ m. 45
3.5 ABER of the mixed dual-hop relaying system with $\sigma_{dB} = 5$, $\phi_i = 37$, $d_{\mathrm{MH}} = 20$ m, and $d_A = 20$m. 46
3.6 ABER of the mixed multihop relaying system with $\sigma_{dB} = 5$, $\phi_i = 37$, $d_{\mathrm{MH}} = 50$ m, and $d_A = 20$m. 47

4.1 Relay assisted THz-RF wireless link. 56
4.2 Outage probability performance of relay-assisted THz-RF wireless link at $\gamma_{\mathrm{th}} = 4$dB with $\phi = 28.9576$ and $S_0 = 0.054$. 68
4.3 Average SNR performance of relay-assisted THz-RF wireless link. 70
4.4 Ergodic capacity performance of relay-assisted THz-RF wireless link. 70
4.5 Average BER performance of relay-assisted THz-RF wireless link. 72
4.6 Outage probability performance of fixed-gain relay-assisted RF-THz wireless link over mixed fading with non-zero antenna misalignment errors at $\alpha_t = 1.5$, $\gamma_{\mathrm{th}} = 4$ dB. 78
4.7 Hybrid multi-antenna RF and THz wireless transmission. 79
4.8 Outage probability of hybrid wireless link (a) different μ and σ_s with $N = 1$ (b) multi-antenna RF receiver with $\alpha_i = 1$ and $\mu_i = 1.2, \forall i$. 88

5.1 System model consisting of data collection from IoT network and triple-technology hybrid backhaul. 100
5.2 Outage probability performance of the Hybrid backhaul link with $m = 0.5, \Delta = 0.9, k = 1, \mu_i = 0, \sigma_i = 0.6$ and strong atmospheric turbulence. 110

5.3 Average BER performance of the hybrid backhaul link with $m = 0.5, \Delta = 0.9, k = 1, \mu_i = 0, \sigma_i = 0.8$ and strong atmospheric turbulence. 111
5.4 Outage probability and average BER performance of integrated link with $m = 0.5, \Delta = 0.9, k = 1, \mu_i = 0, \sigma_i = 0.6$ and strong turbulence with varying number of IoT devices in the access link. 112
5.5 Effect of the number of IoT devices on the average BER performance of the integrated link. 113

6.1 System model for a typical cell-free network. 123
6.2 Generalized channel model for THz propagation with $\alpha = 2$, $\mu = 1$, $\eta = 1$, $\kappa = 1$, $\rho = 4$. 136
6.3 Outage probability for generalized channel model for THz propagation with different ζ and $\alpha = 2$, $\mu = 1$, $\eta = 1$, $\kappa = 1$, $\rho = 4$ at d=100 m.. 137
6.4 Delay and energy consumption performance of random access protocols. 138
6.5 Energy consumption (E_K) of random access protocol using realistic parameters. 139
6.6 Outage probability performance for FTP/ATP protocol over generalized THz channel model at $d = 100$ m. 140

List of Tables

2.1 Parameters for the Molecular Absorption Coefficient k 15
2.2 Shopping mall links parameters of the α-μ distribution. 17
2.3 Special Cases of the Generalized α-η-κ-μ Fading Model 19
2.4 Fitting accuracy metrics of Gaussian mixture distribution with different values of K. 20

3.1 List of Simulation Parameters 42

4.1 Parameters of the molecular absorption coefficient k 68
4.2 List of Simulation Parameters 69
4.3 List of Simulation Parameters 87

5.1 List of Simulation Parameters 109
5.2 Comparison of outage probability for the integrated link using triple, dual, and single-technology based backhaul with $N = 5$ devices in the IoT network. . . . 114

List of Symbols

1. $G_{p,q}^{m,n}\left[z\middle|\begin{matrix}(a_k)_{k=1:p}\\(b_k)_{k=1:q}\end{matrix}\right]$: Meijer's G-function
2. $H_{p,q}^{m,n}\left[z\middle|\begin{matrix}(a_k,A_k)_{k=1:p}\\(b_k,B_k)_{k=1:q}\end{matrix}\right]$: Fox's H-function
3. $\Gamma(a)=\int_0^\infty t^{a-1}e^{-t}dt$: Gamma function
4. $\gamma(a,t)=\int_0^t s^{a-1}e^{-s}ds$: Lower incomplete Gamma function
5. $\Gamma(a,t)=\int_t^\infty s^{a-1}e^{-s}ds$: Upper incomplete Gamma function
6. $(\cdot)_1$: Notation for the first link
7. $(\cdot)_2$: Notation for the second link
8. h : Channel coefficient
9. h_f : Short term fading
10. h_p : Pointing error
11. w : Additive Noise
12. γ : Signal-to-noise ratio with fading
13. $\overline{\mathrm{SNR}}$: Average SNR
14. $\bar{\gamma}$: Signal-to-noise ratio without fading
15. $f(x)$: Probability density function
16. $F(x)$: Cumulative distribution function
17. η : Ergodic capacity
18. P_e : Probability of error
19. J : Complex number

20. $\int_{\mathcal{L}}$: Contour Integral
21. ${}_1F_1(a;b;z) = \sum_{k=0}^{\infty} \frac{\Gamma(a+k)\Gamma(b)}{\Gamma(a)\Gamma(b+k)} \frac{z^k}{k!}$: Confluent Hypergeometric Function of first kind
22. ${}_2\tilde{F}_1$: Regularized Hypergeometric function
23. $\psi^{(0)}(a) = \frac{d}{da} \ln \Gamma(a)$: The psi Function
24. $Q(.) : \frac{1}{\sqrt{2\pi}} \int_{\gamma}^{\infty} e^{\frac{-u^2}{2}} du$
25. $L_n(x)$: Generalized Laguerre polynomial
26. ${}_0\tilde{F}_1$: Regularized hypergeometric function
27. $(\cdot)_{\mathrm{THz}}$: Notation for the THz link
28. $(\cdot)_{\mathrm{RF}}$: Notation for the RF link
29. $(\cdot)_i$: Notation for the i-th element
30. $\mathbb{E}\{\cdot\}$: Expectation operator
31. $\Delta(k,a)$: $\frac{a}{k}$, $\frac{a+1}{k}$, ..., $\frac{a+k-1}{k}$

List of Acronyms/Abbreviations

3GPP	Third Generation Partnership Project
5G	Fifth Generation
6G	Sixth Generation
ABER	Average Bit-Error-Rate
AF	Amplify-and-Forward
AN	Aggregate Node
AP	Access Point
ATP	Adaptive Transmission Protocol
AWGN	Additive White Gaussian Noise
BHL	Backhaul Link
BER	Bit-Error-Rate
BS	Base Station
CA	CSI Assisted
CDF	Cumulative Distribution Function
CSI	Channel State Information
DF	Decode-and-Forward
DO	Diversity Order
FG	Fixed Gain
FPGA	Field-Programmable Gate Array
FSO	Free-Space Optical
FTP	Fixed Transmission Protocol
FTR	Fluctuating Two-Ray

i.i.d	Independent and Identical Distribution
i.ni.d	Independent and Non-Identical Distribution
IoT	Internet of Things
LoS	Line-of-Sight
MAC	Multiple Access Schemes
MIMO	Multi-Input and Multi-Output
MGF	Moment Generating Function
MRC	Maximal-Ratio Combining
mmWave	Millimeter Wave
OSC	Opportunistic Selection Combining
PDF	Probability Density Functions
PLC	Power Line Communication
PSD	Power Spectral Density
QoS	Quality of Service
RAN	Radio Access Network
RIS	Reconfigurable Intelligent Surface
RF	Radio Frequency
SC	Selection Combining
SNR	Signal-to-Noise Ratio
THI	Transceiver Hardware Impairments
TP	Transmission Probability
UAV	Unmanned-Aerial-Vehicle
VLC	Visible Light Communication

Chapter 1

Introduction

Wireless communication has evolved from simple telegraphy to sophisticated global networks, transforming the way people connect and communicate across the world [1–4]. Pioneering work by Maxwell, Hertz, and Marconi in the late 19th century established the foundations for understanding electromagnetic waves. Nyquist and Shannon later set crucial limits on information transmission, laying the theoretical groundwork for subsequent advancements [5, 6]. The 1970s marked the birth of mobile communication with the introduction of the first-generation (1G) cellular networks [7]. Subsequent decades saw the transition to digital communication and the convergence of wireless with the Internet in the late 1990s and early 2000s, giving rise to 2G, 3G, and 4G/LTE. The 2010s witnessed a pivotal moment with the deployment of 5G networks, introducing unparalleled data speeds and low latency in augmented reality and IoT. As we step into the future, ongoing research and development endeavors are focused on 6G, aiming to elevate connectivity, speed, and capabilities to new heights in the ever-evolving landscape of wireless communication.

Fifth-generation (5G) wireless communication is evolving from a theoretical concept to a global reality. This transition is made possible by fundamental technologies, including millimeter-wave (mmWave) propagation, a massive multiple-input multiple-output (mMIMO) antenna array system, and the widespread deployment of ultra-dense networks [8–11]. These technologies collectively deliver high-speed and low-latency wireless connectivity, essential for various applications and services. As 5G networks become more prevalent and advanced, the groundwork for the forthcoming sixth-generation (6G) wireless technology is already being laid [12]. The primary objective of 6G is to push the boundaries of wireless communication even further. It aims to achieve substantially higher data rates, potentially reaching an impressive 1 Terabit per second (1 Tbps), while enhancing reliability and reducing latency. These improvements are crucial to support emerging applications that demand exceptional performance, such as holographic communications, tactile and haptic internet experiences, fully autonomous driving, high-precision manufacturing, and automation in various industries.

To realize the ambitious goals of 6G, several cutting-edge technologies are being considered. Holographic multiple-input multiple-output (MIMO) systems are on the horizon, which

can provide a revolutionary approach to wireless communication [13–15]. Reconfigurable intelligent surfaces (RIS) can enhance wireless signal propagation and coverage by deploying smart, adaptable surfaces in the environment. Artificial intelligence-assisted network management will be pivotal in optimizing network performance, ensuring efficient resource allocation, and enhancing security. Moreover, the exploration of the terahertz (THz) spectrum for wireless communication holds significant promise, offering distinctive possibilities for achieving exceptionally fast and high-capacity wireless connections [16–24].

The THz spectrum represents the next frontier in wireless communication, offering significantly greater and continuous bandwidth (ranging from 0.1 to 10 THz) when compared to the propagation capabilities of mmWave for data transmission. THz wireless technology has the potential to serve as an alternative to both free-space optics (FSO) and mmWave technology for terrestrial backhaul/fronthaul connectivity and last-mile access in the next generation of networks [25, 26]. THz systems possess attractive characteristics, including a continuous and wider channel bandwidth within the license-free spectrum, as well as resilience to atmospheric turbulence, unlike FSO communications [27]. THz communication can facilitate network densification by adding more access points (APs) for the cell-free architecture. In situations where traditional wire-line backhaul options such as digital subscriber lines (DSL) and optical fiber may not be feasible, THz wireless systems emerge as a promising alternative for high-data-rate transmission, contrasting with wireless backhaul/fronthaul operating in the RF/mmWave frequency range [28].

In light of the adoption of mmWave technology in 5G, it is advisable to explore the THz spectrum for 6G wireless communication to address the challenges posed by the scarcity of available spectrum. While the THz band has found applications in spectroscopy, imaging, nano-communication, and various other fields, its utilization for wireless communication is still in its early stages, primarily due to the challenges associated with achieving long-distance communication. At the physical layer, THz propagation faces increased path-loss issues due to factors like molecular absorption, misalignment errors in antennas, intricate signal fading, and transceiver hardware impairments. The path-loss in the THz band is higher due to molecular absorption of the signal at tiny wavelengths [29–32]. The effect of antenna misalignment errors is also detrimental to THz performance, which occurs when transmit and receive antennas fail to adequately align for line-of-sight (LoS) transmissions due to high directivity of the signal beams, significantly limiting the physical communication range [33–36]. In addition to path-loss and misalignment issues, THz transmissions experience complex small-scale signal fading. Simple fading models like Rayleigh and Rician distributions are insufficient to capture the random signal fluctuations at THz frequencies, requiring generalized fading models [29–31, 33, 34, 37–41]. Simple fading models such as Rayleigh and Rician are not adequate to represent the random fluctuation of signal at THz frequencies requiring generalized fading models. Transceiver hardware impairments (THI) represent another significant challenge, as they inevitably degrade the performance of THz communication, especially at high data rates.

These impairments arise from imperfections such as imbalances in in-phase and quadrature-phase signal components, phase noise, and non-linearities in power amplifiers [42].

It is desirable for a thorough performance evaluation of THz wireless communication in diverse propagation conditions, serving as a validation of the concept to enable the effective integration of THz systems into 6G wireless communication. Moreover, developing physical layer algorithms is imperative to seamlessly integrate THz wireless systems into existing infrastructure, including access networks, Internet of things (IoT), and cell-free networks. The proposed research aims to assess the feasibility of THz wireless technology for terrestrial communication in various real-world propagation scenarios and network setups, including backhaul, fronthaul, and access links.

1.1 Literature Survey

In this section, an extensive review of the existing literature is undertaken to identify and emphasize major research gaps in the field of THz wireless communications.

Back in year 2007, the author of the paper [16] envisioned the utilization of the THz band for short-range wireless communications and anticipated its practical implementation by the year 2020. A conceptual discussion on short-range ultra-broadband THz Communications was presented in [17]. The authors in [43] discussed the potential and feasibility of using THz waves in the 100 GHz to 10 THz for future wireless communications and broadly investigated enabling technologies and ongoing research. The authors in [18, 19] provided an overview of the latest advancements in fundamental technologies for THz communications. They also addressed various challenges and technical obstacles that must be considered when planning to implement practical systems in the future. Various facets of Tbps radios operating within the THz frequency spectrum have been addressed in [44]. In their work presented in [20], the authors successfully showcased a wireless connection that attained an impressive data rate of 100 Gbps while covering a 20-meter distance at a carrier frequency of 237.5 GHz. This was achieved by integrating terahertz photonics and terahertz electronics, representing a significant milestone in advancing high-capacity wireless communications.

The THz spectrum can provide tremendously high unlicensed bandwidth, which can be a catalyst for next-generation wireless technologies. However, the path-loss in the THz band is higher due to molecular absorption of the signal at extremely small wavelengths [29–32]. In [29], the authors have presented an experimental characterization of the THz channel (300-320 GHz). The effect of scattering and absorption losses on THz wavelengths in the absence of white noise were examined in [30]. Signal prorogation in the indoor environment with the blockage effects by the walls and human bodies was analyzed in [31]. A spatial modulation technique to mitigate the path-loss at THz frequencies using the properties of densely packed configurable arrays of nano-antennas was presented in [32].

In addition to the path loss, the THz transmissions undergo signal fading due to the multi-path propagation [29–31, 33, 34, 37–41]. The authors in [37] used the radiative transfer theory with molecular absorption to present a propagation channel model for short-distance THz transmissions. In [38], an experimental channel model in an indoor environment at 300 GHz frequency for LOS and non-LOS scenarios was proposed. The authors in [39] have considered m-Nakagami fading to model a 4×4 THz MIMO system. A shadowed Beaulieu-Xie (BX) fading model was suggested in [40]. The authors in [41] used advanced channel characteristics such as spherical wavefront, time-variant velocities, and space-time frequencies to model a three-dimensional non-stationary channel for millimeter-wave and THz transmissions. Recently, the generalized α-μ and fluctuating two ray (FTR) fading models are employed for THz channels due to their tractability in performance analysis [34] [45].

As is for any communication systems, THz systems are impacted by noise, interference [46–50], and antenna misalignment errors [33–36]. A simple and novel noise model and parameters fitting algorithm for THz band considering the molecular noise behavior has been studied in [46]. An analytical model for interference in dense randomly deployed THz network was presented in [47]. The authors in [48] proposed a model for channel noise inside human tissues at the THz band considering the molecular absorption. The authors in [49] presented a noise model for an intra-body system including Johnson-Nyquist, Black-body, and Doppler-shift induced noise at THz frequencies. The effect of misalignment errors at higher frequencies is inevitable even with highly directional signal beams. The authors in [36] improvised antenna gains for THz frequencies under the beam misalignment error due to the movement of antennas. Significant research has recently been carried out to model the noise and interference for THz systems [46–49]. Recently, a statistical model for antenna misalignment errors for the THz system appeared in [51].

Relay-assisted communication is a potential technique to deal with channel fading as well as increase the data rate and extend the coverage range in wireless systems [52–54]. There has been an extensive research on the relay-assisted multihop transmission for radio frequency (RF) systems [55–61] and FSO systems with antenna misalignment errors [62–67]. The authors in [55] and [62] analyzed the exact outage probability of channel state information (CSI) assisted (CA)-multihop transmissions over Nakagami-m and Gamma-Gamma fading channels, respectively. In [56], the authors used the method of induction to derive bounds on the performance of CA and fixed gain (FG)-assisted multihop transmissions over Nakagami-m fading channels. Similarly, the method of induction was used to derive bounds on the performance of CA and FG-assisted multihop transmissions for FSO systems with Gamma-Gamma atmospheric turbulence and antenna misalignment errors [63]. In [65], an exact probability density function (PDF) of FG-assisted multihop transmission for an FSO system with double generalized Gamma with antenna misalignment errors was presented by generalizing the analysis for N hops using the results obtained up to three hops. To this end, it should be mentioned that there is an extensive literature on the decode-and-forward (DF)-based multihop relaying [66, 68–72]. However, the

DF system requires each hop's CSI for decoding. In [72], the DF relaying was used in each hop for the mixed system consisting of multihop-assisted FSO and a single RF link. It should be mentioned that the propagation characteristics and application scenarios for THz are different from other state-of-the-art technologies such as RF and FSO.

In the context of THz, dual-hop THz-THz transmission has been studied in [73–81]. The authors in [73] presented a hybrid precoding design for the dual-hop MIMO THz network. In [74], the authors presented the outage probability analysis of a dual hop THz-THz system using the DF relaying protocol. In [75], the authors analyzed the THz-THz dual-hop system with fixed-gain relaying considering zero-boresight antenna misalignment errors, while the authors in derived an upper bound on the performance analysis of a dual hop THz-THz link utilizing FG amplify-and-forward (AF) relaying technique. The authors in [76] suggested a relaying scheme to optimize the network throughput for THz-band wireless communications. A multi-relay selection strategy to mitigate the antenna misalignment and channel fading was proposed in [77]. The authors in [78] considered an AF relay for nano-scale THz transmissions without considering the effect of short-term fading. Considering Rayleigh fading, [79] studied an AF-assisted cooperative In-Vivo nano communication at THz frequencies. The authors in [80] proposed a simplified hybrid precoding design for THz-MIMO communication system consisting of a two-way AF relay with orthogonal frequency division multiplexing (OFDM). The outage probability of a THz-THz relaying scheme with MIMO is presented in [81]. In [82], an energy-efficient multihop routing protocol for the THz wireless nano-sensor network has been proposed. The authors in [83] investigate the beam-forming techniques for multihop RIS empowered THz communications over Rician fading. A gap exists in the research when it comes to assessing the effectiveness of multihop THz transmissions as a means to extend the communication range.

Incorporating a novel technology into the current network infrastructure is a crucial undertaking when embracing new technological advancements. Mixed or integrated RF-FSO systems have been extensively studied in [84–98]. A dual-hop RF-FSO relay system over the asymmetric links was studied in [84]. The BER performance and the capacity analysis of an AF-based dual-hop mixed RF–FSO were presented in [85]. The authors in [86] have investigated the end-to-end outage performance, where the RF and FSO links were modeled as Rayleigh and M-distributed, respectively. The authors in [87–89] have analyzed the FSO performance under the turbulence and antenna misalignment errors using a dual-hop transmission with a single-relay without direct transmissions. Recently, a dual-hop relaying combined with mmWave and FSO technologies was studied in [91]. It should be emphasized that the FSO system experiences entirely different fading channels (i.e., atmospheric turbulence) compared with the THz. Other hetrogenous networks also exist such as RF-power line communications (PLC) [99], mmWave-FSO[100, 101], PLC-visible light communications (VLC) [102], and RF-underwater wireless communications (UWOC) [103].

In the light of above, there is limited research on the RF-THz integrated network [33]. The authors in [33] considered the DF relaying protocol to facilitate data transmissions between

the THz-RF mixed link. They have developed outage probability, average bit-error-rate (BER), and ergodic capacity performance for THz-RF transmissions by deriving PDF and cumulative distribution function (CDF) of the THz link in terms of incomplete Gamma function over α-μ fading with zero-boresight antenna misalignment errors. It is well known that α-μ is a generalized model which includes Weibull, negative exponential, popular Nakagami-m, and Rayleigh distribution as a particular case to model short-term fading at RF frequencies [104].

Data collection in IoT networks can be challenging due to data volume, difficult terrain, and energy limitations of IoT devices. In recent years, researchers have focused on addressing the issue of efficient data collection in IoT networks [105–111]. The authors in [106] propose an information-centric data collection algorithm, which supports the collection of multimedia sensor data in the short-range between mobile devices and wireless sensors based on their moving speeds. The work presented in [107] focuses on a secure data collection scheme for an IoT-based healthcare system using field-programmable gate array (FPGA) hardware-based ciphers and secret cipher shared algorithms. In [109], the authors have presented a thorough survey of unmanned aerial vehicle (UAV)-assisted data collection technologies, including clustering of sensor nodes, UAV data collection mode, and resource allocation. The authors in [110] have addressed the issue of data collection maximization with an energy constraint UAV in an IoT network. The authors in [111] investigate the use of UAVs to efficiently collect sensed data in wireless rechargeable sensor clusters located in challenging terrains. It is desirable to develop algorithms for distributed selection of AN for efficient data collection.

Recent research investigates various high-speed hybrid wireless backhaul networks as potential alternatives to wireline optical fiber and DSL [112–119]. In [112], the authors have analyzed a point to a multi-point communication system for multiple FSO and RF users employing hybrid FSO-RF link. Another study [114] presented a low-cost hybrid RF/FSO backhaul solution, where base stations are connected using optical fiber or hybrid links. In [115], the authors considered a hybrid FSO/RF backhaul network to provide seamless connectivity in rural areas. The work in [116] focused on a multiuser mixed RF and hybrid FSO/RF system, where multiple mobile users transmit their data to an intermediate DF relay node through a virtual multiple-input multiple-output MIMO RF link. In [117], a switching scheme was proposed for a DF-relaying-based hybrid FSO/RF system using maximal-ratio combining (MRC) at the destination. A study on the performance of a hybrid mmWave/FSO system was described in [118] and supported by Monte Carlo simulations. In [119], the authors proposed a hybrid FSO/THz-based backhaul network to deliver high data rates to terrestrial mobile users through mmWave access lines. Nevertheless, none of these studies have explored the simultaneous combination of all three communication methods (mmWave, FSO, and THz), a possible approach for next-generation wireless communication networks, particularly in high data rate and high bandwidth applications. Note that combined approach for hybrid and mixed wireless communication has also been studied in [120–124].

THz wireless technology holds the potential to play a vital role in access networks, particularly in densely deployed networks with limited coverage, such as cell-free networks [125–128]. Specifically, cell-free networks are envisioned as a crucial wireless communication architecture where multiple access points (APs) are strategically placed within a defined area to serve multiple users in close proximity. Consequently, the distance between users and APs is significantly reduced compared to traditional cellular systems. This inherent characteristic positions the THz band as an ideal candidate for integration into multiuser cell-free networks [129–132].

THz wireless backhaul/fronthaul networks have been investigated specifically in the context of single-user transmission [75, 119, 124], limited research have focused on the multi-user THz wireless communications [133–137]. The authors in [133], the authors propose hybrid beamforming applicable to situations involving single-users as well as multiple users. The authors in [134] introduced a communication system for a multi-user scenario in the terahertz range utilizing a uniform circular array incorporating both downlink and uplink transmission strategies. In [135], the authors propose a sensing-aided THz wideband hybrid precoding for multi-user environment. The authors in [136] address the channel estimation problem for an reconfigurable intelligent surface (RIS)-aided THz multi-user multi-input single-output system utilizing a two-stage channel estimation scheme. In [137] presents a physical random access channel preamble design for the 6G cellular communication systems in the sub-THz bands.

The use of THz band for cell-free wireless communication is studied in [129–132]. The authors in [129] and [130] list qualitative research directions for the use of THz in the cell-free mMIMO systems. The work presented in [131] proposes employing the THz spectrum for wireless backhaul connections connecting UAV base stations to central-processing unit (CPU). The authors in [132] explores the vulnerability of THz wireless technology to physical-layer jamming in the framework of cell-free mMIMO systems.

Multiuser interference cancellation has been studied extensively for cell-free wireless network [138–142]. The interference cancellation requires complex signal processing at the CPU and significant overheads. In this context, random access protocol can be a potential alternative [91, 143–147]. The authors in [143] introduce random access control strategies designed to mitigate collisions and maintain system stability under high traffic loads by limiting the number of transmissions and retransmissions. The authors in [144] present an adaptive protocol design for ad-hoc networks in which mobiles learn the local topology and incorporate this information to adapt their medium access probability (MAP) selection to their local environment. In [145], the authors use an adaptive-opportunistic ALOHA media access control protocol for unmanned aerial vehicle-wireless sensor network (UAV-WSN) systems. In [146], the authors propose a random access scheme for an indoor optical wireless communication (OWC) massive IoT scenario such that collisions occurring at access points are resolved by employing a centralized interference cancellation that harnesses both spatial and temporal diversity. In [91], the work presents an adaptive transmission protocol to improve the performance of slotted ALOHA, which transmits periodically in different time slots to minimize packet collisions. The work

in [147] proposes an adaptive random access protocol for massive IoT networks that exploits nonorthogonal multiple access (NOMA) with short-packet transmissions and automatic request and repeat (ARQ) strategy with a limited number of retransmissions.

Considering the literature discussed above, several research gaps become evident within the field of THz wireless communications. These gaps include topics like multihop THz transmission for extending range, the integration of RF-THz networks across diverse scenarios, data gathering from challenging terrains, and the development of low-complexity multiuser THz transmission techniques for short-range communications.

1.2 Motivation and Objective

This section provides insight into the motivation behind the proposed research, taking into account the existing research gaps within THz wireless communication.

The existing relay-assisted THz wireless system is limited to dual-hop transmission with antenna misalignment errors and short-term fading without considering the shadowing effect. The multihop THz system extending the range of backhaul link has not been studied in the literature. It is well-known that analyzing the performance of multihop transmissions, even for single-parameter RF fading distributions is challenging, especially when multihop links are assisted by the AF relaying. In general, the performance of multihop-assisted AF relaying is approximated by expressing the resultant SNR as the product of SNR of individual links using the inequality of harmonic and geometric mean. Further, the method of induction (generalization for N hops realized through expressions derived for the first few hops) is applied to derive the PDF, and thereby CDF of the multihop system [63]. Note that the mathematical induction method is not applicable for THz transmissions under the combined effect of α-μ fading with antenna misalignment errors and requires novel approaches for its statistical analysis. Moreover, it is desirable to derive exact analytical expressions of a CA relaying, which serves as a benchmark for all practical multihop systems employing AF relays [63].

The existing integrated RF-THz system has several research gaps. Firstly, the statistical analysis is limited to integer values of the fading parameter, μ. Secondly, the assumption of short-term fading being independent and identically distributed (i.i.d) with identical parameters α and μ for both the THz and RF channels may not be feasible considering two technologies operating at different frequency bands. Existing analytical tools are readily applicable to analyze the performance of THz-RF over i.i.d. fading. Moreover, there is a lack of asymptotic results that could offer valuable insights into the relationship between antenna misalignment errors and fading parameters, even in the context of the i.i.d. THz-RF mixed system. Furthermore, there is no analysis for average SNR and ergodic rate performance for THz-RF relaying. Performance bounds, along with in-depth analyses of metrics such as outage probability, average signal-to-noise ratio (SNR), ergodic rate, and average bit-error rate (BER), are crucial for real-time system parameter adjustments, contributing to the efficient deployment of THz-RF

systems. Thirdly, the existing research primarily focuses on single-antenna RF systems. It requires novel approaches to derive statistical results of the end-to-end system in a closed form when the diversity combining technique is applied at the RF receiver and integrated with the THz link over generalized fading channels.

Current research primarily focuses on collecting data from IoT devices to an AP or a UAV with little emphasis on further transmitting it to the core network through a backhaul link. Further, the algorithms used for data collection must be optimized, considering the energy constraints of IoT devices. Moreover, the backhaul must be capable of handling the amounts of data generated by IoT devices while also providing high reliability. Thus, developing a low-complexity data collection algorithm for IoT networks, coupled with a robust backhaul, is essential to ensure seamless connectivity with the core network. The end-to-end data collection performance from an IoT network in hard-to-access terrains transferred to the core network via an intermediate UAV and a high-speed wireless backhaul should be investigated.

The current research on THz wireless communications is predominantly focused on its application in backhaul/fronthaul connectivity with a model appropriate at the sub-THz band. While conventional RF is commonly employed in access links, it is crucial to investigate multiuser transmission schemes based on random access designed for the THz band. Low complexity multiuser transmission for cell free-network is possible by exploiting the combined effect of random atmospheric absorption, non-linearity of fading, hardware impairments, and antenna misalignment errors. The current model assumes a deterministic path-loss, suitable for stable channel environments like backhaul/fronthaul scenarios. The multi-parameter α-η-κ-μ can fit the experimental data at true THz frequencies more accurately in various scenarios. Existing statistical analysis either neglects THI's effect or provides approximate results when analyzing the performance of the THz system combined with channel fading and antenna misalignment. A more general THz model is required to facilitate the development of low-complexity algorithms for multiuser THz transmission.

The efficiency of a random access protocol depends on the quantity of users seeking channel access. Unlike RF, THz signal propagation introduces heightened complexity, encompassing factors such as losses from molecular absorption, short-term fading, antenna misalignment errors, and impairments in transceiver hardware. Currently, there is no research available on a random access protocol designed for a cell-free wireless network that capitalizes on the distinctive features of THz signal propagation.

Motivated by the above discussion, the primary objectives of this dissertation are given as follows:

- Extend coverage for THz wireless backhaul connectivity using multihop transmission.

- Analyze the integration of the THz backhaul link with access network over conventional RF propagation.

- Design distributed protocols for data collection from IoT network assisted by the hybrid THz/mmWave/FSO technologies.

- Develop random access protocols for multi-user cell-free wireless networks exploiting THz channel characteristics.

1.3 Contributions

The thesis consists of seven chapters and delves into the performance analysis and algorithm design for THz wireless communication, along with its integration into various networks, including access, IoT, and cell-free. In the subsequent sections, we provide a detailed overview of the key contributions in each chapter of the thesis.

In the present chapter, we reviewed the related research work to point out various research gaps in the study highlighting motivation to pursue the current research.

Chapter 2 reviews the THz system and its applications. We also explore different types of channel models for signal attenuation, short-term fading, and antenna misalignment errors. Also, an informal overview of the performance metrics for the THz system is presented.

In Chapter 3, we analyze the performance of a multihop-assisted THz link for both uplink and downlink transmissions. We consider the AF relaying for the multihop system and employ DF and AF protocols to interface with the end-user for uplink and downlink, respectively. We consider the generalized independent and not identically distributed (i.ni.d.) α-μ fading distribution for the multihop link and the composite generalized-K shadowed fading for the end-user link, both under the combined effect of antenna misalignment errors. We derive novel PDF and CDF of the end-to-end SNR of the multihop backhaul link employing CA relaying for each hop. We develop an upper bound for the FG relaying based multihop transmission by deriving the exact PDF of the product of N i.ni.d. random variables that are distributed according to the product of α-μ fading and antenna misalignment errors. We develop statistical results of an all FG-relayed downlink transmission by employing the FG protocol in the last hop to mix the FG-multihop and access link in terms of the bivariate Fox's H-function. We validate the derived analysis using Monte-Carlo simulations and demonstrate the significance of multihop relaying to extend the communication range for THz wireless transmissions under the effect of fading, antenna misalignment errors, and shadowing.

In Chapter 4, we analyze the performance of integrated THz-RF link for data transmission between the central processing unit of a core network and a user through an AP in a wireless network over α-μ fading channels. We consider a generalized model for the end-to-end channel with i.ni.d. fading model for THz and RF links, the THz link with antenna misalignment errors, and asymmetrical relay position between the source and destination. We derive a closed-form expression of the CDF for the SNR of the THz link using the combined effect of α-μ fading and antenna misalignment errors. The derived CDF is also valid for non-integer values of μ for a generalized performance analysis over THz fading channels. We also analyze the performance

of a mixed RF-THz wireless system assisted by a fixed-gain AF relaying by considering non-zero boresight antenna misalignment errors with α-μ fading for the THz and generalized α-κ-μ shadowed (α-KMS) fading [148] for the RF link. Finally, we analyze the performance of a two-tier system consisting of a single-antenna THz link and a multiple antenna receiver system for RF transmission in an uplink wireless network.

In Chapter 5, we investigate end-to-end performance of data collection from an IoT network in hard-to-access terrains transferred to the core network via an intermediate UAV and a high-speed wireless backhaul link (BHL). We consider triple technology in the backhaul to harness the diversity of three links without increasing the data rate of the backhaul. We develop a self-configuring protocol for aggregate-node (AN) selection, which sends a data packet collected from the IoT network to a UAV. We utilize a hybrid triple-technology wireless BHL, which simultaneously transmits the information from the UAV to the core network using mW, FSO, and THz links for high-speed and reliable data transmission. The inclusion of THz connectivity into the current hybrid mmWave/FSO system brings about system diversity, resulting in improved performance, increased reliability, and superior quality of service (QoS) in different scenarios, particularly in challenging weather conditions. We also integrate the IoT network and BHL employing the DF protocol at the UAV and analyze the physical layer performance using the outage probability and average BER.

In Chapter 6, we develop a generalized statistical model for signal propagation at THz frequencies encompassing physical layer impairments, including random path-loss with Gamma distribution for the molecular absorption coefficient, short-term fading characterized by the α-η-κ-μ distribution, antenna misalignment errors, and transceiver hardware impairments. Next, we propose random access protocols for a cell-free wireless network, ensuring successful transmission for multiple users with limited delay and energy loss, exploiting the combined effect of random atmospheric absorption, non-linearity of fading, hardware impairments, and antenna misalignment errors. We consider two schemes: a fixed transmission probability (FTP) scheme where the transmission probability (TP) of each user is updated at the beginning of the data transmission and an adaptive transmission probability (ATP) scheme where the TP is updated with each successful reception of the data. We analyze the performance of both protocols using delay, energy consumption, and outage probability with scaling laws for the transmission of a data frame consisting of a single packet from users at a predefined quality of service (QoS).

Chapter 7 concludes this thesis by providing a summary, and indicating possible directions for future research.

Chapter 2

Overview of THz Wireless Communications

THz technology has garnered substantial attention within both the academic and industrial communities for wireless communication [21–24]. This heightened interest can be attributed to the intriguing characteristics of THz waves, which include the availability of tens and hundreds of gigahertz in bandwidth and the relatively low health risk associated with this frequency range. Furthermore, as millimeter-wave communication systems continue to advance, researchers are naturally shifting their focus toward the THz spectrum. In accordance with Shannon's theory, the expansive bandwidth offered by the THz frequency bands has the potential to support Tbps wireless communication systems. This opens up exciting possibilities for various applications, such as holographic communications, tactile and haptic internet experiences, fully autonomous driving, high-precision manufacturing, and automation in various industries. These applications collectively enhance the quality of services and provide users with superior experiences [12]. Nevertheless, while THz technology holds promise for meeting the demand for exceptionally high data rates, it is essential to acknowledge the presence of numerous technical challenges that must be overcome [23, 24].

With growing congestion in the spectrum, even in the mmWave band, the focus of spectrum allocation is shifting towards the THz bands to accommodate various wireless communication applications. The primary aim of this spectrum allocation is to ensure the efficient and interference-free operation of a wide array of wireless services as depicted in Fig. 2.1.

The THz band boasts diverse applications in fields like research and exploration, encompassing spectroscopy, astronomy, and material characterization. Further, it is used for imaging and sensing tasks, such as security screening and medical diagnostics as shown in Fig. 2.2. Furthermore, the THz band holds significant potential in domains including wireless communication, military and defense, and atmospheric and environmental research, owing to its vast bandwidth and distinctive channel characteristics. THz wireless communication opens up possibilities for a wide range of indoor and outdoor applications, spanning from short distances of a few meters to extended connections up to kilometers. In the context of backhaul, wireless

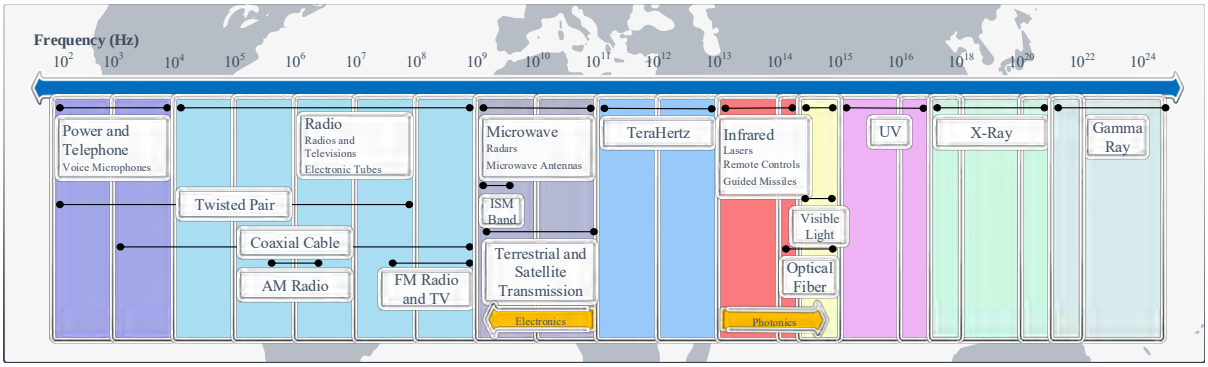

Figure 2.1: Spectrum allocation for different wireless services.

point-to-point links are commonly employed to transmit data to the base stations, particularly in areas where optical fiber infrastructure is unavailable. These areas include rural and remote areas, developing regions, hard-to-access terrains, and temporary installations where installing optical fiber is either challenging or not economically viable. In the case of fronthaul, wireless point-to-point links establish connections between a base station and the remote radio unit. These systems typically require strict LoS conditions between the transceivers at both link ends.

The THz frequency band exhibits specific traits, including high-frequency attenuation, molecular absorption, and distinctive scattering properties [29–32]. Further, using highly directional antenna radiation patterns to counteract high path loss often results in frequent beam misalignments due to the relative movement of transmitting and receiving antennas [51]. The THI also plays a significant role in the performance of the communication systems at the THz frequencies. These effects must be considered during the channel modeling process. Consequently, the existing channel models intended for the RF band are unsuitable for the THz band, as they do not account for various phenomena such as attenuation and noise introduced by molecular absorption and scattering from particles of a size comparable to the very short wavelength of THz waves [149]. These considerations underline the necessity for developing new models that effectively characterize the intricacies of the THz spectrum.

In the following, we describe channel models for THz wireless communication.

2.1 Deterministic Path-Loss Model

Path-loss in THz wireless communication refers to the reduction in signal strength as THz waves propagate through the atmosphere. This loss occurs due to various physical phenomena and interactions unique to the THz frequency range. Path loss is a critical consideration in THz communication system design and analysis. Several factors contribute to path loss in THz wireless communication such as Free-space path-loss, antenna gains, frequency, atmospheric

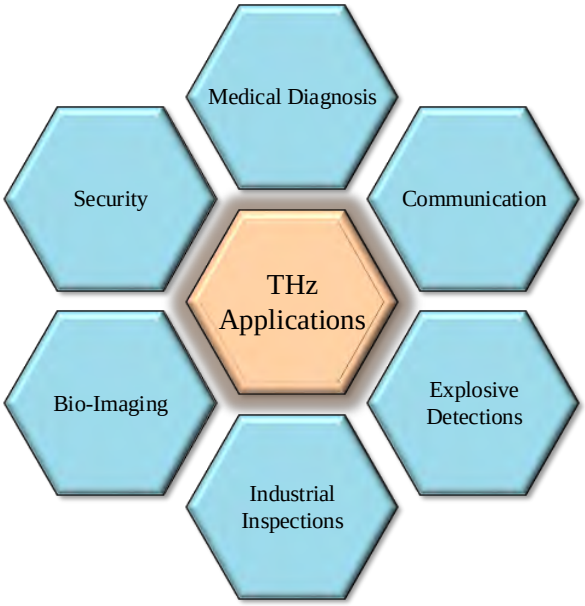

Figure 2.2: THz Applications.

absorption and scattering. The deterministic path-loss H_l for a THz wireless link is mathematically expressed as [34]:

$$H_l = \frac{c\sqrt{G_t G_r}}{4\pi f d} \exp(-\frac{1}{2}k(f,T,\psi,p)d) \tag{2.1}$$

where c, f, and d respectively denote the speed of light, the transmission frequency and distance. G_t, and G_r are the antenna gains of the transmitting antenna and receiving antenna, respectively. The term $k(f,T,\psi,p)$ is the molecular absorption coefficient depends on the temperature T, relative humidity ψ and atmospheric pressure p

$$\begin{aligned} k(f,T,\psi,p) = &\frac{q_1 v(q_2 v + q_3)}{(q_4 v + q_5)^2 + (\frac{f}{100c} - p_1)^2} + \frac{q_6 v(q_7 v + q_8)}{(q_9 v + q_{10})^2 + (\frac{f}{100c} - p_2)^2} \\ &+ c_1 f^3 + c_2 f^2 + c_3 f + c_4 \end{aligned} \tag{2.2}$$

where $v = \frac{\psi}{100}\frac{p_w(T,p)}{p}$. The term $p_w(T,p)$ represents the saturated water vapor partial pressure at temperature T, and can be evaluated based on Buck's equation. The values of the other parameters are given in Table 4.1 [34].

2.2 Antenna Misalignment Errors Model

Antenna misalignment error models in THz wireless communication are critical for understanding the impact of misalignment between transmitting and receiving antennas on signal quality and system performance. Misalignment errors can significantly degrade THz communication links due to the highly directional nature of THz waves.

Table 2.1: Parameters for the Molecular Absorption Coefficient k

Symbol	Value	Symbol	Value
q_1	0.2205	q_2	0.1303
q_3	0.0294	q_4	0.4093
q_5	0.0925	q_6	2.014
q_7	0.1702	q_8	0.0303
q_9	0.537	q_{10}	0.0956
c_1	5.54×10^{-37} Hz^{-3}	c_4	-6.36×10^{-3} Hz^{-3}
c_2	-3.94×10^{-25} Hz^{-2}	p_1	10.835 cm^{-1}
c_3	9.06×10^{-14} Hz^{-1}	p_2	12.664 cm^{-1}

To model antenna misalignment errors, we assume a Gaussian beam with a beamwidth (w_z) propagating over a distance z from the transmitter to the detector with aperture radius r. When there is a misalignment, the antenna misalignment error loss coefficient can be approximated as [150]

$$h_p(\tau; z) = A_0 \exp\left(-\frac{2\tau^2}{w_{z_{\text{eq}}}^2}\right) \tag{2.3}$$

where τ is the radial displacement between the centers of the beam and detector, A_0 is the fraction of collected power at $\tau = 0$ derived through $A_0 = \text{erf}(\upsilon)^2$ with $\upsilon = \sqrt{\pi/2}\, r/w_z$ and w_z as the beam width. Here, $w_{z_{\text{eq}}}$ is the equivalent beamwidth at the receiver [150]. For a statistical modeling of the antenna misalignment error, we can assume horizontal and vertical displacements as Gaussian distributed $\tau_x \sim \mathcal{N}(\mu_x, \sigma_x^2)$ and $\tau_y \sim \mathcal{N}(\mu_y, \sigma_y^2)$, where μ quantifies the boresight and σ^2 is the variance of jitter. Assuming zero-boresight (i.e., $\mu_x = \mu_y = 0$) and equal jitter ($\sigma_x = \sigma_y = \sigma_s$), the radial displacement τ follows a Rayleigh distribution. We define $\rho = \frac{w_{z_{\text{eq}}}}{2\sigma_s}$. Using the Rayleigh distribution of τ and applying transformation of random variables in (2.3), the PDF of h_p is given as [150]:

$$f_{h_p}(x) = \frac{\rho^2}{A_0^{\rho^2}} x^{\rho^2 - 1}, 0 < x \leq A_0 \tag{2.4}$$

Next, we use the generalized non-zero boresight statistical model for h_p [151]:

$$f_{h_p}(h_p) = \frac{\phi \exp\left(\frac{-s^2}{2\sigma^2}\right)}{A_0^{\phi}} h_p^{\phi-1} I_0\left(\frac{s}{\sigma^2}\sqrt{\frac{w_{z_{\text{eq}}}^2 \ln\frac{S_0}{h_p}}{2}}\right) \tag{2.5}$$

where $s = \sqrt{\mu_x^2 + \mu_y^2}$ is the boresight displacement with μ_x and μ_y representing horizontal and vertical boresight values, respectively, S_0 is the fraction of collected power without antenna misalignment errors, ϕ is the ratio of normalized beam-width to the jitter, and $I_0(\cdot)$ denotes the modified Bessel function of the first kind with order zero.

Most of the literature provides statistics of the THz link over short-term fading and FSO antenna misalignment errors. The antenna misalignment errors in the THz band for aerial/mobile communication [51, 152] are statistically modeled using the PDF

$$f_{h_p}(h_p) = -\rho^2 \ln(h_p) h_p^{\rho-1} \tag{2.6}$$

where $0 < x < 1$. $\rho = \sqrt{\frac{w_B^2}{\sigma_\theta^2}}$ determines the severity of the misalignment errors, where w_B is the angular beamwidth (beam divergence) of the signal and σ_θ is the variance of the angular fluctuation, which models the effect of angular fluctuations at both the transmitter and receiver. This model effectively captures the dynamics of UAV-assisted THz transmission. If the standard deviation of the jitter $\sigma_s \to 0$, the antenna misalignment errors parameter ρ will also approaches to infinity ($\rho = \frac{w_{z_{\text{eq}}}}{2\sigma_s} \to \infty$). Therefore, the PDF of antenna misalignment errors h_p will be zero, that means there is no effect of antenna misalignment errors (i.e., $h_p = 1$).

2.3 Short-term Fading Models for THz Link

Short-term fading models for THz wireless communication are essential for understanding the rapid and momentary fluctuations in signal strength that occur over short periods of time. These models help characterize the dynamic nature of THz channels. The choice of a short-term fading model in THz communication depends on the specific characteristics of the channel, including the presence of line-of-sight components, non-linearity of the channel, multipath clusters, power level of signal components, and scattering level of the propagation environment. We have used the following distributions to model the short-term fading in the THz wireless link.

2.3.1 α-μ Model

Recently, the authors in [149] conducted extensive experiments in indoor environments to model short-term fading of THz signal at a frequency of 143 GHz. It is shown in [149] that classical fading models for the RF (Rayleigh, Rice, and Nakagami-m) lack fitting accuracy, whereas the α-μ distribution provides an excellent fit. The PDF of the fading channel $|h_f|$ with the $\alpha - \mu$ distribution for the THz link is given as

$$f_{|h_f|}(x) = \frac{\alpha \mu^\mu}{\Omega^{\alpha\mu}\Gamma(\mu)} x^{\alpha\mu-1} \exp\left(-\mu \frac{x^\alpha}{\Omega^{\alpha\mu}} \right) \tag{2.7}$$

where Ω is the α-root mean value of the fading channel envelope. Here, α denotes the channel non-linearity while μ specifies the number of multipath clusters in the THz channel and $\Gamma(\cdot)$ denotes the Gamma function.

The α-μ is a generalized short-term fading model which includes Weibull, negative exponential, Nakagami-m, and Rayleigh distribution as a special case [104]. Recent experiment campaigns validates α-μ distribution for the short term fading in THz link at a 142 GHz carrier

Table 2.2: Shopping mall links parameters of the α-μ distribution.

Transmitter Number	**Link Distance (m)**	α	μ
1	5.1	3.35467	1.11365
2	10.04	3.28199	1.71725
4	27.51	4.9364	0.31735
7	65.2	4.04712	0.44506
24	3.15	3.37619	2.77203

frequency for a link length within 50 m [149, 153]. A concise table of experimental data in a Shopping mall is presented in Table 2.2[149].

2.3.2 FTR Model

The authors in [45] used the actual measurement data demonstrating the better fit of the FTR model than the α-μ at a frequency of 304.2 GHz. To model the small-scale fading in the THz band, we also use the FTR fading channel. The FTR channel model is specifically designed to capture the statistical properties of a received signal that consists of dominant specular components along with random fluctuations. It has been shown to provide a more accurate representation of small-scale fading measurements in mmWave communications compared to other fading models [154].

To model $|h_{fi}|^2$, we use the FTR fading channel with PDF given as [154]:

$$f_{|h_{fi}|^2}(x) = \frac{m^m}{\Gamma(m)} \sum_{j=0}^{\infty} \frac{K^j d_j x^j}{(\Gamma(j+1))^2 (2\sigma^2)^{j+1}} \exp(-\frac{x}{2\sigma^2}) \tag{2.8}$$

where K is the ratio of the average power of the dominant component and multi-path, m is the index of fading severity, and Δ denotes the similarity of two dominant waves. The term σ^2 represents the variance of diffused components such that $\sigma^2 = \frac{1}{2(1+K)}$ for the normalized averaged SNR. The factor d_j is defined in [154] and recently updated with an additional factor in [155].

2.3.3 Generalized-K Model

In [156], the generalized-K fading distribution is adopted to model the THz transmissions in the access link. We consider the generalized-K distribution to model the instantaneous power $|h_k|^2$ (which includes the short term fading and random path gain) of the shadowed THz access link [157]:

$$f_{|h_k|^2}(x) = \frac{2b^{m_A}}{\Gamma(m_\Omega)\Gamma(m_g)} x^{\frac{m_A}{2}-1} K_{m_M}(2b\sqrt{x}), \tag{2.9}$$

where $m_\Omega = \frac{1}{\exp(\sigma_n^2)-1}$, $\sigma_n>0$ denotes the severity of shadowing with factor $\sigma_{\text{dB}} = 8.686\sigma_n$, $m_g>0$ is frequency dependent parameter characterizing the small-scale fading, $m_A = m_\Omega + m_g$ and $m_M = m_\Omega - m_g$ are the distribution shape parameters of $K_\nu(.)$, which is modified Bessel function of the second kind of ν-th order, and $\Gamma(.)$ denotes the gamma function. Denoting $k_A(f)$ as the absorption coefficient, d_A as the distance of the access link, G_A as the antenna gain, P_A as the transmit power, η as the path loss coefficient, we define $b = \sqrt{\frac{m_\Omega m_g}{G_A^2 P_A \varphi \exp(\sigma_n^2/2)} \left(\frac{c}{4\pi d_A f}\right)^\eta}$, where $\varphi = \exp(k_A(f)d_A)$ is the path loss due the molecular absorption of the signal transmission in the THz band.

2.3.4 α-η-κ-μ Model

In [158], M. D. Yacoub proposed the α-η-κ-μ model as the most flexible and comprehensive wireless channel fading model at high frequencies since it encapsulates various fading characteristics such as nonlinearity of the propagation medium, number of multi-path clusters, scattering level, and power of the dominant signal components. Later, Silva *et al.* [159] improved the mathematical representation of the PDF and CDF of the channel envelope. The multi-parameter α-η-κ-μ model encompasses α-μ, κ-μ, η-μ, α-η-μ, and α-κ-μ as the special cases, and thus can fit the experimental data for mmWave and THz signals more accurately in a variety of scenarios.

The envelope R of the α-η-κ-μ is given by [158][159]

$$R^\alpha = \sum_{i=1}^{\mu_x} (X_i + \lambda_{x_i})^2 + \sum_{i=1}^{\mu_y} (Y_i + \lambda_{y_i})^2 \tag{2.10}$$

where α denotes the non-linearity of the channel, μ_x and μ_y denote the number of multi-path clusters of in-phase component and quadrature component, respectively, λ_{x_i} and λ_{y_i} are the average values of the in-phase and quadrature components of the multi-path waves of the i-th cluster, respectively, and $X_i \sim \mathcal{N}(0, \sigma_x^2)$ and $Y_i \sim \mathcal{N}(0, \sigma_y^2)$ are mutually independent Gaussian processes, where σ_x^2 and σ_y^2 are variances of in-phase and quadrature components of the multi-path waves, respectively. In general, the α-η-κ-μ model is quantified by seven different parameters, namely α, η, κ, μ, p, q, and $\hat{r}$. To define these parameter, denote the power of in-phase (x) and quadrature-phase (y) components of dominant (d) waves and scattered (s) waves as P_{ab}, where $a \in \{d, s\}$ and $b \in \{x, y\}$. Thus, we define the parameters as $\eta = \frac{P_{sx}}{P_{sy}}$, $\kappa = \frac{P_{dx}+P_{dy}}{P_{sx}+P_{sy}}$, $\mu = \frac{\mu_x+\mu_y}{2}$, $p = \frac{\mu_x}{\mu_y}$, $q = \frac{P_{dx}}{P_{dy}} / \frac{P_{sx}}{P_{sy}}$, and $\hat{r} = \sqrt[\alpha]{\mathbb{E}[R^\alpha]}$. It is worth mentioning that by appropriately configuring the parameters, we can obtain a range of fading models. The specific parameter values for different fading models are detailed in Table 2.3.

The authors in [159] presented the PDF $f_R(r)$ of the envelope R in terms of the generalized

Table 2.3: Special Cases of the Generalized α-η-κ-μ Fading Model

Models	$\boldsymbol{\alpha}$	$\boldsymbol{\eta}$	$\boldsymbol{\kappa}$	$\boldsymbol{\mu}$	$\boldsymbol{p}$	$\boldsymbol{q}$
α-η-μ	α	η	0	2μ	1	q
α-κ-μ	α	p	κ	2μ	1	q
α-μ	α	p	0	μ	1	q
η-μ	2	η	0	μ	1	q
κ-μ	2	p	κ	μ	1	q
η-κ	2	η	κ	1	1	q
Nakagami-m	2	1	0	0.7	1	1
hoyt	2	3	0	0.5	1	1
Weibull	3	1	0	1	1	1
Rayleigh	2	1	0	1	1	1

Laguerre polynomial (L_n) and the regularized hypergeometric function ($_0\tilde{F}_1$):

$$f_R(r) = \frac{\alpha(\xi\mu)^{\mu}}{\exp\left(\frac{(1+pq)\kappa\mu}{\delta}\right)}\left(\frac{p}{\eta}\right)^{\frac{p\mu}{1+p}}\frac{r^{\alpha\mu-1}}{\hat{r}^{\alpha\mu}}\exp\Big(-\frac{r^{\alpha}p\xi\mu}{\hat{r}^{\alpha}\eta}\Big)\sum_{n=0}^{\infty}\Big(\frac{r^{\alpha}\xi\mu(p-\eta)}{\hat{r}^{\alpha}\eta}\Big)^{n} \times L_n^{\frac{\mu}{1+p}-1}\Big(\frac{\eta\kappa\mu}{\delta(\eta-p)}\Big)\,{}_0\tilde{F}_1\Big(;\mu+n;\frac{p^2qr^{\alpha}\kappa\xi\mu^2}{\hat{r}^{\alpha}\delta\eta}\Big) \tag{2.11}$$

where $\xi = \frac{(1+\eta)(1+\kappa)}{(1+p)}$ and $\delta = \frac{(1+q\eta)(1+p)}{(1+\eta)}$. It can be seen that the PDF $f_R(r)$ contains an infinite series representation, which approximates the system performance when a finite number of terms are used for the convergence of the distribution function.

2.3.5 Gaussian Mixture Model

For the THz link, recently, the authors in [160] have demonstrated through experiments that short-term fading in outdoor THz environments can be precisely modeled using a Gaussian mixture fading model. The PDF of the Gaussian mixture distribution is given by:

$$f_{|h_f|}^{\mathrm{THz}}(x) = \sum_{i=1}^{K} w_i \frac{\exp\Big(-\frac{(x-\mu_i)^2}{2\sigma_i^2}\Big)}{\sqrt{2\pi}\sigma_i} \tag{2.12}$$

where the mean and standard deviation of the i-th Gaussian mixture component are denoted by μ_i and σ_i, respectively. The number of Gaussian mixture components is represented by K, and the weight of the i-th mixture component is given by $w_i \in [0, 1]$ such that $\sum_{i=1}^{K} w_i = 1$. Table 2.4 showcases a brief summary of experimental data collected in an outdoor environment, as documented in [160].

Table 2.4: Fitting accuracy metrics of Gaussian mixture distribution with different values of K.

Link	**Link Distance (m)**	**KL**	$\hat{R}$ **(dB)**	K
T_{X_1}-R_{X_1}	13.72	0.037	-15.41	4
$T_{X_{13}}$-R_{X_1}	16.41	0.045	-16.71	11
$T_{X_{14}}$-R_{X_1}	38.15	0.018	-18.09	10
$T_{X_{10}}$-R_{X_1}	57.11	0.015	-18.98	13
$T_{X_{18}}$-R_{X_1}	127.86	0.064	-15.05	20

2.4 Transceiver Hardware Impairment Model for THz Link

THI in a THz link can significantly affect the performance and reliability of THz communication systems. These impairments arise from various hardware components within the transceiver and the challenges associated with operating in the THz frequency range.

The complex Gaussian distribution to model the THI has been thoroughly validated through theoretical and experimental approaches, as described in [34, 42, 161–164], and the references therein. Thus, w_t and w_r denote the components for the residual hardware impairment modeled statistically using Gaussian distribution as $w_t \sim \mathcal{CN}(0, k_t^2 P)$, and $w_r \sim \mathcal{CN}(0, k_r^2 P|h_l h|^2)$ with factor k_t and k_r characterizing the extent of hardware imperfections in the transmitter and receiver, respectively. The typical values of k_t and k_r is in the range of $(0\text{-}0.4)$ for the THz band as suggested in [34], while $k_t = k_r = 0$ corresponds to an ideal front-end.

2.5 Performance Metrics

The performance metrics of a wireless system, including average SNR, outage probability, ergodic capacity, and average BER, hold significant importance in the context of wireless communication. Average SNR is an important parameter since it indicates the signal quality, helping to determine if the communication channel can maintain a clear and reliable connection. Outage probability is crucial for assessing the system's reliability, providing insights into the likelihood of signal degradation, which is essential in critical applications where uninterrupted communication is required. Ergodic capacity helps as analyze the long-term performance of a wireless system, assisting in optimizing data transmission rates and resource allocation. Average BER is fundamental in ensuring data integrity, as it reveals the average number of bit errors in received data. These metrics collectively enable network engineers and researchers to fine-tune wireless systems, ensuring that they meet performance requirements, maintain data quality, and guarantee seamless communication under various conditions, thereby enhancing the overall user experience and system efficiency.

In the following, we present various performance metrics for the THz wireless system to highlight the importance of our analytical results and techniques through comparisons with

state-of-the-art approaches.

2.5.1 Average SNR

The SNR is an important parameter for a communication system, which provides a measure of received signal quality. We define the average SNR by taking the expectation operator $\overline{\mathrm{SNR}} = \mathbb{E}\{\gamma\}$ as

$$\overline{\mathrm{SNR}} = \int_0^{\zeta} \gamma f_\gamma(\gamma) d\gamma \tag{2.13}$$

where ζ is the limit of integration and $f_\gamma(\gamma)$ is the PDF of SNR $\gamma = \frac{P^2 h^2}{\sigma_w^2} = \gamma_0 h^2$, P is the average transmitted signal power, h is the random channel coefficient, and noise variance σ_w^2.

2.5.2 Outage probability

Outage probability is a performance measure to demonstrate the effect of the fading channel. It is defined as the probability of failing to reach an SNR threshold value γ_{th}:

$$P_{\mathrm{out}} = P(\gamma < \gamma_{\mathrm{th}}) = F_\gamma(\gamma_{\mathrm{th}}) \tag{2.14}$$

where $F_\gamma(\gamma)$ is the CDF of SNR γ.

2.5.3 Ergodic capacity

Ergodic capacity is another important performance measure that denotes maximum transmission rate with an infinitesimal probability of error:

$$\bar{\eta} = \int_0^{\infty} \log_2(1+\gamma) f_\gamma(\gamma) d\gamma \tag{2.15}$$

where $f_\gamma(\gamma)$ denotes the PDF of SNR γ.

2.5.4 Average BER

Average BER is a measure of occurrence of error in the transmitted bits and is a important performance parameter for any communication system. The average BER of a communication link with Gray coding can be expressed as [165]:

$$\bar{P}_e = \frac{q^p}{2\Gamma(p)} \int_0^{\infty} \gamma^{p-1} e^{-q\gamma} F_\gamma(\gamma) d\gamma \tag{2.16}$$

where $F_\gamma(\gamma)$ is the CDF of SNR γ, and p and q are modulation-dependent parameters. Specifically, $p = 1$ and $q = 1$ denote the differential binary phase-shift keying (DBPSK), $p = 0.5$, $p = 0.5$ and $q = \log_2(M)/(8(M-1)^2)$ for M-ary pulse amplitude modulation (M-PAM), and $p = 0.5, q = 0.125$ for non-return-to-zero (NRZ) on-off keying modulation.

2.6 Meijer's-G/Fox's H-function

In this section, we describe Meijer's G and Fox's H-function, both of which have been extensively utilized in the subsequent chapters to analyze wireless system's performance. The application of these functions is a widespread practice within the research community for the analysis of complex fading channels, and it can be conveniently computed using built-in functions provided by computational software like MATLAB and MATHEMATICA.

The single-variate Meijer-G function is defined as

$$\frac{1}{2\pi i}\int_{\mathcal{L}}\frac{\prod_{j=1}^{m}\Gamma(b_j-s)\prod_{j=1}^{n}\Gamma(1-a_j+s)}{\prod_{j=m+1}^{q}\Gamma(1-b_j+s)\prod_{j=n+1}^{p}\Gamma(a_j-s)}z^s ds=\mathrm{G}_{p,q}^{m,n}\left(z\middle|\begin{matrix}a_1,\cdots,a_p\\ b_1,\cdots,b_q\end{matrix}\right) \tag{2.17}$$

Fox's H-function is a generalized version of Meijer's G-function and is defined as [166]

$$\begin{aligned}&\mathrm{H}_{p,q}^{m,n}\left[z\middle|\begin{matrix}(a_1,A_1),(a_2),A_2\cdots,(a_p,A_p)\\ (b_1,B_1),(b_2,B_2),\cdots,(b_q,B_q)\end{matrix}\right]\\&=\frac{1}{2\pi i}\int_{\mathcal{L}}\frac{\prod_{j=1}^{m}\Gamma(b_j-B_js)\prod_{j=1}^{n}\Gamma(1-a_j+A_js)}{\prod_{j=m+1}^{q}\Gamma(1-b_j+B_js)\prod_{j=n+1}^{p}\Gamma(a_j-A_js)}z^s ds\end{aligned} \tag{2.18}$$

The multivariate Fox's H-function is defined as

$$\begin{aligned}&H_{p,q:p_1,q_1;\cdots;p_r,q_r}^{0,n:m_1,n_1;\cdots;m_r,n_r}\left[z_1\cdots z_r\middle|\begin{matrix}\left(a_j;\alpha_j^{(1)},\cdots,\alpha_j^{(r)}\right)_{1,p}:\left(c_j^{(1)},\gamma_j^{(1)}\right)_{1,p_1};\cdots;\left(c_j^{(r)},\gamma_j^{(r)}\right)_{1,p_r}\\ \left(b_j;\beta_j^{(1)},\cdots,\beta_j^{(r)}\right)_{1,q}:\left(d_j^{(1)},\delta_j^{(1)}\right)_{1,q_1};\cdots;\left(d_j^{(r)},\delta_j^{(r)}\right)_{1,q_r}\end{matrix}\right]\\&=\frac{1}{(2\pi i)^r}\int_{\mathcal{L}_1}\cdots\int_{\mathcal{L}_r}\frac{\prod_{j=1}^{n}\Gamma(1-a_j+\sum_{i=1}^{r}\alpha_j^{(i)}\zeta_i)}{\prod_{j=1}^{q}\Gamma(1-b_j+\sum_{i=1}^{r}\beta_j^{(i)}\zeta_i)\prod_{j=n+1}^{p}\Gamma(a_j-\sum_{i=1}^{r}\alpha_j^{(i)}\zeta_i)}\\&\times\prod_{i=1}^{r}\frac{\prod_{\lambda=1}^{m_i}\Gamma(d_\lambda^{(i)}-\delta_\lambda^{(i)}\zeta_i)\prod_{j=1}^{n_i}\Gamma(1-c_j^{(i)}+\gamma_j^{(i)}\zeta_i)}{\prod_{\lambda=m_i+1}^{q_i}\Gamma(1-d_\lambda^{(i)}+\delta_\lambda^{(i)}\zeta_i)\prod_{j=n_i+1}^{p_i}\Gamma(c_j^{(i)}-\gamma_j^{(i)}\zeta_i)}z_i^{\zeta_r}d\zeta_r\end{aligned} \tag{2.19}$$

Most of the mathematical functions can be represented using Meijer's G or Fox's H-functions, which utilizes the inverse Mellin's transform to represent a particular mathematical function.

Define Mellin's transform for a mathematical function $f(x)$ as

$$\varphi(s)=\int_0^\infty x^{s-1}f(x)dx \tag{2.20}$$

Similarly the inverse Mellin's transform is defined as

$$f(x)=\frac{1}{2\pi i}\int_{c-i\infty}^{c+i\infty}x^{-s}\varphi(s)ds \tag{2.21}$$

In the following, we illustrate the representation of $f(x)=e^{-x}$ using Meijer's G function. The

Mellin's transform of $f(x) = e^{-x}$ is given by

$$\varphi(s) = \int_0^\infty x^{s-1} e^{-x} dx = \Gamma(s) \tag{2.22}$$

which is denoted as Gamma function. Applying the inverse Mellin's transform and the definition (2.17), the exponential function can be represented in terms of Meijer's G function as

$$e^{-x} = \frac{1}{2\pi i} \int_{c-i\infty}^{c+i\infty} \Gamma(s) x^{-s} ds = \mathrm{G}_{0,1}^{1,0}\left(x \middle| \begin{matrix} - \\ 0 \end{matrix} \right) \tag{2.23}$$

Using the above approach, mathematical functions under certain conditions can be represented in terms of Meijer's-G/Fox's H-function for a unified performance analysis.

2.7 Chapter Summary

In this chapter, we have examined different channel impairments and presented statistical models for path-loss, short-term fading, antenna misalignment errors, and transceiver hardware impairments. Furthermore, we have presented a range of performance metrics for evaluation of the THz system under consideration in this dissertation. In the next chapter, we develop multihop THz transmission for extending the range of communication.

Chapter 3

THz Wireless Communication for Extended Coverage: A General Analysis for Multihop Transmission

3.1 Introduction

High-speed THz connectivity can be set in hard-to-access terrains more efficiently than the infrastructure-based fiber-optic wireline link. Although THz wireless transmission has a great potential to be a major disruptive technology, it suffers from higher atmospheric attenuation caused by molecular absorption, hardware impairments, and misalignment errors when the transmit and receive antennas do not align for line-of-sight (LOS) transmissions limiting the physical range of communication significantly. Hence, it is desirable to devise methods for extending the communication range of THz wireless systems under adverse propagation conditions such as higher path loss, misalignment errors, and the shadowing effect between the source and destination.

Cooperative relaying is a potential technique to extend the communication range and improve the quality of system performance. The popular AF and DF relaying schemes have been extensively investigated for RF [55–61, 68–70] and free-space optics (FSO) [62–67, 71] over various fading scenarios. Fixed-gain (FG) and channel-assisted (CA) are two practical approaches for AF relaying. In the FG relaying, the statistical information of the received signal from the previous hop is used to control the gain of the relay. Moreover, the near-optimal CA relaying uses instantaneous CSI of the previous hop to control the gain introduced by the relay

---

The research contributions in this chapter have been reported in these publications:

1. **P. Bhardwaj** and S. M. Zafaruddin, "On the Performance of Multihop THz Wireless System Over Mixed Channel Fading With Shadowing and Antenna Misalignment," in **IEEE Transactions on Communications**, vol. 70, no. 11, pp. 7748-7763, Nov. 2022.

2. V. U. Pai, **P. Bhardwaj**, and S. M. Zafaruddin, "Performance Analysis of Dual-Hop THz Wireless Transmission for Backhaul Applications," **2021 IEEE International Conference on Advanced Networks and Telecommunications Systems (ANTS)**, Hyderabad, India, 2021, pp. 438-443.

and, as a result, fix the power of the retransmitted signal[167].

Recently, there has been an increased research interest for mixed dual-hop THz relaying systems [33, 74, 75]. In [33], the average bit-error rate (ABER) performance of a DF-assisted THz-RF link in a backhaul-broadband access framework is studied over α-μ fading. The α-μ is a generalized short-term fading model which includes Weibull, negative exponential, Nakagami-m, and Rayleigh distribution as a special case [104]. Recent experiment campaigns validates α-μ distribution for the short term fading in THz link at a 142 GHz carrier frequency for a link length within 50 m [149, 153]. To extend the range of THz transmissions, dual-hop relaying has been investigated [74, 75]. In [74], the authors analyzed the performance of a dual-hop THz-THz backhaul system employing the DF protocol with α-μ fading model with pointing errors for both the links. Considering similar fading distributions, the FG relaying was studied for the dual-hop THz-THz system [75].

3.2 Motivation and Contribution

In the aforementioned and related research, relaying is limited to dual-hop, and the access link operates over conventional RF frequencies. It is expected that the high bandwidth THz transmissions can be employed for 6G radio access network (RAN). Although the THz radio is immune to atmospheric turbulence and adverse weather conditions than the FSO technology, it is susceptible to human movement between the transmitter and the receiver leading to dynamic shadowing [77, 156]. In [156], the generalized-K fading distribution is adopted to model the THz transmissions in the access link. However, the effect of antenna misalignment errors is not considered in [156] for a better estimate of the THz performance. Moreover, the multihop THz system extending the range of backhaul link has not been studied in the literature. It is well-known that analyzing the performance of multihop transmissions, even for single-parameter RF fading distributions is challenging, especially when multihop links are assisted by the AF relaying. In general, the performance of multihop-assisted AF relaying is approximated by expressing the resultant SNR as the product of SNR of individual links using the inequality of harmonic and geometric mean. Further, the method of induction (generalization for N hops realized through expressions derived for the first few hops) is applied to derive the PDF, and thereby CDF of the multihop system [63]. Note that the mathematical induction method is not applicable for THz transmissions under the combined effect of α-μ fading with antenna misalignment errors and requires novel approaches for its statistical analysis. Moreover, it is desirable to derive exact analytical expressions of a CA relaying, which serves as a benchmark for all practical multihop systems employing AF relays [63].

In this chapter, we analyze the performance of a multihop-assisted backhaul mixed with a shadowed access link over the THz band for both uplink and downlink transmissions. We consider the AF relaying for the multihop system and employ DF and AF protocols to interface with the radio access link for uplink and downlink, respectively. We consider the generalized i.ni.d. α-μ fading distribution for the multihop link and the composite generalized-K shadowed

fading for the radio access link, both under the combined effect of antenna misalignment errors. We list the major contributions of the chapter as follows:

- We derive novel PDF and CDF of the end-to-end SNR of the multihop backhaul link employing CA relaying for each hop.
- We develop an upper bound for the FG relaying based multihop transmission by deriving the exact PDF of the product of N i.ni.d. random variables that are distributed according to the product of α-μ fading and antenna misalignment errors.
- Using the derived statistical results, we analyze the outage probability and ABER performance for CA-multihop and FG-multihop systems. We also analyze the multihop transmissions for some special cases of the THz channel and present an asymptotic analysis in high SNR regime for a better insight into the system behavior.
- We develop statistical results of an all FG-relayed downlink transmission by employing the FG protocol in the last hop to mix the FG-multihop and access link in terms of the bivariate Fox's H-function. We analyze the $N+1$-hop downlink system by deriving upper bounds on the outage probability and ABER. Note that our derived analytical expressions become exact for a single-relay ($N = 1$) system resulting in a typical dual-hop mixed transmission. We also analyze the performance of uplink transmission by employing the DF relaying protocol in the first hop to mix the access link and CA-multihop.
- We derive asymptotic expressions of the outage probability and ABER in high SNR region and develop diversity order to provide design aspects of channel and system parameters for the integrated backhaul-access relaying transmissions.
- We validate the derived analysis using Monte-Carlo simulations and demonstrate the significance of multihop relaying to extend the communication range for THz wireless transmissions under the effect of fading, antenna misalignment error, and shadowing.

3.3 System Model

We consider a multihop-assisted backhaul transmission mixed with a broadband access link, both operating in the THz band. The transmission system consists of N+1 hops from the source (S) to the destination (D), where N hops correspond to the backhaul connectivity and a single link of the access network, as shown in Fig. 3.1. We consider both uplink and downlink scenarios: signal transmission from the access node to the backhaul in the uplink and backhaul to the access node in the downlink transmission.

We consider i.ni.d. α-μ distributed fading parameters $\{\alpha_i, \mu_i\}_{i=1}^{N}$ combined with antenna misalignment errors and deterministic path loss to model the channel of each hop of the backhaul THz link. Of course, the α-μ model has only been experimentally validated at a single

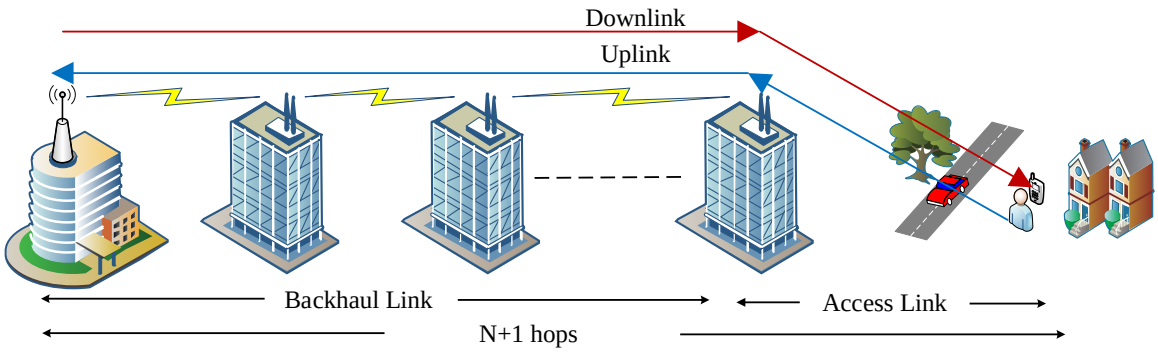

Figure 3.1: Multihop relay-assisted backhaul transmissions integrated with shadowed access link.

carrier frequency (142 GHz with a bandwidth of 4 GHz). The generalization of α-μ distribution may accurately model other THz frequencies by varying distribution parameters. However, this needs to be validated through experimentation. Suppose the α-μ fading model is not applicable at a given THz frequency. In that case, a more generalized α-η-κ-μ model [158] can be used to parameterize the experimental data. The proposed analysis is also applicable for α-η-κ-μ model since its infinite series representation resembles the α-μ fading model mathematically.

Using AF relaying protocol and denoting G_i as the gain of i-th relay with $G_0 = 1$, the received signal at the N-th relay is given by [63]. Note that there is a typo error in equation (17) [63]. In the second term of R.H.S., the product range should be from $j = i$ to $j = N - 1$. Thus, the received signal is given by

$$y_N = \prod_{i=1}^{N} G_{i-1} h_i x + \sum_{i=1}^{N-1} w_i \left(\prod_{j=i}^{N-1} G_j h_{j+1} \right) + w_N, \tag{3.1}$$

where x is the transmitted signal with power P_i and w_i is the additive white Gaussian noise (AWGN) of the i-th relay with variance σ_{wi}^2 and w_N is the AWGN of the N-th relay. The channel coefficient of the i-th hop is given as $h_i = h_{l_i} h_{p_i} h_{f_i}$, which includes the path gain h_{li}, short-term fading h_{fi}, and antenna misalignment errors h_{pi}. The path gain for the i-th link is $h_{li} = \frac{c\sqrt{G_t G_r}}{4\pi f d_i} \exp\big(-\frac{1}{2} k_i d_i\big)$, where c is the speed of light, G_t and G_r are the gains of transmitting and receiving antennas, respectively, f is the frequency of operation, k_i is the absorption coefficient and d_i denotes the link distance of the i-th hop such that $d_1 = \sum_{i=1}^{N} d_i$ is the total distance of the backhaul link.

We use the zero boresight statistical model for the antenna misalignment errors h_{pi} with PDF [150]:

$$f_{h_{p_i}}(h_p) = \frac{\phi_i^2}{S_i^{\phi_i^2}} h_p^{\phi_i^2 - 1}, 0 \leq h_p \leq S, \tag{3.2}$$

where S_i and ϕ_i depict antenna misalignment error parameters for the i-th power. Here, the

term S_i denotes the fraction of collected power when the transmitter and receiver antennas are perfectly aligned, and ϕ_i denotes the ratio of normalized beam-width to the standard deviation of the jitter.

Using (3.2) and the PDF of α-μ distribution [104, eq. (1)], the PDF of $h_{p_i f_i} = h_{pi} h_{fi}$, which combines the effect of short-term fading and antenna misalignment errors is presented in [33]:

$$f_{|h_{p_i f_i}|}(x) = A_i x^{\phi_i - 1} \Gamma(B_i, C_i x^{\alpha_i}), \tag{3.3}$$

where $A_i = \frac{\phi_i S_i^{-\phi_i} \mu_i^{\frac{\phi_i}{\alpha_i}}}{\Omega_i^{\phi_i} \Gamma(\mu_i)}$, $B_i = \frac{\alpha_i \mu_i - \phi_i}{\alpha_i}$ and $C_i = \frac{\mu_i}{\Omega_i^{\alpha_i}} S_i^{-\alpha_i}$. Here, α_i and μ_i are the distribution parameter of the i-th link. Ω_i is the α_i root-mean value of the fading channel envelope. We denote instantaneous SNR of the i-th link as $\gamma_i = \bar{\gamma}_i |h_i|^2$, where $\bar{\gamma}_i = \frac{P_i |h_{li}|^2}{\sigma_{wi}^2}$ is the average SNR of the i-th link. Applying the transformation of random $\gamma_i = \bar{\gamma}_i |h_i|^2$ and representing the incomplete Gamma function using Meijer's G-function, the PDF of the SNR for the i-th hop can be expressed as

$$f_{\gamma_i}(\gamma) = \frac{A_i \gamma_i^{0 - \frac{\phi_i}{2}} \gamma^{\frac{\phi_i}{2} - 1}}{2} G_{1,2}^{2,0}\left(\frac{C_i \gamma^{\frac{\alpha_i}{2}}}{\bar{\gamma}_i^{\frac{\alpha_i}{2}}} \middle| \begin{matrix} 1 \\ B_i, 0 \end{matrix} \right). \tag{3.4}$$

We adopt both CA and FG AF relaying protocols for each hop of the multihop-assisted backhaul link. The gain of the CA relay can be computed using the inverse of the channel of the previous hop. Thus, using $G_i^2 = \frac{1}{|h_i|^2}$ in (3.1), the end-to-end SNR with the CA relaying in each hop is given by [55]:

$$\gamma_N^{\mathrm{CA}} = \left(\sum_{i=1}^{N} \frac{1}{\gamma_i} \right)^{-1}. \tag{3.5}$$

Note that (3.5) becomes an upper bound if the gain of the relay also includes the effect of additive noise. Further, using $G_i = \sqrt{\frac{1}{\psi_i \sigma_{wi}^2}}$ in (3.1), where ψ_i is a constant, we can obtain the end-to-end SNR of the FG relaying [55]:

$$\gamma_N^{\mathrm{FG}} = \left(\sum_{i=1}^{N} \prod_{j=1}^{i} \frac{\psi_j - 1}{\gamma_j} \right)^{-1}. \tag{3.6}$$

To this end, we interface the multihop backhaul with a single access link by applying DF and FG relaying protocols for uplink and downlink transmissions, respectively. We take into account the shadowing effect along with the channel fading and antenna misalignment errors for the THz access link since the transmitted signal may be obstructed by the objects present in a typical access network scenario. We denote the SNR of the access link as $\gamma_A = \gamma_A^0 |h_A|^2$, where $h_A = h_k h_{p_A}$ and γ_A^0 is the average SNR of the shadowed access link. Here, h_{p_A} models the

antenna misalignment error (with parameters S_A and ϕ_A) and h_k models the channel coefficient of the access link. We consider the generalized-K distribution to model the instantaneous power $|h_k|^2$ (which includes the short term fading and random path gain) of the shadowed access link [157]:

$$f_{|h_k|^2}(x) = \frac{2b^{m_A}}{\Gamma(m_\Omega)\Gamma(m_g)} x^{\frac{m_A}{2}-1} K_{m_M}(2b\sqrt{x}), \tag{3.7}$$

where $m_\Omega = \frac{1}{\exp(\sigma_n^2)-1}$, $\sigma_n{>}0$ denotes the severity of shadowing with factor $\sigma_{\text{dB}} = 8.686\sigma_n$, $m_g{>}0$ is frequency dependent parameter characterizing the small-scale fading, $m_A = m_\Omega + m_g$ and $m_M = m_\Omega - m_g$ are the distribution shape parameters of $K_\nu(.)$, which is modified Bessel function of the second kind of ν-th order, and $\Gamma(.)$ denotes the gamma function. Denoting $k_A(f)$ as the absorption coefficient, d_A as the distance of the access link, G_A as the antenna gain, P_A as the transmit power, η as the path loss coefficient, we define $b = \sqrt{\frac{m_\Omega m_g}{G_A^2 P_A \varphi \exp(\sigma_n^2/2)} \left(\frac{c}{4\pi d_A f}\right)^\eta}$, where $\varphi = \exp(k_A(f)d_A)$ is the path loss due the molecular absorption of the signal transmission in the THz band.

3.4 Multihop Terahertz Transmission for Backhaul Link

In this section, we derive analytical expressions for the PDF and CDF of the end-to-end SNR of an N-hop THz wireless system. First, we develop statistical results of the CA-multihop system in terms of multivariate Fox's H-function. Next, we use Mellin transform to derive the exact PDF and CDF of the product of N i.ni.d. random variables distributed according to (3.4) and raised to a rational power. Finally, we present the outage probability and ABER performance for CA-multihop and FG-multihop links.

3.4.1 Statistical Results

In the following theorem, we present PDF and CDF of the resultant SNR γ_N^{CA} (as given in (3.5)) for the CA-multihop system. We use the moment generating function (MGF) for the reciprocal of SNR in (3.5) to find the CDF [55]:

$$F_{\gamma_N}^{\text{CA}}(\gamma) = 1 - \mathcal{L}^{-1}\left(\frac{\mathcal{M}_{\frac{1}{\gamma_N^{\text{CA}}}}(s)}{s}\right)\Bigg|_{s=1/\gamma}, \tag{3.8}$$

where $\mathcal{L}^{-1}(\cdot)$ denotes the inverse Laplace transform and s is the complex-valued variable. The MGF of sum of N independent random variables $\frac{1}{\gamma_N^{\text{CA}}}$ of (3.5) is defined as

$$\mathcal{M}_{\frac{1}{\gamma_N^{\text{CA}}}}(s) = \prod_{i=1}^{N} \mathcal{M}_{\frac{1}{\gamma_i}}(s), \tag{3.9}$$

where the MGF of $\frac{1}{\gamma_i}$ is given by

$$\mathcal{M}_{\frac{1}{\gamma_i}}(s) = \int_0^\infty e^{-s/\gamma_i} f_{\gamma_i}(\gamma) d\gamma. \tag{3.10}$$

Theorem 3.1. *If γ_i is the SNR of the i-th hop distributed according to* (3.4)*, then CDF and PDF of the SNR for N-hop CA relaying in* (3.5) *are given as*

$$F_{\gamma_N}^{\mathrm{CA}}(\gamma) = 1 - \prod_{i=1}^{N} \frac{A_i \bar{\gamma}_i^{-\frac{\phi_i}{2}}}{2} \gamma^{\left(\sum_{i=1}^{N} \frac{\phi_i}{2}\right)} H_{1,0;1,3;\ldots;1,3}^{0,0;3,0;\ldots;3,0} \left[\begin{array}{c|c} \frac{C_1 \gamma^{\frac{\alpha_1}{2}}}{\bar{\gamma}_i^{\frac{\alpha_1}{2}}} & \\ \vdots & \tilde{Q}_1(\gamma) \\ \frac{C_N \gamma^{\frac{\alpha_N}{2}}}{\bar{\gamma}_i^{\frac{\alpha_N}{2}}} & \tilde{Q}_2(\gamma) \end{array} \right], \tag{3.11}$$

where $\tilde{Q}_1(\gamma) = \left\{ \left\{ \left(1 - \sum_{i=1}^{N} \frac{\phi_i}{2}; \frac{\alpha_1}{2}, \cdots, \frac{\alpha_N}{2}\right) \right\}; \left\{(1,1), \cdots, (1,1)_N\right\} \right\}$ *and* $\tilde{Q}_2(\gamma) = \left\{ \{-\}; \left\{(B_1, 1), (0,1), \left(\frac{-\phi_1}{2}, \frac{\alpha_1}{2}\right), \cdots, (B_N, 1), (0,1), \left(\frac{-\phi_N}{2}, \frac{\alpha_N}{2}\right) \right\} \right\}$.

$$f_{\gamma_N}^{\mathrm{CA}}(\gamma) = -\prod_{i=1}^{N} \frac{A_i \bar{\gamma}_i^{-\frac{\phi_i}{2}}}{2} \gamma^{\left(\sum_{i=1}^{N} \frac{\phi_i}{2} - 1\right)} H_{2,1;1,3;\ldots;1,3}^{0,1;3,0;\ldots;3,0} \left[\begin{array}{c|c} \frac{C_1 \gamma^{\frac{\alpha_1}{2}}}{\bar{\gamma}_i^{\frac{\alpha_1}{2}}} & \\ \vdots & Q_1(\gamma) \\ \frac{C_N \gamma^{\frac{\alpha_N}{2}}}{\bar{\gamma}_i^{\frac{\alpha_N}{2}}} & Q_2(\gamma) \end{array} \right], \tag{3.12}$$

where $Q_1(\gamma) = \left\{ \left\{ \left(\sum_{i=1}^{N} -\frac{\phi_i}{2}; \frac{\alpha_1}{2}, \cdots, \frac{\alpha_N}{2} \right) \right\}, \left\{ \left(1 - \sum_{i=1}^{N} \frac{\phi_i}{2}; \frac{\alpha_1}{2}, \cdots, \frac{\alpha_N}{2}\right) \right\}; \left\{(1,1), \cdots, (1,1)_N\right\} \right\}$
and $Q_2(\gamma) = \left\{ \left\{ \left(\sum_{i=1}^{N} 1 - \frac{\phi_i}{2}; \frac{\alpha_1}{2}, \cdots, \frac{\alpha_N}{2} \right) \right\}; \left\{(B_1, 1), (0,1), \left(\frac{-\phi_1}{2}, \frac{\alpha_1}{2}\right), \cdots, (B_N, 1), (0,1), \left(\frac{-\phi_N}{2}, \frac{\alpha_N}{2}\right) \right\} \right\}$

Proof. The proof is presented in Appendix 3.1. ■

Note that efficient computational programs are available for evaluating the multivariate Fox's H-function of (3.12) and (3.11) for the CA-multihop system. In the following Corollary, we provide statistical results of the CA multihop system in terms of simpler functions considering special cases for the THz channel:

Corollary 3.1. *1. If γ_i is the SNR of the i-th hop distributed according to* (3.4) *with $\alpha_i = 2$, $\mu_i = 1$ (i.e. Rayleigh fading) and negligible antenna misalignment errors $\phi_i \to \infty$, $\forall i$, then the MGF of the end-to-end SNR for N-hop CA relaying is given as*

$$\mathcal{M}_{\frac{1}{\gamma}}(s) = \prod_{i=1}^{N} \frac{2\sqrt{2}}{\sqrt{\bar{\gamma}_i}\sigma} \sqrt{s} K\left[1, \frac{\sqrt{2}\sqrt{s}}{\sqrt{\bar{\gamma}_i}\sigma}\right]. \tag{3.13}$$

where $K[\cdot, \cdot]$ denotes the modified Bessel function of the second kind. We substitute $N = 2$ in (3.13) *to develop a statistical analysis for the dual-hop system over Rayleigh fading. Using* (3.13) *with $N = 2$ in* (3.8) *and taking the inverse Laplace transform, we get the*

CDF of the end-to-end SNR of dual-hop CA relaying with Rayleigh fading as $F_{\gamma_{DH}}^{\mathrm{CA}}(\gamma_{\mathrm{th}}) = 1 - \frac{2\gamma_{\mathrm{th}}}{\sqrt{\bar{\gamma}_1\bar{\gamma}_2\sigma^2}} e^{\frac{\gamma_{\mathrm{th}}(\bar{\gamma}_1+\bar{\gamma}_2)}{(\bar{\gamma}_1\bar{\gamma}_2\sigma^2)}} K\left[1, \frac{\gamma_{\mathrm{th}}}{\sqrt{\bar{\gamma}_1\bar{\gamma}_2\sigma^2}}\right]$. *The derived CDF expression is similar to [167], verifying our approach to the proposed analysis for multihop-CA transmission for THz.*

2. *If* γ_i *is the SNR of the* i*-th hop distributed according to* (3.4) *with* $\alpha_i = 2$, $\mu_i = 2$ *(i.e. Nakagami-*2 *fading) and higher antenna misalignment errors* $\phi_i = 2$, $\forall i$, *then the MGF of the end-to-end SNR for* N*-hop CA relaying is given as*

$$\mathcal{M}_{\frac{1}{\gamma_i}}(s) = \prod_{i=1}^{N} \frac{\sqrt{s}}{S_i\sqrt{\bar{\gamma}_i}} K\Big[1, \frac{2\sqrt{2}\sqrt{s}}{\sqrt{\bar{\gamma}_i}S_i}\Big]. \tag{3.14}$$

3. *The CDF of the end-to-end SNR for* N*-hop CA relaying for the backhaul link with antenna misalignment errors over composite (short-term fading with shadowing) fading channel is given by*

$$F_{\gamma_N}^{CA}(\gamma) = 1 - \prod_{i=1}^{N} \frac{b^{m_A}\phi_A(S_A^2)^{\frac{\phi_A - m_A}{2}+1}}{\bar{\gamma}_A^{\frac{m_A}{2}}\Gamma(m_\Omega)\Gamma(m_g)} \Big(\frac{1}{\gamma}\Big)^{\sum_{i=1}^{N}\left(\frac{m_A}{2}+1\right)} H_{1,0;1,4,\cdots,1,4}^{0,0;4,0,\cdots,4,0}\left[\begin{matrix} \frac{b^2 s}{S{1_A}^2\bar{\gamma}_A\gamma} \\ \vdots \\ \frac{b^2 s}{SN_A{}^2\bar{\gamma}_A\gamma} \end{matrix}\middle| \begin{matrix} Q_3(\gamma) \\ Q_4(\gamma) \end{matrix}\right], \tag{3.15}$$

where $Q_3(\gamma) = \Big\{\big\{\big(\sum_{i=1}^{N}\frac{m_A}{2}; 1, \cdots, 1\big)\big\} : \{-\}\Big\}$ *and* $Q_4(\gamma) = \Big\{\{-\} : \big\{\big(m_M, 1\big), \big(m_M, 1\big), \big(\frac{\phi_1 - m_A}{2}, 1\big), \big(\frac{-m_A}{2}, 1\big), \cdots, \big(m_M, 1\big), \big(m_M, 1\big), \big(\frac{\phi_N - m_A}{2}, 1\big), \big(\frac{-m_A}{2}, 1\big)\big\}\Big\}$.

Proof. For part (a), we use the Rayleigh distribution PDF $f_{\gamma_i}(\gamma) \rightarrow \frac{1}{\bar{\gamma}_i\sigma^2} e^{-\frac{\gamma_i}{2\bar{\gamma}_i\sigma^2}}$ in (3.9), and apply the identity [168, 3.324,1] to get the MGF in (3.13). Further, we can use (3.8) and apply the inverse Laplace transform to get the CDF for N-hop CA over Rayleigh fading channel. For part (b), we use $\alpha_i = 2$, $\mu_i = 2$ and $\phi_i = 2$ in (3.4) to get the PDF of Nakagami-2 fading as $f_{\gamma_i}(x) = \frac{x}{S_i^2} e^{-\frac{2x^2}{S_i^2}}$. Applying a similar procedure for the proof of part (a), we get (3.14). For part (c), we follow the similar procedure used to derive (3.11) of Theorem 3.1 using the PDF of the generalized-K fading model combined with antenna misalignment errors, as presented in Proposition 3.2. ■

Although multivariate Fox's H-function can be evaluated using computational software [169], it is desirable to simplify the analytical expressions in single-variate Fox's H-function for better insights into the system performance. Further, It is known that the FG relaying is simpler than the CA-assisted technique requiring the CSI at each relay. However, analyzing the exact PDF of the end-to-end SNR of the FG-multihop system as depicted in (3.6) is quite

complicated. Thus, we use an upper bound on γ_N^{FG} [64]:

$$\gamma_N^{\mathrm{FG}} = \frac{1}{N}\prod_{i=1}^{N}\zeta_i\gamma_i^{\frac{l_i}{N}}, \tag{3.16}$$

where $l_i = N+1-i$, $\zeta_i = C_i^{-\frac{(N-i)}{N}}$.

Proposition 3.1. *If γ_i, $i = 1, 2, \cdots, N$ are i.ni.d random variables with PDF $f_{\gamma_i}(\gamma)$, then the PDF of γ_N in* (3.16) *is given by*

$$f_{\gamma_N}^{\mathrm{FG}}(\gamma) = \frac{1}{\gamma}\frac{1}{2\pi\jmath}\int_{\mathcal{L}}\frac{1}{N}\prod_{i=1}^{N}\zeta_i\mathbb{E}[\gamma_i^r]\gamma^{-r}dr, \tag{3.17}$$

where $\mathbb{E}[\gamma_i^r]$ denotes the r-th moment:

Proof. We use the Mellin transform pair to develop exact PDF and CDF of (3.16). We know that Mellin transform for a function $\phi(x)$ is given as $\phi(t) = \int_0^\infty x^{t-1}\phi(x)dx$ with inverse Mellin transform as $\phi(x) = \frac{1}{2\pi\jmath}\int_{\mathcal{L}} x^{-t}\phi(t)dt$. Expressing the r-th moment of γ_N in (3.16) as $\mathbb{E}[\gamma_N^r] = \int_0^\infty \gamma^{r-1}[\gamma f_{\gamma_N}(\gamma)]d\gamma$, we use inverse Mellin transform to get:

$$f_{\gamma_N}^{\mathrm{FG}}(\gamma) = \frac{1}{\gamma}\frac{1}{2\pi\jmath}\int_{\mathcal{L}}\gamma^{-r}\mathbb{E}[\gamma_N^r]dr. \tag{3.18}$$

Since random variables $\gamma_i, i = 1, \cdots, N$ are independent, we substitute $\mathbb{E}[\gamma_N^r] = \frac{1}{N}\prod_{i=1}^{N}\zeta_i\mathbb{E}[\gamma_i^r]$ in (3.18) to get (3.17), where the r-th moment is defined as

$$\mathbb{E}[\gamma_i^r] = \int_0^\infty \gamma^{\frac{rl_i}{N}} f_{\gamma_i}(\gamma)d\gamma. \tag{3.19}$$

■

A straightforward application of the Fox's H-function reveals that the PDF of the FG-multihop in (3.17) can be presented using a single variate Fox's H-function if the r-th moment of the SNR for the i-th hop can be expressed using the ratio of Gamma functions.

Substituting (3.4) in (3.19) and applying the identity [170, 2.8], the r-th moment of the SNR for the i-th hop can be computed as

$$\mathbb{E}[\gamma_i^r] = \frac{A_1\bar{\gamma}_N^{-\frac{\phi}{2}}}{2}\int_0^\infty \gamma^{\frac{2rl_i+N\phi}{2N}-1}G_{1,2}^{2,0}\left(\frac{C_1\gamma^{\frac{\alpha}{2}}}{\bar{\gamma}_N^{\frac{\alpha}{2}}}\middle|\begin{matrix}1\\B_1, 0\end{matrix}\right)d\gamma. \tag{3.20}$$

Substituting $\gamma^{\frac{\alpha}{2}} = t$ with the identity [171, 07.34.21.0009.01], we solve (3.20):

$$\mathbb{E}[\gamma_i^r] = \frac{A_i\bar{\gamma}_N^{-\frac{\phi_i}{2}}}{\alpha_i}\frac{\Gamma\left(\frac{2rl_i+N\phi_i}{N\alpha_i}+B_i\right)\Gamma\left(\frac{2rl_i+N\phi_i}{N\alpha_i}\right)}{\Gamma\left(\frac{2rl_i+N\phi_i}{N\alpha_i}+1\right)}\left(C_i\bar{\gamma}_N^{-\frac{\alpha_i}{2}}\right)^{-\left(\frac{2rl_i+N\phi_i}{N\alpha_i}\right)}. \tag{3.21}$$

In the following Theorem, we present PDF and CDF of γ_N^{FG} to analyze the performance of FG-assisted multihop system:

Theorem 3.2. *If γ_i is the SNR of the i-th hop distributed according to* (3.4)*, then PDF and CDF of the SNR for N-hop FG-relaying in* (3.16) *are bounded as*

$$f_{\gamma_N}^{\mathrm{FG}}(\gamma) = \prod_{i=1}^{N} \frac{\zeta_i A_i C_i^{-\frac{\phi_i}{\alpha_i}}}{N\alpha_i \gamma} H_{2N,N}^{0,2N}\left[\prod_{i=1}^{N} \frac{\bar{\gamma}_i^{\frac{l_i}{N}}}{C_i^{\frac{2l_i}{N\alpha_i}} \gamma} \middle| \begin{matrix} U_1(\gamma) \\ U_2(\gamma) \end{matrix} \right], \tag{3.22}$$

$$F_{\gamma_N}^{\mathrm{FG}}(\gamma) = \prod_{i=1}^{N} \frac{\zeta_i A_i C_i^{-\frac{\phi_i}{\alpha_i}}}{N\alpha_i} H_{1+2N,1+N}^{1,2N}\left[\prod_{i=1}^{N} \frac{\bar{\gamma}_i^{\frac{l_i}{N}}}{C_i^{\frac{2l_i}{N\alpha_i}} \gamma} \middle| \begin{matrix} U_1(\gamma), (1,1) \\ (0,1), U_2(\gamma) \end{matrix} \right], \tag{3.23}$$

where $U_1(\gamma) = \big\{\big(1-\mu_1, \frac{2l_1}{N\alpha_1}\big), \cdots, \big(1-\mu_N, \frac{2l_N}{N\alpha_N}\big), \big(1-\frac{\phi_1}{\alpha_1}, \frac{2l_1}{N\alpha_1}\big), \cdots, \big(1-\frac{\phi_N}{\alpha_N}, \frac{2l_N}{N\alpha_N}\big)\big\}$ *and* $U_2(\gamma) = \big\{\big(-\frac{\phi_1}{\alpha_1}, \frac{2l_1}{N\alpha_1}\big), \cdots, \big(-\frac{\phi_N}{\alpha_N}, \frac{2l_N}{N\alpha_N}\big)\big\}$.

Proof. The proof is presented in Appendix 3.2. ■

It should be mentioned that the single-variate PDF and CDF derived in Theorem 3.2 can facilitate in developing more insightful analytical expressions for the multihop system albeit with an upper bound performance.

Further, we can use Proposition 3.1 to develop the PDF of the FG-multihop transmission for other wireless systems since the r-th moment of the SNR for the i-th hop can be expressed using the ratio of Gamma functions for various fading channels of interest. In the following, we present the r-th moment of the SNR for some special cases for the THz wireless system:

Corollary 3.2. *If γ_i is the SNR of the i-th hop distributed according to* (3.4) *with $\alpha_i = 2$, $\mu = 1$ (i.e. Rayleigh) with negligible antenna misalignment errors $\phi_i \to \infty$, $\forall i$, then the r-th moment of SNR is:*

$$\mathbb{E}[\gamma_i^r] = \frac{1}{\Omega^2 \bar{\gamma}_i} \Gamma\Big(\frac{rl_i}{N} + 1\Big) \left(\frac{-1}{\Omega^2 \bar{\gamma}_i}\right)^{\frac{rl_i}{N}+1}. \tag{3.24}$$

If γ_i is the SNR of the i-th hop distributed according to (3.4) *with $\alpha_i = 2$, $\mu_i = 2$ (i.e. Nakagami-2) and higher antenna misalignment errors $\phi_i = 2$, $\forall i$, then the r-th moment of SNR is:*

$$\mathbb{E}[\gamma_i^r] = \frac{1}{S_i^2 \Omega^4 \bar{\gamma}_i} \Gamma\Big(\frac{rl_i}{N} + 1\Big) \left(\frac{2}{S_i^2 \Omega^4 \bar{\gamma}_i}\right)^{\frac{rl_i}{N}+1}. \tag{3.25}$$

The r-th moment of end-to-end SNR for N-hop CA relaying for the backhaul link with antenna misalignment errors over composite (short-term fading with shadowing) fading channel is

given by

$$\mathbb{E}[\gamma_i^r] = \frac{b^{m_A}\phi_A (S_A^2)^{\frac{\phi_A - m_A}{2}+1}}{\bar{\gamma}_A^{\frac{m_A}{2}}\Gamma(m_\Omega)\Gamma(m_g)} \left(\frac{b^2\gamma}{S_A^2\bar{\gamma}_A}\right)^{-\frac{rl_i}{N}-\frac{m_A}{2}} \frac{\Gamma(\frac{rl_i}{N}+\frac{m_A}{2}+m_M)\Gamma(\frac{rl_i}{N}+\frac{m_A}{2}+m_M)}{\frac{rl_i}{N}+\frac{m_A}{2}+\frac{\phi_A-m_A}{2}+1} \tag{3.26}$$

Proof. The proof of part (a) and part (b) is a straightforward application of the identity [171, 07.34.21.0009.01]. For part (c), apply the identity [171, 07.34.21.0009.01] on the PDF of the generalized-K fading model combined with antenna misalignment errors, as derived in Proposition 3.2. ■

Note that we can use (3.24), (3.25) and (3.26) in (3.17) to develop PDF using single-variate Fox's H-functions for the above special THz systems.

3.4.2 Performance Analysis for CA-multihop and FG-multihop Backhaul Transmission

In this subsection, we present analytical expressions for outage probability and ABER for both CA-multihop and FG-multihop systems.

Outage Probability

The outage probability is defined as the probability of instantaneous SNR failing to reach a threshold value. Thus, we can use $\gamma = \gamma_{\rm th}$ in (3.11) and (3.23) to get the outage probability for CA and FG multihop systems, respectively.

To get an insight on the outage behavior in high SNR regime, we can use [172] to compute the residue of multiple Mellin-Barnes integrals at the dominant pole in (3.11) for the CA-multihop and apply series expansion of Fox's H-function [166, Th. 1.7] in (3.23) for an asymptotic analysis for the FG-multihop system. However, the result of [172] is not directly applicable to the CDF form in (3.11). Since the CA-AF and the DF protocols are asymptotically equivalent at a high SNR, we can express $\overline{OP}_{\gamma_N}^{\rm CA^\infty} \approx \sum_{i=1}^{N} F_{\gamma_i}^{\infty}(\gamma_{\rm th})$. Using (3.4) in $F_{\gamma_i}(\gamma_{\rm th}) = \int_0^{\gamma_{\rm th}} f_{\gamma_i}(\gamma)d\gamma$ and applying [166, Th. 1.11], we get the asymptotic outage probability for the CA-multihop transmission as

$$\overline{OP}_{\gamma_N}^{\rm CA^\infty} \approx \sum_{i=1}^{N} \frac{A_i \gamma^{\frac{\phi_i}{2}}}{\bar{\gamma}_i^{\frac{\phi}{2}}} \left[\frac{\Gamma(-B_i)\Gamma\left(\frac{\phi}{2}+\frac{\alpha_i B_i}{2}\right)}{\Gamma(1-B_i)\Gamma\left(1+\frac{\phi}{2}+\frac{\alpha_i B_i}{2}\right)} \left(\frac{C_i \gamma^{\frac{\alpha_i}{2}}}{\bar{\gamma}_i^{\frac{\alpha}{2}}}\right)^{B_i} + \frac{\Gamma(B_i)\Gamma\left(\frac{\phi}{2}\right)}{\Gamma(1-B_i)}\right] \tag{3.27}$$

To derive the outage probability of the FG-multihop system in high SNR region, we apply

the asymptotic expansion of a single variate Fox's H-function [166, Th. 1.7]:

$$\overline{OP}_{\gamma_N}^{\mathrm{FG}^{\infty}} = \prod_{i=1}^{N} \frac{\zeta_i A_i C_i^{-\frac{\phi_i}{\alpha_i}}}{2l_i} \sum_{j=1}^{N} \left[\frac{\Gamma(-\frac{N\alpha_j\mu_j}{2l_j})\Gamma(\frac{\phi_j}{\alpha_j}-\mu_j)}{\Gamma(1+\frac{N\alpha_j\mu_j}{2l_j})\Gamma(1+\frac{\phi_j}{\alpha_j}-\mu_j)} \left(\prod_{j=1}^{N} \frac{\bar{\gamma}_j^{\frac{l_j}{N}}}{C_j^{\frac{2l_j}{N\alpha_j}}\gamma} \right)^{\frac{-N\alpha_j\mu_j}{2l_j}} \right.$$
$$\left. \times + \frac{\Gamma(-\frac{N\phi_i}{2l_i})\Gamma(1+\mu_i-\frac{\phi_i}{\alpha_i})}{\Gamma\big(1+\frac{N\phi_i}{2l_i}\big)} \left(\prod_{i=1}^{N} \frac{\bar{\gamma}_i^{\frac{l_i}{N}}}{C_i^{\frac{2l_i}{N\alpha_i}}\gamma} \right)^{\frac{-N\phi_i}{2l_i}} \right]. \tag{3.28}$$

Using $\gamma_i^0 = \gamma^0, \forall i$, and compiling the exponent of γ^0 in (3.27) and (3.28), the diversity order of for both CA and FG multihop systems can be obtained as

$$M_{\mathrm{out}}^{\mathrm{CA}} = M_{\mathrm{out}}^{\mathrm{FG}} = \min\left\{ \frac{\alpha_i\mu_i}{2}, \frac{\phi_i}{2} \right\} ; i = 1, 2, \cdots, N. \tag{3.29}$$

The diversity order in (3.29) shows that multiple relay units in the backhaul link improve the system performance.

ABER

The ABER of a communication system for a general modulation scheme over fading channel with CDF $F(\gamma)$ is given by [173]:

$$\bar{P}_e = \frac{\delta}{2\Gamma(p)} \sum_{n=1}^{k} q_n^p \int_0^{\infty} \gamma^{p-1} e^{-q\gamma} F_{\gamma}(\gamma) d\gamma, \tag{3.30}$$

where the constants p, q, δ and k determine the type of modulation scheme. Thus, we substitute (3.11) in (3.30) to get

$$\bar{P}_{e_N}^{\mathrm{CA}} = 1 - \prod_{i=1}^{N} \frac{A_i \bar{\gamma}_i^{-\frac{\phi_i}{2}} \delta}{4\Gamma(p)} \sum_{n=1}^{k} q_n^p \left[\left(\frac{1}{2\pi i}\right)^N \int_{\mathcal{L}_i} \frac{\prod_{i=1}^{N} \Gamma(B_i - S_i)\Gamma(0-S_i)\Gamma\big(-\frac{\phi_i}{2}-\frac{\alpha_i S_i}{2}\big)}{\prod_{i=1}^{N}\Gamma(1-S_i)} \right.$$
$$\left. \times \left(\prod_{i=1}^{N} \frac{C_i}{\bar{\gamma}_i^{\frac{\alpha_i}{2}}} \right)^{S_i} \frac{1}{\Gamma\big(-\sum_{i=1}^{N}\frac{\phi_i+\alpha_i S_i}{2}+1\big)} dS_i \right] I_1, \tag{3.31}$$

where $I_1 = \int_0^{\infty} \gamma^{\left(\sum_{i=1}^{N}\frac{\phi_i+\alpha_i S_i}{2}+p-1\right)} e^{-q\gamma} d\gamma = q^{-\left(\sum_{i=1}^{N}\frac{\phi_i+\alpha_i S_i}{2}+p\right)} \Gamma\Big(\sum_{i=1}^{N}\frac{\phi_i+\alpha_i S_i}{2}+p\Big)$[168, 3.381/4]. To represent the multiple Barnes integrals of (3.31) in terms of Fox's H-function, we use $S_i \to -S_i$, and apply the definition of Fox's H-function [170] to get the ABER of the

CA-multihop:

$$\bar{P}_{e_N}^{\mathrm{CA}} = 1 - \prod_{i=1}^{N} \frac{A_i \bar{\gamma}_i^{-\frac{\phi_i}{2}} \delta}{4\Gamma(p)} \sum_{n=1}^{k} \frac{1}{q_n^{\left(\sum_{i=1}^{N} \frac{\phi_i}{2}\right)}} H_{1,1;3,1;\ldots;3,1}^{0,1;0,3;\ldots;0,3} \left[\begin{array}{c|c} \frac{\bar{\gamma}_i^{\frac{\alpha_1}{2}}}{C_1 q_n^{\left(\frac{\alpha_1 S_1}{2}\right)}} & T_1(\gamma) \\ \vdots & T_2(\gamma) \\ \frac{\bar{\gamma}_i^{\frac{\alpha_N}{2}}}{C_N q_n^{\left(\frac{\alpha_N S_N}{2}\right)}} & \end{array} \right], \quad (3.32)$$

where $T_1(\gamma) = \Big\{ \big\{ \big(1-p+\sum_{i=1}^{N} \frac{\phi_i}{2}; \frac{\alpha_1}{2}, \cdots, \frac{\alpha_N}{2}\big) \big\}; \big\{ (1-B_1,1), (1,1), \big(1+\frac{\phi_1}{2}, \frac{\alpha_1}{2}\big), \cdots, (1-B_N,1), (1,1), \big(1+\frac{\phi_N}{2}, \frac{\alpha_N}{2}\big) \big\} \Big\}$ and $T_2(\gamma) = \Big\{ \big\{ \big(\sum_{i=1}^{N} \frac{\phi_i}{2}; \frac{\alpha_1}{2}, \cdots, \frac{\alpha_N}{2}\big) \big\}; \big\{ (0,1), \cdots, (0,1)_N \big\} \Big\}$.

To get the ABER for the FG-multihop system, we use (3.23) in (3.30) with the Fox's H-definition:

$$\begin{aligned} \bar{P}_{e_N}^{\mathrm{FG}} = & \left[\prod_{i=1}^{N} \frac{\zeta_i A_i C_i^{-\frac{\phi_i}{\alpha_i}}}{N\alpha_i} \frac{1}{2\pi\jmath} \int_{\mathcal{L}} \prod_{i=1}^{N} \left(C_i^{\frac{2l_i}{N\alpha_i}} \bar{\gamma}_i^{-\frac{l_i}{N}} \right)^{-r} \right. \\ & \left. \times \frac{\prod_{i=1}^{N} \Gamma\big(\frac{2rl_i}{N\alpha_i} + \frac{B_i\alpha_i+\phi_i}{\alpha_i}\big) \Gamma\big(\frac{2rl_i}{N\alpha_i} + \frac{\phi_i}{\alpha_i}\big)}{\prod_{i=1}^{N} \Gamma\big(\frac{2rl_i}{N\alpha_i} + \frac{\phi_i+\alpha_i}{\alpha_i}\big)} \frac{\Gamma(-r)}{\Gamma(1-r)} dr \right] I_3, \end{aligned} \quad (3.33)$$

where $I_3 = \frac{\delta}{2\Gamma(p)} \sum_{n=1}^{k} q_n^p \int_0^\infty e^{-q_n\gamma} \gamma^{p-r-1} d\gamma = q_n^{-p+r} \Gamma(p-r)$ [168, 3.381/4]. Thus, we use the definition of Fox's H-function [170] to express (3.33) as

$$\begin{aligned} \bar{P}_{e_N}^{\mathrm{FG}} = & \prod_{i=1}^{N} \frac{\zeta_i A_i C_i^{-\frac{\phi_i}{\alpha_i}}}{N\alpha_i 2\Gamma(p)} \sum_{n=1}^{k} q_n^{-p} H_{1+2N,2+N}^{2,2N} \\ & \times \left[\prod_{i=1}^{N} \frac{\bar{\gamma}_i^{\frac{l_i}{N}} q}{C_i^{\frac{2l_i}{N\alpha_i}}} \middle| \begin{array}{c} \prod_{i=1}^{N} \big(1-\mu_i, \frac{2l_i}{N\alpha_i}\big), \prod_{i=1}^{N} \big(1-\frac{\phi_i}{\alpha_i}, \frac{2l_i}{N\alpha_i}\big), (1,1) \\ (p,1), (0,1), \prod_{i=1}^{N} \big(-\frac{\phi_i}{\alpha_i}, \frac{2l_i}{N\alpha_i}\big) \end{array} \right]. \end{aligned} \quad (3.34)$$

We can obtain asymptotic expression (not written for brevity) for the ABER in high SNR region for the CA and FG multihop by applying the similar method used in deriving the asymptotic expressions for the outage probability.

In what follows, we use the statistical results of Theorem 3.1 and Theorem 3.2 to analyze the performance of a mixed system consisting of multihop backhaul link with a shadowed access link.

3.5 Performance Analysis of Multihop Backhaul Mixed with Access Link

In this section, we analyze the end-to-end performance of a mixed system when an access link is connected to the backhaul. We consider both uplink (UL) and downlink (DL) scenarios. In the uplink transmission, the near-optimal DF relaying protocol is used to mix the access link

with the CA-assisted N-hop backhaul link. The DF relay is more appropriate for the uplink since perfect decoding of the transmitted signal can be achieved in the first hop between the access and backhaul links. However, we use the FG relaying to integrate the backhaul and access links in the downlink transmission since perfect decoding of the signal after many hops in the backhaul may not be possible Moreover, we consider FG-multihop to realize an all FG relaying protocol for the downlink transmission. It should be mentioned that the additional hop between the backhaul and access network may not be readily included as an $N+1$- hop backhaul transmission since the propagation characteristics of the access network may be different from the backhaul.

In the following, we develop statistical results for the access link in the THz band considering the combined effect of short-term fading, shadowing, and antenna misalignment errors:

Proposition 3.2. *If γ_A is the SNR of shadowed access link distributed according to* (3.7)*, then the PDF and CDF of the generalized-K fading combined with antenna misalignment errors:*

$$f_{\gamma_A}(\gamma) = \frac{b^{m_A}\gamma^{\frac{m_A}{2}-1}\phi_A(S_A^2)^{\frac{\phi_A-m_A}{2}+1}}{\bar{\gamma}_A^{\frac{m_A}{2}}\Gamma(m_\Omega)\Gamma(m_g)} G_{1,3}^{3,0}\left(\frac{b^2\gamma}{S_A^2\bar{\gamma}_A}\middle| \begin{matrix} 1+\frac{\phi_A-m_A}{2} \\ m_M, m_M, \frac{\phi_A-m_A}{2}\end{matrix}\right), \tag{3.35}$$

$$F_{\gamma_A}(\gamma) = \frac{b^{m_A}\gamma^{\frac{m_A}{2}}\phi_A(S_A^2)^{\frac{\phi_A-m_A}{2}+1}}{\bar{\gamma}_A^{\frac{m_A}{2}}\Gamma(m_\Omega)\Gamma(m_g)} G_{2,4}^{3,1}\left(\frac{b^2\gamma}{S_A^2\bar{\gamma}_A}\middle| \begin{matrix} 1-\frac{m_A}{2}, 1+\frac{\phi_A-m_A}{2} \\ m_M, m_M, \frac{\phi_A-m_A}{2}, -\frac{m_A}{2}\end{matrix}\right). \tag{3.36}$$

Proof. The proof is presented in Appendix 3.3. ■

In the next two subsections, we use (3.35) and (3.36) to analyze the performance of the mixed link for both uplink and downlink transmissions.

3.5.1 Uplink Transmissions

Assuming perfect decoding of the received signal, the resultant SNR of the mixed multihop system for the uplink transmission is given by

$$\gamma = \min\{\gamma_N^{\mathrm{CA}}, \gamma_A\}. \tag{3.37}$$

In the following subsections, we derive exact analytical expressions of the uplink transmissions. As such, we use results of Theorem 3.1 and Proposition 3.2 to analyze the system performance.

Outage Probability

We use (3.11) and (3.36) at $\gamma = \gamma_{\mathrm{th}}$ to get the outage probability of the uplink transmission as [174]

$$\overline{OP}^{\mathrm{UL}} = F_{\gamma_N}^{\mathrm{CA}}(\gamma_{\mathrm{th}}) + F_{\gamma_A}(\gamma_{\mathrm{th}}) - F_{\gamma_N}^{\mathrm{CA}}(\gamma_{\mathrm{th}})F_{\gamma_A}(\gamma_{\mathrm{th}}). \tag{3.38}$$

To derive the diversity order of the system, asymptotic expressions of the outage probability in high SNR regime for both $F_{\gamma_N}^{\mathrm{CA}}(\gamma_{\mathrm{th}})$ (as derived in (3.27)) and $F_{\gamma_A}(\gamma_{\mathrm{th}})$ is required. To get an asymptotic outage probability of the shadowed access link, we use the asymptotic series expansion of the Meijer's G-function at $\gamma_A^0 \to 0$ [171, 07.34.06.0006.01] in (3.36):

$$F_{\gamma_A}^{\infty} = \frac{b^{m_A}\phi_A\gamma^{-\frac{m_A}{4}}(S_A^2)^{\frac{\phi_A-m_A}{2}+1}}{\bar{\gamma}_A^{\frac{m_A}{2}}\Gamma(m_\Omega)\Gamma(m_g)} \sum_{k=1}^{m} \frac{\prod_{j=1,j\neq k}^{m}\Gamma(b_j-b_k)\prod_{j=1}^{n}\Gamma(1-a_j+b_k)}{\prod_{j=n+1}^{p}\Gamma(a_j-b_k)\prod_{j=m+1}^{q}\Gamma(1-b_j+b_k)}\Big(\frac{b^2\gamma}{\bar{\gamma}_A}\Big)^{b_k}. \tag{3.39}$$

where $b_j = b_k = \{\underbrace{m_M, m_M, \frac{\phi_A-m_A}{2}}_{m}, \underbrace{-\frac{m_A}{2}}_{q-m}\}$ and $a_j = \{\underbrace{1-\frac{m_A}{2}}_{n}, \underbrace{1+\frac{\phi_A-m_A}{2}}_{p-n}\}$. Thus, the diversity order for the access link is $b_k + \frac{m_A}{2}$, where $k = 1, \cdots, m$. Using (3.27) and (3.39) in (3.38) and applying $\gamma_i^0 = \gamma^0 = \gamma_A^0, \forall i$, the diversity order of the uplink transmissions can be expressed as

$$M_{\mathrm{out}}^{\mathrm{UL}} = \min\left\{\frac{\alpha_i\mu_i}{2}, \frac{\phi_i}{2}, \frac{m_A}{2}+m_M, \frac{\phi_A}{2}\right\}; i = 1, 2, ..N. \tag{3.40}$$

The diversity order in (3.40) shows that multiple relay units in the backhaul link improve the system performance. Thus, the asymptotic performance becomes limited to short-term fading and shadowing of the access link when sufficient higher N and higher beam-width for signal transmission in the access link is employed.

ABER

The ABER of the DF relaying system with gray coding be expressed as [62]:

$$\bar{P}_e^{\mathrm{UL}} = \bar{P}_{e_N}^{\mathrm{CA}} + \bar{P}_{e_A} - \bar{P}_{e_N}^{\mathrm{CA}}\bar{P}_{e_A}, \tag{3.41}$$

where $\bar{P}_{e_N}^{\mathrm{CA}}$ (already derived in (3.32)) and $\bar{P}_{e_A}$ are the ABER of backhaul and shadowed access link, respectively. To get $\bar{P}_{eA}$, we use (3.36) in (3.30) and apply the definition of the Meijer's G-function:

$$\bar{P}_{e_A} = \left[\frac{b^{m_A}\phi_A(S_A^2)^{\frac{\phi_A-m_A}{2}+1}}{2\Gamma(p)\bar{\gamma}_A^{\frac{m_A}{2}}\Gamma(m_\Omega)\Gamma(m_g)}\frac{1}{2\pi i}\int_{\mathcal{L}}\frac{\Gamma\big(\frac{m_A}{2}+s\big)}{\Gamma\big(1+\frac{m_A}{2}+s\big)}\right.$$
$$\left.\times\frac{\Gamma\big(m_M-s\big)\Gamma\big(m_M-s\big)\Gamma\big(\frac{\phi_A-m_A}{2}-s\big)}{\Gamma\big(1+\frac{\phi_A-m_A}{2}-s\big)}\left(\frac{b^2}{S_A^2\bar{\gamma}_A}\right)^s\right]I_2, \tag{3.42}$$

where $I_2 = \frac{\delta}{2\Gamma(p)}\sum_{n=1}^{k}q_n^p\int_0^\gamma e^{-q_n\gamma}\gamma^{\frac{m_A}{2}+s+p-1}d\gamma = q_n^{-\left(\frac{m_A}{2}+s+p\right)}\Gamma\big(\frac{m_A}{2}+s+p\big)$. Using I_2 and applying the definition of Meijer's G-function in (3.42), the ABER for the access link can be

expressed as:

$$\bar{P}_{e_A} = \frac{b^{m_A}\phi_A(S_A^2)^{\frac{\phi-m_A}{2}+1}\delta}{2\Gamma(p)\bar{\gamma}_A^{\frac{m_A}{2}}\Gamma(m_\Omega)\Gamma(m_g)}\sum_{n=1}^{k} q_n^{-\frac{m_A}{2}} G_{3,4}^{3,2}\left(\frac{b^2}{q_n S_A^2\gamma_A^0}\middle| \begin{matrix} 1-\frac{m_A}{2}-p, 1-\frac{m_A}{2}, 1+\frac{\phi_A-m_A}{2} \\ m_M, m_M, \frac{\phi_A-m_A}{2}, -\frac{m_A}{2}\end{matrix}\right). \tag{3.43}$$

Similar to the outage probability, we can obtain the asymptotic expression of the ABER for the uplink system.

3.5.2 Downlink Transmission

We apply the FG relaying to mix the FG-multihop and access links such that the end-to-end SNR becomes

$$\gamma^{\mathrm{DL}} = \frac{\gamma_N^{\mathrm{FG}}\gamma_A}{\psi+\gamma_A}, \tag{3.44}$$

where $\psi = (\mathbb{E}_{\gamma_N}(1+\gamma)^{-1})^{-1}$ is computed using the semi-blind method of statistical information of the received signal [53]. To analyze the all FG-multihop system, we need to derive the PDF of the resultant SNR, as given in [53]:

$$f_\gamma^{\mathrm{DL}}(z) = \int_0^\infty f_{\gamma_N^{\mathrm{FG}}}\Big(\frac{z(x+\psi)}{x}\Big) f_{\gamma_A}(x)\frac{x+\psi}{x}dx. \tag{3.45}$$

In the following Theorem, we derive analytical expressions of the PDF $f_\gamma^{\mathrm{DL}}(z)$ and CDF $F_\gamma^{\mathrm{DL}}(z)$ using bivariate Fox's H-function.

Theorem 3.3. *If γ_N^{FG} is the SNR of N-hop backhaul link and γ_A is the SNR of the shadowed access link, then CDF and PDF of the resultant SNR in* (3.44) *is given by*

$$f_\gamma^{\mathrm{DL}}(\gamma) = \prod_{i=1}^{N}\frac{\zeta_i A_i C_i^{-\frac{\phi_i}{\alpha_i}} b^{m_A}\phi_A(S_A^2)^{\frac{\phi_A-m_A}{2}+1}\psi^{\frac{m_A}{2}}}{2N\alpha_i\bar{\gamma}_A^{\frac{m_A}{2}}\Gamma(m_\Omega)\Gamma(m_g)\gamma} H_{1,0:2N,1+N:1,4}^{0,1:0,2N:4,0}\left[\prod_{i=1}^{N}\frac{\bar{\gamma}_i^{\frac{l_i}{N}}}{C_i^{\frac{2l_i}{N\alpha_i}}\gamma}, \frac{b^2\psi}{S_A^2\bar{\gamma}_A}\middle| \begin{matrix} V_1(\gamma) \\ V_2(\gamma)\end{matrix}\right], \tag{3.46}$$

where $V_1(\gamma) = \Big\{\big\{\big(1-\frac{m_A}{2},1,1\big)\big\};\big\{\big(1-\mu_1,\frac{2l_1}{N\alpha_1}\big),\cdots,\big(1-\mu_N,\frac{2l_N}{N\alpha_N}\big),\big(1-\frac{\phi_1}{\alpha_1},\frac{2l_1}{N\alpha_1}\big),\cdots,\big(1-\frac{\phi_N}{\alpha_N},\frac{2l_N}{N\alpha_N}\big)\big\};\big\{1+\frac{\phi_A-m_A}{2},1\big\}\Big\}$ *and* $V_2(\gamma) = \Big\{\big\{-\big\};\big\{\big(-\frac{\phi_1}{\alpha_1},\frac{2l_1}{N\alpha_1}\big),\cdots\big(-\frac{\phi_N}{\alpha_N},\frac{2l_N}{N\alpha_N}\big),(1,1)\big\};\big\{\big(m_M,1\big),\big(m_M,1\big),\big(\frac{\phi_A-m_A}{2},1\big),\big(-\frac{m_A}{2},1\big)\big\}\Big\}$.

$$F_\gamma^{\mathrm{DL}}(\gamma) = \prod_{i=1}^{N}\frac{\zeta_i A_i C_i^{-\frac{\phi_i}{\alpha_i}} b^{m_A}\phi_A(S_A^2)^{\frac{\phi_A-m_A}{2}+1}\psi^{\frac{m_A}{2}}}{2N\alpha_i\bar{\gamma}_A^{\frac{m_A}{2}}\Gamma(m_\Omega)\Gamma(m_g)} H_{1,0:1+2N,2+N:1,4}^{0,1:1,2N:4,0}\left[\prod_{i=1}^{N}\frac{\bar{\gamma}_i^{\frac{l_i}{N}}}{C_i^{\frac{2l_i}{N\alpha_i}}\gamma_{\mathrm{th}}}, \frac{b^2\psi}{S_A^2\bar{\gamma}_A}\middle| \begin{matrix} \tilde{V}_1(\gamma) \\ \tilde{V}_2(\gamma)\end{matrix}\right]. \tag{3.47}$$

where $\tilde{V}_1(\gamma) = \Big\{\big\{\big(1-\frac{m_A}{2},1,1\big)\big\};\big\{\big(1-\mu_1,\frac{2l_1}{N\alpha_1}\big),\cdots,\big(1-\mu_N,\frac{2l_N}{N\alpha_N}\big),\big(1-\frac{\phi_1}{\alpha_1},\frac{2l_1}{N\alpha_1}\big),\cdots,\big(1-\frac{\phi_N}{\alpha_N},\frac{2l_N}{N\alpha_N}\big),\big(1,1\big)\big\};\big\{1+\frac{\phi_A-m_A}{2},1\big\}\Big\}$ *and* $\tilde{V}_2(\gamma) = \Big\{\big\{-\big\};\big\{\big(0,1\big),\big(-\frac{\phi_1}{\alpha_1},\frac{2l_1}{N\alpha_1}\big),\cdots\big(-\frac{\phi_N}{\alpha_N},\frac{2l_N}{N\alpha_N}\big),\big(1,1\big)\big\};\big\{\big(m_M,1\big),\big(m_M,1\big),\big(\frac{\phi_A-m_A}{2},1\big),\big(-\frac{m_A}{2},1\big)\big\}\Big\}$.

Proof. The proof is presented in Appendix 3.4. ■

In what follows next, we use the results of Theorem 3.3 to analyze the system performance for the mixed THz transmissions.

Outage Probability

We derive an exact expression of the outage probability by evaluating the CDF in (3.47) at $\gamma = \gamma_{\rm th}$. We can also develop asymptotic analysis of the outage probability in high SNR regime. However, the asymptotic expansion of the multivariate Fox's H-function at the dominant pole [172] can not be readily applied to the bivariate Fox's H-function in (3.47) since the average SNR term appears in both numerator and denominator of the contour integrals. Thus, we expand the Mellin-Barnes integrals of the bivariate Fox's H-function and adopt the asymptotic expansion of the single-variate Fox's H-function [166, Th. 1.11] by converting $S_1 \to -S_1$. We compute the corresponding poles of the first contour integral $\mathcal{L}_1$: $S_1 = \{\frac{m_A+2S_2}{2}, \sum_{i=1}^{N}\frac{N\alpha_i\mu_i}{2l_i}, \sum_{i=1}^{N}\frac{N\phi_i}{2l_i}\}$ and poles of the second contour integral $\mathcal{L}_2$: $S_2 = \{\frac{m_A}{2}, m_M, \frac{\phi-m_A}{2}, -\frac{m_A}{2}\}$. Evaluating the residues of the contour integrals at these poles with $\bar{\gamma}_i = C$ and $\bar{\gamma}_A = \bar{\gamma}_i = \bar{\gamma}, \forall i$, we present the asymptotic expression of the outage probability in (3.48) for different scenarios depending on the relative magnitude of channel and system parameters. Combining the dominant terms of $\bar{\gamma}$ in (3.48), we get the diversity order of the system as

$$M_{\rm out}^{\rm DL} = \min\left\{\frac{\alpha_i\mu_i}{2}, \frac{\phi_i}{2}, \frac{m_A}{2}+m_M, \frac{\phi_A}{2}\right\}. \tag{3.49}$$

ABER

Next, we analyze the ABER of the downlink transmission by substituting (3.47) in (3.30) to get

$$\begin{aligned}\bar{P}_e^{\rm DL} = &\left[\prod_{i=1}^{N}\frac{\zeta_i A_i C_i^{-\frac{\phi_i}{\alpha_i}} b^{m_A}\phi_A (S_A^2)^{\frac{\phi_A-m_A}{2}+1}\psi^{\frac{m_A}{2}}}{4N\Gamma(p)\alpha_i\bar{\gamma}_A^{\frac{m_A}{2}}\Gamma(m_\Omega)\Gamma(m_g)}\frac{1}{2\pi i}\int_{\mathcal{L}_1}\Gamma\left(\frac{m_A}{2}+S_1+S_2\right)\frac{\Gamma(-S_1)}{\Gamma(1-S_1)}\right.\\
&\times\left(\prod_{i=1}^{N}\frac{\bar{\gamma}_i^{\frac{l_i}{N}}}{C_i^{\frac{2l_i}{N\alpha_i}}}\right)^{S_1}\frac{\prod_{i=1}^{N}\Gamma\big(\frac{B_i\alpha_i+\phi_i}{\alpha_i}+\frac{2l_i}{N\alpha_i}S_1\big)\Gamma\big(\frac{\phi_i}{\alpha_i}+\frac{2l_i}{N\alpha_i}S_1\big)}{\prod_{i=1}^{N}\Gamma\big(\frac{\phi_i+\alpha_i}{\alpha_i}+\frac{2l_i}{N\alpha_i}S_1\big)\Gamma(S_1)}dS_1\\
&\times\left.\frac{1}{2\pi i}\int_{\mathcal{L}_2}\frac{\Gamma(m_M-S_2)\Gamma(m_M-S_2)\Gamma\big(\frac{\phi_A-m_A}{2}-S_2\big)}{\Gamma\big(1+\frac{\phi_A-m_A}{2}-S_2\big)}\Gamma\big(-\frac{m_A}{2}-S_2\big)\left(\frac{b^2\psi}{S_A^2\bar{\gamma}_A}\right)^{S_2}dS_2\right]I_7,\end{aligned} \tag{3.50}$$

$$\overline{OP}_{\gamma}^{\mathrm{DL}^{\infty}} \approx \begin{cases} \left(T_{11}\left(\frac{b^2\psi}{S_A^2\bar{\gamma}_A}\right)^{m_M} + T_{12}\left(\frac{b^2\psi}{S_A^2\bar{\gamma}_A}\right)^{\frac{-m_A}{2}} + T_{13}\left(\frac{b^2\psi}{S_A^2\bar{\gamma}_A}\right)^{\frac{\phi_A-m_A}{2}}\right) \\ \times\left(\prod_{i=1}^{N}\frac{C_i^{\frac{2l_i}{N\alpha_i}}\gamma_{\mathrm{th}}}{\bar{\gamma}_i^{\frac{l_i}{N}}}\right)^{\frac{N\alpha_i\mu_i}{2l_i}} : \text{ if } \frac{\alpha_i\mu_i}{2} \text{ is the minimum ,} \\ \left(T_{21}\left(\frac{b^2\psi}{S_A^2\bar{\gamma}_A}\right)^{m_M} + T_{22}\left(\frac{b^2\psi}{S_A^2\bar{\gamma}_A}\right)^{\frac{\phi_A-m_A}{2}} + T_{23}\left(\frac{b^2\psi}{S_A^2\bar{\gamma}_A}\right)^{\frac{-m_A}{2}}\right) \\ \times\left(\prod_{i=1}^{N}\frac{C_i^{\frac{2l_i}{N\alpha_i}}\gamma_{\mathrm{th}}}{\bar{\gamma}_i^{\frac{l_i}{N}}}\right)^{\frac{N\phi_i}{2l_i}} : \text{if } \frac{\phi_i}{2} \text{ is the minimum,} \\ T_{31}\left(\prod_{i=1}^{N}\frac{C_i^{\frac{2l_i}{N\alpha_i}}\gamma_{\mathrm{th}}}{\bar{\gamma}_i^{\frac{l_i}{N}}}\right)^{\frac{m_A+2m_M}{2}}\left(\frac{b^2\psi}{S_A^2\bar{\gamma}_A}\right)^{m_M} : \text{if } \frac{m_A}{2}+m_M \text{ is the minimum,} \\ T_{41}\left(\prod_{i=1}^{N}\frac{C_i^{\frac{2l_i}{N\alpha_i}}\gamma_{\mathrm{th}}}{\bar{\gamma}_i^{\frac{l_i}{N}}}\right)^{\frac{\phi_A}{2}}\left(\frac{b^2\psi}{S_A^2\bar{\gamma}_A}\right)^{\frac{\phi_A-m_A}{2}} : \text{if } \frac{\phi_A}{2} \text{ is the minimum .} \end{cases} \tag{3.48}$$

where

$T_0 = \prod_{i=1}^{N}\frac{\zeta_i A_i C_i^{-\frac{\phi_i}{\alpha_i}} b^{m_A}\phi_A (S_A^2)^{\frac{\phi-m_A}{2}+1}\psi^{\frac{m_A}{2}}}{2N\alpha_i\Gamma(m_\Omega)\Gamma(m_g)\bar{\gamma}_A^{\frac{m_A}{2}}}$, $T_{11} = \frac{T_0\Gamma\left(-\frac{m_A}{2}-m_M\right)\prod_{i=1}^{N}2\Gamma\left(\frac{m_A}{2}-\frac{N\alpha_i\mu_i}{2l_i}+m_M\right)}{\prod_{i=1}^{N}\left(\frac{\phi_i}{\alpha_i}-\mu_i\right)\left(\frac{N\alpha_i\mu_i}{2l_i}\right)\Gamma(-\frac{N\alpha_i\mu_i}{2l_i})\left(\frac{\phi_A-m_A}{2}-m_M\right)}$,

$T_{12} = \frac{T_0\Gamma(m_M+\frac{m_A}{2})\Gamma(m_M+\frac{m_A}{2})}{\frac{\phi_A}{2}\prod_{i=1}^{N}\left(\frac{\phi_i}{\alpha_i}-\mu_i\right)\left(\frac{N\alpha_i\mu_i}{2l_i}\right)}$, $T_{13} = \frac{T_0\Gamma\left(m_M-\frac{\phi_A-m_A}{2}\right)\Gamma\left(m_M-\frac{\phi_A-m_A}{2}\right)\Gamma\left(-\frac{\phi_A}{2}\right)\prod_{i=1}^{N}\Gamma\left(-\frac{N\alpha_i\mu_i}{2l_i}+\frac{\phi_A}{2}\right)}{\prod_{i=1}^{N}\left(\frac{\phi_i}{\alpha_i}-\mu_i\right)\left(\frac{N\alpha_i\mu_i}{2l_i}\right)\Gamma(-\frac{N\alpha_i\mu_i}{2l_i})}$,

$T_{21} = \frac{T_0\Gamma\left(-\frac{m_A}{2}-m_M\right)\prod_{i=1}^{N}2\Gamma\left(\frac{m_A}{2}-\frac{N\phi_i}{2l_i}+m_M\right)\Gamma\left(\mu_i-\frac{\phi_i}{\alpha_i}\right)}{\left(\frac{\phi_A-m_A}{2}-m_M\right)\prod_{i=1}^{N}\Gamma\left(-\frac{N\phi_i}{2l_i}\right)\left(\frac{N\phi_i}{2l_i}\right)}$,

$T_{22} = \frac{T_0\Gamma\left(m_M-\frac{\phi_A-m_A}{2}\right)\Gamma\left(m_M-\frac{\phi_A-m_A}{2}\right)\Gamma\left(\frac{-\phi_A}{2}\right)\prod_{i=1}^{N}\Gamma\left(-\frac{N\phi_i}{2l_i}+\frac{\phi_A}{2}\right)\Gamma\left(\mu_i-\frac{\phi_i}{\alpha_i}\right)}{\prod_{i=1}^{N}\Gamma\left(-\frac{N\phi_i}{2l_i}\right)\left(\frac{N\phi_i}{2l_i}\right)}$,

$T_{23} = \frac{T_0\Gamma\left(m_M+\frac{m_A}{2}\right)\Gamma\left(m_M+\frac{m_A}{2}\right)\prod_{i=1}^{N}\Gamma\left(\mu_i-\frac{\phi_i}{\alpha_i}\right)}{\frac{\phi_A}{2}\prod_{i=1}^{N}(\frac{N\phi_i}{2l_i})}$,

$T_{31} = \frac{2T_0\Gamma\left(-\frac{m_A}{2}-m_M\right)\prod_{i=1}^{N}\Gamma\left(\mu_i-\frac{l_i(m_A-2m_M)}{N\alpha_i}\right)}{\left(\frac{m_A-2m_M}{2}\right)\left(1+\frac{\phi-m_A}{2}-m_M\right)\Gamma\left(\frac{2m_M-m_A}{2}\right)\prod_{i=1}^{N}\left(\frac{\phi_i}{\alpha_i}-\frac{l_i(m_A-2m_M)}{N\alpha_i}\right)}$ and

$T_{41} = \frac{T_0\Gamma\left(m_M-\left(\frac{\phi_A-m_A}{2}\right)\right)\Gamma\left(m_M-\left(\frac{\phi_A-m_A}{2}\right)\right)\prod_{i=1}^{N}\Gamma\left(\mu_i-\frac{l_i(2m_A-\phi_A)}{N\alpha_i}\right)}{\left(\frac{2m_A-\phi_A}{2}\right)\left(-\frac{\phi_A}{2}\right)\Gamma\left(\frac{\phi_A-2m_A}{2}\right)\prod_{i=1}^{N}\left(\frac{\phi_i}{\alpha_i}-\frac{l_i(2m_A-\phi_A)}{N\alpha_i}\right)}$.

Table 3.1: List of Simulation Parameters

Parameter	Value	Parameter	Value
THz carrier frequency	300 GHz [175]	α	1-2 [153]
THz signal bandwidth	10 GHz [175]	μ	0.5-2[153]
Antenna Gain (Backhaul link)	33 dBi[22]	Ω	1
Antenna Gain (Access link)	10 dBi	σ_{dB}	2-8.6 [156]
Transmit power	0-40 dBm	m_Ω	–
Noise PSD	-174 dBm/Hz [175]	m_g	1-5
Noise figure	5 dB [175]	ϕ_i	37
Antenna aperture radius (r_1)	10 cm	ϕ_A	$2.3 - 14.5$
Jitter standard deviation (σ_s)	5-20 cm [150]	w_z/r	6 [150]

where $I_7 = \frac{\delta}{2\Gamma(p)} \sum_{n=1}^{k} q_n^p \int_0^\infty \gamma^{p-1-S_1} e^{-q_n\gamma} d\gamma$ is solved utilizing [168, 3.381/4] to get $q_n^{S_1-p}\Gamma(p-S_1)$. Substituting I_7 in (3.50) and applying the definition of Fox's H-function [170], we get the ABER for downlink transmissions as

$$\bar{P}_e^{\mathrm{DL}} = \prod_{i=1}^{N} \frac{\zeta_i A_i C_i^{-\frac{\phi_i}{\alpha_i}} b^{m_A} \phi_A (S_A^2)^{\frac{\phi_A - m_A}{2}+1} \psi^{\frac{m_A}{2}} \delta}{4N\Gamma(p)\alpha_i \bar{\gamma}_A^{\frac{m_A}{2}} \Gamma(m_\Omega)\Gamma(m_g)}$$
$$\sum_{n=1}^{k} H_{1,0:1+2N,3+N:1,4}^{0,1:2,2N:4,0} \left[\prod_{i=1}^{N} \frac{\bar{\gamma}_i^{\frac{l_i}{N}} q_n}{C_i^{\frac{2l_i}{N\alpha_i}}}, \frac{b^2\psi}{S_A^2 \bar{\gamma}_A} \middle| \begin{matrix} X_1(\gamma) \\ X_2(\gamma) \end{matrix} \right], \tag{3.51}$$

where $X_1(\gamma) = \Big\{ \big\{ \big(1-\frac{m_A}{4}, 1, 1\big) \big\}; \big\{ \big(1-\mu_1, \frac{2l_1}{N\alpha_1}\big), \cdots, \big(1-\mu_N, \frac{2l_N}{N\alpha_N}\big), \big(1-\frac{\phi_1}{\alpha_1}, \frac{2l_1}{N\alpha_1}\big), \cdots, \big(1-\frac{\phi_N}{\alpha_N}, \frac{2l_N}{N\alpha_N}\big), \big(1,1\big) \big\}; \big\{ 1+\frac{\phi_A - m_A}{2}, 1 \big\} \Big\}$ and $X_2(\gamma) = \Big\{ \big\{ - \big\}; \big\{ \big(p,1\big), \big(0,1\big), \big(-\frac{\phi_1}{\alpha_1}, \frac{2l_1}{N\alpha_1}\big), \cdots \big(-\frac{\phi_N}{\alpha_N}, \frac{2l_N}{N\alpha_N}\big), \big(1,1\big) \big\}; \big\{ \big(m_M,1\big), \big(m_M,1\big), \big(\frac{\phi_A - m_A}{2}, 1\big), \big(-\frac{m_A}{2}, 1\big) \big\} \Big\}$.

The asymptotic expression of ABER for the downlink transmissions can be obtained by following the similar procedure as adopted for outage probability with the same diversity order expression, as given in (3.49).

3.6 Simulation and Numerical Analysis

In this section, we demonstrate the performances of multihop-assisted backhaul mixed with the shadowed access link using computer simulations. We validate the derived analytical and asymptotic expressions with Monte-Carlo simulations by numerically evaluating Meijer's G and Fox's H-functions. To compute Meijer's G-function and single-variate Fox's H-function, we use the standard library in MATLAB and Mathematica, and use implementation codes of bivariate Fox's H-function and multivariate Fox's H-function [169] [176]. We consider varying backhaul link distance in the range of $d_{\mathrm{MH}} = 20$ m to $d_{\mathrm{MH}} = 100$ m with equidistant relay position and a fixed distance of $d_A = 20$ m for the access link. The absorption coefficient k_i and k_A is calculated for both backhaul and access link using relative humidity 50%, atmospheric

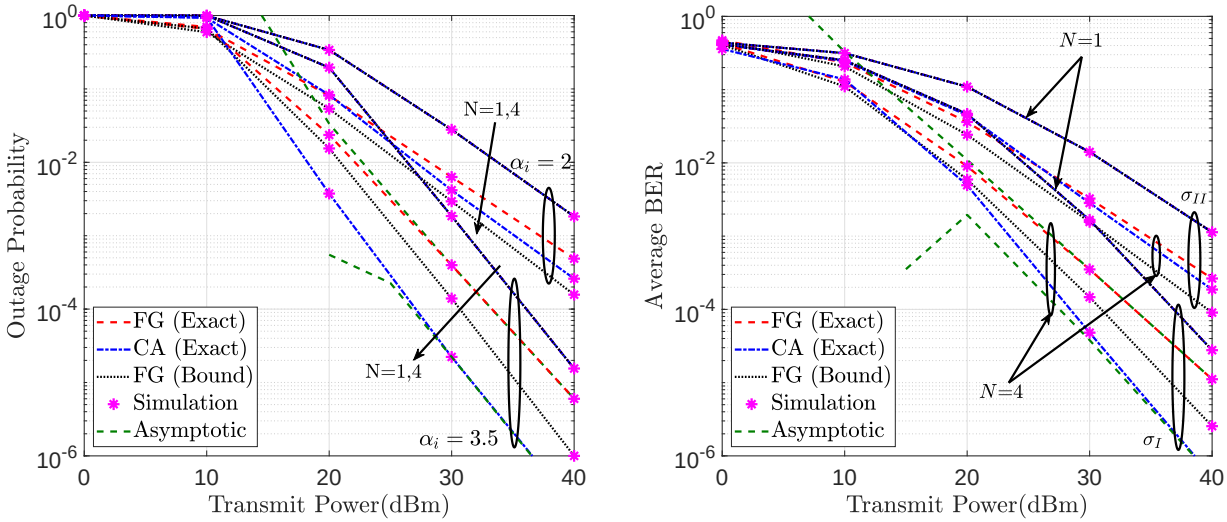

(a) Outage Probability, $\mu = 1.2$, $\sigma_s = 5$cm.

(b) ABER, $\alpha = 1.5$, $\mu = 2.5$.

Figure 3.2: Performance of multihop THz backhaul link with 100 m.

pressure 101325 Pa, temperature 296^o K at a carrier frequency 300 GHz [33]. We list the parameters for channel fading, AWGN, and antenna misalignment errors in Table 3.1. As such, we consider various non-linearity parameters α and multipath clustering μ for the backhaul link with varying shadowing severity (σ_{dB}) and short term fading (m_g) in the access link. Unless specified, we adopt higher antenna misalignment errors in the access link than the backhaul link, i.e., $\phi_A < \phi_i, \forall i$.

3.6.1 Multihop Backhaul Transmission

In Fig. 3.2, we demonstrate the effect of system and channel parameters on the outage and ABER performance versus transmit power for the backhaul link. We consider i.i.d. channel parameters for each hop, which is a reasonable assumption for short link distances. The outage probability improves with an increase in the fading parameter α_i since the channel becomes more linear, as depicted in Fig 3.2(a). The figure shows that a change in the parameter $\alpha_i = 2$ to $\alpha_i = 3.5$ requires 15 dBm less transmit power to achieve an outage probability of 5×10^{-3} with the 4-hop CA system. Further, the FG-multihop transmission performs close to the CA-multihop for highly non-linear THz channels. The benefit of multiple relays is also evident from the figure when the direct link ($N = 1$) plot is compared with the 4 hop transmission. It can be seen that the outage performance improves 100 folds for the 4-hop FG system compared with the direct transmission at an average SNR of 30 dB.

In Fig. 3.2(b), we simulate i.ni.d. antenna misalignment errors for each hop to demonstrate the ABER performance of the multihop system. We consider two scenarios of antenna misalignment errors: standard deviation of jitter $\sigma_I : \sigma_s = 5 + i$ cm for $i = 1, 2, 3, 4$ hops and $\sigma_{II} : \sigma_s = 17 + i$ cm for $i = 1, 2, 3, 4$ hops. The figure shows a significant degradation in the ABER with an increase in the jitter. The FG-multihop performs close to the CA-multihop when

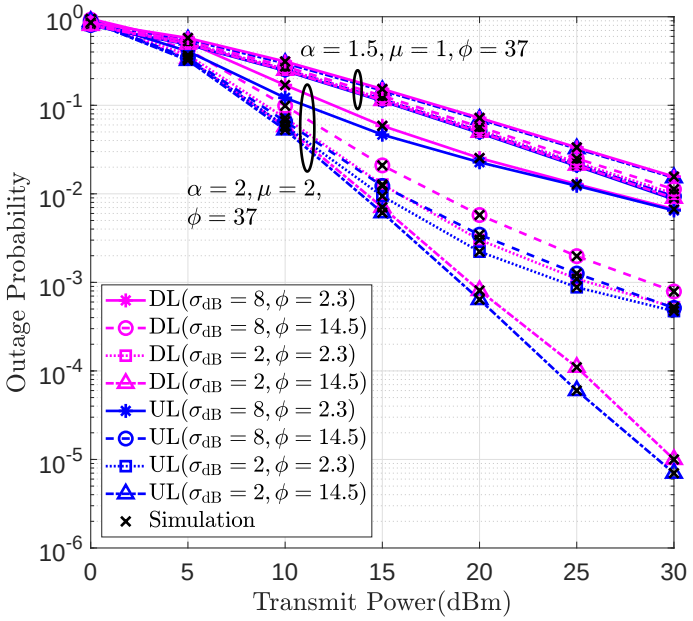

Figure 3.3: Outage probability of the mixed dual-hop relaying system with $m_g = 1$, $\phi_i = 37$, $d_{\text{MH}} = 20$ m, and $d_A = 20$ m.

the effect of antenna misalignment errors is high. Further, an increase in the number of hops from $N = 1$ to $N = 4$ reduces the required transmit power by 10 dBm and 5 dBm for the CA and FG multihop systems, respectively.

In the next two subsections, we integrate the backhaul with the access and delve into the inquisition "how many AF-assisted relays are required in the backhaul to extend the communication range with $N + 1$ hops to achieve at least the same performance of the mixed link with the popular dual-hop system ($N = 2$) as a reference?" Thus, we demonstrate the impact of the number of hops in the backhaul link on the outage probability and ABER of the mixed link for both uplink and downlink transmission. Unless stated otherwise, we consider the transmission distance of the backhaul link $d_{\text{MG}} = 20$ m for the $N = 2$ scenario and the extended link distance $d_{\text{MH}} = 50$ m with multihop relaying at a fixed access link $d_A = 20$ m.

3.6.2 Uplink and Downlink Transmission for Mixed Backhaul-Access Link

We plot the outage probability of the mixed relaying system for both uplink and downlink in Fig. 3.3 and 3.4. We demonstrate the impact of channel fading, shadowing, and antenna misalignment errors on the performance of the mixed system by considering a single relay (i.e., a typical dual-hop transmission with $N = 1$) to integrate the backhaul with the access system in Fig. 3.3. We vary channel characteristics of the access link at different shadowing factors $\sigma_{\text{dB}} = 2$ and $\sigma_{\text{dB}} = 8$ at a short-term fading $m_g = 1$ considering both lower ($\phi_A = 2.3$) and higher ($\phi_A = 14.5$) antenna misalignment errors with the backhaul link consisting of two sets $\alpha = 2$, $\mu = 2$ and $\alpha = 1.5$, $\mu = 1$ with antenna misalignment error parameter $\phi = 37$. Note that $\phi = 37$, $\phi_A = 14.5$, and 2.3 corresponds to the jitters variance of $\sigma_s^2 = 5$ cm, $\sigma_s^2 = 8$ cm,

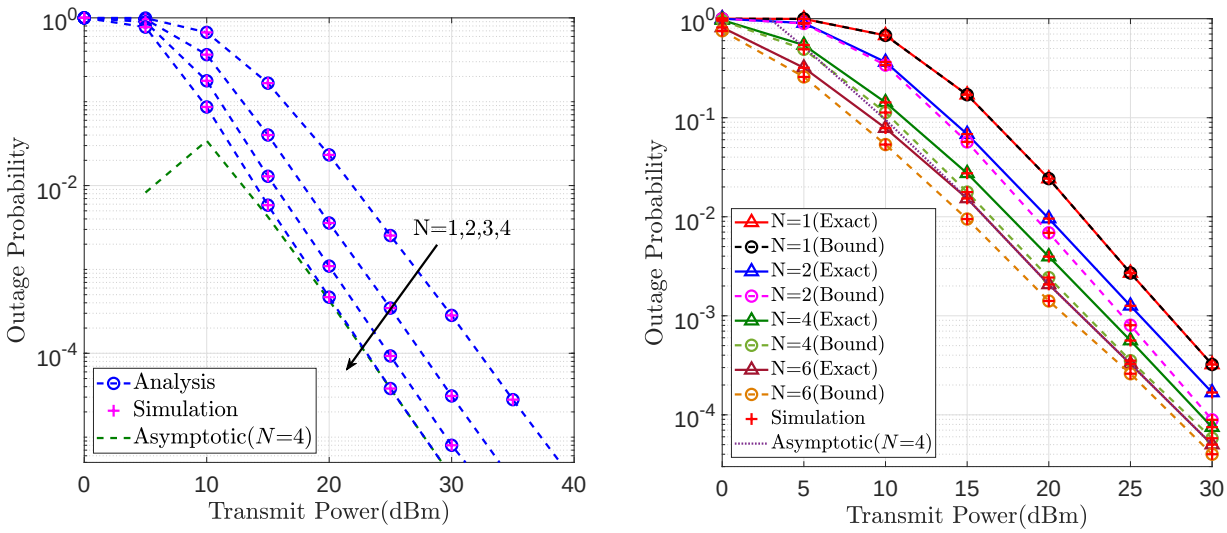

(a) Uplink transmission. (b) Downlink transmission.

Figure 3.4: Outage probability of the mixed multihop relaying system with $m_g = 1$, $\phi_i = 37$, $d_{\text{MH}} = 50$ m and $d_A = 20$ m.

and 20 cm, respectively [150]. We fix the link distance of 20 m for both the hops. It can be seen from Fig. 3.3 that higher values of α and μ improve the outage probability since an increase in α and μ reduces the non-linearity effect and improves multi-path clustering, respectively. Further, Fig. 3.3 shows that an increase in the antenna misalignment errors (depicted by a decrease of ϕ_A from 14.5 to 2.3) of the access link decreases the outage performance by a factor 10 when $\alpha = 2$, $\mu = 2$, and $\phi = 14.5$ at a transmit power of 30dBm. Moreover, the outage probability is significantly degraded when the shadowing factor is increased from 2 dB (less shadowing) to 8 dB (severe shadowing).

To this end, we choose judicially channel parameters in Fig. 3.3 to demonstrate the diversity order of the system. Note that $m_A = m_\Omega + m_g$ and $m_M = m_\Omega - m_g$, where $m_\Omega = 18.36$ when $\sigma_{\text{dB}} = 2$ and $m_\Omega = 0.75$ when $\sigma_{\text{dB}} = 8$. Using $M_{\text{out}} = \min\left\{\frac{\alpha\mu}{2}, \frac{\phi}{2}, \frac{m_A}{2} + m_M, \frac{\phi_A}{2}\right\}$, the diversity order is $M_{\text{out}} = \frac{\alpha\mu}{2} = 0.75$ (when $\alpha = 1.5$ and $\mu = 1$) since $\frac{\alpha\mu}{2}$ is the minimum among other channel and antenna misalignment error parameters. Thus, the slope of plots for $\alpha = 1.5$ and $\mu = 1$ in Fig. 3.3 remains independent of other channel parameters i.e., σ_{dB}, ϕ_A, and m_g. However, when $\alpha = 2$ and $\mu = 2$, the outage-diversity order $M_{\text{out}} = 0.62$ depends on the fading parameters of the access link when $\sigma_{\text{dB}} = 8$ and becomes $M_{\text{out}} = 1.15$ when $\sigma_{\text{dB}} = 2$, which depends on the minimum of antenna misalignment errors of the backhaul and shadowed links. Hence, the slope of the plots in Fig. 3.3 confirms our analysis of the diversity order.

We demonstrate the impact of multihop relaying on the outage performance as illustrated in Fig. 3.4(a) (for uplink) and Fig. 3.4(b) (for downink) by considering $\sigma_{dB} = 2$, $\phi_A = 14.5$, $\alpha = 2$, and $\mu = 2$. It can be seen that the outage probability of the mixed link significantly improves with an increase in the number of relays employed in the backhaul link. As such the

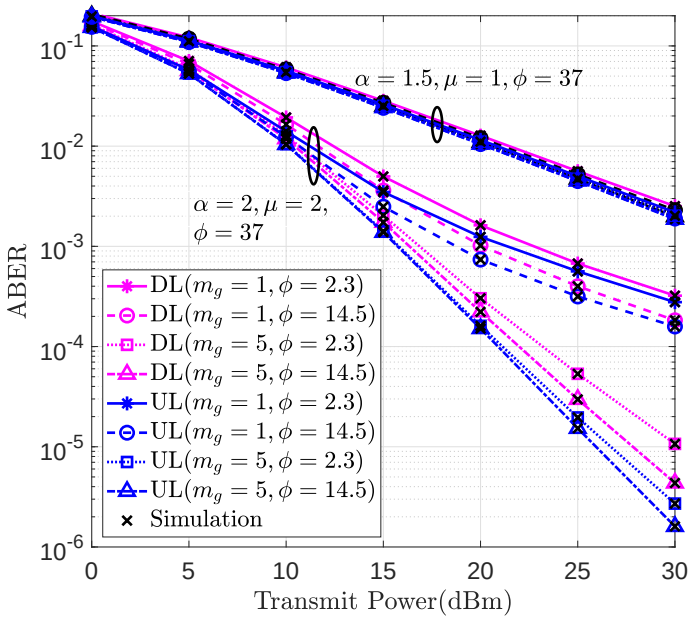

Figure 3.5: ABER of the mixed dual-hop relaying system with $\sigma_{dB} = 5$, $\phi_i = 37$, $d_{\text{MH}} = 20$ m, and $d_A = 20$m.

uplink transmission with an $N = 4$ relays requires 10 dBm lesser transmit power to get a typical outage probability of 3×10^{-3}, as shown in Fig. 3.4(a). However, there is a 5 dBm transmit power saving with the downlink transmission, as depicted in Fig. 3.4(b) due to the folding of background noise from previous hops. Comparing the two AF relaying schemes, the FG-assisted system requires 6 hops as compared with only 3 hops when the CA relaying is employed to achieve a similar outage performance 2×10^{-4} at a transmit power of 25 dBm. Further, observing the scaling of outage probability with N, it can be seen that the cumulative gain of the AF-assisted multihop system (see Fig. 3.4(a) and Fig. 3.4(b)) reduces with an increase in the number of hops advocating the use of a limited number of relays. Comparing the outage probability in Fig. 3.3 and plot with $N = 4$ in Fig. 3.4(b), it can be seen that the multihop relaying in the backhaul extends the communication range from $d_1 = 20$ m to $d_1 = 50$ m with similar outage performance using 3 relays providing an average of 8 m range extension with each additional relay. The effect of multihop relaying N on the diversity order can also be observed from the slope of plots, as shown in Fig. 3.4(a) and Fig. 3.4(b).

In Fig. 3.5, we demonstrate the ABER performance of the mixed relaying system. We compare the ABER performance of the $N = 2$ system (see Fig. 3.5) with $N > 2$ uplink (see Fig. 3.6(a)) and downlink transmission (see Fig. 3.6(b)). Comparing Fig. 3.5 and 3.6 with the outage probability in Fig. 3.3 and 3.4, we can draw similar conclusions since the ABER follows a similar trend as that of the outage probability with for the same network configuration. We investigate the impact of short-term fading m_g of the access link on the ABER. Fig. 3.5 shows that the ABER significantly degraded when the factor m_g is reduced from 5 to 1. This happens due to a decrease in the multi-path clustering, thereby worsening the channel condition. We can

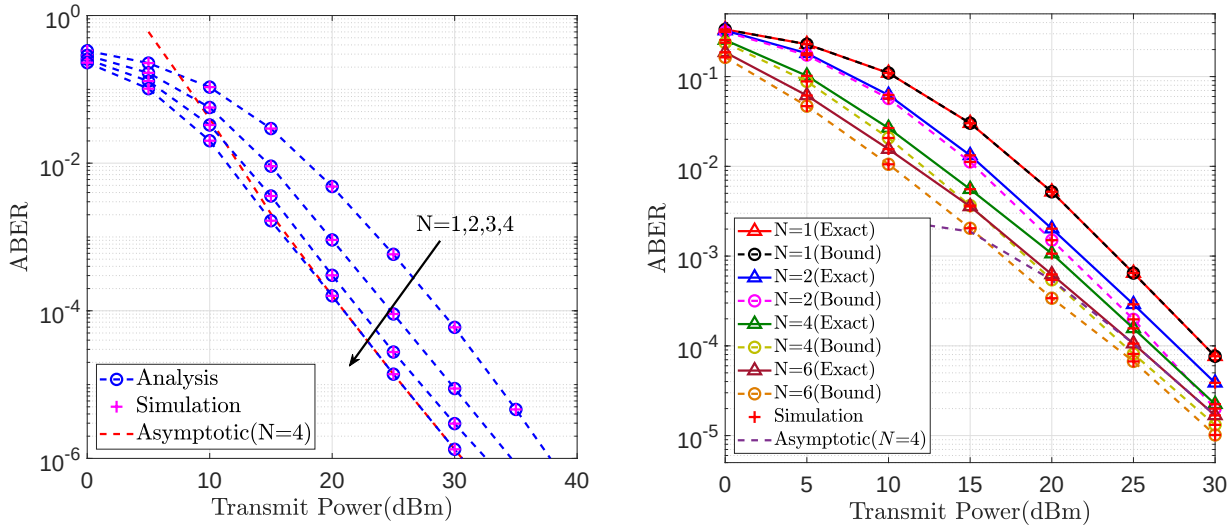

(a) Uplink transmission.

(b) Downlink transmission.

Figure 3.6: ABER of the mixed multihop relaying system with $\sigma_{dB} = 5$, $\phi_i = 37$, $d_{\text{MH}} = 50$ m, and $d_A = 20$m.

compare Fig. 3.6(a) and Fig. 3.6(b) with Fig. 3.5 to infer that multihop relaying with additional 3 relays (i.e., $N = 4$) in the backhaul extends the communication link to 70m achieving the similar ABER performance with $N = 1$ system at a total link distance of 40m. Further, the diversity order using ABER is $M_{\bar{P}_e} = \frac{\alpha\mu}{2} = 0.75$ when $\sigma_{\text{dB}} = 5$ (i.e., $m_\Omega = 2.5$) with $\alpha = 1.5$ and $\mu = 1$ since the slope of the plots in Fig. 3.5 does not change with variation in other channel parameters. However, with $\alpha = 2$ and $\mu = 2$, the ABER-diversity order becomes $M_{\bar{P}_e} = 1.15$ when $m_g = 5$ and becomes $M_{\bar{P}_e} = 3.25$ when $m_g = 1$. The slope of the plots in Fig. 3.5 and 3.6 clearly demonstrate the impact of antenna misalignment errors, fading parameters, and number of relays on the ABER performance.

In all the above plots, we validated the numerical evaluation of analytical and asymptotic expressions with the simulation results. The figures show that the numerical computation of the derived analytical expressions has an excellent agreement with the simulations for the CA-multihop and uplink systems. However, there exists a gap between the derived upper bound and simulation results when the number of relays becomes large for the FG-multihop and downlink systems. Note that the derived expressions are exact for $N = 2$ uplink and downlink transmission systems.

3.7 Chapter Summary

In this chapter, we evaluated the performance of an N+1-hop THz system consisting of an N-hop backhaul link and a single-hop shadowed radio access link over the THz band. We modeled the backhaul with generalized i.ni.d α-μ fading and the last link with a composite generalized-K shadowed fading channel, combined with antenna misalignment errors and path loss due to the atmospheric turbulence. We developed statistical results of the mixed N+1-hop

link by deriving the exact and upper bounds of the PDF and CDF of the SNR for the CA-multihop and FG-multihop systems integrated with shadowed access link using DF and FG relaying protocols for uplink and downlink transmissions, respectively. We analyzed the impact of multiple relays in the backhaul link for extending the communication range using outage probability and ABER performance the mixed transmission system. The diversity order shows that a sufficient number of relays can mitigate the effect of fading and antenna misalignment errors in the multihop-assisted backhaul, limiting the high SNR performance of the mixed system on the channel fading of the single-hop access link when a sufficient beam-width is used in the access link for signal transmission. Extensive simulation and numerical analysis are presented to show that 4 relays are required to extend the backhaul range from 20 m to 50 m using CA-assisted multihop relaying while few more relays are required for the simpler FG-assisted multihop due to the folding of background noise from previous hops. The cumulative gain of the AF-assisted multihop system reduces with an increase in the number of hops advocating the use of a limited number of relays. Further, the simpler FG-multihop transmission performs close to the CA-multihop when the non-linear characteristic of the THz channel increases.

The following chapter explores integrating a THz-RF link, aiming to establish seamless connectivity between the THz backhaul and the traditional RF access network.

3.8 Appendix

3.8.1 Appendix 3.1: Proof of Theorem 3.1

Substituting (3.4) in (3.10) and solving the inner integral $\int_0^\infty e^{-s/\gamma}\gamma^{\frac{\phi_i+\alpha_i S_1}{2}-1}d\gamma = s^{\frac{\phi_i+\alpha_i S_1}{2}}\Gamma\big(-\frac{\phi_i}{2}-\frac{\alpha_i S_1}{2}\big)$ with the definition of Fox's H-function [170], we get

$$\mathcal{M}_{\frac{1}{\gamma_i}}(s)=\frac{A_i s^{\frac{\phi_i}{2}}}{2\bar{\gamma}_N^{\frac{\phi_i}{2}}}H_{1,3}^{3,0}\left[\frac{C_i s^{\frac{\alpha_i}{2}}}{\bar{\gamma}_N^{\frac{\alpha_i}{2}}}\middle|\begin{matrix}(1,1)\\(B_i,1),(0,1),\big(\frac{-\phi_i}{2},\frac{\alpha_i}{2}\big)\end{matrix}\right]. \tag{3.52}$$

Using (3.52) and (3.9) in (3.8) and applying the inverse Laplace transform with expansion of the Fox's H-function of (3.52) in terms of Mellin-Barnes integral, we get

$$\begin{aligned}F_{\gamma_N}^{\mathrm{CA}}(\gamma) =& 1-\prod_{i=1}^{N}\frac{A_i s^{\frac{\phi_i}{2}}}{2s\bar{\gamma}_N^{\frac{\phi_i}{2}}}\frac{1}{2\pi i}\int_{\mathcal{L}}\left[\Big(\frac{1}{2\pi i}\Big)^N\int_{\mathcal{L}_i}\frac{\prod_{i=1}^{N}\Gamma(B_i-S_i)\Gamma(0-S_i)\Gamma\big(-\frac{\phi_i}{2}-\frac{\alpha_i S_i}{2}\big)}{\prod_{i=1}\Gamma(1-S_i)}\right.\\ &\left.\times\left(\prod_{i=1}^{N}\frac{C_i s^{\frac{\alpha_i}{2}}}{\bar{\gamma}_N^{\frac{\alpha_i}{2}}}\right)^{S_i}dS_i\right]e^{s\gamma}ds,\end{aligned} \tag{3.53}$$

where $\mathcal{L}$ is contour integral for the Laplace inverse transform and $\mathcal{L}_i$ is the the i-th Mellin-Barnes integral. Changing the order of the integrals and solving the the inner integral

$\frac{1}{2\pi i}\int_{\mathcal{L}} s^{\left(\sum_{i=1}^{N}\frac{\phi_i+\alpha_i S_i}{2}-1\right)}e^{s\gamma}ds$ using [168, 8.315], (3.53) can be represented as

$$F_{\gamma_N}^{\mathrm{CA}}(\gamma) =1-\prod_{i=1}^{N}\frac{A_i}{2\bar{\gamma}_N^{\frac{\phi_i}{2}}}\gamma^{\left(\sum_{i=1}^{N}\frac{\phi_i}{2}\right)}\Bigg[\left(\frac{1}{2\pi i}\right)^N\int_{\mathcal{L}_i}\frac{\prod_{i=1}^{N}\Gamma(B_i-S_i)\Gamma(0-S_i)\Gamma\left(-\frac{\phi_i}{2}-\frac{\alpha_i S_i}{2}\right)}{\prod_{i=1}^{N}\Gamma(1-S_i)} \times\left(\prod_{i=1}^{N}\frac{C_i\gamma^{\frac{\alpha_i}{2}}}{\bar{\gamma}_N^{\frac{\alpha_i}{2}}}\right)^{S_i}\frac{1}{\Gamma\left(-\sum_{i=1}^{N}\frac{\phi_i+\alpha_i S_i}{2}+1\right)}dS_i\Bigg]. \tag{3.54}$$

We apply the definition of multivariate Fox's H-function [170] to get the CDF in (3.11). To get the PDF, we differentiate (3.54) with respect to γ to get

$$f_{\gamma_N}^{\mathrm{CA}}(\gamma) =\Bigg[1-\prod_{i=1}^{N}\frac{A_i\bar{\gamma}^{-\frac{\phi_i}{2}}}{2}\Bigg[\left(\frac{1}{2\pi i}\right)^N\int_{\mathcal{L}_i}\frac{\prod_{i=1}^{N}\Gamma(B_i-S_i)\Gamma(0-S_i)\Gamma\left(-\frac{\phi_i}{2}-\frac{\alpha_i S_i}{2}\right)}{\prod_{i=1}^{N}\Gamma(1-S_i)} \times\left(\prod_{i=1}^{N}\frac{C_i}{\bar{\gamma}^{\frac{\alpha_i}{2}}}\right)^{S_i}\frac{1}{\Gamma\left(-\sum_{i=1}^{N}\frac{\phi_i+\alpha_i S_i}{2}+1\right)}dS_i\Bigg]D_1\Bigg], \tag{3.55}$$

where $D_1=\frac{d}{d\gamma}\gamma^{\left(\sum_{i=1}^{N}\frac{\phi_i+\alpha_i S_i}{2}\right)}=\sum_{i=1}^{N}\frac{\phi_i+\alpha_i S_i}{2}\gamma^{\left(\sum_{i=1}^{N}\frac{\phi_i+\alpha_i S_i}{2}-1\right)}$. Hence, applying the definition of multivariate Fox's H-function in (3.55), we obtain the PDF in (3.12) to conclude the proof.

3.8.2 Appendix 3.2: Proof of Theorem 3.2

We use (3.21) in (3.18) to represent the PDF of AF-assisted multihop link as

$$f_{\gamma_N}^{\mathrm{FG}}(\gamma)=\prod_{i=1}^{N}\frac{\zeta_i A_i C_i^{-\frac{\phi_i}{\alpha_i}}}{N\alpha_i\gamma}\frac{1}{2\pi\jmath}\int_{\mathcal{L}}\prod_{i=1}^{N}\left(C_i^{\frac{2l_i}{N\alpha_i}}\bar{\gamma}_N^{-\frac{l_i}{N}}\gamma\right)^{-r}\frac{\prod_{i=1}^{N}\Gamma\left(\frac{2rl_i}{N\alpha_i}+\frac{B_i\alpha_i+\phi_i}{\alpha_i}\right)\Gamma\left(\frac{2rl_i}{N\alpha_i}+\frac{\phi_i}{\alpha_i}\right)}{\prod_{i=1}^{N}\Gamma\left(\frac{2rl_i}{N\alpha_i}+\frac{\phi_i+\alpha_i}{\alpha_i}\right)}dr. \tag{3.56}$$

Finally, we apply the definition of Fox's H-function [166] to get the PDF of γ_N in (3.22). Further, we use (3.56) in $F_{\gamma_N}(\gamma)=\int_0^{\gamma}f_{\gamma_N}(\gamma)d\gamma$, and solve the resultant inner integral $\int_0^{\gamma}\gamma^{-r-1}d\gamma$ to $\frac{\gamma^{-r}}{-r}=\frac{\gamma^{-r}\Gamma(-r)}{\Gamma(1-r)}$ in order to apply the definition of Fox's H-function [170] to represent the CDF in (3.23), which concludes the proof of Theorem 3.2.

3.8.3 Appendix 3.3: Proof of Proposition 3.2

Transforming random variable h_p with PDF of (3.2) for the access link as $z=h_p^2$, we get

$$f_z(x)=\frac{1}{2}\phi_A^2 S_A^{-\phi_A^2}x^{\frac{\phi_A^2}{2}-1},\quad 0\le x\le S_A^2. \tag{3.57}$$

Using the limits of PDF in (3.7) and (3.57), the PDF of $|h_A|^2=h_k h_p^2$ is given by [174]:

$$f_{h_A^2}(x)=\frac{b^{m_A}x^{\frac{m_A}{2}-1}\phi_A S_A^2}{\Gamma(m_\Omega)\Gamma(m_g)}\int_0^{S_A^2}y^{\left(\frac{\phi_A-m_A}{2}-1\right)}K_{m_M}\left(2b\sqrt{\frac{x}{y}}\right)dy. \tag{3.58}$$

Using the Bessel function in terms of Meijer's G-function [177, eq (14)], we represent (3.58) as

$$f_{|h_{kp}|^2}(x) = \frac{b^{m_A} x^{\frac{m_A}{2}-1}\phi_A S_A^2}{\Gamma(m_\Omega)\Gamma(m_g)} \int_0^{A_0^2} y^{\left(\frac{\phi_A - m_A}{2}-1\right)} G_{0,2}^{2,0}\left(b^2 xy^{-1}\middle| \begin{matrix} - \\ m_M, m_M \end{matrix}\right) dy. \tag{3.59}$$

Further, we apply the integral representation of Meijer's G-function [170] to express (3.59) as

$$f_{h_A^2}(x) = \frac{b^{m_A} x^{\frac{m_A}{2}-1}\phi_A (S_A^2)^{\frac{\phi_A - m_A}{2}+1}}{\Gamma(m_\Omega)\Gamma(m_g)} \frac{1}{2\pi i} \int_{\mathcal{L}} \Gamma\big(m_M - s\big)\Gamma\big(m_M - s\big)(b^2 x)^s I_{in}, \tag{3.60}$$

where $I_{in} = \int_0^{S_A^2} y^{\frac{\phi_A - m_A}{2}-1} y^{-s} ds = \frac{(S_A^2)^{\frac{\phi_A - m_A - 2s}{2}}}{\frac{\phi_A - m_A - 2s}{2}} = \frac{(S_A^2)^{\frac{\phi_A - m_A}{2}}(S_A^2)^{-s}\Gamma(\frac{\phi_A - m_A}{2}-s)}{\Gamma(1+\frac{\phi_A - m_A}{2}-s)}$. Finally, we apply the definition of Meijer's G-function in (3.60) with the transformation of the random variable $f_{\gamma_A}(\gamma) = \frac{1}{\gamma_A^0} f_{h_A}\big(\frac{\gamma}{\gamma_A^0}\big)$ to get the PDF in (3.35). Substituting (3.35) in $\int_0^\gamma f_{\gamma_A}(\gamma)d\gamma$, and solving the definite integral involving a single Meijer's G-function, we get CDF of SNR of the shadowed access link.

3.8.4 Appendix 3.4: Proof of Theorem 3.3

Using (3.4) and (3.35) in (3.45), applying the definition of Meijer's G and Fox's H-functions, and changing the order of integration. we get

$$\begin{aligned} f_\gamma^{\mathrm{DL}}(z) = &\left[\prod_{i=1}^N \frac{\zeta_i A_i C_i^{-\frac{\phi_i}{\alpha_i}} b^{m_A}\phi_A (S_A^2)^{\frac{\phi_A - m_A}{2}+1} z^{-1}}{2N\alpha_i \bar{\gamma}_A^{\frac{m_A}{2}}\Gamma(m_\Omega)\Gamma(m_g)}\right. \\ &\times \frac{1}{2\pi i}\int_{\mathcal{L}_1} \frac{\prod_{i=1}^N \Gamma\big(\frac{B_i\alpha_i+\phi_i}{\alpha_i} + \frac{2l_i}{N\alpha_i}S_1\big)\prod_{i=1}^N \Gamma\big(\frac{\phi_i}{\alpha_i} + \frac{2l_i}{N\alpha_i}S_1\big)}{\prod_{i=1}^N \Gamma\big(\frac{\phi_i+\alpha_i}{\alpha_i} + \frac{2l_i}{N\alpha_i}S_1\big)} \\ &\left.\times \frac{1}{2\pi i}\int_{\mathcal{L}_2} \frac{\Gamma(m_M - S_2)\Gamma(m_M - S_2)\Gamma\big(\frac{\phi_A - m_A}{2} - S_2\big)}{\Gamma\big(1 + \frac{\phi_A - m_A}{2} - S_2\big)} \left(\prod_{i=1}^N \frac{\bar{\gamma}_i^{\frac{l_i}{N}}}{C_i^{\frac{2l_i}{k\alpha_i}} z}\right)^{S_1} \left(\frac{b^2}{S_A^2 \bar{\gamma}_A^{\frac{1}{2}}}\right)^{S_2} dS_1 dS_2\right] I_9, \end{aligned} \tag{3.61}$$

where $I_9 = \int_0^\infty \big(\frac{x+\psi}{x}\big)^{-S_1} x^{\left(\frac{m_A - 2 + 2S_2}{2}\right)} dx$ can be represented as $\frac{\psi^{\frac{m_A}{2}}\psi^{S_2}\Gamma\left(-\frac{m_A}{2} - S_2\right)\Gamma\left(\frac{m_A}{2} + S_1 + S_2\right)}{\Gamma(S_1)}$ [168, 3.241/4]. Substituting I_9 in (3.61) and applying the definition of bivariate Fox's H-function [178, 1.1], we get the PDF of Theorem 3.3 in (3.46).

We use the PDF (3.46) in $\int_0^\gamma f_\gamma(z)d\gamma$ and solve the resultant integral applying the Mellin-Barnes integral representation of the Fox's H-function [178, 1.1] to get the CDF in (3.47), which concludes the proof.

Chapter 4

THz Backhaul Transmission Integrated with Access Network

4.1 Introduction

The propagation characteristics and application scenarios of THz technology distinguish it from other contemporary technologies like RF and FSO communication. As we move toward a complete shift to THz systems, it becomes imperative to seamlessly integrate THz communication with existing wireless technologies and infrastructure. This integration is important to facilitate a smooth transition and harmonious coexistence with previous generations of communication systems. Therefore, it is desirable to realize a mixed wireless link consisting of backhaul/fronthaul and broadband access network both over THz wireless technology where each hop of transmission being integrated using low complexity relaying protocols.

Generally, the devices are connected over the RF to a nearby AP, which transports data to the core network through a high-speed back-haul link. The wire-line back-haul may consist of DSL and optical fiber. However, wire-line links might not be feasible in some adverse situations [28]. In contrast to the wireless back-haul link over the RF frequencies, THz wireless systems can be a promising alternative for high data rate transmission between the core and AP. Until

---

The research contributions in this chapter have been reported in these publications:

1. **P. Bhardwaj** and S. M. Zafaruddin, "Performance of Hybrid THz and Multiantenna RF System with Diversity Combining," in **IEEE Systems Journal**, vol. 17, no. 2, pp. 2546-2557, June 2023.
2. **P. Bhardwaj** and S. M. Zafaruddin, "Fixed-Gain AF Relaying for RF-THz Wireless System over α-κ-μ Shadowed and α-μ Channels," in **IEEE Communications Letters**, vol. 26, no. 5, pp. 999-1003, May 2022.
3. **P. Bhardwaj** and S. M. Zafaruddin, "Performance Analysis of Dual-Hop Relaying for THz-RF Wireless Link over Asymmetrical α-μ Fading" in **IEEE Transactions on Vehicular Technology**, Volume 70 , Issue 10, Jul 2021.
4. **P. Bhardwaj** and S. M. Zafaruddin, "Performance Analysis of Cooperative Relaying for Multi-Antenna RF Transmissions over THz Wireless Link," **2022 IEEE 95th Vehicular Technology Conference: (VTC2022-Spring)**, Helsinki, Finland, 2022, pp. 1-5.
5. **P. Bhardwaj** and S. M. Zafaruddin, "Performance of Dual-Hop Relaying for THz-RF Wireless Link," **2021 IEEE 93rd Vehicular Technology Conference (VTC2021-Spring)**, Helsinki, Finland, 2021, pp. 1-5.

the transition to a complete THz system, the communication link between a user and the AP will continue on the conventional low-frequency RF transmissions. It is desirable to evaluate the performance of a heterogeneous THz-RF link for the next generation of wireless networks.

Cooperative relaying is an efficient technique to integrate two heterogeneous networks. The use of relaying at THz frequencies has recently been studied [33, 74, 76–80, 83]. However, there is limited research on the RF-THz hybrid network[33]. The authors in [33] considered the DF relaying protocol to facilitate communication for a heterogeneous THz-RF system. They analyzed the outage probability and average bit-error-rate of the mixed system by developing PDF and CDF of the SNR considering i.i.d. α-μ fading for both the links. The authors in [34] have analyzed the ergodic capacity and outage probability for a single-link THz system by deriving distribution functions for the combined effect of antenna misalignment errors[150] and α-μ fading [104].

It is a well-known fact that the FG-AF relaying possesses desirable characteristics of lower computational complexity and does not require continuous monitoring of the CSI for decoding at the relay [53]. There is limited research on AF relaying for THz systems. The authors in [78] considered an AF relay for nano-scale THz transmissions without considering the effect of short-term fading. Considering Rayleigh fading, [79] studied an AF-assisted cooperative In-Vivo nano communication at THz frequencies. The authors in [75] analyzed the THz-THz dual-hop system with FG relaying considering zero-boresight pointing errors. It should be mentioned that the AF relaying has been extensively studied for various wireless technologies such as RF-RF [53, 179], RF-FSO [97, 180], RF-PLC [99], mmWave-FSO[100, 101], PLC-VLC [102], and RF-UWOC [103].

It should be mentioned that the mixed system of FSO (operating over different frequency band than RF and THz) interfaced with multi-antenna/multi-user RF system has been extensively investigated [92–96, 98].

4.2 Motivation and Contribution

The initial publication introducing mixed THz-RF with DF relaying [33] provided statistical analysis for the average BER and the outage probability. However, derived distribution functions are valid only for integer values of the fading parameter μ. It should be noted that non-integer values of μ can provide flexibility to match with measurement data at a fixed α for THz applications. Further, the short-term fading is assumed to be symmetric with the same parameters α and μ for both THz and RF channels. The symmetric model might not be possible considering two technologies operating over the different spectrum. Existing analytical tools are readily applicable to analyze the performance of THz-RF over i.i.d. fading. Still, there is no asymptotic results to provide insightful dependence of antenna misalignment errors and fading parameters even for the i.i.d. THz-RF mixed system. Moreover, there is no analysis available in the open literature for the average SNR and ergodic rate performance for the THz-RF relaying. Performance bounds with insightful analysis on the outage probability, average

SNR, ergodic rate, and average BER are desirable for real-time tuning of system parameters for efficient deployment of the THz-RF system.

While scanning the related research for the mixed RF-THz network, we found that a single-antenna RF system has been considered. In general, RF base-station (BS)/AP employ multiple antennas to harness spatial diversity to deal with the signal fading and thus enhance the system performance. Further, the channel fading affects both the RF and THz links besides the fact that attenuation is higher for the THz which can be mitigated by considering shorter THz link distance. To make the RF signal energy level comparable to the THz for a cooperative relay system, we need to increase the energy level of the RF signal using multiple antennas. The performance analysis of a fixed-gain AF relaying for multi-antenna RF over α-μ channel fading mixed with high frequency technologies (such as FSO and THz) is not available in the literature. It requires novel approaches to derive statistical results of the end-to-end system in a closed-form when the diversity combining technique is applied at the RF receiver and integrated with the THz link over generalized fading channels.

In this chapter, we analyze the performance of an integrated THz-RF link for data transmission between the central processing unit of a core network and a user through an AP in a wireless network over α-μ fading channels. We analyze the performance of integrated RF-THz wireless systems assisted by DF and FG-AF relaying protocols by considering non-zero boresight and generalized antenna misalignment errors. We also analyze the performance of a two-tier system consisting of a single-antenna THz link and a multiple antenna receiver system for RF transmission in an uplink wireless network. The major contributions of the chapter are as follows:

- We consider a generalized model for the end-to-end channel with i.ni.d. fading model for THz and RF links, the THz link with antenna misalignment errors, and asymmetrical relay position between the source and destination.

- We derive a closed-form expression of the CDF for the SNR of the THz link using the combined effect of α-μ fading and antenna misalignment errors. The derived CDF is also valid for non-integer values of μ for a generalized performance analysis over THz fading channels.

- We provide statistical results on the SNR by deriving PDF and CDF of the THz link under the joint effect of deterministic path-loss, α-μ short-term fading, and generalized antenna misalignment errors model.

- We develop PDF and CDF of the end-to-end SNR of the integrated system by employing both selection combining (SC) and maximal ratio combining (MRC) diversity techniques for the multi-antenna equipped RF receiver over i.ni.d α-μ fading channels with a statistical model for the antenna misalignment in the THz link.

- We analyze the performance of the THz-RF integrated system by deriving analytical expressions of diversity order, moments of SNR, ergodic capacity, and average BER in terms of system parameters. It requires novel approaches to deal with the product of a rational polynomial and two incomplete Gamma functions with dissimilar rational arguments in the generalized i.ni.d model.

4.3 Integrated THz-RF Wireless Link

4.3.1 System Model

We consider a wireless system where a user terminal lies in a highly shadowed region to the source, which precludes direct RF transmissions. To facilitate transmissions, we consider a dual-hop THz-RF system where a source node communicates with the destination node through a relay node employed with the DF protocol, as illustrated in Fig.4.1. The considered system may find applications in ultra-dense heterogeneous small cells, cell-free wireless networks, and to establish communication links in difficult-to-access terrain. For small cell and cell-free systems, the THz link can be deployed for backhauling/fronthauling with the central processing unit as the source, AP for relaying, and RF link for radio access. The THz link can also bridge a difficult-to-access terrain where wireline connection is infeasible to solve the last mile connectivity over RF. It is reasonable to assume that the two hops might experience asymmetrical channel fading considering two different technologies operating over the different spectrum for these applications.

We establish the communication of the first hop (i.e., between the source and the relay) by the THz transmission while the RF is used in the second hop (i.e., between the AP and the user). The authors in [33, 34] have considered the generalized α-μ fading to analyze the THz communications while the FTR short-term fading model is adopted in [45]. The α-μ is a generalized model that includes other fading models such Rayleigh and Nakagami-m as a particular case, and can accurately model the THz channel by adapting α and μ parameters. It should be noted that the FTR model consists of an infinite sum to generate the PDF, which can provide an approximation on the system performance with a finite number of terms. Thus, we consider the generalized α-μ short-term with i.ni.d fading for THz and RF links with parameters α_1, μ_1 and α_2, μ_2 to model the THz and RF links, respectively. We also consider antenna misalignment errors as a channel impairment for the THz link in addition to the short-term fading and path loss.

In the first hop, the received signal y_1 at the relay is expressed as

$$y_1 = H_{l,1} h_{p,1} h_{f,1} s + w_1 \tag{4.1}$$

where s is the transmitted signal in the THz band and w_1 is the additive noise with variance σ^2_{w1}. The terms $h_{f,1}$ and $h_{p,1}$ model the channel coefficient due to short term fading and antenna misalignment errors, respectively. The deterministic path gain $H_{l,1}$ is dependent on antenna

gains, frequency, and molecular absorption coefficient as given in [34]:

$$H_{l,1} = \frac{c\sqrt{G_t G_r}}{4\pi f d} \exp(-\frac{1}{2}k(f,T,\psi,p)d) \tag{4.2}$$

where c, f, and d respectively denote the speed of light, the transmission frequency and distance. G_t, and G_r are the antenna gains of the transmitting antenna and receiving antenna, respectively. The term $k(f,T,\psi,p)$ is the molecular absorption coefficient depends on the temperature T, relative humidity ψ and atmospheric pressure p

$$k(f,T,\psi,p) = \frac{q_1 v(q_2 v + q_3)}{(q_4 v + q_5)^2 + (\frac{f}{100c} - p_1)^2} + \frac{q_6 v(q_7 v + q_8)}{(q_9 v + q_{10})^2 + (\frac{f}{100c} - p_2)^2} + c_1 f^3 + c_2 f^2 + c_3 f + c_4 \tag{4.3}$$

where $v = \frac{\psi}{100}\frac{p_w(T,p)}{p}$. The term $p_w(T,p)$ represents the saturated water vapor partial pressure at temperature T, and can be evaluated based on Buck's equation. The values of the other parameters are given in Table II [181].

The PDF of zero-boresight antenna misalignment errors $h_{p,1}$ is given as [150]:

$$f_{h_{p,1}}(h_p) = \frac{\phi}{S_0^{\phi}} h_p^{\phi-1}, 0 \leq h_p \leq S_0, \tag{4.4}$$

where $S_0 = \text{erf}(v)^2$ with $v = \sqrt{\pi/2}\,(r_1/\omega_z)$ and ω_z is the beam-width, ϕ=$\frac{\omega_{z_{\text{eq}}}^2}{4{\sigma_s}^2}$ with $\omega_{z_{\text{eq}}}$ as the equivalent beam-width at the receiver, which is given as $\omega_{z_{\text{eq}}}^2 = \omega_z^2\sqrt{\pi}\text{erf}(v)/(2v\exp(-v^2))$, and σ_s is the variance of antenna misalignment errors displacement characterized by the horizontal sway and elevation [150].

The short term fading $|h_f|$ with the $\alpha-\mu$ distribution for the THz link is given as

$$f_{|h_{f,1}|}(x) = \frac{\alpha\mu_1^{\mu_1}}{\Omega^{\alpha_1\mu_1}\Gamma(\mu_1)} x^{\alpha_1\mu_1-1} \exp\left(-\mu_1 \frac{x^{\alpha_1}}{\Omega^{\alpha_1\mu_1}}\right) \tag{4.5}$$

where Ω is the α-root mean value of the fading channel envelope.

Using (4.4) and (4.5), the PDF of the combined short term fading and antenna misalignment errors $|h_{pf,1}| = |h_p h_{f,1}|$ is given as [34]:

$$f_{|h_{pf,1}|}(x) = \phi S_0^{-\phi} \frac{\mu_1^{\frac{\phi}{\alpha_1}} x^{\phi-1}}{\Omega^{\phi}\Gamma(\mu_1)} \Gamma\left(\frac{\alpha_1\mu_1 - \phi}{\alpha_1}, \mu_1 \frac{S_0^{-\alpha_1}}{\Omega^{\alpha_1}} x^{\alpha_1}\right) \tag{4.6}$$

In the second hop, assuming that the signal received through the direct link is negligible, the received signal y_2 at the destination is expressed as

$$y_2 = H_{l,2} h_{f,2} \hat{s} + w_2 \tag{4.7}$$

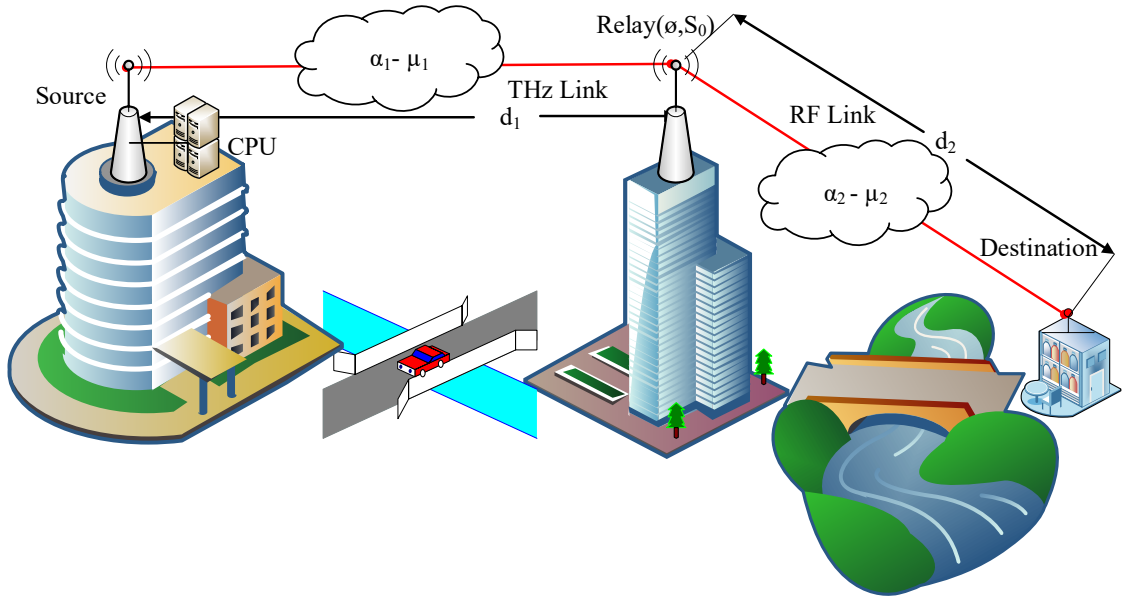

Figure 4.1: Relay assisted THz-RF wireless link.

where $\hat{s}$ is the decoded symbol at the relay, $H_{l,2}$ is the channel path gain of RF link, w_2 is the additive noise with variance σ_{w2}^2 and $h_{f,2}$ is the short-term fading with α-μ distribution for the RF link, which is

$$f_{|h_{f,2}|}(x) = \frac{\alpha \mu_2^{\mu_2}}{\Omega_f^{\alpha_2\mu_2}\Gamma(\mu_1)} x^{\alpha_2\mu_2-1} \exp\left(-\mu_2 \frac{x^{\alpha_2}}{\Omega_f^{\alpha_2\mu_2}}\right) \tag{4.8}$$

In what follows, we use the distribution functions of channel fading and antenna misalignment errors to analyze the performance of relay-assisted THz-RF system.

To this end, we denote instantaneous SNR of the THz link as $\gamma_1 = \bar{\gamma}_1 |h_{fp}|^2$ and the instantaneous SNR of RF as $\gamma_2 = \bar{\gamma}_2 |h_f|^2$, where $\bar{\gamma}_1 = \frac{P_t |H_{l,1}|^2}{\sigma_{w_1}^2}$ and $\bar{\gamma}_2 = \frac{P_r |H_{l,2}|^2}{\sigma_{w_2}^2}$ are the SNR terms without fading for the THz and RF links, respectively. Using (4.6), we can represent the PDF of the THz link in terms of SNR [174]

$$f_{\gamma_1}(\gamma) = \frac{A_1}{2\sqrt{\gamma\bar{\gamma}_1}} \left(\sqrt{\gamma/\bar{\gamma}_1}\right)^{\phi-1} \Gamma\left(B_1, C_1 \left(\sqrt{\gamma/\bar{\gamma}_1}\right)^{\alpha_1}\right) \tag{4.9}$$

where $A_1 = \phi S_0^{-\phi} \frac{\mu_1^{\frac{\phi}{\alpha_1}}}{\Omega^{\phi}\Gamma(\mu_1)}$, $B_1 = \frac{\alpha_1\mu_1 - \phi}{\alpha_1}$, and $C_1 = \frac{\mu_1}{\Omega^{\alpha_1}} S_0^{-\alpha_1}$.

Similarly, we can express (4.8) in terms of SNR for the RF link as

$$f_{\gamma_2}(\gamma) = \frac{A_2\alpha_2}{2\Gamma(\mu_2)\sqrt{\gamma\bar{\gamma}_2}} \left(\sqrt{\gamma/\bar{\gamma}_2}\right)^{\alpha_2\mu_2-1} e^{-B_2\left(\sqrt{\gamma/\bar{\gamma}_2}\right)^{\alpha_2}} \tag{4.10}$$

$$P_{\text{out}} \approx P_{\text{out}}^{0} = 1 - \frac{e^{-B_2\left(\frac{\gamma}{\bar{\gamma}_2}\right)^{\frac{\alpha_2}{2}}}}{\Gamma(\mu_2)} B_2^{\mu_2-1}\left(\frac{\gamma}{\bar{\gamma}_2}\right)^{\frac{\alpha_2(\mu_2-1)}{2}} + \frac{A_1 C_1^{-\frac{\phi}{\alpha_1}} e^{-B_2\left(\frac{\gamma}{\bar{\gamma}_2}\right)^{\frac{\alpha_2}{2}}}}{\phi \Gamma(\mu_2)} B_2^{\mu_2-1}\left(\frac{\gamma}{\bar{\gamma}_2}\right)^{\frac{\alpha_2(\mu_2-1)}{2}}$$
$$\left[\left(\Gamma(\mu_1) + C_1^{\frac{\phi}{\alpha_1}}\left(\frac{\gamma}{\bar{\gamma}_1}\right)^{\frac{\phi}{2}}\right) e^{-C_1\left(\frac{\gamma}{\bar{\gamma}_1}\right)^{\frac{\alpha_1}{2}}} C_1\left(\frac{\gamma}{\bar{\gamma}_1}\right)^{\frac{\alpha_1}{2}} - e^{-C_1\left(\frac{\gamma}{\bar{\gamma}_1}\right)^{\frac{\alpha_1}{2}}} \Gamma(\mu_1) C_1^{\mu_1-1}\left(\frac{\gamma}{\bar{\gamma}_1}\right)^{\frac{\alpha_1(\mu_1-1)}{2}}\right] \tag{4.12}$$

$$P_{\text{out}} \approx P_{\text{out}}^{\infty} = \frac{S_0^{-\alpha_1\mu_1}\mu_1^{\mu_1}}{\Gamma(\mu_1)}\left(\frac{1}{\mu_1} - \frac{1}{B_1}\right)\left(\frac{\gamma}{\bar{\gamma}_1}\right)^{\frac{\alpha_1\mu_1}{2}} + \frac{S_0^{-\phi}\mu_1^{\frac{\phi}{\alpha_1}}\Gamma(B_1)}{\Gamma(\mu_1)}\left(\frac{\gamma}{\bar{\gamma}_1}\right)^{\frac{\phi}{2}} + \frac{\mu_2^{\mu_2}}{\Gamma(\mu_2)\mu_2}\left(\frac{\gamma}{\bar{\gamma}_2}\right)^{\frac{\alpha_2\mu_2}{2}} \tag{4.13}$$

---

where $A_2 = \frac{\mu_2^{\mu_2}}{\Omega^{\phi}}$ and $B_2 = \frac{\mu_2}{\Omega^{\alpha_2}}$.

Finally, the CDF of the SNR for the RF link:

$$F_{\gamma_2}(\gamma) = 1 - \left(\frac{\Gamma\left(\mu_2, B_2\left(\sqrt{\gamma/\bar{\gamma}_2}\right)^{\alpha_2}\right)}{\Gamma(\mu_2)}\right) \tag{4.11}$$

In what follows, we analyze the performance of the integrated THz-RF system. First, we derive a closed-form expression on the CDF of THz link over i.ni.d α-μ fading channel with antenna misalignment error. Next, we use the derived PDFs and CDFs to analyze the outage probability, moments of SNR, ergodic capacity, and average BER performance of the THz-RF relay system.

4.3.2 Cumulative Distribution Function of THz Link

In the following, we derive a closed-form expression of the CDF for the THz Link.

Theorem 4.1. *If ϕ and S_0 be the parameters of antenna misalignment errors, and α_1 and μ_1 are the fading parameters, then the CDF of the THz link is given by*

$$F_{\gamma_1}(\gamma) = \frac{A_1 C_1^{-\frac{\phi}{\alpha_1}}}{\phi}\left[\gamma\left(\mu_1, C_1\left(\sqrt{\gamma/\bar{\gamma}_1}\right)^{\alpha_1}\right) + C_1^{\frac{\phi}{\alpha_1}}\left(\sqrt{\gamma/\bar{\gamma}_1}\right)^{\phi}\Gamma\left(B_1, C_1\left(\sqrt{\gamma/\bar{\gamma}_1}\right)^{\alpha_1}\right)\right] \tag{4.14}$$

Proof. Using (4.9) and substituting $\left(\sqrt{\gamma/\bar{\gamma}_1}\right)^{\alpha_1} = t$, the CDF of SNR for the THz link is given by

$$F_{\gamma_1}(\gamma) = \frac{A_1}{\alpha_1}\int_0^{\left(\sqrt{\gamma/\bar{\gamma}_1}\right)^{\alpha_1}} t^{(\frac{\phi}{\alpha_1}-1)}\Gamma(B_1, C_1 t)dt \tag{4.15}$$

To solve the above integral, we use the following identity:

$$\int x^{b-1}\Gamma(s,x)\mathrm{d}x = -\frac{1}{b}\big(x^{b}\Gamma(s,x)+\Gamma(s+b,x)\big) \tag{4.16}$$

Applying the limits of (4.15) in the indefinite integral of (4.16), we get (4.14). ■

It can be seen that the CDF in (4.14) consists of gamma and incomplete gamma functions and is applicable for continuous values of μ_1, in contrast to [33], which is applicable only for the integer values of μ_1. Further, the derived CDF might facilitate performance analysis in closed-forms.

Finally, we provide the distribution functions of the relay-assisted system. Since γ_1 and γ_2 are independent, the expression of end-to-end SNR with DF relaying is given as:

$$\gamma = \min(\gamma_1, \gamma_2) \tag{4.17}$$

Thus, the CDF and PDF of γ can be given as [174]

$$F_{\gamma}(\gamma) = F_{\gamma_1}(\gamma) + F_{\gamma_2}(\gamma) - F_{\gamma_1}(\gamma)F_{\gamma_2}(\gamma) \tag{4.18}$$

$$f_{\gamma}(\gamma) = f_{\gamma_1}(\gamma) + f_{\gamma_2}(\gamma) - f_{\gamma_1}(\gamma)F_{\gamma_2}(\gamma) - F_{\gamma_1}(\gamma)f_{\gamma_2}(\gamma) \tag{4.19}$$

where $f_{\gamma_1}(\gamma)$, $f_{\gamma_2}(\gamma)$ are the PDF of the THz and RF link, respectively. Similarly, $F_{\gamma_1}(\gamma)$ and $F_{\gamma_2}(\gamma)$ are the CDF of the THz and RF link, respectively.

Corollary 4.1. *1. An exact expression for the outage probability is $P_{\mathrm{out}} = F_{\gamma}(\gamma_{\mathrm{th}})$, where $F_{\gamma}(\gamma)$ is given in* (4.18) *and γ_{th} is the threshold value of SNR.*

2. *Asymptotically, for a low SNR regime, an expression of the outage probability P_{out}^{0} is given in* (4.12).

3. *Asymptotically, for a high SNR regime, an expression of the outage probability $P_{\mathrm{out}}^{\infty}$ is given in* (4.13).

4. *The diversity order M^{out} of the THz-RF relay-assisted system using the outage probability is given by*

$$M^{\mathrm{out}} = \min\left\{\frac{\alpha_1\mu_1}{2}, \frac{\alpha_2\mu_2}{2}, \frac{\phi}{2}\right\} \tag{4.20}$$

Proof. Proof for part (a) is trivial. For part (b), we use the asymptotic expression of $\lim_{x\to\infty}\Gamma(a,x) = e^{-x}x^{a-1}$ [182] in (4.18) containing $F_{\gamma_1}(\gamma)$ (see (4.11)) and $F_{\gamma_2}(\gamma)$ (see (4.14)). For part (c), we use $F_{\gamma_1}(\gamma_{\mathrm{th}}) + F_{\gamma_2}(\gamma_{\mathrm{th}}) >> F_{\gamma_1}(\gamma_{\mathrm{th}})F_{\gamma_2}(\gamma_{\mathrm{th}})$ and $\lim_{x\to 0}\gamma(s,x) =$

$$\overline{\mathrm{SNR}}_{12}^{(n)} = \overline{\mathrm{SNR}}_1 + \frac{A_1 C_1^{-\frac{\phi+2n}{\alpha_1}} \bar{\gamma}_1^n \alpha_1^{(\mu_2-\frac{1}{2})} \alpha_2^{(B_1+\frac{\phi+2n}{\alpha_1}-\frac{3}{2})}}{\Gamma(\mu_2)\alpha_1(2\pi)^{(\frac{\alpha_1+\alpha_2-2}{2})}} \times G_{\alpha_1+2\alpha_2,2\alpha_1+\alpha_2}^{2\alpha_1,2\alpha_2}\left(\begin{matrix}\Delta\big(\alpha_2, 1-(\frac{\phi+2n}{\alpha_1}-B_1)\big), \Delta\big(\alpha_2, 1-(\frac{\phi+2n}{\alpha_1})\big), \Delta(\alpha_1,1) \\ \Delta(\alpha_1,\mu_2), \Delta(\alpha_1,0), \Delta\big(\alpha_2, -(\frac{\phi+2n}{\alpha_1})\big)\end{matrix}\middle| \frac{B_2'^{\alpha_1}\alpha_1^{-\alpha_1}}{C_1^{\alpha_2}\alpha_2^{-\alpha_2}}\right) \tag{4.22}$$

$$\begin{aligned}\overline{\mathrm{SNR}}_{21}^{(n)} &= \frac{A_1 C_1^{\frac{-\phi}{\alpha_1}}\Gamma(\mu_1)}{\phi}\overline{\mathrm{SNR}}_2 + \frac{A_1 A_2 C_1^{\frac{-\phi}{\alpha_1}} C_1' \bar{\gamma}_2^n \alpha_1^{(\mu_2-\frac{\phi+2n}{\alpha_2}-\frac{1}{2})} \alpha_2^{(B_1-\frac{1}{2})} B_2^{-(\mu_2+\frac{\phi+2n}{\alpha_2})}}{\Gamma(\mu_2)\phi(2\pi)^{(\frac{\alpha_1+\alpha_2-2}{2})}} \\ &\times G_{\alpha_1+\alpha_2,2\alpha_2}^{2\alpha_2,\alpha_1}\left(\begin{matrix}\Delta\big(\alpha_1, \alpha_1-(\mu_2+\frac{\phi+2n}{\alpha_2})\big), \Delta(\alpha_2,1) \\ \Delta(\alpha_2,B_1), \Delta(\alpha_2,0)\end{matrix}\middle| \frac{C_1'^{\alpha_2}\alpha_1^{\alpha_1}}{B_2^{\alpha_1}\alpha_2^{\alpha_2}}\right) \\ &+ \frac{A_1 A_2 C_1^{\frac{-\phi}{\alpha_1}} \bar{\gamma}_2^n \alpha_1^{(\mu_2+\frac{2n}{\alpha_2}-\frac{1}{2})} \alpha_2^{(\mu_2-1)} B_2^{-(\mu_2+\frac{2n}{\alpha_2})}}{\Gamma(\mu_2)\phi(2\pi)^{(\frac{\alpha_1+\alpha_2-2}{2})}} \\ &\times G_{\alpha_1+\alpha_2,2\alpha_2}^{2\alpha_2,\alpha_1}\left(\begin{matrix}\Delta\big(\alpha_1, \alpha_1-(\mu_2+\frac{2n}{\alpha_2})\big), \Delta(\alpha_2,1) \\ \Delta(\alpha_2,\mu_1), \Delta(\alpha_2,0)\end{matrix}\middle| \frac{C_1'^{\alpha_2}\alpha_1^{\alpha_1}}{B_2^{\alpha_1}\alpha_2^{\alpha_2}}\right)\end{aligned} \tag{4.23}$$

where $B_2' = B_2\sqrt{\bar{\gamma}_1/\bar{\gamma}_2}$ and $C_1' = C_1\sqrt{\bar{\gamma}_2/\bar{\gamma}_1}$.

x^s/s [182] in (4.18), to get (4.13). For part (d), the diversity order can be obtained using the exponent of SNR (i.e., dominant terms of the outage probability at high SNR) in (4.13). ■

The expression of diversity order in (4.20) shows that the effect of antenna misalignment errors can be mitigated if the normalized beam width is adjusted sufficiently to get $\phi > \min\{\alpha_1\mu_1, \alpha_2\mu_2\}$.

4.3.3 Statistical Analysis of SNR

In this subsection, we derive the nth moment of SNR, which can be used to analyze other statistical parameters such as average SNR and amount of fading (AoF). The AoF is a key performance parameter to analyze the severity of channel fading.

Using (4.19), the n-th moment of SNR for the relay assisted system under the considered fading channel is given as

$$\overline{\mathrm{SNR}}^{(n)} = \int_0^\infty \gamma^n f_\gamma(\gamma) d\gamma \tag{4.21}$$

We denote $\overline{\mathrm{SNR}}_1 = \int_0^\infty \gamma^n f_{\gamma_1}(\gamma)d\gamma$ the n-th moment of THz link, $\overline{\mathrm{SNR}}_2 = \int_0^\infty \gamma^n f_{\gamma_2}(\gamma)d\gamma$ the n-th moment of RF link, $\overline{\mathrm{SNR}}_{12} = \int_0^\infty \gamma^n f_{\gamma_1}(\gamma)F_{\gamma_2}(\gamma)d\gamma$, and $\overline{\mathrm{SNR}}_{21} = \int_0^\infty \gamma^n f_{\gamma_2}(\gamma)F_{\gamma_1}(\gamma)d\gamma$. In the following theorem, we derive the n-th moment of SNR considering the generalized i.ni.d. fading model.

Theorem 4.2. *Let ϕ and S_0 be the parameters of antenna misalignment errors of the THz link. If α_1, μ_1 and α_2, μ_2 are the fading parameters of THz and RF links, respectively, then the n-th moment of SNR of the relay assisted THz-RF link is given as:*

$$\overline{\mathrm{SNR}}^{(n)} = \overline{\mathrm{SNR}}_1^{(n)} + \overline{\mathrm{SNR}}_2^{(n)} - \overline{\mathrm{SNR}}_{12}^{(n)} - \overline{\mathrm{SNR}}_{21}^{(n)} \tag{4.24}$$

where

$$\overline{\mathrm{SNR}}_1^{(n)} = \frac{A_1 C_1^{-(\frac{\phi+2n}{\alpha_1})} \bar{\gamma}_1^n \Gamma(\frac{\alpha_1 B_1+\phi+2n}{\alpha_1})}{2n+\phi}, \overline{\mathrm{SNR}}_2^{(n)} = \frac{B_2^{-\frac{2n}{\alpha_2}} \bar{\gamma}_2^n \Gamma(\frac{2n}{\alpha_2}+\mu_2)}{\Gamma(\mu_2)}, \tag{4.25}$$

$\overline{\mathrm{SNR}}_{12}^{(n)}$*, and* $\overline{\mathrm{SNR}}_{21}^{(n)}$ *are given in* (4.22) *and* (4.23)*, respectively.*

Proof. The proof is presented in Appendix 4.1. ■

It should be noted that $\overline{\mathrm{SNR}}_1^{(n)}$ and $\overline{\mathrm{SNR}}_2^{(n)}$ are the n-th moment of SNR for the THz and RF links, respectively. Note that popular computational software packages, e. g., MATLAB and MATHEMATICA have a built-in function for Meijer's G computation. In the following Lemma, we describe a special case of Theorem 4.2 by considering the i.i.d model where short-term fading between source to relay and relay to destinations is identical.

Lemma 4.1. *Let ϕ and S_0 be the parameters of antenna misalignment errors, and α, μ be the fading parameters, then the n-th moment of SNR of the relay assisted THz-RF link is given as*

$$\overline{\mathrm{SNR}}^{(n)} = \overline{\mathrm{SNR}}_1^{(n)} + \overline{\mathrm{SNR}}_2^{(n)} - \overline{\mathrm{SNR}}_{12}^{(n)} - \overline{\mathrm{SNR}}_{21}^{(n)} \tag{4.26}$$

where

$$\begin{aligned} \overline{\mathrm{SNR}}_1^{(n)} &= \frac{A_1 C_1^{-(\frac{\phi+2n}{\alpha})} \bar{\gamma}_1^n \Gamma(\frac{\alpha B_1+\phi+2n}{\alpha})}{2n+\phi} \\ \overline{\mathrm{SNR}}_2^{(n)} &= \frac{B_2^{-\frac{2n}{\alpha}} \bar{\gamma}_2^n \Gamma(\frac{2n}{\alpha}+\mu)}{\Gamma(\mu)} \end{aligned} \tag{4.27}$$

$$\begin{aligned} \overline{\mathrm{SNR}}_{12}^{(n)} &= \overline{\mathrm{SNR}}_1^{(n)} - \frac{1}{(\phi+2n)\Gamma(\mu)} \Bigg[A_1 B_2'^{-\frac{\phi+2n}{\alpha}} \bar{\gamma}_1^n \Bigg(\Gamma(B_1)\Gamma\Bigg(\frac{\alpha\mu+\phi+2n}{\alpha}\Bigg) \\ &+ B_2'^{-B_1} C_1^{B_1} \Gamma\left(\frac{\alpha(B_1+\mu)+\phi+2n}{\alpha}\right) \\ &\times \Bigg(\frac{\alpha\ {}_2\tilde{F}_1\left[\frac{\alpha B_1+\phi+2n}{\alpha}, \frac{\alpha(B_1+\mu)+\phi+2n}{\alpha}, \frac{\alpha B_1+\alpha+\phi+2n}{\alpha}, -\frac{C_1}{B_2'}\right]}{\alpha B_1+\phi+2n} \\ &- \Gamma(B_1)\ {}_2\tilde{F}_1\left[B_1, \frac{\alpha(B_1+\mu)+\phi+2n}{\alpha}, 1+B_1, -\frac{C_1}{B_2'}\right] \Bigg) \Bigg) \Bigg] \end{aligned} \tag{4.28}$$

$$\overline{\mathrm{SNR}}_{21}^{(n)} = \frac{A_1 C_1^{\frac{-\phi}{\alpha}} \Gamma(\mu) \overline{\mathrm{SNR}}_2^{(n)}}{\phi} + \frac{1}{\phi\Gamma(\mu)} \Bigg[\alpha A_1 A_2 C_1^{-\frac{\phi}{\alpha}} C_1'^{-\frac{\alpha\mu+\alpha+2n}{\alpha}} \bar{\gamma}_2^n \times \Bigg(- \frac{\Gamma(1+\frac{2n}{\alpha}+2\mu)\ {}_2\tilde{F}_1\big[1+\frac{2n}{\alpha}+\mu, 1+\frac{2n}{\alpha}+2\mu, 2+\frac{2n}{\alpha}+\mu, -\frac{B_2}{C_1'}\big]}{\alpha\mu+\alpha+2n} + (\alpha\mu+\alpha+\phi+2n)^{-1}\Gamma\Big(\frac{\alpha(\mu+B_1+1)+\phi+2n}{\alpha}\Big) \times {}_2\tilde{F}_1\Big[\frac{\alpha\mu+\alpha+\phi+2n}{\alpha}, \frac{\alpha(\mu+B_1+1)+\phi+2n}{\alpha}, \frac{\alpha(\mu+2)+\phi+2n}{\alpha}, -\frac{B_2}{C_1'}\Big]\Bigg)\Bigg] \tag{4.29}$$

Proof. The proof is presented in Appendix 4.2. ■

The derived expressions of the n-th moment of SNR in Theorem 4.2 and Lemma 4.1 can be used to find the average SNR of the relay assisted link by substituting $n = 1$ in (4.24) and (4.26). Further, a closed-form expression for the 2^{nd} order AoF is expressed as

$$\mathrm{AoF} = \frac{\overline{\mathrm{SNR}}^{(2)}}{(\overline{\mathrm{SNR}}^{(1)})^2} - 1 \tag{4.30}$$

Although the derived expressions in (4.24) and (4.26) involves standard mathematical functions, it is desirable to simplify further the analysis under practically relevant scenarios in order to provide insights on the system behavior. Thus, we present much simplified expressions of the average SNR by considering some specific fading conditions and antenna misalignment error parameters in the following Corollary 2.

Corollary 4.2. *1. Considering the THz-link as the Nakagami-m fading ($\alpha_1 = 2$, $\mu_1 = 2$) with antenna misalignment error parameter $\phi = 2$, and the Rayleigh fading ($\alpha_2 = 2$ $\mu_2 = 1$) for the RF-link, the average SNR of the relay assisted link is given as*

$$\begin{aligned}\overline{\mathrm{SNR}} =& \bar{\gamma}_1 + 2\bar{\gamma}_2 - 2S_0^{-2}\bar{\gamma}_1\left(\bar{\gamma}_1 - \frac{1}{\left(\sqrt{\bar{\gamma}_1/\bar{\gamma}_2} + 2S_0^{-2}\right)^2}\right) \\ & - \bar{\gamma}_2\left(\frac{2(1+2S_0^{-2})^4 + 6 - (1+2S_0^{-2})^2}{(1+2S_0^{-2})^4}\right)\end{aligned} \tag{4.31}$$

2. Considering the THz-link ($\alpha_1 \to \infty$, $\mu_1 = 1$) as a linear Weibull fading with $\phi = 2$, and the Rayleigh fading ($\alpha_2 = 2$ $\mu_2 = 1$) for the RF-link, the average SNR of the relay assisted link:

$$\overline{\mathrm{SNR}} = \bar{\gamma}_2 - \frac{S_0^{-\phi}\bar{\gamma}_2}{\phi} \tag{4.32}$$

Proof. Using $n = 1$ and $f_\gamma(\gamma)$ from (4.19) in (4.21) with special cases of α and μ enumerated in (a) and (b), and applying the standard procedure, we can get (4.31) and (4.32). ■

The special case in (4.31) considers popular fading models, which significantly simplifies the analysis comparing with Theorem 4.2. Further, the scenario in (b) is chosen to provide insights on the performance asymptotically. As the parameter $\alpha_1 \to \infty$ (highly linear behavior i.e., good channel conditions), the performance should be determined by the RF link with finite α_2, which is verified using (4.32).

4.3.4 Ergodic Capacity

In contrast to the conventional RF-RF relaying, there is no pre-log factor $1/2$ in the ergodic capacity formulation (2.15) even with half-duplex relaying since both THz and RF technologies operate on different carrier frequencies. Further, we assume that the relay requires negligible processing time to implement the DF protocol.

In the following Lemma, we use (4.19) in (2.15) to derive analytical expression of the ergodic capacity for the relay-assisted system considering the i.i.d fading model. We denote $\bar{\eta}_1 = \int_0^\infty \log_2(1+\gamma) f_{\gamma_1}(\gamma) d\gamma$ the ergodic capacity of THz link, $\bar{\eta}_2 = \int_0^\infty \log_2(1+\gamma) f_{\gamma_2}(\gamma) d\gamma$ the ergodic capacity of RF link, $\bar{\eta}_{12} = \int_0^\infty \log_2(1+\gamma) f_{\gamma_1}(\gamma) F_{\gamma_2}(\gamma) d\gamma$, and $\bar{\eta}_{21} = \int_0^\infty \log_2(1+\gamma) f_{\gamma_2}(\gamma) F_{\gamma_1}(\gamma) d\gamma$. We denote by $B_2' = B_2\sqrt{\bar{\gamma}_1/\bar{\gamma}_2}$ and $C_1' = C_1\sqrt{\bar{\gamma}_2/\bar{\gamma}_1}$.

Lemma 4.2. *If ϕ and S_0 are the parameters of antenna misalignment errors, and α, μ are the fading parameters, then an expression on the ergodic capacity of the relay assisted THz-RF link is:*

$$\bar{\eta} = \bar{\eta}_1 + \bar{\eta}_2 - \bar{\eta}_{12} - \bar{\eta}_{21}, \tag{4.33}$$

where

$$\bar{\eta}_1 \geq \frac{A_1 C_1^{-\frac{\phi}{\alpha}} \Gamma(\mu)\big(-2(\alpha + \phi \ln(\mathrm{C}_1)) + \alpha\phi \ln(\bar{\gamma}_1) + 2\phi\psi(0,\mu)\big)}{\alpha\phi^2 \ln(2)} \tag{4.34}$$

$$\bar{\eta}_2 \geq \frac{-2\ln(\mathrm{B}_2) + \alpha \ln(\bar{\gamma}_2) + 2\psi(0,\mu)}{\alpha \ln(2)} \tag{4.35}$$

$$\bar{\eta}_{12} \approx \bar{\eta}_1 + \sum_{k=0}^{\mu-1} \frac{2A_1 B_2'^{-\frac{\phi}{\alpha}}}{\alpha^2 \ln(2) \mathrm{k}!} G_{0,0:2:0}^{0,1:4:2}\left(1 - \tfrac{\phi}{\alpha} - K \middle| \begin{matrix} 1 \\ - \end{matrix} \middle| \begin{matrix} 1,1 \\ B_1, 0 \end{matrix} \middle| \begin{matrix} 1,1 \\ 1,0 \end{matrix} \middle| \frac{C_1}{B_2'}, \frac{\bar{\gamma}_1^{\frac{\alpha}{2}}}{B_2'}\right) \tag{4.36}$$

$$\begin{aligned}\bar{\eta}_{21} \approx & \frac{\left(A_1 C_1^{\frac{\phi}{\alpha}} \Gamma(\mu)\right)}{\phi} \bar{\eta}_2 + \frac{2A_1 A_2 C_1^{-\frac{\phi}{\alpha}} C_1' B_2^{-(\mu+\frac{\phi}{\alpha})}}{\Gamma(\mu)\phi \ln(2)\alpha} G_{0,0:2:0}^{0,1:4:2}\left(1 - \mu - \tfrac{\phi}{\alpha} \middle| \begin{matrix} 1 \\ - \end{matrix} \middle| \begin{matrix} 1,1 \\ B_1, 0 \end{matrix} \middle| \begin{matrix} 1,1 \\ 1,0 \end{matrix} \middle| \frac{C_1'}{B_2}, \frac{\bar{\gamma}_2^{\frac{\alpha}{2}}}{B_2}\right) \\ & - \sum_{k=0}^{\mu-1} \frac{2A_1 A_2 C_1^{-\frac{\phi}{\alpha}} C_1'^k (B_2 + C_1')^{\mu+k}}{\alpha\phi \ln(2) k!} G_{3,2}^{1,3}\left(\begin{matrix} 1,1,1-\mu \\ 1,0 \end{matrix} \middle| \frac{\bar{\gamma}_2^{\frac{\alpha}{2}}}{B_2 + C_1'}\right)\end{aligned} \tag{4.37}$$

Proof. The proof is presented in Appendix 4.3. ■

Note that $\bar{\eta}_{12}$ and $\bar{\eta}_{21}$ has been expressed in terms of η_1 and η_2, respectively. Further, the derived expressions of the ergodic capacity of THz (see (4.34)) and RF (see (4.35)) links can be used to compare the performance of the relay-assisted system with direct links. It should be noted that the authors in [34] have derived an upper bound on the ergodic capacity of the THz link.

Analyzing the ergodic capacity of the relay-assisted system with i.ni.d fading using the PDF of (4.19) in (2.15) becomes intractable since the integral contains the product of a logarithmic function and two incomplete Gamma functions with different rational arguments. Considering integration by parts with $\log_2(1+\gamma)$ as the first term and $f_\gamma(\gamma)$ as the second term, the ergodic capacity can also be expressed using the CDF of SNR [183]

$$\bar{\eta} = \frac{1}{\ln(2)} \int_0^\infty (1+\gamma)^{-1}(1 - F_\gamma(\gamma))d\gamma \tag{4.38}$$

Now, we derive analytical expressions of the ergodic capacity of the relay-assisted system by considering the CDF-based formula in (4.38). Expressing $F_{\gamma_2}(\gamma) = 1 - F'_{\gamma_2}(\gamma)$, where $F'_{\gamma_2}(\gamma) = \frac{\Gamma(\mu_2, B_2(\sqrt{\gamma/\bar{\gamma}_2})^{\alpha_2})}{\Gamma(\mu_2)}$, and using (4.18) in (4.38), we get

$$\bar{\eta} = \frac{1}{\ln(2)} \int_0^\infty (1+\gamma)^{-1}(F'_{\gamma_2}(\gamma) - F'_{\gamma_2}(\gamma)F_{\gamma_1}(\gamma))d\gamma \tag{4.41}$$

Observing (4.41), a closed-form expression of the first term of integral can be readily obtained. However, the challenge lies in solving the integral of product of a rational polynomial and two incomplete Gamma functions with dissimilar rational arguments. We use $1+\gamma \approx \gamma$, an asymptotic approximation on an incomplete Gamma function, and a representation of the rational arguments to develop a tight approximation and an asymptotic expression (in terms of simpler Gamma function) at high SNR on the ergodic capacity of the relay-assisted system for the i.ni.d fading model, as given in the following Theorem.

Theorem 4.3. *Let ϕ and S_0 be the parameters of antenna misalignment errors of the THz link. If α_1, μ_1 and α_2, μ_2 are the fading parameters of THz and RF links, respectively. The ergodic capacity of the relay assisted link can be approximated as*

$$\bar{\eta} \approx \mathcal{F}_\eta(\alpha_1, \alpha_2, \mu_1, \mu_2, \phi, S_0) \tag{4.42}$$

and asymptotically at high SNR, the ergodic capacity is given by

$$\bar{\eta}^\infty = \mathcal{F}_\eta^\infty(\alpha_1, \alpha_2, \mu_1, \mu_2, \phi, S_0) \tag{4.43}$$

where $\mathcal{F}_\eta(\alpha_1, \alpha_2, \mu_1, \mu_2, \phi, S_0)$ and $\mathcal{F}_\eta^\infty(\alpha_1, \alpha_2, \mu_1, \mu_2, \phi, S_0)$ are given in (4.39) *and* (4.40)*,*

$$\mathcal{F}_{\eta}(\alpha_1,\alpha_2,\mu_1,\mu_2,\phi,S_0)=\left(1-\frac{A_1C_1^{-\frac{\phi}{\alpha_1}}\Gamma(\mu_1)}{\phi}\right)\frac{2^{(\mu_2-\frac{1}{2})}}{\Gamma(\mu_2)\ln(2)(2\pi)^{(\alpha_2-\frac{1}{2})}}$$
$$G_{2+\alpha_2,4+\alpha_2}^{4+\alpha_2,\alpha_2}\left(\begin{matrix}\Delta(\alpha_2,0),\Delta(2,1)\\ \Delta(\alpha_2,0),\Delta(2,\mu_2),\Delta(2,0)\end{matrix}\middle|\frac{(B_2\bar{\gamma}_1^{-\frac{\alpha_2}{2}})^2}{4}\right)$$
$$-\frac{2A_1C_1^{-\frac{\phi}{\alpha_1}}\epsilon^{\left(\frac{\phi}{\alpha_1}+B_1-\frac{3}{2}\right)}}{\alpha_1(2\pi)^{(\frac{\epsilon-1}{2})}\phi\Gamma(\mu_2)\ln(2)}G_{1+2\epsilon,2+\epsilon}^{\ 2,\ 2\epsilon}\left(\begin{matrix}\Delta(\epsilon,1-\frac{\phi}{\alpha_1}-\mu_2),\Delta(\epsilon,1-\frac{\phi}{\alpha_1}),\Delta(1,1)\\ \Delta(1,\mu_2),\Delta(1,0),\Delta(\epsilon,-\frac{\phi}{\alpha_1})\end{matrix}\middle|\frac{\left(B_2\bar{\gamma}_2^{-\frac{\alpha_2}{2}}\right)}{\left(C_1\bar{\gamma}_1^{-\frac{\alpha_1}{2}}\right)^{\epsilon}\epsilon^{-\epsilon}}\right)$$
$$+\frac{A_1C_1^{-\frac{\phi}{\alpha_1}}\Gamma(\mu_2)}{(2\pi)^{(\alpha_1-\frac{1}{2})}\phi\ln(2)\Gamma(\mu_2)}G_{2+\alpha_1,4+\alpha_1}^{4+\alpha_1,\alpha_1}\left(\begin{matrix}\Delta(\alpha_1,0),\Delta(2,1)\\ \Delta(2,\mu_1),\Delta(2,0),\Delta(\alpha_1,0)\end{matrix}\middle|\frac{\left(C_1\bar{\gamma}_1^{-\frac{\alpha_1}{2}}\right)^2}{4}\right)$$
$$-\frac{A_1C_1^{-\frac{\phi}{\alpha_1}}\left(B_2\bar{\gamma}_2^{-\frac{\alpha_2}{2}}\right)^{\mu_2}2^{(\mu_1-\frac{1}{2})}}{\mu_2(2\pi)^{(\alpha_1-\frac{1}{2})}\phi\ln(2)\Gamma(\mu_2)}G_{2+\alpha_1,4+\alpha_1}^{4+\alpha_1,\alpha_1}\left(\begin{matrix}\Delta(\alpha_1,1-\frac{\alpha_2\mu_2+2}{2}),\Delta(2,1)\\ \Delta(2,\mu_1),\Delta(2,0),\Delta(\alpha_1,1-\frac{\alpha_2\mu_2+2}{2})\end{matrix}\middle|\frac{\left(C_1\bar{\gamma}_1^{-\frac{\alpha_1}{2}}\right)^2}{4}\right) \tag{4.39}$$

$$\mathcal{F}_{\eta}^{\infty}(\alpha_1,\alpha_2,\mu_1,\mu_2,\phi,S_0)=\frac{1}{\ln(2)\Gamma(\mu_2)}\sum_{j=1}^{3}\frac{1}{\zeta_j}\frac{\prod_{k=1,k\neq j}^{3}\Gamma\left(a_k-a_j\frac{\zeta_k}{\zeta_j}\right)\Gamma\left(1+a_j\frac{\alpha_2}{2\zeta_j}\right)}{\Gamma\left(1-a_j\frac{1}{\zeta_j}\right)}\left(B_2\bar{\gamma}_2^{-\frac{\alpha_2}{2}}\right)^{\frac{a_j}{\zeta_j}}$$
$$-\frac{A_1C_1^{-\frac{\phi}{\alpha_1}}}{\phi\Gamma(\mu_2)\ln(2)}\left[\Gamma(\mu_1)\sum_{j=1}^{3}\frac{1}{\zeta_j}\frac{\prod_{k=1,k\neq j}^{3}\Gamma\left(a_k-a_j\frac{A_k}{A_j}\right)\Gamma\left(1+a_j\frac{\alpha_2}{2\zeta_j}\right)}{\Gamma\left(1-a_j\frac{1}{\zeta_j}\right)}\left(B_2\bar{\gamma}_2^{-\frac{\alpha_2}{2}}\right)^{\frac{a_j}{\zeta_j}}\right.$$
$$+\sum_{j=1}^{2}\frac{\prod_{k=1,k\neq j}^{2}\Gamma\left(b_k-b_j\right)\Gamma\left(\frac{\phi}{\alpha_1}+B_1+b_j\epsilon\right)\Gamma\left(\frac{\phi}{\alpha_1}+b_j\epsilon\right)}{\Gamma\left(1-b_j\right)\Gamma\left(1+\frac{\phi}{\alpha_1}+b_j\epsilon\right)}\left(\frac{B_2\bar{\gamma}_2^{-\frac{\alpha_2}{2}}}{\left(C_1\bar{\gamma}_1^{-\frac{\alpha_1}{2}}\right)^{\epsilon}}\right)^{\frac{b_j}{B_j}}$$
$$-\sum_{j=1}^{2}\sum_{t=0}^{\mu_1-1}\frac{\Gamma(\mu_2)\Gamma(\mu_1)\left(C_1\bar{\gamma}_1^{\frac{-\alpha_1}{2}}\right)^t}{t!Q_j}\prod_{k=1,k\neq j}^{2}\Gamma\left(c_k-c_j\frac{Q_k}{Q_j}\right)\Gamma\left(1+k\alpha_1+c_j\frac{\alpha_1}{2Q_j}\right)\left(C_1\bar{\gamma}_1^{-\frac{\alpha_1}{2}}\right)^{\frac{c_j}{Q_j}}$$
$$\left.+\sum_{j=1}^{3}\frac{1}{D_j}\frac{\prod_{k=1,k\neq j}^{3}\Gamma\left(d_k-d_j\frac{D_k}{D_j}\right)\Gamma\left(1+\frac{\alpha_2\mu_2}{2}+d_j\frac{\alpha_1}{2D_j}\right)}{\Gamma\left(1-d_j\frac{1}{D_j}\right)}\left(C_1\bar{\gamma}_1^{-\frac{\alpha_1}{2}}\right)^{\frac{d_j}{D_j}}\right] \tag{4.40}$$

where $a_k=a_j=\{\mu_2,0,0\}$ and $\zeta_k=\zeta_j=\{1,1,\frac{\alpha_2}{2}\}$; $b_k=b_j=\{\mu_2,0\}$; $c_k=c_j=\{0,\frac{-k\alpha_1}{2}\}$ and $Q_k=Q_j=\{1,\frac{\alpha_1}{2}\}$; $d_k=d_j=\{\mu_1,0,1-\frac{\alpha_2\mu_2+2}{2}\}$ and $D_k=D_j=\{1,1,\frac{\alpha_1}{2}\}$

respectively.

Proof. The proof is presented in Appendix 4.4. ■

Since the derivation for the ergodic capacity in (4.39) involves the use of $1+\gamma \approx \gamma$ in one term and application of asymptotic approximation on the incomplete Gamma function once (see (4.103)), the derived approximation can be accurate for various system parameters of practical relevance. We examine the accuracy of derived approximation and asymptotic analysis using computer simulations and numerical analysis in Section IV.

Although the ergodic capacity can be computed using functional representation of Meijer G and Gamma function, we present simplified analysis on the ergodic capacity for some specific fading channel conditions and antenna misalignment error parameters:

Corollary 4.3. *1. Considering the THz-link as Nakagami-m fading ($\alpha_1 = 2$, $\mu_1 = 2$) with antenna misalignment errors parameter $\phi = 2$, and the Rayleigh fading ($\alpha_2 = 2$ $\mu_2 = 1$) for the RF-link, the ergodic capacity of the relay assisted link is given as*

$$\bar{\eta} = -\frac{1-(\bar{\gamma}_2+2S_0^{-2}\bar{\gamma}_1)e^{(\bar{\gamma}_2+2S_0^{-2}\bar{\gamma}_1)}\Gamma(0,\bar{\gamma}_2+2S_0^{-2}\bar{\gamma}_1)}{\ln(2)(\bar{\gamma}_2+2\mathrm{S}_0^{-2}\bar{\gamma}_1)} + \frac{e^{(\bar{\gamma}_2+2S_0^{-2}\bar{\gamma}_1)}\Gamma(0,\bar{\gamma}_2+2S_0^{-2}\bar{\gamma}_1)}{\ln(2)} \tag{4.44}$$

2. Considering the THz-link ($\alpha_1 \to \infty$, $\mu_1 = 1$) as a linear Weibull fading with $\phi = 2$, and the Rayleigh fading ($\alpha_2 = 2$ $\mu_2 = 1$) for the RF-link, the ergodic capacity of the relay assisted link:

$$\bar{\eta} = \frac{e^{\bar{\gamma}_2}\Gamma(0,\bar{\gamma}_2)}{\ln(2)} \tag{4.45}$$

Proof. Using $F_\gamma(\gamma)$ from (4.18) in (4.38) with special cases of α and μ enumerated in (a) and (b), and applying the standard procedure, we get (4.44) and (4.45). ■

The special case in (4.44) is a simplified expression of the ergodic capacity with Nakagami-m and Rayleigh fading channels. Further, the scenario in (b) is chosen to show the effect of imbalance of fading channels in both the links: as the non-linearity of fading channel reduces to $\alpha \to \infty$ (i.e, good channel conditions), the performance is determined by another link with finite α (see (4.45)).

4.3.5 Average Bit Error Rate

In this subsection, we derive the average BER of the relay-assisted THz-RF link. Using (4.18) in (2.16), we can obtain a closed form expression of the average BER by solving three integrals with $F_{\gamma_1}(\gamma)$, $F_{\gamma_2}(\gamma)$, and $F_{\gamma_1}(\gamma)F_{\gamma_2}(\gamma)$ in (2.16). However, the average BER for the

$$\bar{P}_{e1} = \frac{A_1 C_1^{-\frac{\phi}{\alpha_1}} \Gamma(\mu_1)}{2\phi} + \frac{A_1 \bar{\gamma}_1^{\frac{-\phi}{2}} \alpha_1^{\frac{\phi+2p-1}{2}} 2^{(B_1-\frac{1}{2})} q^{-\frac{\phi}{2}}}{2\phi\Gamma(p)(2\pi)^{\frac{\alpha_1}{2}}} G_{2+\alpha_1,4}^{4,\alpha_1}\left(\begin{matrix}\Delta(\alpha_1, 1-\frac{\phi+2p}{2}), \Delta(2,1) \\ \Delta(2,B_1), \Delta(2,0)\end{matrix}\middle| \frac{(C_1 \bar{\gamma}_1^{-\frac{\alpha_1}{2}})^2 \alpha_1^{\alpha_1}}{4q^{(\alpha_1)}}\right)$$
$$- \frac{A_1 C_1^{-\frac{\phi}{\alpha_1}} 2^{(\mu_1-\frac{1}{2})} \alpha_1^{\frac{2p-1}{2}}}{2\phi\Gamma(p)(2\pi)^{\frac{\alpha_1}{2}}} G_{2+\alpha_1,4}^{4,\alpha_1}\left(\begin{matrix}\Delta(\alpha_1, 1-p), \Delta(2,1) \\ \Delta(2,\mu_1), \Delta(2,0)\end{matrix}\middle| \frac{(C_1 \bar{\gamma}_1^{-\frac{\alpha_1}{2}})^2 \alpha_1^{\alpha_1}}{4q^{(\alpha_1)}}\right) \tag{4.47}$$

$$\bar{P}_{e2} = \frac{1}{2} - \frac{2^{(\mu_2-\frac{1}{2})} \alpha_2^{\frac{2p-1}{2}}}{2\Gamma(p)\Gamma(\mu_2)(2\pi)^{\frac{\alpha_2}{2}}} G_{2+\alpha_2,4}^{4,\alpha_2}\left(\begin{matrix}\Delta(\alpha_2, 1-p), \Delta(2,1) \\ \Delta(2,\mu_2), \Delta(2,0)\end{matrix}\middle| \frac{(B_2 \bar{\gamma}_2^{-\frac{\alpha_2}{2}})^2 \alpha_2^{\alpha_2}}{4q^{(\alpha_2)}}\right) \tag{4.48}$$

DF relaying with Gray coding can also be expressed as [184]:

$$\bar{P}_e = \bar{P}_{e1} + \bar{P}_{e2} - 2\bar{P}_{e1}\bar{P}_{e2} \tag{4.46}$$

where $\bar{P}_{e1}$ and $\bar{P}_{e2}$ denote the average BER of THz and RF links, respectively.

Theorem 4.4. *Let ϕ and S_0 be the parameters of antenna misalignment errors of the THz link. If α_1, μ_1 and α_2, μ_2 are the fading parameters of THz and RF links, respectively, then an exact expression of average BER for the relay assisted THz-RF link is given as:*

$$\bar{P}_e = \bar{P}_{e1} + \bar{P}_{e2} - 2\bar{P}_{e1}\bar{P}_{e2} \tag{4.49}$$

where $\bar{P}_{e1}$ and $\bar{P}_{e2}$ are given in (4.47) *and* (4.48)*, respectively. and asymptotically at high SNR, the average BER is given by*

$$\begin{aligned}\bar{P}_e^{\infty} = & \frac{A_1 C_1^{-\frac{\phi}{\alpha_1}} \Gamma(\mu_1)}{2\phi} + \frac{1}{2} + \frac{A_1 \bar{\gamma}_1^{-\frac{\phi}{2}} q^{-\frac{\phi}{2}}}{2\Gamma(p)\phi} \\ & \times \sum_{j=1}^{2} \frac{\prod_{k=1,k\neq j}^{2} \Gamma\big(b_k - b_j\big)\Gamma\big(\frac{\phi+2p}{2} + b_j\frac{\alpha_1}{2}\big)}{\Gamma\big(1-b_j\big)} \big(C_1 (q\bar{\gamma}_1)^{-\frac{\alpha_1}{2}}\big)^{b_j} \\ & - \frac{A_1 C_1^{-\frac{\phi}{\alpha_1}}}{2\Gamma(p)\phi} \sum_{j=1}^{2} \frac{\prod_{k=1,k\neq j}^{2} \Gamma\big(c_k - c_j\big)\Gamma\big(p + c_j\frac{\alpha_1}{2}\big)}{\Gamma\big(1-c_j\big)} \big(C_1 (q\bar{\gamma}_1)^{-\frac{\alpha_1}{2}}\big)^{c_j} \\ & - \frac{1}{2\Gamma(p)\Gamma(\mu_2)} \sum_{j=1}^{2} \frac{\prod_{k=1,k\neq j}^{2} \Gamma\big(d_k - d_j\big)\Gamma\big(p + d_j\frac{\alpha_2}{2}\big)}{\Gamma\big(1-d_j\big)} \big(B_2 (q\bar{\gamma}_2)^{-\frac{\alpha_2}{2}}\big)^{d_j}\end{aligned} \tag{4.50}$$

where $b_k = b_j = \{B_1, 0\}$, $c_k = c_j = \{\mu_1, 0\}$ and $d_k = d_j = \{\mu_2, 0\}$.

Proof. See Appendix 4.5. ■

In what follows, we discuss few simplified scenarios to derive insights on the average BER performance of the THz-RF system.

Corollary 4.4. *1. The diversity order M^{BER} using the average BER performance of the THz-RF relay assisted system is given by*

$$M^{\mathrm{BER}} = \min\left\{\frac{\alpha_1\mu_1}{2}, \frac{\alpha_2\mu_2}{2}, \frac{\phi}{2}\right\} \tag{4.51}$$

Note that the BER-diversity order is same as the outage-diversity order in (4.20).

2. *Considering the THz-link as Nakagami-m fading ($\alpha_1 = 2$, $\mu_1 = 2$) with $\phi = 2$, and the Rayleigh fading ($\alpha_1 = 2$ $\mu_1 = 1$) for the RF-link, the average BER of the relay assisted link is given as*

$$\bar{P}_e = 1 - \frac{1}{1+\bar{\gamma}_2} + \frac{1}{2(1+2S_0^{-2}\bar{\gamma}_1+\bar{\gamma}_2)} - \frac{1+3\bar{\gamma}_2}{(1+2\bar{\gamma}_2)^2} \tag{4.52}$$

3. *Considering the THz-link ($\alpha_1 \to \infty$, $\mu_1 = 1$) as a linear Weibull fading with $\phi = 2$, and the Rayleigh fading ($\alpha_2 = 2$ $\mu_2 = 1$) for the RF-link, the average BER of the relay assisted link:*

$$\bar{P}_e = \frac{\bar{\gamma}_2 + 2S_0^{-\phi}}{1+\bar{\gamma}_2} \tag{4.53}$$

Proof. For part (a), the diversity order can be readily obtained using the exponent of SNR (i.e., dominant terms of the average BER at high SNR) of the asymptotic expression in (4.50). Using $F_\gamma(\gamma)$ from (4.18) in (3.30) with special cases of α and μ enumerated in (b) and (c), and applying the standard procedure, we can get (4.52) and (4.53). ■

The results in Corollary 4.4 simplifies the average BER performance at high SNR and for a few values of α and μ in order to provide insights on system behavior analytically. In the next section, we demonstrate the performance of the proposed relaying scheme for various values of α, μ, and other system parameters.

4.4 Simulation and Numerical Results

In this section, we use numerical analysis and Monte Carlo simulations (averaged over 10^8 channel realizations) to demonstrate the performance of the THz-RF relay assisted system. Although a direct link between the source and destination may not exist, we compare the performance of direct link with THz and relay-assisted transmissions for various scenarios. We consider the THz link with a distance in the range of $30 - 50$ m. This range is typical for the THz link, as adopted in [25, 33, 34]. To compute the path loss for the THz link, we consider relative humidity, atmospheric pressure, and temperature as 50%, 101325 Pa, and 296°K, respectively. The parameters for the calculation of the molecular absorption coefficient k are provided in Table 4.1. For parameters S_0 and ϕ, we need radius r_1 of the receiver antenna's effective aperture area A_e. Using $A_e = \pi {r_1}^2 = \lambda^2 G_1/4\pi$ [185], we can get $r_1 = \lambda\sqrt{G_1}/2\pi$,

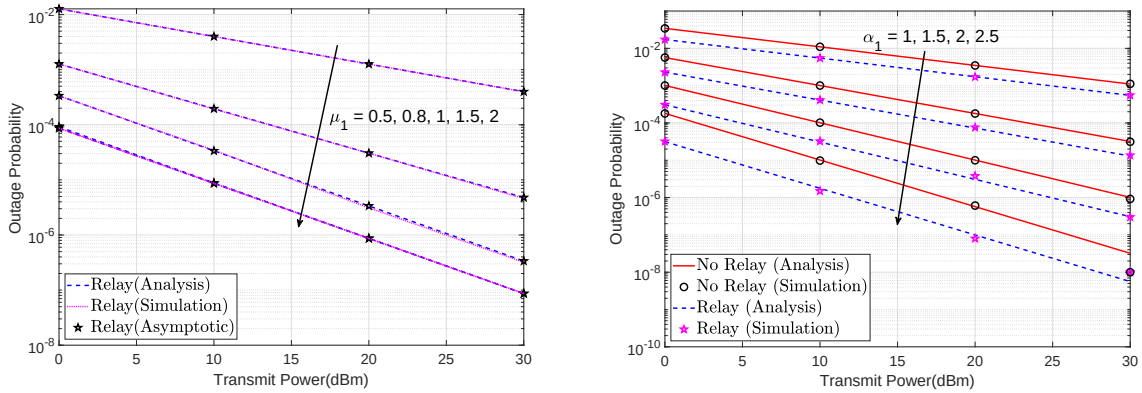

(a) Different values of μ_1 with $\alpha_1 = 2, \alpha_2 = 2, \mu_2 = 1$. (b) Different values of α_1 with $\mu_1 = 1, \alpha_2 = 2, \mu_2 = 4$.

Figure 4.2: Outage probability performance of relay-assisted THz-RF wireless link at $\gamma_{\text{th}} = 4$dB with $\phi = 28.9576$ and $S_0 = 0.054$.

Table 4.1: Parameters of the molecular absorption coefficient k

Symbol	Value	Symbol	Value
q_1	0.2205	q_2	0.1303
q_3	0.0294	q_4	0.4093
q_5	0.0925	q_6	2.014
q_7	0.1702	q_8	0.0303
q_9	0.537	q_{10}	0.0956
c_1	5.54×10^{-37} Hz^{-3}	c_4	-6.36×10^{-3} Hz^{-3}
c_2	-3.94×10^{-25} Hz^{-2}	p_1	10.835 cm^{-1}
c_3	9.06×10^{-14} Hz^{-1}	p_2	12.664 cm^{-1}

Table 4.2: List of Simulation Parameters

Parameter	Value
THz carrier frequency	275 GHz
RF carrier frequency	6 GHz
THz signal bandwidth	10 GHz
RF signal bandwidth	20 MHz
Noise PSD	-174 dBm/Hz
Noise figure	5 dB
Antenna Gain (dBi)	55 (THz), 25 (RF)
α_1, α_2	$1-6$
μ_1, μ_2	$0.5-4$
Ω	1
p, q	$1, 1$ (DBPSK)
Jitter standard deviation (σ_s)	$5-12$ cm
Antenna aperture radius (r_1)	10 cm

where G_1 is the receiver antenna gain of the THz link. To simulate the antenna misalignment error, we consider the normalized beam-width w_z/r_1 in the range of 6 to 12. The RF link distance is taken up to 50 m, which is reasonable when users are connected to a nearby AP in a cell-free architecture. We compute the path gain $H_{l,2}$ of the RF link using the 3GPP path loss model $32.4+17.3\log_{10}(d_2)+20\log_{10}(10^{-9}f_2)$, where d_2 (in m) is the distance and f_2 (in Hz) is the carrier frequency of the RF link. We use AWGN power of -69.4 dBm of the THz link over a bandwidth of 10 GHz and -104.4 dBm of the RF link over a bandwidth of 20 MHz [175]. Other simulation parameters for THz and RF systems as presented in Table 4.2.

First, we demonstrate the outage probability performance of the relay assisted system, as shown in Fig. 4.2 by considering $\sigma_s = 5.66$cm and normalized beam-width $w_z/r_1 = 6$. In Fig. 4.2a, we show the impact of the parameter μ on the outage probability by adopting the RF link as Rayleigh fading $\alpha_2 = 2$, $\mu_2 = 1$, and the THz link as the Nakagami-m fading $\alpha_1 = 2$ at different μ_1. The outage performance improves with an increase in the parameter μ since an increase in μ_1 accounts for dense clustering in the fading channel (i.e., good channel conditions). A very low value of $\mu_1 < 1$ (i.e., worse channel conditions, a typical scenario for the THz link) shows significant degradation in the outage performance. The derived CDF in Theorem 4.1 allows the computation of the outage probability for continuous (non-integer) values of μ_1, which is necessary to evaluate the performance for a broader range of μ_1, especially when $\mu_1 < 1$. Note that the plots for $\mu = 1.5$ and $\mu = 2$ overlap with each other. It should be emphasized that the state of art research use only integer values of μ_1 to compute the CDF of the THz link [33]. Further, we show the effect of the non-linearity parameter α_1 on the outage probability. In Fig. 4.2(b), we consider $\alpha_2 = 2$, $\mu_2 = 4$ (Nakagami-m fading with higher

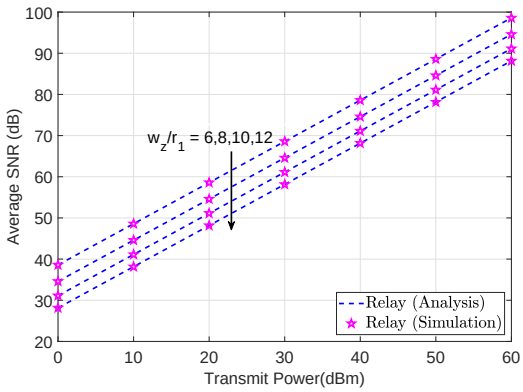

(a) Different values of w_z/r_1 with α_1=2, μ_1=4, α_2=2, and μ_2=1.

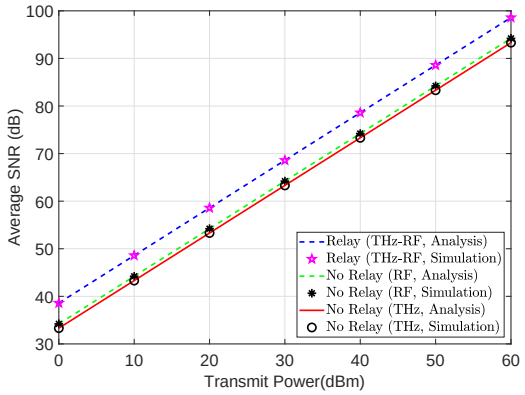

(b) Comparison between relayed and individual links with $\alpha_1 = 2, \mu_1 = 4, \alpha_2 = 2, \mu_2 = 1, w_z/r_1 = 6, \phi = 8.2368$, and $S_0 = 0.054$.

Figure 4.3: Average SNR performance of relay-assisted THz-RF wireless link.

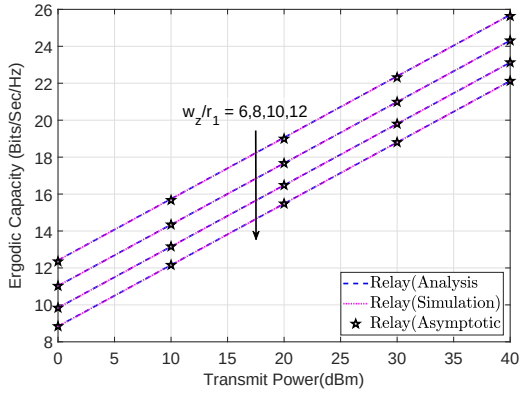

(a) Different values of w_z/r_1 with α_1=2, μ_1=1.5, α_2=4, μ_2=1, and $\epsilon = 2$.

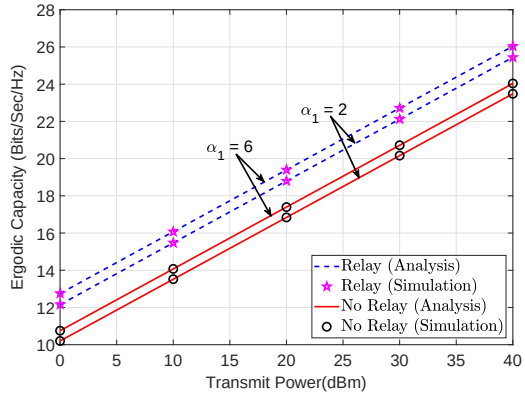

(b) Different values of α_1 with $\mu_1 = 1, \alpha_2 = 2, \mu_2 = 4, w_z/r_1 = 6, \phi = 8.2368$, and $S_0 = 0.054$.

Figure 4.4: Ergodic capacity performance of relay-assisted THz-RF wireless link.

clustering) for the RF link and $\mu_1 = 2$ with different α_1 of the THz link. The outage probability improves with an increase in the parameter α_1 (i.e., a decrease in the non-linearity of the THz fading). The outage probability dramatically improves with an increase in the parameter α_1: a factor of 10^4 decrease in the outage probability when the parameter α_1 increases from 1 to 3 at the same 10 dBm of transmit power.

Observing Fig. 4.2a and Fig. 4.2b, it can be emphasized that the diversity order depends on $\alpha-\mu$ parameters of either of the links since the parameter ϕ is higher (low antenna misalignment errors) due to strong beam-width $w_z = 0.6$. As such, analysis in (4.20)) shows that the diversity order $M = \mu_1$ depends on the THz link when $\mu_1 < 1$, and after that, there is no effect of the parameter μ_1 since the diversity order becomes $M = 1$, which is confirmed in Fig. 4.2a. Similar conclusions on the outage probability behavior on the parameter α_1 can be inferred from Fig. 4.2b.

Next, we demonstrate the effect of antenna misalignment errors on the average SNR and ergodic rate performance of the relay-assisted system with $\sigma_s = 10.61$cm, as shown in Fig. 4.3 and Fig. 4.4. We consider Rayleigh fading ($\alpha_2 = 2$, $\mu_2 = 1$) for the RF and Nakagami-m fading ($\alpha_1 = 2$, $\mu_1 = 4$) for the THz link with different values of normalized beam-width w_z/r_1. Fig. 4.3(a) and Fig. 4.4(a) demonstrate that the effect of antenna misalignment errors can be minimized by decreasing the normalized beam-width. It should be noted that the model of antenna misalignment errors in (4.4) is applicable when $w_z/r_1 \geq 6$. In Fig. 4.3(b), we compare the performance of mixed THz-RF transmissions with direct RF and THz. It can be seen that the relay-assisted system provides a significant (around 5 dB) than the direct transmissions. There is a significant increase of 2 bits/sec/Hz in the ergodic rate performance, as shown in Fig. 4.4(b). Although the direct link performance of THz and RF are almost similar, the THz has an enormous bandwidth (in the range of 10 GHz) in comparison to the RF to get an enhanced channel capacity. It should be noted that the throughput of the THz-RF system is limited by the bandwidth of RF link.

Finally, we demonstrate the average BER performance in Fig. 4.5 with $\sigma_s = 10.61$cm. We show the effect of fading parameter α_1 and normalized beam-width w_z/r_1 on the average BER in Fig. 4.5(a). The figure shows a dramatic improvement in the average BER with an increase in α_1 from 1 to 2.5. However, the effect of normalized beam-width w_z/r_1 on the average BER is nominal. In Fig. 4.5(b), we show the impact of relay location on the average BER performance for a link distance of 80 m. It can be seen that a shorter THz link provides significant performance for the THz-RF relay system since the path loss at the THz frequencies is high.

In all the above plots (Fig. 4.2 to Fig. 4.5), we verify our derived expressions (by directly evaluating equations (4.13), (4.18), (4.26), (4.39), (4.40), (4.46), and (4.50)) with the simulation and numerical results. We use MATLAB function '*meijergG(a,b,c,d,z)*' to compute the Meijer G functions involved in closed-form expressions. It can be seen that the derived analytical expressions of the outage probability and average SNR for both i.i.d and i.ni.d fading

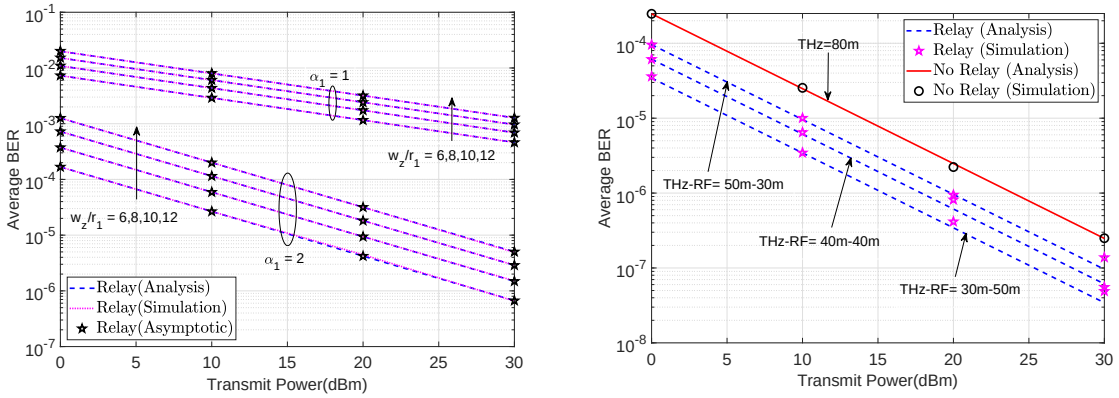

(a) Different values of α_1 and w_z/r_1 with $\mu_1 = 0.8, \alpha_2 = 2$, and $\mu_2 = 2.5$.

(b) Different link distances with $\alpha_1 = 2, \mu_1 = 1, \alpha_2 = 2, \mu_2 = 4, w_z/r_1 = 6, \phi = 8.2368$, and $S_0 = 0.054$.

Figure 4.5: Average BER performance of relay-assisted THz-RF wireless link.

scenarios and average BER for the i.i.d. fading have an exact match with the simulation results. The analytical results of ergodic capacity and average BER for the i.ni.d fading can overestimate/underestimate the exact results due to asymptotic bound $\Gamma(a, x) \to e^{-x}x^{a-1}$ in few terms of integration. However, Fig. 4.4 and Fig. 4.5 show that the difference between analysis and simulation is indistinguishable. Further, the analytical results of ergodic capacity for the i.i.d fading are very close to the exact even with approximation $\log_2(1 + x^a) \approx a \log_2(1 + x)$. Furthermore, it can be observed from Fig. 4.2(a), Fig. 4.4(a), and Fig. 4.5(a) that the asymptotic results are very close to the exact for a wide range of transmit power since average SNR is reasonably high for considered link distances. Indeed, the asymptotic performance may deviate from the exact in a low SNR regime.

4.5 Integrated THz-RF Wireless Link: Generalized Antenna Misalignment Errors

In the preceding section of this chapter, our focus was on zero-boresight antenna misalignment errors in the context of integrating RF with THz using the DF protocol. In this section, we expand our scope to encompass more comprehensive channel models, including scenarios with non-zero boresight antenna misalignment errors, and the utilization of a simplified AF relaying technique to integrate THz with RF, considering the generalized α-κ-μ shadowed channel fading, also known as α-KMS fading model.

In the first hop, the received signal y_R[1] at the relay is expressed as $y_R = H_r h_{fr} S + w_r$, where S is the transmitted signal from the source, w_r is the additive white Gaussian noise (AWGN) signal with variance $\sigma^2_{w_1}$, H_r is the RF channel path-gain, and h_{fr} is the fading coefficient. We use the generalized α-κ-μ shadowed (a.k.a α-KMS) distribution to model the short

[1]*Notations*: Subscripts $(\cdot)_R$, $(\cdot)_D$, $(\cdot)_r$, and $(\cdot)_t$ denote the relay, destination, the first link RF, and second link THz, respectively. $G^{m,n}_{p,q}(.|.)$ and $H^{m,n}_{p,q}(.|.)$ denotes Meijer's G and Fox's H-functions, respectively.

term fading $|h_{fr}|$ for the RF link with PDF [148]:

$$f_{|h_{fr}|}(x) = \frac{m_r^{m_r}\alpha_r}{2c_r^{\mu}\Gamma(\mu_r)(\mu_r\kappa_r + m_r)_r^m\bar{\gamma}_r}\Big(\frac{x}{\bar{\gamma}_r}\Big)^{\frac{\alpha_r\mu_r}{2}-1} \times\exp\Big(-\frac{1}{c}\Big(\frac{x}{\bar{\gamma}_r}\Big)^{\frac{\alpha_r}{2}}\Big){}_1F_1\Big(m_r,\mu_r;\frac{\mu_r\kappa_r}{c(\mu_r\kappa_r+m_r)}\Big(\frac{x}{\bar{\gamma}_r}\Big)^{\frac{\alpha_r}{2}}\Big) \tag{4.54}$$

where $\{\alpha_r, \kappa_r, \mu_r, m_r\}$ are the fading parameters, ${}_1F_1$ is the confluent Hypergeometric function and the parameter c is defined in [148]. In the second hop, the relay amplifies the incoming signal y_R with a gain $\mathcal{G}$ to get the received signal at the destination (assuming negligible hardware distortions [33, 186]) $y_D = H_t h_p h_{ft}\mathcal{G}y_R + w_t$, where H_t is the path gain of THz link, w_t is the AWGN with variance $\sigma_{w_t}^2$, h_p models antenna misalignment errors, and $|h_{ft}|$ is the short-term fading of the THz link with PDF:

$$f_{|h_{ft}|}(x) = \frac{\alpha\mu_t^{\mu_t}}{\Omega^{\alpha_t\mu_t}\Gamma(\mu_t)}x^{\alpha_t\mu_t-1}\exp\Big(-\frac{\mu_t}{\Omega^{\alpha_t\mu_t}}x^{\alpha_t}\Big) \tag{4.55}$$

where $\{\alpha_t, \mu_t, \Omega\}$ are the fading parameters for the THz link, and $\Gamma(\cdot)$ denotes the Gamma function. We use the generalized non-zero boresight statistical model for h_p [151]:

$$f_{h_p}(h_p) = \frac{\phi\exp\left(\frac{-s^2}{2\sigma^2}\right)}{A_0^{\phi}}h_p^{\phi-1}I_0\left(\frac{s}{\sigma^2}\sqrt{\frac{w_{z_{\text{eq}}}^2\ln\frac{S_0}{h_p}}{2}}\right) \tag{4.56}$$

where $s = \sqrt{\mu_x^2+\mu_y^2}$ is the boresight displacement with μ_x and μ_y representing horizontal and vertical boresight values, respectively, S_0 is the fraction of collected power without antenna misalignment errors, ϕ is the ratio of normalized beam-width to the jitter, and $I_0(\cdot)$ denotes the modified Bessel function of the first kind with order zero.

We denote by $A_t = \frac{\alpha_t\mu_t^{\mu_t}}{\Omega^{\alpha_t\mu_t}\Gamma(\mu_t)}$, and $B_t = \frac{\mu_t}{\Omega^{\alpha_t\mu_t}}$. Denoting $\bar{\gamma}_r = \frac{P_r|H_r|^2}{\sigma_{w_r}^2}$ with P_r as the transmit power at the source for the RF transmission and $\bar{\gamma}_t = \frac{P_t|H_t|^2}{\sigma_{w_t}^2}$ with P_t as the transmit power at the relay for the THz transmission, we express the SNR of the RF link as $\gamma_r = \bar{\gamma}_r|h_f|^2$ and the SNR of the THz as $\gamma_t = \bar{\gamma}_t|h_f h_p|^2$. The end-to-end SNR AF relaying system is given by $\gamma = \frac{\gamma_r\gamma_t}{\gamma_t+C}$ [53] where $C = P_t/\mathcal{G}^2\sigma_{w_t}^2$. For the blind AF relaying, an arbitrary value of $\mathcal{G}$ can be selected. However, in a semi-blind approach the fixed gain relaying factor $\mathcal{G}$ can be obtained using statistics of received signal of the first hop $C = (\mathbb{E}_{\gamma_r}(1+\gamma)^{-1})^{-1}$[53], where $\mathbb{E}_{\gamma_r}$ denotes the expectation operator over the random variable γ_r. Hence, the well-known PDF of end-to-end SNR γ of the fixed-gain AF relayed system is given by

$$f_{\gamma}(z) = \int_0^{\infty} f_{\gamma_r}\Big(\frac{z(x+C)}{x}\Big)f_{\gamma_t}(x)\frac{x+C}{x}dx \tag{4.57}$$

4.5.1 Density and Distribution Functions

In the following, we present the PDF and CDF of SNR for the THz link subjected to short-term fading and antenna misalignment errors. Using the limits of $|h_{ft}|$ and h_p in (4.55) and (4.56), respectively, the PDF of $|h_{fp}| = h_p|h_{ft}|$ can represented as

$$f_{|h_{fp}|}(h) = \int_0^{S_0} \frac{1}{h_p} f_{h_f}\left(\frac{h}{h_p}\right) f_{|h_p|}(h_p)\mathrm{d}h_p \tag{4.58}$$

Using (4.56) with the series expansion $I_0(x) = \sum_{k=0}^{\infty} \frac{\left(\frac{x}{2}\right)^{2k}}{(k!)^2}$ in (4.58) and utilizing the integral form of Meijer's G-function:

$$f_{h_{fp}}(h) = \frac{A_t\phi \exp\left(\frac{-s^2}{2\sigma^2}\right) h^{(\alpha_t\mu_t-1)}}{A_0^{\phi}} \sum_{j=0}^{\infty} \frac{1}{(j!)^2}\left(\frac{s^2 w_{z_{\mathrm{eq}}}^2}{8\sigma^4}\right)^j \frac{1}{2\pi i}\int_{\mathcal{L}} \Gamma(0-u_1)(B_t h^{\alpha_t})^u du I_1 \tag{4.59}$$

where $I_1 = \int_0^{S_0} h_p^{(\phi-\alpha\mu-1)} h_p^{-\alpha_t u}\big(\ln\frac{S_0}{h_p}\big)^j \mathrm{d}h_p$. Substituting $\ln\frac{S_0}{h_p} = t$, we obtain $I_1 = S_0^{(\phi-\alpha_t\mu_t+1-\alpha_t u)}\Gamma(j+1)\Big(\frac{\Gamma(1+\phi-\alpha\mu-\alpha u)}{\Gamma(\phi-\alpha\mu-\alpha u)}\Big)^{-(j+1)}$. Further, using I_1 in (4.59) and applying the definition of Fox's H-function [166] with a transformation of the random variable $f_{\gamma_t}(\gamma) = \frac{1}{2\sqrt{\gamma\bar{\gamma}_t}} f_{h_{pf}}\left(\sqrt{\frac{\gamma}{\bar{\gamma}_t}}\right)$ we get the PDF

$$\begin{aligned} f_{\gamma_t}(\gamma) = {} & \frac{A_t\phi \exp\left(\frac{-s^2}{2\sigma^2}\right) S_0^{(-\alpha_t\mu_t+1)} \gamma^{\frac{\alpha_t\mu_t}{2}-1}}{2\bar{\gamma}_t^{\frac{\alpha_t\mu_t}{2}}} \sum_{j=0}^{\infty} \frac{1}{j!}\Big(\frac{s^2 w_{z_{\mathrm{eq}}}^2}{8\sigma^4}\Big)^j \\ & \times H_{j+1,k+2}^{k+2,0}\left[\frac{B_t\gamma^{\frac{\alpha_t}{2}}}{S_0^{\alpha_t}\bar{\gamma}_t^{\frac{\alpha_t}{2}}}\middle| \begin{matrix}(1+\phi-\alpha\mu,1)^{j+1}\\ (0,1),(\phi-\alpha\mu,1)^{j+1}\end{matrix}\right] \end{aligned} \tag{4.60}$$

We use the PDF (4.60) in $\int_0^{\gamma} f_{\gamma}(z)dz$ and simplify the integral using the Mellin Barnes integral representation of the Fox's H-function to get the CDF:

$$\begin{aligned} F_{\gamma_t}(x) = {} & \frac{A_t\phi \exp\left(\frac{-s^2}{2\sigma^2}\right) S_0^{(-\alpha_t\mu_t+1)} \gamma^{\frac{\alpha_t\mu_t}{2}}}{2\bar{\gamma}_t^{\frac{\alpha_t\mu_t}{2}}} \sum_{j=0}^{\infty} \frac{1}{j!}\Big(\frac{s^2 w_{z_{\mathrm{eq}}}^2}{8\sigma^4}\Big)^j \\ & \times H_{j+1,j+3}^{k+2,1}\left[\frac{B_t\gamma^{\frac{\alpha_t}{2}}}{S_0^{\alpha_t}\bar{\gamma}_t^{\frac{\alpha_t}{2}}}\middle| \begin{matrix}\big(1-\frac{\alpha_t\mu_t}{2},\frac{\alpha_t}{2}\big),(1+\phi-\alpha\mu,1)^{j+1}\\ (0,1),(\phi-\alpha\mu,1)^{j+1},\big(-\frac{\alpha_t\mu_t}{2},\frac{\alpha_t}{2}\big)\end{matrix}\right] \end{aligned} \tag{4.61}$$

Note that the use of Meijer's G and Fox's H functions is common in the research fraternity and can be efficiently evaluated using built-in functions available in computational software such as MATLAB and MATHEMATICA. We capitalize results of (4.60) and (4.61) to present the PDF of SNR for the AF relaying in terms of bivariate Fox's H function.

Representing exponential and hypergeometric functions of (4.54) into Meijer's G-function

with à transformation of random variable $\gamma_r = \bar{\gamma}_r |h_f|^2$, we get

$$f_{\gamma_r}(x) = \frac{m_r^{m_r}\alpha_r}{2c_r^{\mu}\Gamma(\mu_r)(\mu\kappa_r + m_r)^{m_r}\bar{x}}\left(\frac{x}{\bar{\gamma}_r}\right)^{\frac{\alpha_r\mu_r}{2}-1} G_{0,1}^{1,0}\left(\frac{x^{\frac{\alpha_r}{2}}}{c\bar{\gamma}_r^{\frac{\alpha_r}{2}}}\middle|\begin{matrix}-\\0\end{matrix}\right) \times \frac{\Gamma(\mu_r)}{\Gamma(m_r)} G_{1,2}^{1,1}\left(\frac{-\mu_r\kappa_r x^{\frac{\alpha_r}{2}}}{c(\mu_r\kappa_r + m_r)\bar{\gamma}_r^{\frac{\alpha}{2}}}\middle|\begin{matrix}1-m_r\\0, 1-\mu_r\end{matrix}\right) \tag{4.62}$$

Substituting (4.60) and (4.62) in (4.57) and utilizing the integral representation of Fox's H-function with a change in the order of integration:

$$\begin{aligned} f_{\gamma}(\gamma) =& \frac{m_r^{m_r}\alpha_r\gamma^{\frac{\alpha_r\mu_r}{2}-1}}{2c^{\mu_r}(\mu_r\kappa_r + m_r)^{m_r}\bar{\gamma}_r\Gamma(m_r)\bar{\gamma}_r^{\frac{\alpha_r\mu_r}{2}-1}} \frac{A_t\phi\exp\left(\frac{-s^2}{2\sigma^2}\right)S_0^{(-\alpha_t\mu_t+1)}}{2\bar{\gamma}_t^{\frac{\alpha_t\mu_t}{2}}} \sum_{j=0}^{\infty}\frac{\Gamma(j+1)}{(j!)^2}\left(\frac{s^2 w_{z_{\text{eq}}}^2}{8\sigma^4}\right)^j \\ &\times \frac{1}{2\pi i}\int_{\mathcal{L}_1}\frac{\Gamma(0-u_1)\Gamma(0-u_1)\Gamma(m_r+u_1)}{\Gamma(\mu_r+u_1)}\left(\frac{-\mu_r\kappa_r\gamma^{\alpha_r}}{c^2(\mu_r\kappa_r+m_r)\bar{\gamma}_r^{\alpha_r}}\right)^{u_1}du_1 \\ &\times \frac{1}{2\pi i}\int_{\mathcal{L}_2}\frac{\Gamma(0-u_2)\Gamma(\phi-\alpha_t\mu_t-\alpha u_2)^{(j+1)}}{\Gamma(1+\phi-\alpha_t\mu_t-\alpha_t u_2)^{(j+1)}}\left(\frac{B_t}{S_0^{\alpha_t}\bar{\gamma}_t^{\frac{\alpha_t}{2}}}\right)^{u_2}du_2 I_2 \end{aligned} \tag{4.63}$$

where $\mathcal{L}_1$ and $\mathcal{L}_2$ denote the contour integrals. We use [168, (3.194/3)] and [168, (8.384/1)] to solve the inner integral I_2 in terms of the compatible Gamma function:

$$\int_0^{\infty}\left(\frac{\gamma+C}{x}\right)^{\left(\frac{\alpha_r\mu_r}{2}+\alpha_r u_1\right)}\gamma^{\frac{\alpha_t\mu_t+\alpha_t u_2}{2}-1}d\gamma = \frac{C^{\frac{\alpha_t\mu_t+\alpha_t u_2}{2}}\Gamma(\frac{-\alpha_t\mu_t-\alpha_t u_2}{2})\Gamma(\frac{-\alpha_r\mu_r-2\alpha_r u_1+\alpha_t\mu_t+\alpha_t u_2}{2})}{\Gamma(\frac{-\alpha_r\mu_r-2\alpha_r u_1}{2})} \tag{4.64}$$

Finally, we substitute (4.64) in (4.63), and to apply the definition of Fox's H function [178, (1.1)], we use $u_1 \to -u_1$ in (4.63) to get the PDF for fixed-gain relaying:

$$\begin{aligned} f_{\gamma}(\gamma) =& \frac{m_r^{m_r}\alpha_r C^{\frac{\alpha_t\mu_t}{2}}A_t\phi\exp\left(\frac{-s^2}{2\sigma^2}\right)S_0^{(-\alpha_t\mu_t+1)}\gamma^{\frac{\alpha_r\mu_r}{2}-1}}{4c^{\mu_r}(\mu_r\kappa_r+m_r)^{m_r}\Gamma(m_r)\bar{\gamma}_r^{\frac{\alpha_r\mu_r}{2}}\bar{\gamma}_t^{\frac{\alpha_t\mu_t}{2}}} \sum_{j=0}^{\infty}\frac{1}{j!}\left(\frac{s^2 w_{z_{\text{eq}}}^2}{8\sigma^4}\right)^j \\ &\times H_{1,0:3,2:j+1,j+3}^{0,1:1,2:j+3,0}\left[\frac{c^2(\mu_r\kappa_r+m_r)\bar{\gamma}_r^{\alpha_r}}{-\mu_r\kappa_r\gamma^{\alpha_r}}; \frac{B_t C^{\frac{\alpha_t}{2}}}{S_0^{\alpha_t}\bar{\gamma}_t^{\frac{\alpha_t}{2}}}\middle|\begin{matrix}V_1\\V_2\end{matrix}\right] \end{aligned} \tag{4.65}$$

where $V_1 = \left\{\left(1-\frac{\alpha_t\mu_t-\alpha_r\mu_r}{2}; \alpha_r, \frac{\alpha_t}{2}\right)\right\}; \left\{\left(1,1\right), \left(1,1\right), \left(\mu_r, 1\right)\right\}; \left\{\left(1+\phi-\alpha_t\mu_t, \alpha_t\right)^{j+1}\right\}$, and $V_2 = \left\{-\right\}; \left\{\left(m_r, 1\right), \left(1+\frac{\alpha_r\mu_r}{2}, \alpha_r\right)\right\}; \left\{\left(0,1\right), \left(\phi-\alpha_t\mu_t, \alpha_t\right)^{j+1}, \left(-\frac{\alpha_t\mu_t}{2}, \frac{\alpha_t}{2}\right)\right.$.

4.5.2 Outage Probability

Using (4.65) in $F_\gamma(\gamma) = \int_0^\gamma f_\gamma(z)dz$, and applying the definition of Fox's H function with the following inner integral

$$\int_0^\gamma z^{\frac{\alpha_r\mu_r}{2}-1} z^{-\alpha_r u_1} dz = \frac{z^{\frac{\alpha_r\mu_r}{2}} z^{-\alpha_r u_1} \Gamma\left(\frac{\alpha_r\mu_r - 2\alpha_r u_1}{2}\right)}{\Gamma\left(1+\frac{\alpha_r\mu_r-2\alpha_r u_1}{2}\right)} \tag{4.66}$$

we get the CDF as

$$\begin{aligned} F_\gamma(\gamma) = &\frac{m_r^{m_r}\alpha_r C^{\frac{\alpha_t\mu_t}{2}} A_t \phi \exp\left(\frac{-s^2}{2\sigma^2}\right) S_0^{(-\alpha_t\mu_t+1)} \gamma^{\frac{\alpha_r\mu_r}{2}}}{4c^{\mu_r}(\mu_r\kappa_r + m_r)^{m_r}\Gamma(m_r)\bar{\gamma}_r^{\frac{\alpha_r\mu_r}{2}}\bar{\gamma}_t^{\frac{\alpha_t\mu_t}{2}}} \sum_{j=0}^{\infty} \frac{1}{j!}\left(\frac{s^2 w_{z_{\text{eq}}}^2}{8\sigma^4}\right)^j \\ &\times H_{1,0:4,3:j+1,j+3}^{0,1:2,2:j+3,0}\left[\frac{c^2(\mu_r\kappa_r+m_r)\bar{\gamma}_r^{\alpha_r}}{-\mu_r\kappa_r\gamma^{\alpha_r}}; \frac{B_t C^{\frac{\alpha_t}{2}}}{S_0^{\alpha_t}\bar{\gamma}_t^{\frac{\alpha_t}{2}}}\middle| \begin{matrix} Q_1 \\ Q_2 \end{matrix}\right] \end{aligned} \tag{4.67}$$

where $Q_1 = \left\{\left(1-\frac{\alpha_t\mu_t-\alpha_r\mu_r}{2}; \alpha_r, \frac{\alpha_t}{2}\right)\right\}; \left\{\left(1,1\right), \left(1,1\right), \left(\mu_r, 1\right), \left(1+\frac{\alpha_r\mu_r}{2}, \alpha_r\right)\right\}; \left\{\left(1+\phi-\alpha_t\mu_t, \alpha_t\right)^{j+1}\right\}$, and $Q_2 = \left\{-\right\}; \left\{\left(m_r, 1\right), \left(\frac{\alpha_r\mu_r}{2}, \alpha_r\right), \left(1+\frac{\alpha_r\mu_r}{2}, \alpha_r\right)\right\}; \left\{\left(0,1\right), \left(\phi-\alpha_t\mu_t, \alpha_t\right)^{j+1}, \left(-\frac{\alpha_t\mu_t}{2}, \frac{\alpha_t}{2}\right)\right\}$.

To derive the asymptotic outage probability in the high SNR regime, we use [166, Theorems 1.7, 1.11] and compute residues of (4.67) for both contours $\mathcal{L}_1$ and $\mathcal{L}_2$ at poles $u_1 = 0, 0$, $\frac{-\alpha_r\mu_r+\alpha_t\mu_t+\alpha_t u_2}{2\alpha_r}$ and $s_2 = 0$, $-\mu_t$, and $\frac{\phi-\alpha_t\mu_t}{\alpha_t}$. Simplifying the derived residues, we present the asymptotic expression in (4.68). It should be emphasized that the consideration of all the poles may result into our asymptotic analysis close to the exact for a wide range of SNR. Further, it can be easily seen from (4.68) that the outage diversity order of the system is $\min\left\{\frac{\alpha_r\mu_r}{2}, \frac{\alpha_t\mu_t}{2}, \frac{\phi}{2}\right\}$. Note that the derived diversity order for the THz-RF can be confirmed individually with previous results on α-μ fading [186] and α-KMS [148].

4.5.3 Simulation and Numerical Results

We demonstrate the performance of the considered RF-THz wireless system and validate our derived analytical results using numerical analysis and Monte-Carlo simulations. To evaluate the analytical expressions, we use MATLAB implementation of bivariate Fox's H function [176], and take 10 terms for the convergence of infinite series. The bivariate Fox's H-function requires the computation of two contour integrals involving the ratio of the product of Gamma functions. We also compare the proposed method with the existing DF relaying for the RF-THz system with zero-boresight antenna misalignment errors [33, 186]. To compute the path gain of the RF link with antenna gain $G_r = 26$dBi, we use path loss $L_r(\text{dB}) = 32.4 + 17.3\log_{10}(d_2) + 20\log_{10}(10^{-9}f_r)$ [186], where d_r is taken in the range of 50m to 200m, and $f_r = 6$GHz is the carrier frequency of the RF. We compute path gain of THz link as $H_t = \frac{cG_t}{4\pi f_t d_t}\exp(-\frac{1}{2}kd_t)$, where $G_t = 55$dBi, $k = 2.8\times10^{-4}$ is the absorption coefficient [33], c is the speed of light, $f_t = 0.275$ THz, and $d_t = 50$m. We use [151] to compute the parameters of antenna misalignment errors with 10cm antenna aperture radius. A noise floor

$$\Psi^{\infty} = G_0\Bigg[G_1\bigg(\frac{-\mu_r\kappa_r\gamma^{\alpha_r}}{c^2(\mu_r\kappa_r+m_r)}\bigg)^{\frac{\alpha_t\mu_t}{2\alpha_r}-\frac{\mu_r}{2}}\bar{\gamma}_r^{-\frac{\alpha_t\mu_t}{2}} + G_2\Big(\frac{B_tC^{\frac{\alpha_t}{2}}}{S_0^{\alpha_t}\bar{\gamma}_t^{\frac{\alpha_t}{2}}}\Big)^{\frac{\phi-\alpha_t\mu_t}{\alpha_t}}\bigg(\frac{-\mu_r\kappa_r\gamma^{\alpha_r}}{c^2(\mu_r\kappa_r+m_r)}\bigg)^{\frac{\phi}{2\alpha_r}-\frac{\mu_r}{2}}\bar{\gamma}_r^{-\frac{\phi}{2}} + G_3\bar{\gamma}_r^{-\frac{\alpha_r\mu_r}{2}}\Bigg] \tag{4.68}$$

where $G_0 = \frac{m_r^{m_r}\alpha_r A_t\phi\exp\left(\frac{-s^2}{2\sigma^2}\right)S_0^{(-\alpha_t\mu_t+1)}\varphi}{4c^{\mu_r}(\mu_r\kappa_r+m_r)^{m_r}\Gamma(m_r)}\sum_{j=0}^{\infty}\frac{1}{j!}\left(\frac{s^2w_{z_{\text{eq}}}^2}{8\sigma^4}\right)^j$, $G_1 = \frac{\Gamma(\frac{\alpha_r\mu_r-\alpha_t\mu_t}{2\alpha_r})\Gamma(\frac{\alpha_r\mu_r-\alpha_t\mu_t}{2\alpha_r})\Gamma(m_r+\frac{-\alpha_r\mu_r+\alpha_t\mu_t}{2\alpha_r})\Gamma(\frac{-\alpha_t\mu_t}{2})C^{\frac{\alpha_t\mu_t}{2}}\zeta_1}{\Gamma(\mu_r+\frac{-\alpha_r\mu_r+\alpha_t\mu_t}{2\alpha_r})\Gamma(-\alpha_t\mu_t)\alpha_t\mu_t(\phi-\alpha_t\mu_t)^{(j+1)}\bar{\gamma}_t^{\frac{\alpha_t\mu_t}{2}}}$

$G_2 = \frac{\Gamma(\frac{\alpha_r\mu_r-\phi}{2\alpha_r})\Gamma(\frac{\alpha_r\mu_r-\phi}{2\alpha_r})\Gamma(m_r+\frac{-\alpha_r\mu_r\phi}{2\alpha_r})\Gamma(\frac{\alpha_t\mu_t-\phi}{\alpha_t})\Gamma(\frac{-\phi}{2})C^{\frac{\alpha_t\mu_t}{2}}\zeta_2}{\Gamma(\mu_r+\frac{-\alpha_r\mu_r+\phi}{2\alpha_r})\Gamma(-\phi)\phi\bar{\gamma}_t^{\frac{\alpha_t\mu_t}{2}}}$ $G_3 = \left(\frac{2C^{\frac{\alpha_t\mu_t}{2}}\zeta_3}{\bar{\gamma}_t^{\frac{\alpha_t\mu_t}{2}}}\right)\Bigg(\frac{\Gamma(\frac{-\alpha_r\mu_r+\alpha_t\mu_t}{2})\Gamma(m_r)\Gamma(\frac{-\alpha_t\mu_t}{2})}{\Gamma(\mu_r)\Gamma(\frac{-\alpha_r\mu_r}{2})\frac{\alpha_r\mu_r}{2}(\phi-\alpha_t\mu_t)^{(j+1)}} + \frac{\Gamma(m_r)\Gamma(\mu_t)}{\Gamma(\mu_r)\frac{\alpha_r\mu_r}{2}(\phi)^{(j+1)}}\left(\frac{B_tC^{\frac{\alpha_t}{2}}}{S_0^{\alpha_t}\bar{\gamma}_t^{\frac{\alpha_t}{2}}}\right)^{-\mu_t} + \frac{\Gamma(\frac{-\alpha_r\mu_r+\phi}{2})\Gamma(m_r)\Gamma(\frac{\alpha_t\mu_t-\phi}{\alpha_t})\Gamma(\frac{-\phi}{2})}{\Gamma(\mu_r)\Gamma(\frac{-\alpha_r\mu_r}{2})\frac{\alpha_r\mu_r}{2}}\left(\frac{B_tC^{\frac{\alpha_t}{2}}}{S_0^{\alpha_t}\bar{\gamma}_t^{\frac{\alpha_t}{2}}}\right)^{\frac{\phi-\alpha_t\mu_t}{\alpha_t}} + \frac{\Gamma(\frac{\mu_r}{2})\Gamma(m_r+\frac{-\mu_r}{2})\Gamma(\mu_t)C^{\frac{\alpha_t\mu_t}{2}}\zeta_4}{(\phi)^{(j+1)}\bar{\gamma}_t^{\frac{\alpha_t\mu_t}{2}}}\left(\frac{-\mu_r\kappa_r\gamma^{\alpha_r}}{c^2(\mu_r\kappa_r+m_r)}\right)^{\frac{-\mu_r}{2}}\left(\frac{B_tC^{\frac{\alpha_t}{2}}}{S_0^{\alpha_t}\bar{\gamma}_t^{\frac{\alpha_t}{2}}}\right)^{-\mu_t}\Bigg)$; $\Psi^{\infty} = P_{\text{out}}^{\infty}$ when $\varphi = \gamma_{\text{th}}^{\frac{\alpha_t\mu_t}{2}}$ and $\zeta_1 = \zeta_2 = \zeta_3 = \zeta_4 = 1$; $\Psi^{\infty} = \overline{BER}^{\infty}$ when $\varphi = \frac{q^{-(\frac{\alpha_r\mu_r}{2}+p)}}{2\Gamma(p)}$, $\zeta_1 = \Gamma\big(p+\frac{\alpha_r\mu_r}{2}\big)$, $\zeta_2 = \Gamma(p)$, $\zeta_3 = \Gamma\big(p+\frac{\alpha_t\mu_t}{2}\big)$, and $\zeta_4 = \Gamma\big(p+\frac{\phi}{2}\big)$.

of -170dBm/Hz is taken for both THz and RF systems with 10GHz and 20MHz as the signal bandwidth for THz and RF transmissions, respectively [175].

First, we illustrate the impact of multipath clustering on the THz link (i.e., μ_t) and the effect of non-zero boresight and jitter of antenna misalignment errors (i.e., σ_s and s) by plotting the outage probability versus average SNR of the RF link $\bar{\gamma}_r$, as depicted in Fig. 4.6. We consider α-KMS parameters as $\{\alpha_r = 1.8, \mu_r = 2, \kappa_r = 4, m_r = 2\}$. Fig. 4.6 shows that the outage probability improves with an increase in μ_t since the multipath clustering enhances channel conditions. Further, the figure shows that the effect of jitter is marginal at a lower $\mu_t = 1.2$ and low RF average SNR but incurs a penalty of almost 5 dB if σ_s is increased from 5 cm to 15cm at a higher $\mu_t = 2.4$ and outage probability 10^{-4}. It can also be seen from Fig. 4.6 that the non-zero values of boresight incurs higher antenna misalignment errors degrading the outage probability 5 times as compared to the zero-boresight at an average SNR of 40 dB. The figure also shows that fixed-gain AF relaying performs close to the DF without expensive decoding procedure and continuous monitoring of CSI in most of the scenarios.

We demonstrate the impact of various parameters on the outage probability for a better insight into system performance. Note that $\phi = 37$ when $\sigma_s = 5$ and cm) and $\phi = 4.1184$ when $\sigma_s = 15$ cm [151]. When $\mu_t = 1.2$, the outage diversity order is 0.9 since $\alpha_t\mu_t = 1.8$ is the minimum of $\alpha_r\mu_r = 3.6$ and $\phi = 4.1184$. Similarly, the diversity order becomes 1.8 when $\mu_t = 2.4$. Fig. 4.6 shows that there is a change in the slope of plots corresponding to $\mu_t = 1.2$ and $\mu_t = 2.4$, but there is no change in the slope when antenna misalignment error

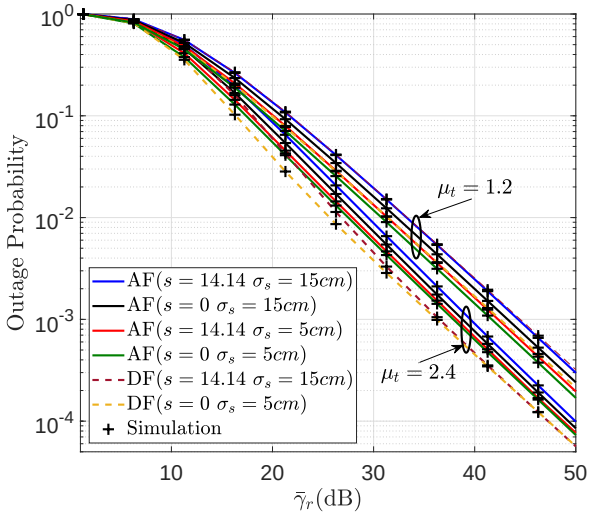

Figure 4.6: Outage probability performance of fixed-gain relay-assisted RF-THz wireless link over mixed fading with non-zero antenna misalignment errors at $\alpha_t = 1.5$, $\gamma_{\text{th}} = 4$ dB.

parameters are changed. Thus, the diversity order analysis provides a design consideration to use high beam-width to compensate for the effect of antenna misalignment errors. Thus, the proposed analysis provides an insight into the deployment scenarios for the mixed RF-THz relaying considering various system and channel configurations.

4.6 Integrated THz-RF Wireless Link: Multi-antenna Systems

Finally, we delve into the integrated THz-RF network, taking into consideration the deployment of multi-antenna base stations or access points (BS/AP) within the access network. The primary objective of this section is to illustrate how the performance is influenced by the presence of multiple antennas, while extending upon the findings from the preceding two sections of this chapter. It is important to note that channel fading has an impact on both RF and THz links, with the THz link experiencing higher attenuation. This challenge can be alleviated by reducing the distance of the THz link. Consequently, in order to establish efficient integrated F-THz transmission, it becomes imperative to boost the power level of the RF signal through the use of multiple antennas to make it comparable to the THz signal.

We consider a user in an access network that intends to transmit a signal to a destination point in the backhaul link through an AP equipped with multiple antennas ($N \geq 1$). In the first hop, the received signal vector $\mathbf{y}^{(R)}$ at the relay can expressed as

$$\mathbf{y}^{(R)} = H_r \mathbf{h}_\mathbf{r} s + w_r, \tag{4.69}$$

where is $\mathbf{y}^{(R)} = [Y_1^{(R)}, Y_2^{(R)}, \cdots, Y_N^R]^{\mathrm{T}}$ with $Y_i^{(R)}$ denoting the received signal at the i-th antenna, s is the transmitted signal from the source with power P, w_r is the additive white

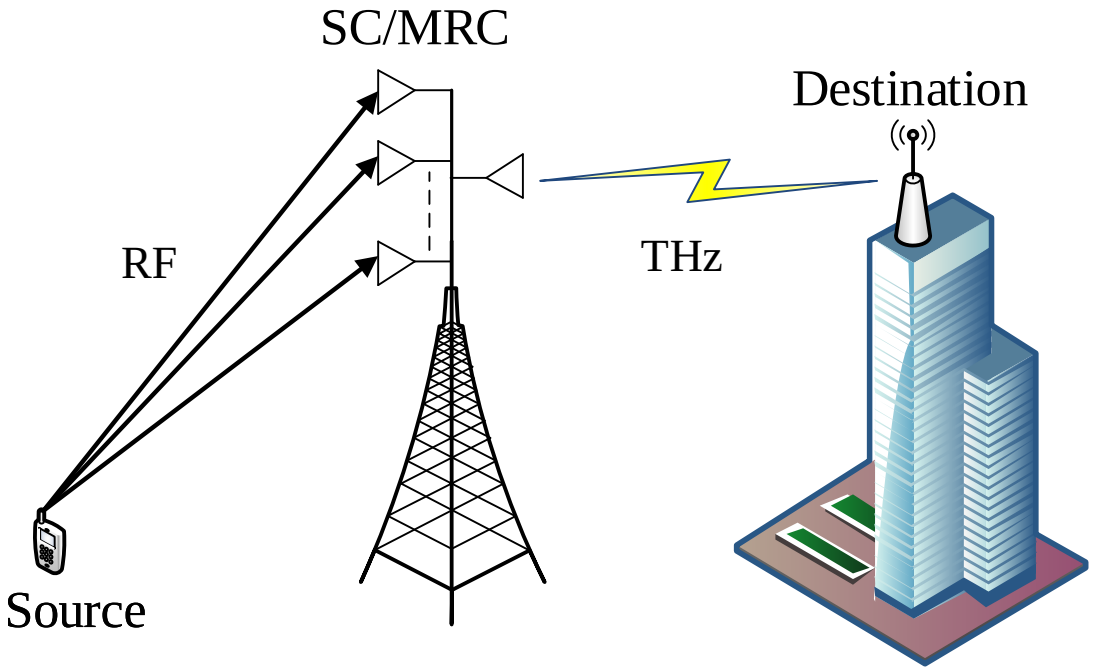

Figure 4.7: Hybrid multi-antenna RF and THz wireless transmission.

Gaussian noise (AWGN) signal with variance $\sigma^2_{w_r}$, H_r is the deterministic channel path-gain, and $\mathbf{h_r} = [h_1, h_2, \cdots, h_N]^{\mathrm{T}}$with h_i denoting the fading coefficient from the source to the i-th antenna at the relay. We use generalized α-μ distribution to model instantaneous SNR $\gamma_i = \frac{|H_r|^2|h_i|^2P}{\sigma^2_{w_r}}$ of the RF link from the source to the i-th antenna [104]:

$$f_{\gamma_i}(\gamma) = \frac{A_i \gamma^{\frac{\alpha_i\mu_i}{2}-1}}{2\bar{\gamma}_{\mathrm{RF}}^{\frac{\alpha_i\mu_i}{2}}} \exp\Big(- B_i \Big(\frac{\gamma}{\bar{\gamma}_{\mathrm{RF}}}\Big)^{\frac{\alpha_i}{2}}\Big) \tag{4.70}$$

where $A_i = \frac{\alpha_i \mu_i^{\mu_i}}{\Omega^{\alpha_i\mu_i}\Gamma(\mu_i)}$, $B_i = \frac{\mu_i}{\Omega^{\alpha_i}}$, $i = 1, 2, \cdots, N$, and $\{\alpha_i, \mu_i, \Omega_i\}$ are the channel fading parameters from the source to the i-th antenna of the RF link, and $\bar{\gamma}_{\mathrm{RF}}$ is the average SNR of the RF link. The α-μ distribution is a general fading model, which accounts for the non-linearity of a non-homogeneous propagation environment. The power parameter α represents the nonlinear characteristics of the fading and the parameter μ depicts number of multipath clusters. Using (4.70), the CDF of the SNR is given by

$$F_{\gamma_i}(\gamma) = 1 - \left(\frac{\Gamma\big(\mu_i, B_i\gamma^{\frac{\alpha_i}{2}}\big)}{\Gamma(\mu_i)\bar{\gamma}_{\mathrm{RF}}^{\frac{\alpha_i}{2}}}\right) \tag{4.71}$$

The THz band suffers from higher path losses due to molecular absorption at a lower wavelength. The path gain for the THz link is modeled by $H_t = \frac{cG_{\mathrm{THz}}}{4\pi f_{\mathrm{THz}} d_{\mathrm{THz}}} \exp(-\frac{1}{2}\kappa d_{\mathrm{THz}})$, where c, G_{THz}, f_{THz}, d_{THz} denotes the speed of light, antenna gain, carrier frequency, and link distance,

respectively. Here, κ is the absorption coefficient that depends on the temperature, relative humidity, and atmospheric pressure [34]. Further the THz suffers from antenna misalignment errors due to the misalignment between the transmitter and the receiver antenna. The PDF of the zero-boresight antenna misalignment errors given by [150]

$$f_{h_p}(h_p) = \frac{\phi^2}{S_0^{\phi^2}} h_p^{\phi^2-1}, 0 \leq h_p \leq S_0, \tag{4.72}$$

where the term S_0 denotes the fraction of collected power and ϕ denotes the ratio of normalized beam-width to jitter.

The THz also suffers from the channel fading along with the deterministic path loss and antenna misalignment errors. Despite these, the THz has emerged as a potential technology for backhaul link since it is immune to foggy and turbulent weather conditions (a limiting factor for FSO deployment) and fiber optics may not be suitable in difficult terrains. Recent research [20, 21, 26] clearly demonstrate the applicability of THz communication as a potential technology to transport the data from an AP or BS to the core network with multiple Gbps data rate transmission, which can be central to ubiquitous wireless communications in beyond-5G or 6G networks.

Recently, the authors in [153] have shown that α-μ distribution fits well at the THz frequencies using extensive measurement campaigns. Thus, we consider i.ni.d α-μ channel to model the fading for THz link with the PDF of the combined effect of channel fading and antenna misalignment errors [34][2]

$$f_{\gamma_{\mathrm{THz}}}(\gamma) = \frac{A\phi S_0^{-\phi} \gamma^{\frac{\phi}{2}-1}}{2\bar{\gamma}_{\mathrm{THz}}^{\frac{\phi}{2}}} \Gamma\left(\frac{\alpha\mu - \phi}{\alpha}, \frac{S_0^{-\alpha}\gamma^{\frac{\alpha}{2}}}{\bar{\gamma}_{\mathrm{THz}}^{\frac{\alpha}{2}}}\right) \tag{4.73}$$

where $\bar{\gamma}_{\mathrm{THz}} = \frac{P|H_t|^2}{\sigma_{w_t}^2}$ is the average SNR of the THz link, $A = \frac{\mu^{\frac{\phi}{\alpha}}}{\Omega^{\phi}\Gamma(\mu)}$, and $B = \frac{\mu}{\Omega^{\alpha}}$ with $\{\alpha, \mu, \Omega\}$ are the channel fading parameters from the AP to the destination.

The CDF of the THz link combined with antenna misalignment error for a general μ is given by [186]

$$F_{\gamma_{\mathrm{THz}}}(\gamma) = \frac{AB^{-\frac{\phi}{\alpha}}\phi}{\phi}\left[\gamma\left(\mu, \frac{B}{S_0^{\alpha}}\left(\sqrt{\frac{\gamma}{\bar{\gamma}_{\mathrm{THz}}}}\right)^{\alpha}\right) + \frac{B^{\frac{\phi}{\alpha}}}{S_0^{\phi}}\left(\sqrt{\frac{\gamma}{\bar{\gamma}_{\mathrm{THz}}}}\right)^{\phi} \times \Gamma\left(\frac{\alpha\mu-\phi}{\alpha}, \frac{B}{S_0^{\alpha}}\left(\sqrt{\frac{\gamma}{\bar{\gamma}_{\mathrm{THz}}}}\right)^{\alpha}\right)\right] \tag{4.74}$$

Finally, we employ a frequency up-converter to match the carrier frequency of the RF with the THz and a fixed gain AF relay to forward the signal from the source to the destination. Note that the noise power spectral density (PSD) for the THz link is higher (-74 dBm/Hz) than the

[2]There is a typo in the equation (26) of [34]. It should be $\gamma^2 A_0^{-\gamma^2} \frac{\mu^{\frac{\gamma^2}{\alpha}}}{\tilde{h}_f^{\phi}\Gamma(\mu)} x^{\gamma^2-1}\Gamma\left(\frac{\alpha\mu-\gamma^2}{\alpha}, \mu\frac{x^{\alpha}}{\tilde{h}_f^{\alpha}}A_0^{-\alpha}\right)$.

RF (-101 dBm/Hz) [175].

The end-to-end SNR for the AF relaying system is given by $\gamma = \frac{\gamma_{\rm RF}\gamma_{\rm THz}}{\gamma_{\rm THz}+C}$ where C can be obtained statistically from the received signal of the RF link and transmit power at the relay. Given the PDF of SNR for individual links as $f_{\gamma_{\rm RF}}(\gamma)$ and $f_{\gamma_{\rm THz}}(\gamma)$, the PDF of the end-to-end SNR γ for the dual-hop system can be represented as [187]

$$f_{\gamma}(z) = \int_0^{\infty} f_{\gamma_{\rm RF}}\left(\frac{z(x+C)}{x}\right) f_{\gamma_{\rm THz}}(x)\frac{x+C}{x}dx \tag{4.75}$$

Similarly, the CDF of the end-to-end system using the CDF of individual links $F_{\gamma_{\rm RF}}(\gamma)$ and $F_{\gamma_{\rm THz}}(\gamma)$ is [187]:

$$F_{\gamma}(\gamma) = F_{\gamma_{\rm RF}}(\gamma) + \int_{\gamma}^{\infty} F_{\gamma_{\rm THz}}\big(\frac{C\gamma}{x-\gamma}\big) f_{\gamma_{\rm RF}}(x)dx \tag{4.76}$$

In the following sections, we derive the PDF of the RF link denoted as $f_{\gamma_{\rm RF}}(\gamma)$ using both SC and MRC diversity techniques to develop statistical results on the end-to-end SNR using the general representation in (4.75) and (4.76).

4.7 Performance of SC-RF and THz

In this section, we employ selection combining diversity receiver for the multi-antenna RF and study the performance when mixed with the THz wireless link using the fixed-gain AF relaying. Denote by γ_i, where $i = 1, 2, \cdots N$ the SNR between the source and the i-th antenna using RF transmission in the first hop. The selection combining opportunistically selects a single antenna with maximum SNR to harness the spatial diversity. Thus, the SNR in the first link using the selection combining is given as $\gamma_{\rm RF} = \max(\gamma_1, \gamma_2, ...\gamma_N)$. Assuming independent but non-identical fading, the CDF $F_{\gamma_{\rm RF}}(\gamma)$ of the end-to-end SNR of the first link is given by $F_{\gamma_{\rm RF}}(\gamma) = \prod_{i=1}^{N} F_{\gamma_i}(\gamma)$, where $F_{\gamma_i}(\gamma)$ can be obtained from (4.71). Assuming identical fading characteristics among multi-antenna system (which is a reasonable assumption and has been widely considered in the literature), the CDF of the first link can be expressed as

$$F_{\gamma_{\rm RF}}(\gamma) = [F_{\gamma_i}(\gamma)]^N \tag{4.77}$$

Substituting (4.77) in (4.76), we can develop the CDF of the mixed link using multivariate Fox's-H function. In the following Theorem, we develop novel statistical results on the mixed link using bivariate Fox's H-function.

Theorem 4.5. *The PDF and CDF of end-to-end SNR of the RF link with selection combining mixed with THz using the fixed-gain AF relay is given in* (4.78) *and* (4.79)*, respectively.*

Proof. See Appendix 4.6. ■

Note that computation of the bivariate Fox's H-function is available in MATHEMATICA

$$f_{\gamma}^{\mathrm{SC}}(z)=\frac{NAA_i\phi S_0^{-\alpha\mu}C^{\frac{\alpha\mu}{2}}}{2\alpha^2\bar{\gamma}_{\mathrm{RF}}^{\frac{\alpha_i\mu_i}{2}}\bar{\gamma}_{\mathrm{THz}}^{\frac{\alpha\mu}{2}}}\sum_{k_0+k_1+\cdots+k_{\mu_i-1}=N-1}\binom{N-1}{k_0+k_1+\cdots+k_{\mu_i-1}}\prod_{t=o}^{\mu_i-1}\frac{B^{k_t}(z)^{(\sum_{t=0}^{\mu_i-1}\frac{t\alpha_ik_t}{2}+\frac{\alpha_i\mu_i}{2}-1)}}{(t!)^{k_t}\bar{\gamma}_{\mathrm{RF}}^{(\frac{t\alpha_ik_t}{2})}}$$
$$H_{1,0:1,1:2,4}^{0,1:0,1:3,1}\left[\begin{matrix}\{\big(1-\frac{\alpha\mu}{2}+\sum_{t=0}^{\mu_i-1}\frac{t\alpha_ik_t}{2}+\frac{\alpha_i\mu_i}{2};\frac{\alpha_i}{2},\frac{\alpha}{2}\big)\};\{\big(1,1\big)\};\{\big(1-\mu,1\big),\big(1-\mu+\frac{\phi}{\alpha},1\big)\}\\ \{-\};\{\big(1+\sum_{t=0}^{\mu_i-1}\frac{t\alpha_ik_t}{2}+\frac{\alpha_i\mu_i}{2},\frac{\alpha_i}{2}\big)\};\{\big(-\mu+\frac{\phi}{\alpha},1\big),\big(0,1\big),\big(-\frac{\alpha\mu}{2},\frac{\alpha}{2}\big)\big(-\mu,1\big)\}\end{matrix}\middle|\frac{\bar{\gamma}_{\mathrm{RF}}^{\frac{\alpha_i}{2}}}{Nz^{\frac{\alpha_i}{2}}B_i};\frac{BC^{\frac{\alpha}{2}}}{S_o^{\alpha}\bar{\gamma}_{\mathrm{THz}}^{\frac{\alpha}{2}}}\right] \tag{4.78}$$

$$F_{\gamma}^{\mathrm{SC}}(\gamma)=\frac{NAA_i\phi S_0^{-\alpha\mu}C^{\frac{\alpha\mu}{2}}}{2\alpha^2\bar{\gamma}_{\mathrm{RF}}^{\frac{\alpha_i\mu_i}{2}}\bar{\gamma}_{\mathrm{THz}}^{\frac{\alpha\mu}{2}}}\sum_{k_0+k_1+\cdots+k_{\mu_i-1}=N-1}\binom{N-1}{k_0+k_1+\cdots+k_{\mu_i-1}}\prod_{t=o}^{\mu_i-1}\frac{B^{k_t}(\gamma)^{(\sum_{t=0}^{\mu_i-1}\frac{t\alpha_ik_t}{2}+\frac{\alpha_i\mu_i}{2})}}{(t!)^{k_t}\bar{\gamma}_{\mathrm{RF}}^{(\frac{t\alpha_ik_t}{2})}}$$
$$H_{1,0:2,2:2,4}^{0,1:1,1:3,1}\left[\begin{matrix}\{(1-\frac{\alpha\mu}{2}+\sum_{t=0}^{\mu_i-1}\frac{t\alpha_ik_t}{2}+\frac{\alpha_i\mu_i}{2};\frac{\alpha_i}{2},\frac{\alpha}{2})\};\{(1,1),(1+\sum_{t=0}^{\mu_i-1}\frac{t\alpha_ik_t}{2}+\frac{\alpha_i\mu_i}{2},\frac{\alpha_i}{2})\};\{(1-\mu,1),(1-\mu+\frac{\phi}{\alpha},1)\}\\ \{-\};\{(\sum_{t=0}^{\mu_i-1}\frac{t\alpha_ik_t}{2}+\frac{\alpha_i\mu_i}{2},\frac{\alpha_i}{2}),(1+\sum_{t=0}^{\mu_i-1}\frac{t\alpha_ik_t}{2}+\frac{\alpha_i\mu_i}{2},\frac{\alpha_i}{2})\};\{(-\mu+\frac{\phi}{\alpha},1),(0,1),(-\frac{\alpha\mu}{2},\frac{\alpha}{2})(-\mu,1)\}\end{matrix}\middle|\frac{\bar{\gamma}_{\mathrm{RF}}^{\frac{\alpha_i}{2}}}{N\gamma^{\frac{\alpha_i}{2}}B_i};\frac{BC^{\frac{\alpha}{2}}}{S_o^{\alpha}\bar{\gamma}_{\mathrm{THz}}^{\frac{\alpha}{2}}}\right] \tag{4.79}$$

and MATLAB. In the following subsections, we use the statistical result of Theorem 4.5 to analyze the performance of the mixed RF-THz system.

4.7.1 Outage Probability

Outage probability is an important performance metric that describes the reliability of a communication system by comparing the received SNR with a threshold SNR γ_{th}: $P_{\mathrm{out}}=P(\gamma<\gamma_{th})$. We can get an exact expression of the outage probability by substituting $\gamma=\gamma_{\mathrm{th}}$ in the CDF (4.79) in terms of bivariate Fox's H-function. We also simplify the expression of the outage probability in high SNR regime by deriving $\lim_{\bar{\gamma}\to\infty}P_{\mathrm{out}}$, where $\bar{\gamma}=\bar{\gamma}_{\mathrm{RF}}=\bar{\gamma}_{\mathrm{THz}}$. We apply [166, Th. 1.7, 1.11] by calculating residues at poles $S_1=\frac{\alpha\mu-\sum_{t=0}^{\mu_i-1}t\alpha_ik_t-\alpha_i\mu_i+\alpha S_2}{\alpha_i},0$ and $S_2=\frac{-\alpha\mu+\sum_{t=0}^{\mu_i-1}t\alpha_ik_t+\alpha_i\mu_i}{\alpha},-\mu+\frac{\phi}{\alpha},0,-\mu$ to get the asymptotic outage probability in (4.81). Applying $\bar{\gamma}_{\mathrm{RF}}\to\infty$ and $\bar{\gamma}_{\mathrm{THz}}\to\infty$ in (4.81), the diversity order can be obtained as

$$DO^{\mathrm{SC}}=\left\{\frac{\alpha_i\mu_i}{2},\frac{\phi-\sum_{t=0}^{\mu_i-1}t\alpha_ik_t}{2},\frac{\alpha\mu-\sum_{t=0}^{\mu_i-1}t\alpha_ik_t}{2},\frac{-\sum_{t=0}^{\mu_i-1}t\alpha_ik_t}{2}\right\} \tag{4.80}$$

The diversity order in (4.80) is applicable for i.i.d fading scenario for multi-antenna RF transmissions with an implicit presence of spatial diversity parameter N. to To derive the diversity order for the general scenario, we can directly use (4.76) with asymptotic expansion of incomplete gamma function. We use (4.71) in $F_{\gamma_{\mathrm{RF}}}(\gamma)=\prod_{i=1}^{N}F_{\gamma_i}(\gamma)$ and apply the asymptotic expression of $\lim_{t\to0}\gamma(a,t)=t^a/a$ [182] with the identity $\Gamma(a,t)=\Gamma(a)-\gamma(a,t)$ to get the diversity order of the RF ink as $\frac{1}{2}\sum_{i=1}^{N}\alpha_i\mu_i$. Substituting (4.71) and (4.74) in $\int_{\gamma}^{\infty}F_{\gamma_{\mathrm{THz}}}\big(\frac{C\gamma}{t-\gamma}\big)f_{\gamma_{\mathrm{RF}}}(t)dt$ with $\lim_{t\to\infty}\Gamma(a,t)=e^{-t}t^{a-1}$ and $\lim_{t\to0}\gamma(a,t)=t^a/a$, the integral can be simplified as $\min\big\{\frac{\alpha\mu}{2},\frac{\phi}{2}\big\}$. Thus, the diversity order of the RF-THz is given by $\min\big\{\frac{\sum_{i=1}^{N}\alpha_i\mu_i}{2},\frac{\alpha\mu}{2},\frac{\phi}{2}\big\}$.

The diversity order provides an important insight on the system deployment: the performance of the hybrid system can be made independent from RF fading and antenna misalignment errors by employing a sufficient number of antennas for RF reception and higher beam-width

$$P_{\text{out}}^{\text{SC},\infty} = \frac{NAA_i\phi S_0^{-\alpha\mu}C^{\frac{\alpha\mu}{2}}}{2\alpha^2\bar{\gamma}^{\frac{\alpha_i\mu_i}{2}}\bar{\gamma}^{\frac{\alpha\mu}{2}}} \sum_{k_0+k_1+\cdots+k_{\mu_i-1}=N-1} \binom{N-1}{k_0+k_1+\cdots+k_{\mu_i-1}} \prod_{t=o}^{\mu_i-1} \frac{B_i^{k_t}(\gamma)^{(\sum_{t=0}^{\mu_i-1}\frac{t\alpha_i k_t}{2}+\frac{\alpha_i\mu_i}{2})}}{(t!)^{k_t}\bar{\gamma}^{(\frac{t\alpha_i k_t}{2})}}$$
$$\times \Bigg[\Bigg(\frac{\Gamma\big(\frac{\sum_{t=0}^{\mu_i-1} t\alpha_i k_t+\alpha_i\mu_i}{2}\big)\Gamma\big(\frac{\alpha\mu-\sum_{t=0}^{\mu_i-1} t\alpha_i k_t-\alpha_i\mu_i}{\alpha}\big)}{\Gamma\big(\frac{2+\sum_{t=0}^{\mu_i-1} t\alpha_i k_t+\alpha_i\mu_i}{2}\big)\big(\frac{\phi-\sum_{t=0}^{\mu_i-1} t\alpha_i k_t-\alpha_i\mu_i}{\alpha}\big)\big(\frac{\sum_{t=0}^{\mu_i-1} t\alpha_i k_t+\alpha_i\mu_i}{\alpha}\big)} \Big(\frac{BC^{\frac{\alpha}{2}}}{S_o^{\alpha}\bar{\gamma}^{\frac{\alpha}{2}}}\Big)^{\frac{-\alpha\mu+\sum_{t=0}^{\mu_i-1} t\alpha_i k_t+\alpha_i\mu_i}{\alpha}}$$
$$+ \frac{\Gamma\big(\frac{-\sum_{t=0}^{\mu_i-1} t\alpha_i k_t-\alpha_i\mu_i+\phi}{2}\big)\Gamma\big(\sum_{t=0}^{\mu_i-1}\frac{t\alpha_i k_t+\alpha_i\mu_i}{2}\big)}{\Gamma\big(\frac{-\sum_{t=0}^{\mu_i-1} t\alpha_i k_t-\alpha_i\mu_i}{2}\big)\Gamma\big(\frac{2+\sum_{t=0}^{\mu_i-1} t\alpha_i k_t+\alpha_i\mu_i}{2}\big)} \frac{\Gamma(\mu-\frac{\phi}{\alpha})\Gamma(\frac{\phi}{2})}{(\frac{\phi}{\alpha})} \Big(\frac{BC^{\frac{\alpha}{2}}}{S_o^{\alpha}\bar{\gamma}^{\frac{\alpha}{2}}}\Big)^{-\mu+\frac{\phi}{\alpha}}$$
$$+ \frac{\Gamma\big(\frac{\alpha\mu-\sum_{t=0}^{\mu_i-1} t\alpha_i k_t-\alpha_i\mu_i}{2}\big)\Gamma\big(\sum_{t=0}^{\mu_i-1}\frac{t\alpha_i k_t+\alpha_i\mu_i}{2}\big)}{\Gamma\big(\frac{-\sum_{t=0}^{\mu_i-1} t\alpha_i k_t-\alpha_i\mu_i}{2}\big)\Gamma\big(\frac{2+\sum_{t=0}^{\mu_i-1} t\alpha_i k_t+\alpha_i\mu_i}{2}\big)} \frac{\Gamma(\frac{-\alpha\mu}{2})}{(\mu+\frac{\phi}{\alpha})(\mu)} + \frac{\Gamma\big(\sum_{t=0}^{\mu_i-1}\frac{t\alpha_i k_t+\alpha_i\mu_i}{2}\big)}{\Gamma\big(\frac{2+\sum_{t=0}^{\mu_i-1} t\alpha_i k_t+\alpha_i\mu_i}{2}\big)} \frac{\Gamma(\mu)}{(\frac{\phi}{\alpha})} \Big(\frac{BC^{\frac{\alpha}{2}}}{S_o^{\alpha}\bar{\gamma}^{\frac{\alpha}{2}}}\Big)^{-\mu} \Bigg) \Big(\bar{\gamma}^{-\frac{\alpha_i\mu_i}{2}}\Big)$$
$$+ \Bigg(\frac{\Gamma\big(\frac{\sum_{t=0}^{\mu_i-1} t\alpha_i k_t+\alpha_i\mu_i-\phi}{\alpha_i}\big)\Gamma(\frac{\phi}{2})}{\Gamma(-\frac{\phi}{2})\Gamma(\frac{2+\phi}{2})} \Big(\frac{N\gamma^{\frac{\alpha_i}{2}}B_i}{\bar{\gamma}^{\frac{\alpha_i}{2}}}\Big)^{\frac{-\sum_{t=0}^{\mu_i-1} t\alpha_i k_t-\alpha_i\mu_i+\phi}{\alpha_i}} \frac{\Gamma(\frac{\phi}{\alpha})\Gamma(\frac{\phi}{2})}{(\frac{\phi}{\alpha})} \Big(\frac{BC^{\frac{\alpha}{2}}}{S_o^{\alpha}\bar{\gamma}^{\frac{\alpha}{2}}}\Big)^{-\mu+\frac{\phi}{\alpha}} \Bigg) \Big(\bar{\gamma}^{\frac{\sum_{t=0}^{\mu_i-1} t\alpha_i k_t}{2}}\bar{\gamma}^{-\frac{\phi}{2}}\Big)$$
$$+ \Bigg(\frac{\Gamma\big(\frac{-\alpha\mu+\sum_{t=0}^{\mu_i-1} t\alpha_i k_t+\alpha_i\mu_i}{\alpha_i}\big)\Gamma(\frac{\alpha\mu}{2})}{\Gamma(\frac{-\alpha\mu}{2})\Gamma(\frac{2+\alpha\mu}{2})} \Big(\frac{N\gamma^{\frac{\alpha_i}{2}}B_i}{\bar{\gamma}^{\frac{\alpha_i}{2}}}\Big)^{\frac{\alpha\mu-\sum_{t=0}^{\mu_i-1} t\alpha_i k_t-\alpha_i\mu_i}{\alpha_i}} \frac{\Gamma(\frac{-\alpha\mu}{2})}{(-\mu+\frac{\phi}{\alpha})(\mu)} \Bigg) \Big(\bar{\gamma}^{-\frac{\alpha\mu}{2}}\bar{\gamma}^{\frac{\sum_{t=0}^{\mu_i-1} t\alpha_i k_t}{2}}\Big)$$
$$+ \Bigg(\Gamma\Big(\frac{\sum_{t=0}^{\mu_i-1} t\alpha_i k_t+\alpha_i\mu_i}{\alpha_i}\Big) \Big(\frac{N\gamma^{\frac{\alpha_i}{2}}B_i}{\bar{\gamma}^{\frac{\alpha_i}{2}}}\Big)^{\frac{-\sum_{t=0}^{\mu_i-1} t\alpha_i k_t-\alpha_i\mu_i}{\alpha_i}} \frac{\Gamma(\mu)}{(\frac{\phi}{\alpha})} \Big(\frac{BC^{\frac{\alpha}{2}}}{S_o^{\alpha}\bar{\gamma}^{\frac{\alpha}{2}}}\Big)^{-\mu} \Bigg) \Big(\bar{\gamma}^{\frac{\sum_{t=0}^{\mu_i-1} t\alpha_i k_t}{2}}\Big) \Bigg] \tag{4.81}$$

for THz transmissions.

4.8 Performance of MRC-RF and THz

In this section, we analyze the performance of the hybrid system by employing the optimal MRC diversity technique, which combines coherently the received signals at N-antennas. Thus, $\gamma_{\text{RF}} = \sum_{i=1}^{N}\gamma_i$ is the resultant SNR of the RF link after the MRC. It should be noted that performance analysis can also be carried out when equal-gain combining (EGC) based multi-antenna diversity technique is applied for the RF using the SNR $\gamma_{\text{RF}} = \frac{1}{N}\Big(\sum_{i=1}^{N}\sqrt{\gamma_i}\Big)^2$. In the following theorem, we derive the exact PDF and CDF of the SNR for the hybrid system consisting of the MRC-RF and THz:

Theorem 4.6. *The exact PDF and CDF of end-to-end SNR of the RF link with the MRC mixed with THz using the fixed-gain AF relay in terms of $N+1$ variate Fox's H-function is given by:*

$$f_{\gamma}^{\text{MRC}}(\gamma) = \prod_{i=1}^{N} \frac{A_i\gamma^{\left(\sum_{i=1}^{N}\frac{\alpha_i\mu_i}{2}-1\right)}A\phi S_0^{-\alpha\mu}C^{\frac{\alpha\mu}{2}}}{2\bar{\gamma}_{\text{RF}}^{\frac{\alpha_i\mu_i}{2}}\alpha^2\bar{\gamma}_{\text{THz}}^{\frac{\alpha\mu}{2}}} H_{2,1;1,1;\cdots;1,1;2,4}^{0,1;1,1;\cdots;1,1;3,1}\left[\begin{matrix}\left\{\frac{\bar{\gamma}_{\text{rf}}^{\frac{\alpha_i}{2}}}{B_i\gamma^{\frac{\alpha_i}{2}}}\right\}_{i=1}^{N} \\ \frac{BC^{\frac{\alpha}{2}}}{S_o^{\alpha}\bar{\gamma}_{\text{THz}}^{\frac{\alpha}{2}}}\end{matrix}\middle|\begin{matrix}U_3 \\ V_3\end{matrix}\right] \tag{4.82}$$

where $U_3 = \Big\{\Big(1-\frac{\alpha\mu}{2}+\sum_{i=1}^{N}\frac{\alpha_i\mu_i}{2};\frac{\alpha_1}{2},\cdots,\frac{\alpha_i}{2},\frac{\alpha}{2}\Big);\Big(\sum_{i=1}^{N}\frac{\alpha_i\mu_i}{2};\frac{\alpha_1}{2},\cdots,\frac{\alpha_i}{2},0\Big)\Big\}:\big\{(1,1),\cdots,(1,1)_N\big\};\big\{\big(1-\mu,1\big),\big(1-\mu=\frac{\phi}{\alpha},1\big)\big\}$, *and* $V_3 = \Big\{\Big(1+\sum_{i=1}^{N}\frac{\alpha_i\mu_i}{2};\frac{\alpha_1}{2},\cdots,\frac{\alpha_i}{2},0\Big)\Big\}:\Big\{\Big(\frac{\alpha_1\mu_1}{2},\frac{\alpha_1}{2}\Big),\cdots,\Big(\frac{\alpha_i\mu_i}{2},\frac{\alpha_i}{2}\Big)\Big\};\Big\{\big(-\mu+\frac{\phi}{\alpha},1\big),\big(0,1\big),\big(-\mu,1\big),\big(\frac{-\alpha\mu}{2},\frac{\alpha}{2}\big)\Big\}$.

$$F_{\gamma}^{\mathrm{MRC}}(\gamma)=\prod_{i=1}^{N}\frac{A_i\gamma^{\left(\sum_{i=1}^{N}\frac{\alpha_i\mu_i}{2}\right)}A\phi S_0^{-\alpha\mu}C^{\frac{\alpha\mu}{2}}}{2\bar{\gamma}_{\mathrm{RF}}^{\frac{\alpha_i\mu_i}{2}}\alpha^2\bar{\gamma}_{\mathrm{THz}}^{\frac{\alpha\mu}{2}}}H_{3,1;1,1;\cdots;1,1;2,4}^{0,1;1,1;\cdots;1,1;3,1}\left[\begin{array}{c|c}\left\{\frac{\frac{\alpha_i}{2}}{\bar{\gamma}_{\mathrm{RF}}^{\frac{\alpha_i}{2}}B_i\gamma^{\frac{\alpha_i}{2}}}\right\}_{i=1}^{N} & U_4\\ \frac{BC^{\frac{\alpha}{2}}}{S_o^{\alpha}\bar{\gamma}_{\mathrm{THz}}^{\frac{\alpha}{2}}} & V_4\end{array}\right] \tag{4.83}$$

where $U_4=\Big\{\Big(1-\frac{\alpha\mu}{2}+\frac{\sum_{i=1}^{N}\alpha_i\mu_i}{2};\frac{\alpha_1}{2},\cdots,\frac{\alpha_i}{2},\frac{\alpha}{2}\Big);\Big(\frac{\sum_{i=1}^{N}\alpha_i\mu_i}{2};\frac{\alpha_1}{2},\cdots,\frac{\alpha_i}{2},0\Big);\Big(\frac{\sum_{i=1}^{N}\alpha_i\mu_i}{2};\frac{\alpha_1}{2},\cdots,\frac{\alpha_i}{2},0\Big)\Big\}:\big\{(1,1),\cdots,(1,1)_N\big\};\big\{\big(1-\mu,1\big),\big(1-\mu-\frac{\phi}{\alpha},1\big)\big\}$ *and* $V_4=\Big\{\Big(1+\sum_{i=1}^{N}\frac{\alpha_i\mu_i}{2};\frac{\alpha_1}{2},\cdots,\frac{\alpha_i}{2},0\Big)\Big\}:\Big\{\Big(\frac{\alpha_1\mu_1}{2},\frac{\alpha_1}{2}\Big),\cdots,\Big(\frac{\alpha_i\mu_i}{2},\frac{\alpha_i}{2}\Big)\Big\};\Big\{\big(-\mu+\frac{\phi}{\alpha},1\big),\big(0,1\big),\big(-\mu,1\big),\big(\frac{-\alpha\mu}{2},\frac{\alpha}{2}\big)\Big\}$.

Proof. See Appendix 4.7. ■

The diversity order for the outage probability can be computed using the residue of the multivariate Fox's H-function at dominant poles with a specific representation [166], [172]. However, the multivariate Fox's H-function in (4.83) consists of N variables with average SNR $\bar{\gamma}_{\mathrm{RF}}$ in the numerator, while the $N+1$-th variable contains the average SNR $\bar{\gamma}_{\mathrm{THz}}$ in the denominator, precluding the direct application of [172] for the asymptotic analysis. In the following lemma, we present the diversity order of the considered hybrid system:

Lemma 4.3. *The diversity order of the RF link with the MRC receiver mixed with the THz over i.ni.d channel fading is:*

$$DO^{\mathrm{MRC}}=\min\left\{\frac{\sum_{i=1}^{N}\alpha_i\mu_i}{2},\frac{\alpha\mu}{2},\frac{\phi}{2}\right\} \tag{4.84}$$

Proof. We decompose the analysis in two parts: applying $\bar{\gamma}_{\mathrm{THz}}\to\infty$ in (4.83) for the first N-variables to get dominant poles as $p_i=\frac{\alpha_i\mu_i}{2}$, $i=1,2,\cdots,N$ and $\bar{\gamma}_{\mathrm{RF}}\to 0$ in (4.83) to get $N+1$-th pole as $p_{N+1}=\min\{\frac{\alpha\mu}{2},\frac{\phi}{2}\}$. Computing residues of (4.83) at these poles, we get

$$\begin{aligned}P_{\mathrm{out}}^{\mathrm{MRC},\infty}=&\prod_{i=1}^{N}\frac{2A_iA\phi C^{\frac{\alpha\mu}{2}}}{\alpha_i^2\alpha^3B_i^{\mu_i}B^{\mu}}\frac{\Gamma(p_1+\cdots+p_N)}{\Gamma(p_1+\cdots+p_N)\Gamma(-p_1-\cdots-p_N)\Gamma(-p_1-\cdots-p_N)}\\&\Gamma\Big(1+\mu_i+\frac{2}{\alpha_i}p_i\Big)\Big(\frac{\bar{\gamma}_{\mathrm{RF}}}{B_i^{\frac{2}{\alpha_i}}\gamma_{\mathrm{th}}}\Big)^{-p_i}\frac{\Gamma(\frac{\phi}{\alpha}-\frac{2}{\alpha}p_{N+1})\Gamma(\mu-\frac{2}{\alpha}p_{N+1})\Gamma(-\frac{2}{\alpha}p_{N+1})\Gamma(\frac{2}{\alpha}p_{N+1})}{\Gamma(1-\frac{\phi}{\alpha}-\frac{2}{\alpha}p_{N+1})\Gamma(1+p_{N+1})}\\&\Big(\frac{B^{\frac{2}{\alpha}}C}{S_0^2\bar{\gamma}_{\mathrm{THz}}}\Big)^{p_{N+1}}\end{aligned} \tag{4.85}$$

Using $\bar{\gamma}=\bar{\gamma}_{\mathrm{RF}}=\bar{\gamma}_{\mathrm{THz}}$ and combining the exponents of $\bar{\gamma}$ in (4.85), we get the diversity order of the system, as given in (4.84). ■

Further, we can use the statistical results of Theorem (4.6) to derive the average BER and ergodic capacity of the hybrid system, however, in terms of $N+1$ variate Fox's H-function.

It is desirable to simplify the analysis and reduce the dimension of the Fox's H-function. The authors in [188] have shown that the sum of α-μ variates can be accurately approximated by a single α-μ distribution [189–192]. Hence, we use [188] to simplify the statistical performance of the hybrid RF-THz system.

We use (4.70) in $\gamma_{\rm RF} = \sum_{i=1}^{N} \gamma_i$ to get the PDF of the SNR for the first link as

$$f_{\gamma_{\rm RF}}(\gamma) \approx \frac{A_m \gamma^{\frac{\alpha_m \mu_m}{2}-1}}{2\bar{\gamma}_{\rm RF}^{\frac{\alpha_m \mu_m}{2}}} \exp\left(- B_m \Big(\sqrt{\frac{\gamma}{\bar{\gamma}_{\rm RF}}}\Big)^{\alpha_m}\right) \tag{4.86}$$

where $A_m = \frac{\alpha_m \mu_m^{\mu_m}}{\Omega^{\alpha_m \mu_m}\Gamma(\mu_m)}$, $B_m = \frac{\mu_m}{\Omega^{\alpha_m}}$, and $\{\alpha_m, \mu_m, \Omega_m\}$ can be obtained by moment matching method [188]. Using Meijer's G-representation of exponential function, we can express the PDF of SNR of the RF link $f_{\gamma_{\rm RF}}(\gamma)$ in (4.86) as

$$f_{\gamma_{\rm RF}}(\gamma) \approx \frac{A_m \gamma^{\frac{\alpha_m \mu_m}{2}-1}}{2\bar{\gamma}_{\rm RF}^{\frac{\alpha_m \mu_m}{2}}} G_{0,1}^{1,0}\left(\frac{B_m \gamma^{\frac{\alpha_m}{2}}}{\bar{\gamma}_{\rm RF}^{\frac{\alpha_m}{2}}} \middle| \begin{matrix} - \\ 0 \end{matrix}\right) \tag{4.87}$$

Next, we substitute (4.73) and (4.87) in (4.75), and adopt the similar procedure used in deriving Theorem 4.5 to get the PDF as

$$f_{\gamma}^{\rm MRC}(\gamma) \approx \frac{A A_m \phi S_0^{-\alpha\mu} \bar{\gamma}_{\rm THz}^{-\frac{\alpha\mu}{2}} C^{\frac{\alpha\mu}{2}} \bar{\gamma}_{\rm RF}^{-\frac{\alpha_m \mu_m}{2}} \gamma^{\frac{\alpha_m \mu_m - 2}{2}}}{4\alpha} H_{1,0:1,3:1,1}^{0,1:3,0:0,1}\left[\frac{BC^{\frac{\alpha}{2}}}{S_0^{\alpha} \bar{\gamma}_{\rm THz}^{\frac{\alpha}{2}}}, \frac{\bar{\gamma}_{\rm RF}^{\frac{\alpha_m}{2}}}{B_m \gamma^{\frac{\alpha_m}{2}}} \middle| \begin{matrix} U_5 \\ V_5 \end{matrix}\right] \tag{4.88}$$

where $U_5 = \big\{\big(1 - \big(\frac{\alpha\mu - \alpha_m \mu_m}{2}\big); \frac{\alpha}{2}, \frac{\alpha_m}{2}\big)\big\} : \big\{\big(1 + \frac{\phi}{\alpha} - \mu, 1\big)\big\} : \big\{\big(1, 1\big)\big\}$, and $V_5 = \big\{ - \big\} : \big\{\big(\frac{\phi}{\alpha} - \mu, 1\big), \big(0, 1\big), \big(\frac{-\alpha\mu}{2}, \frac{\alpha}{2}\big)\big\} : \big\{\big(1 + \frac{\alpha_m \mu_m}{2}, \frac{\alpha_m}{2}\big)\big\}$.

To derive an approximate expression of the outage probability for the RF-MRC and THz, we substitute (4.88) in $F_{\gamma}(\gamma) = \int_0^{\gamma_{\rm th}} f_{\gamma}(z) dz$, and apply the definition of Fox's H function with

$$\int_0^{\gamma_{\rm th}} z^{\frac{\alpha_m \mu_m - \alpha_m s_2 - 2}{2}} dz = \frac{\gamma_{\rm th}^{\frac{\alpha_m \mu_m - \alpha_m s_2}{2}} \Gamma\big(\frac{\alpha_m \mu_m + \alpha_m s_2}{2}\big)}{\Gamma\big(1 + \frac{\alpha_m \mu_m + \alpha_m s_2}{2}\big)} \tag{4.89}$$

to get the outage probability using the bivariate Fox's-H function:

$$P_{\rm out}^{\rm MRC} \approx \frac{A A_m \phi S_0^{-\alpha\mu} \bar{\gamma}_{\rm THz}^{-\frac{\alpha\mu}{2}} C^{\frac{\alpha\mu}{2}} \bar{\gamma}_{\rm RF}^{-\frac{\alpha_m \mu_m}{2}} \gamma_{\rm th}^{\frac{\alpha_m \mu_m}{2}}}{4\alpha} H_{1,0:1,3:2,2}^{0,1:3,0:1,1}\left[\frac{BC^{\frac{\alpha}{2}}}{S_0^{\alpha} \bar{\gamma}_{\rm THz}^{\frac{\alpha}{2}}}, \frac{\bar{\gamma}_{\rm RF}^{\frac{\alpha_m}{2}}}{B_m \gamma_{\rm th}^{\frac{\alpha_m}{2}}} \middle| \begin{matrix} U_6 \\ V_6 \end{matrix}\right] \tag{4.90}$$

where $U_6 = \big\{\big(1 - \frac{\alpha\mu - \alpha_m \mu_m}{2}; \frac{\alpha}{2}, \frac{\alpha_m}{2}\big)\big\} : \big\{\big(1 + \frac{\phi}{\alpha} - \mu, 1\big)\big\} : \big\{\big(1, 1\big), \big(1 + \frac{\alpha_m \mu_m}{2}, \frac{\alpha_m}{2}\big)\big\}$, and $V_6 = \big\{ - \big\} : \big\{\big(\frac{\phi}{\alpha} - \mu, 1\big), \big(0, 1\big), \big(\frac{-\alpha\mu}{2}, \frac{\alpha}{2}\big)\big\} : \big\{\big(\frac{\alpha_m \mu_m}{2}, \frac{\alpha_m}{2}\big), \big(1 + \frac{\alpha_m \mu_m}{2}, \frac{\alpha_m}{2}\big)\big\}$.

We use [166, Th. 1.7, 1.11] and compute residues of (4.90) for both contours L_1 and L_2 at poles $s_1 = 0$, $\frac{\phi}{\alpha} - \mu$, $-\mu$ and $s_2 = 0$, $\frac{\alpha s_1 + \alpha\mu - \alpha_m \mu_m}{\alpha_m}$ to express the CDF in the high SNR regime,

$$F_{\gamma}^{\mathrm{MRC},\infty} = \frac{AA_m\phi S_0^{-\alpha\mu}\gamma^{\frac{\alpha\mu}{2}}}{4\alpha}\Bigg[\Bigg(\frac{2\Gamma\big(\frac{\phi-\alpha_m\mu_m}{2}\big)\Gamma(\mu-\frac{\phi}{\alpha})\Gamma(-\frac{\phi}{2})C^{\frac{\phi}{2}}}{\alpha_m\mu_m\Gamma(\frac{-\alpha_m\mu_m}{2})\bar{\gamma}^{\frac{\phi}{2}}}\Big(\frac{B}{{S_0}^{\alpha}}\Big)^{\frac{\phi}{\alpha}-\mu}$$
$$+\frac{2\Gamma\big(\frac{\alpha\mu-\alpha_m\mu_m}{2}\big)\Gamma(\frac{\phi}{\alpha}-\mu)\Gamma(\frac{-\alpha\mu}{2})C^{\frac{\alpha\mu}{2}}\bar{\gamma}^{-\frac{\alpha\mu}{2}}}{\Gamma(1+\frac{\phi}{\alpha})\alpha_m\mu_m\Gamma(\frac{-\alpha_m\mu_m}{2})}+\frac{4\Gamma(\mu)}{\phi\alpha_m\mu_m}\Big(\frac{B}{{S_0}^{\alpha}}\Big)^{-\mu}$$
$$+\frac{8\Gamma\big(\frac{\alpha\mu-\alpha_m\mu_m}{\alpha}\big)C^{\frac{\alpha_m\mu_m}{2}}}{\alpha_m(\phi-\alpha_m\mu_m)\alpha_m\mu_m\bar{\gamma}^{\frac{\alpha_m\mu_m}{2}}}\Big(\frac{B}{{S_0}^{\alpha}}\Big)^{\frac{\alpha_m\mu_m-\alpha\mu}{\alpha}}\Bigg)\bar{\gamma}^{-\frac{\alpha_m\mu_m}{2}}$$
$$+\Bigg(\frac{4\Gamma\big(\mu-\frac{\phi}{\alpha}\big)\Gamma\big(\frac{-\phi+\alpha_m\mu_m}{\alpha_m}\big)B_m{}^{\frac{\phi}{\alpha_m}-\mu_m}C^{\frac{\phi}{2}}}{\alpha_m\phi\bar{\gamma}^{\frac{\phi}{2}}}\Big(\frac{B}{{S_0}^{\alpha}}\Big)^{\frac{\phi}{\alpha}-\mu}\Bigg)\big(\bar{\gamma}\big)^{-\frac{\phi}{2}}$$
$$+\Bigg(\frac{4\Gamma\big(\frac{-\alpha\mu+\alpha_m\mu_m}{\alpha_m}\big)B_m{}^{\frac{\alpha\mu-\alpha_m\mu_m}{\alpha_m}}C^{\frac{\alpha\mu}{2}}}{\alpha_m(\frac{\phi}{\alpha}-\mu)\alpha\mu\bar{\gamma}^{\frac{\alpha\mu}{2}}}\Bigg)\bar{\gamma}^{-\frac{\alpha\mu}{2}}\Bigg] \tag{4.91}$$

as presented in (4.91).

4.9 Simulation Analysis

In this section, we demonstrate the performance of the hybrid RF-THz system and validate the derived analytical results using Monte-Carlo simulations. We analyze the performance of the considered system when multi-antenna MRC, SC, and EGC diversity techniques are applied. The simulation parameters are provided in Table 4.3. The α-μ fading channel is generated by appropriately adjusting the MATLAB function "gamrnd". To evaluate the bivariate Fox's H-function, we use MATLAB implementation, as given in [176].

First, we demonstrate the outage probability of the considered hybrid link over different system and channel configurations, as depicted in Fig. 4.8. In 4.8a, we consider $N = 1$ to show the effect of multi-path clustering parameter μ and antenna misalignment errors parameter σ_s on the outage probability by considering $d_{\mathrm{RF}} = 100$m, $d_{\mathrm{THz}} = 50$m, $\alpha = 1.5, \alpha_1 = 2, \mu_1 = 2.5$, and $\gamma_{\mathrm{th}} = 4$dB. The figure illustrates that the outage probability reduces with an increase in μ since clustering improves the channel. Further, the impact of jitter is marginal at a lower $\mu = 0.8$ and low RF average SNR but requires almost 4dB additional SNR if σ_s is increased from 8cm to 15cm at a higher $\mu = 2.4$ and outage probability 10^{-6}. Since $\phi = 14.4788$ for $\sigma_s = 8$cm and $\phi = 4.1184$ for $\sigma_s = 15$cm, and $\alpha_1\mu_1 = 5$, the diversity order for different μ is determined from the first link as $M = 0.6, 1.2, 1.8$, which can be observed from the slope of corresponding plots. Moreover, it can be seen that there is no change in the slope for the same μ even with different σ_s since the diversity order is independent of antenna misalignment errors for the considered scenario.

In Fig. 4.8(b), we demonstrate the use of multiple antennas ($N \geq 1$) at the RF to improve the overall performance of the hybrid system. Here, we compare the performance of a single-antenna system ($N = 1$) with a multiple antenna RF system ($N = 2$, $N = 3$, and $N = 5$)

Table 4.3: List of Simulation Parameters

Parameter	Value
Number of RF antennas (N)	1-20
d_{RF}	50m-150m
d_{THz}	50m
Absorption coefficient (THz)	$\kappa = 2.8 \times 10^{-4}$
THz carrier frequency (f_{THz})	275 GHz
RF carrier frequency (f_{RF})	800 MHz
THz antenna gain (G_{THz})	55 dBi
RF antenna gain (G_{RF})	25 dBi
α-parameter	1-2
μ-parameter	0.8-2.6
Ω-parameter	1
ϕ	$4.11 - 231$
S_0	0.054
Jitter standard deviation (σ_s)	2-15cm
Transmit power	0-40 dBm
Noise Power (RF)	-101 dBm
Noise Power (THz)	-74 dBm [175]
p, q	$0.5, 1$

using different diversity methods. We take system parameters ($\alpha = 2$, $\mu = 2.6$, $\sigma_s = 10$cm, $d_{\mathrm{RF}} = 100$m, and $d_{\mathrm{THz}} = 50$m) such that the THz link is stronger (in average sense) than the RF with $N = 1$. It can be observed from Fig. 4.8(b) that the outage performance improves significantly with an increase in the number of antennas achieving a higher gain with $N = 2$ system. The outage probability reduces by 30 times when N is increased from 1 to 2 and by 5 times when N is increased from 2 to 3 at an average RF SNR of 40 dB. Further, the cumulative gain decreases with an increase in the number of antennas advocating its limited usage. The performance of the hybrid system depends predominantly on the weaker of both (RF or THz) links, and thus an increase in the number of antennas at the RF link achieves a similar channel quality compared with the THz saturating the overall performance. Conventionally, the multi-antenna reception for a single link suffers from this limitation due to the channel correlation with an increase in the number of antennas.

It can be seen from the figures that the derived analytical expressions are in good agreement with Monte Carlo simulations and asymptotic results attain the exact at a relatively lower SNR. Further, the approximation involved in the analysis of MRC is quite accurate since a single α-μ variate can accurately approximate the sum of α-μ variates [188]. Figures also demonstrate the characteristics of different diversity combining techniques: the MRC is optimal, the SC is inferior to MRC but marginally with a simpler implementation, and the performance of the EGC lies between the SC and the MRC.

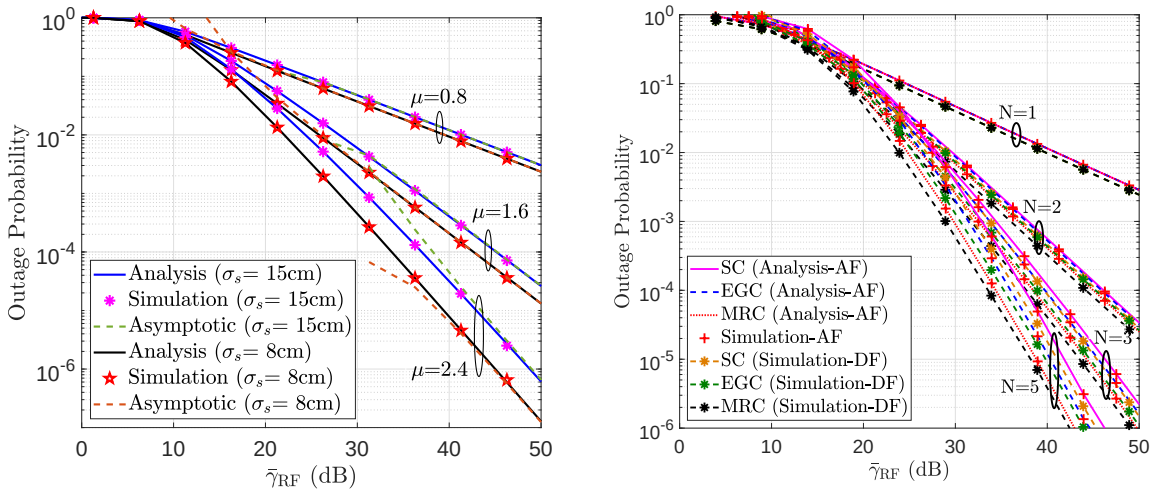

Figure 4.8: Outage probability of hybrid wireless link (a) different μ and σ_s with $N = 1$ (b) multi-antenna RF receiver with $\alpha_i = 1$ and $\mu_i = 1.2$, $\forall i$.

4.10 Chapter Summary

First, we investigated the performance of a THz-RF integrated link over α-μ fading with antenna misalignment errors. We considered a generalized i.ni.d. fading model by considering different α and μ parameters to model the short term fading for both the THz and RF links, along with the statistical distribution of antenna misalignment errors for the THz link. By deriving a closed-form expression of the CDF for the THz link, we analyzed the outage probability and diversity order of the system for real-valued μ and α. We also develop simplified expressions to provide insight on the system behavior analytically under various practically relevant scenarios. Next, we analyzed the performance of a fixed-gain relaying for the RF-THz link by considering α-μ fading for the THz system, non-zero boresight pointing errors, and the α-KMS fading model for the RF link. Using the derived PDF and CDF, we provided exact analytical expressions for the outage probability, average BER, and ergodic capacity of the system under consideration. Finally, we analyzed the performance of a hybrid system consisting of multi-antenna RF in the access link and THz in the backhaul integrated through the fixed-gain AF relaying. We derived the PDF and CDF of the end-to-end SNR of the hybrid system by employing both SC and MRC diversity receivers considering α-μ channel fading for both links along with pointing errors in the THz link.

The following chapter focuses on the development of a distributed algorithm for the selection of an aggregate node within an IoT network, mainly to gather data from challenging-to-reach terrain through a triple technology backhaul, which incorporates THz transmission.

4.11 Appendices

4.11.1 Appendix 4.1: Proof of Theorem 4.2

Using (4.9), we define $\overline{\mathrm{SNR}}_1^{(n)} = \int_0^\infty \gamma^n f_{\gamma_1}(\gamma) d\gamma$, and substituting $\left(\sqrt{\gamma/\bar{\gamma}_1}\right)^{\alpha_1} = t$, we get the n-th moment of SNR of the THz link

$$\overline{\mathrm{SNR}}_1^{(n)} = \frac{A_1 \bar{\gamma}_1^n}{\alpha_1} \int_0^\infty t^{(\frac{\phi-\alpha_1+2n}{\alpha_1})} \Gamma(B_1, C_1 t) dt \tag{4.92}$$

Using the identity [193, 8.14.4] in (4.92), we solve the integral to get $\gamma_1^{(n)}$ of (4.25). Similarly, the n-th moment of SNR of the RF link is $\overline{\mathrm{SNR}}_2^{(n)}$=$\int_0^\infty \gamma^n f_{\gamma_2}(\gamma) d\gamma$, which can be solved easily to get (4.25). Using (4.9) and (4.11) in $\overline{\mathrm{SNR}}_{12}^{(n)} = \int_0^\infty \gamma^n f_{\gamma_1}(\gamma) F_{\gamma_2}(\gamma) d\gamma$, and substituting $\left(\sqrt{\gamma/\bar{\gamma}_1}\right)^{\alpha_1} = t$, we get

$$\begin{aligned}\overline{\mathrm{SNR}}_{12}^{(n)} = \frac{A_1 \bar{\gamma}_1^n}{\alpha_1} \Bigg[& \int_0^\infty t^{(\frac{\phi-\alpha_1+2n}{\alpha_1})} \, \Gamma(B_1, C_1 t) \, dt \\ & - \frac{1}{\Gamma(\mu_2)} \int_0^\infty t^{(\frac{\phi-\alpha_1+2n}{\alpha_1})} \Gamma(B_1, C_1 t) \Gamma\left(\mu_2, B_2' t^{\frac{\alpha_2}{\alpha_1}}\right) dt \Bigg]\end{aligned} \tag{4.93}$$

where $B_2' = B_2 \sqrt{\bar{\gamma}_1/\bar{\gamma}_2}$. The first integral in (4.93) is same as (4.92). To solve the second integral, we use the Meijer G representation of $\Gamma(B_1, C_1 t)$ and $\Gamma\left(\mu_2, B_2' t^{\frac{\alpha_2}{\alpha_1}}\right)$ to get the second integral as

$$I_2 = \int_0^\infty t^{(\frac{\phi-\alpha_1+2n}{\alpha_1})} G_{1,2}^{2,0}\left(\begin{matrix}1 \\ B_1, 0\end{matrix}\middle| C_1 t\right) G_{1,2}^{2,0}\left(\begin{matrix}1 \\ \mu_2, 0\end{matrix}\middle| B_2' t^{(\frac{\alpha_2}{\alpha_1})}\right) dt \tag{4.94}$$

Using the identity [171, 07.34.21.0013.01] of definite integration of product of two Meijer G functions to get (4.22). Similarly, using (4.10) and (4.14) in $\overline{\mathrm{SNR}}_{21}^{(n)} = \int_0^\infty \gamma^n f_{\gamma_2}(\gamma) F_{\gamma_1}(\gamma) d\gamma$, and substituting $\left(\sqrt{\gamma/\bar{\gamma}_2}\right)^{\alpha} = t$, we get

$$\begin{aligned}\overline{\mathrm{SNR}}_{21}^{(n)} = & \frac{A_1 A_2 C_1^{-\frac{\phi}{\alpha_1}} \bar{\gamma}_2^n}{\Gamma(\mu_2)\phi} \Bigg[\int_0^\infty t^{(\mu_2 - 1 + \frac{2n}{\alpha_2})} e^{(-B_2 t)} \Gamma(\mu_1) dt + \int_0^\infty t^{(\mu_2 - 1 + \frac{2n}{\alpha_2})} e^{(-B_2 t)} C_1' t^{\frac{\phi}{\alpha_2}} \\ & \times \Gamma(B_1, C_1' t^{(\frac{\alpha_1}{\alpha_2})}) dt - \int_0^\infty t^{(\mu_2 - 1 + \frac{2n}{\alpha_2})} e^{(-B_2 t)} \Gamma(\mu_1, C_1' t^{(\frac{\alpha_1}{\alpha_2})}) dt \Bigg]\end{aligned} \tag{4.95}$$

where $C_1' = C_1 \sqrt{\bar{\gamma}_2/\bar{\gamma}_1}$. The first integral in (4.95) is similar to $\overline{\mathrm{SNR}}_2^{(n)}$ and can be similarly derived. To solve the second and third integrals, we use the identity [171, 07.34.21.0088.01] of definite integration of the product of two Meijer G functions to get (4.23).

4.11.2 Appendix 4.2: Proof of Lemma 4.1

The proof of $\overline{\mathrm{SNR}}_1^{(n)}$ and $\overline{\mathrm{SNR}}_2^{(n)}$ follows as given in Appendix A. We provide alternate expressions for $\overline{\mathrm{SNR}}_{12}^{(n)}$ and $\overline{\mathrm{SNR}}_{21}^{(n)}$.

Using (4.9) and (4.11) in $\overline{\mathrm{SNR}}_{12}^{(n)} = \int_0^\infty \gamma^n f_{\gamma_1}(\gamma) F_{\gamma_2}(\gamma) d\gamma$, and substituting $\left(\sqrt{\gamma/\bar{\gamma}_1}\right)^\alpha = t$, we get

$$\overline{\mathrm{SNR}}_{12}^{(n)} = \frac{A_1 \bar{\gamma}_1^n}{\alpha} \left[\int_0^\infty t^{(\frac{\phi-\alpha+2n}{\alpha})} \Gamma(B_1, C_1 t) dt - \int_0^\infty t^{(\frac{\phi-\alpha+2n}{\alpha})} \Gamma(B_1, C_1 t) \left(\frac{\Gamma\left(\mu, B_2' t\right)}{\Gamma(\mu)} \right) dt \right] \tag{4.96}$$

where $B_2' = B_2 \sqrt{\bar{\gamma}_1/\bar{\gamma}_2}$. The first integral in (4.96) is the same as (4.92). To solve the second integral, we apply the integration by parts tasking $\Gamma\left(\mu, B_2' t\right)$ as the first term and $t^{(\frac{\phi-\alpha+2n}{\alpha})} \Gamma(B_1, C_1 t)$ as the second term, and use the identity [168, 6.455/1] to get (4.28). Similarly, using (4.10) and (4.14) in $\overline{\mathrm{SNR}}_{21}^{(n)} = \int_0^\infty \gamma^n f_{\gamma_2}(\gamma) F_{\gamma_1}(\gamma) d\gamma$, and substituting $\left(\sqrt{\gamma/\bar{\gamma}_2}\right)^\alpha = t$, we get

$$\begin{aligned} \overline{\mathrm{SNR}}_{21}^{(n)} = \frac{A_1 A_2 C_1^{-\frac{\phi}{\alpha}} \bar{\gamma}_2^n}{\Gamma(\mu)\phi} \Bigg[& \int_0^\infty t^{(\mu-1+\frac{2n}{\alpha})} e^{(-B_2 t)} \Gamma(\mu) dt + \int_0^\infty t^{(\mu-1+\frac{2n}{\alpha})} e^{(-B_2 t)} C_1' t^{\frac{\phi}{\alpha}} \Gamma(B_1, C_1' t) dt \\ & - \int_0^\infty t^{(\mu-1+\frac{2n}{\alpha})} e^{(-B_2 t)} \Gamma(\mu, C_1' t) dt \Bigg] \end{aligned} \tag{4.97}$$

where $C_1' = C_1 \sqrt{\bar{\gamma}_2/\bar{\gamma}_1}$. The first integral in (4.97) is similar to $\overline{\mathrm{SNR}}_2^{(n)}$ and can be similarly derived. For the second and third integrals, we use the identity [168, 6.455/1] to get (4.29).

4.11.3 Appendix 4.3: Proof of Lemma 4.2

Using (4.9) in (2.15), we define $\bar{\eta}_1 \geq \int_0^\infty \log_2(\gamma) f_{\gamma_1}(\gamma) d\gamma$, and substituting $\left(\sqrt{\gamma/\bar{\gamma}_1}\right)^\alpha = t$, we get a lower bound average capacity of THz link:

$$\bar{\eta}_1 \geq \frac{A_1}{\alpha \log(2)} \int_0^\infty \log(\bar{\gamma}_1 t^{\frac{2}{\alpha}}) t^{(\frac{\phi}{\alpha}-1)} \Gamma(B_1, C_1 t) dt \tag{4.98}$$

It is noted that η_1 is a lower bound on the ergodic capacity of the THz link since $\log_2(1+\gamma) \geq \log_2(\gamma)$. To find a closed-form expression, we use integration by-parts with $\Gamma(B_1, C_1 t)$ as the first term and $\log(\bar{\gamma}_1 t^{\frac{2}{\alpha}}) t^{(\frac{\phi}{\alpha}-1)}$ as the second term, and apply the identity [168, 4.352/1] to get $\bar{\eta}_1$ in (4.34). Similarly, substituting $\left(\sqrt{\gamma/\bar{\gamma}_2}\right)^\alpha = t$ in $\bar{\eta}_2 \geq \int_0^\infty \log_2(\gamma) f_{\gamma_2}(\gamma) d\gamma$ for a lower bound on the average capacity of the RF link:

$$\bar{\eta}_2 \geq \frac{A_2}{\Gamma(\mu)\log(2)} \int_0^\infty \log(\bar{\gamma}_2 t^{\frac{2}{\alpha}}) t^{(\mu-1)} e^{(-B_2 t)} dt \tag{4.99}$$

We use the identity [168, 4.352/1] in (4.99) to get $\bar{\eta}_2$ of (4.35). Defining $\bar{\eta}_{12} = \int_0^\infty \log_2(\gamma) f_{\gamma_1}(\gamma) F_{\gamma_2}(\gamma) d\gamma$, using (4.9) and (4.11), and substituting $\left(\sqrt{\gamma/\bar{\gamma}_1}\right)^\alpha = t$, we get

$$\bar{\eta}_{12} \geq \frac{A_1}{\alpha \log(2)} \Bigg[\int_0^\infty \log(\bar{\gamma}_1 t^{\frac{2}{\alpha}}) t^{(\frac{\phi}{\alpha}-1)} \Gamma(B_1, C_1 t) dt - \int_0^\infty \log(\bar{\gamma}_1 t^{\frac{2}{\alpha}}) t^{(\frac{\phi}{\alpha}-1)} \Gamma(B_1, C_1 t) \left(\frac{\Gamma(\mu, B_2' t)}{\Gamma(\mu)} \right) dt \Bigg] \tag{4.100}$$

The first integral in (4.100) is the same as (4.98). To solve the second integral, we use the series expansion of Gamma function $\Gamma(\mu, B_2' t) = (\mu-1)! \exp(-B_2' t) \sum_{k=0}^{\mu-1} \frac{(B_2' t)^k}{k!}$. Using $\log(\bar{\gamma}_1 t^{\frac{2}{\alpha}}) \approx \frac{2}{\alpha} \log(1 + \bar{\gamma}_1^{\frac{\alpha}{2}} t)$, and with Meijer G representation of $\log(1 + \bar{\gamma}_1^{\frac{\alpha}{2}} t)$, $\Gamma(B_1, C_1 t)$ and $\Gamma(\mu, B_2' t)$, we get the second integral as

$$I_2 \approx \sum_{k=0}^{\mu-1} \frac{2 A_1 (\mu-1)! B_2'^k}{\alpha^2 \ln(2) \Gamma(\mu) \mathrm{k}!} \int_0^\infty t^{(\frac{\phi}{\alpha}+k-1)} G_{0,1}^{1,0}\left(\begin{matrix} - \\ 0 \end{matrix} \middle| B_2' t \right) G_{1,2}^{2,0}\left(\begin{matrix} 1 \\ B_1, 0 \end{matrix} \middle| C_1 t \right) \left[G_{2,2}^{1,2}\left(\begin{matrix} 1, 1 \\ 1, 0 \end{matrix} \middle| (\bar{\gamma}_1)^{\frac{\alpha}{2}} t \right) \right] dt \tag{4.101}$$

Finally, we apply the identity of definite integration of the product of three Meijer G function [171, 07.34.21.0081.01] to get $\bar{\eta}_{12}$ in (4.36). Similarly, using (4.10) and (4.14) we define $\bar{\eta}_{21} \geq \int_0^\infty \log_2(\gamma) f_{\gamma_2}(\gamma) F_{\gamma_1}(\gamma) d\gamma$ and substituting $\left(\sqrt{\gamma/\bar{\gamma}_2}\right)^\alpha$=$t$, we get

$$\bar{\eta}_{21} \approx \frac{A_1 C_1^{-\frac{\phi}{\alpha}} A_2}{\Gamma(\mu) \phi \log(2)} \Bigg[\int_0^\infty \log(\bar{\gamma}_2 t^{\frac{2}{\alpha}}) t^{(\mu-1)} e^{(-B_2 t)} \Gamma(\mu) dt + \int_0^\infty \log(\bar{\gamma}_2 t^{\frac{2}{\alpha}}) t^{(\mu-1)} e^{(-B_2 t)} C_1' t^{\frac{\phi}{\alpha}} \Gamma(B_1, C_1' t) dt - \int_0^\infty \log(\bar{\gamma}_2 t^{\frac{2}{\alpha}}) t^{(\mu-1)} e^{(-B_2 t)} \Gamma(\mu, C_1' t) dt \Bigg] \tag{4.102}$$

The first integral in (4.102) is similar to η_2 of (4.99). To solve the second integral, we apply the identity of definite integration of the Meijer G function [171, 07.34.21.0081.01]. Finally, to solve the third integration, we use the series expansion of Gamma function $\Gamma(\mu, C_1' t) = (\mu-1)! \exp(-C_1' t) \sum_{k=0}^{\mu-1} \frac{(C_1' t)^k}{k!}$ and apply the identity of definite integration of product of the Meijer G functions [171, 07.34.21.0088.01]. Combining these three integrals, we get $\bar{\eta}_{21}$ in (4.37).

4.11.4 Appendix 4.4: Proof of Theorem 4.3

Using (4.18) in (4.38), we represent the ergodic capacity of the relay assisted THz-RF link:

$$\begin{aligned}\bar{\eta} =&\frac{1}{\Gamma(\mu_2)\ln(2)}\int_0^{\infty}\frac{1}{1+\gamma}\Gamma\left(\mu_2, B_2\bar{\gamma}_2^{\frac{-\alpha_2}{2}}\gamma^{\frac{\alpha_2}{2}}\right)d\gamma\\ &-\frac{A_1C_1^{-\frac{\phi}{\alpha_1}}\Gamma(\mu_1)}{\phi\Gamma(\mu_2)\ln(2)}\Bigg[\int_0^{\infty}\frac{1}{1+\gamma}\Gamma\left(\mu_2, B_2\bar{\gamma}_2^{\frac{-\alpha_2}{2}}\gamma^{\frac{\alpha_2}{2}}\right)d\gamma\\ &-\int_0^{\infty}\frac{\gamma^{\frac{\phi}{2}}}{1+\gamma}C_1\bar{\gamma}_1^{\frac{-\phi}{2}}\Gamma\big(B_1, C_1\bar{\gamma}_1^{\frac{-\alpha_1}{2}}\gamma^{\frac{\alpha_1}{2}}\big)\Gamma\big(\mu_2, B_2\bar{\gamma}_2^{\frac{-\alpha_2}{2}}\gamma^{\frac{\alpha_2}{2}}\big)d\gamma\\ &+\int_0^{\infty}\frac{1}{1+\gamma}\Gamma\big(\mu_1, C_1\bar{\gamma}_1^{\frac{-\alpha_1}{2}}\gamma^{\frac{\alpha_1}{2}}\big)\Gamma\big(\mu_2, B_2\bar{\gamma}_2^{\frac{-\alpha_2}{2}}\gamma^{\frac{\alpha_2}{2}}\big)d\gamma\Bigg]\end{aligned} \tag{4.103}$$

We solve the first and second integral in (4.103) by representing $\frac{1}{1+\gamma}$ and the incomplete gamma function in terms of Meijer's G equivalent and apply the identity of definite integration of Meijer G function [171, 07.34.21.0086.01]. For the third integral, we approximate $\frac{1}{1+\gamma} \approx \frac{1}{\gamma}$, use $\alpha_2 = \epsilon\alpha_1$, where $\epsilon > 0$, and substitute $\gamma^{\frac{\alpha_1}{2}} = t$ to represent the integral to apply the identity of definite integration of one linear and two Meijer's G functions with one function having rational argument [171, 07.34.21.0013.01]. Finally, for the last integral in (4.103), we express $\Gamma\big(\mu_2, B_2\bar{\gamma}_2^{\frac{-\alpha_2}{2}}\gamma^{\frac{\alpha_2}{2}}\big) = \Gamma(\mu_2) - \gamma\big(\mu_2, B_2\bar{\gamma}_2^{\frac{-\alpha_2}{2}}\gamma^{\frac{\alpha_2}{2}}\big)$, and use the asymptotic bound $\lim_{s\to 0}\gamma(a,x) = x^a a^{-1}$ such that the fourth integral becomes

$$I_4 = \Gamma(\mu_2)\int_0^{\infty}\frac{1}{1+\gamma}\Gamma\big(\mu_1, C_1\bar{\gamma}_1^{\frac{-\alpha_1}{2}}\gamma^{\frac{\alpha_1}{2}}\big)d\gamma - \frac{\big(B_2\bar{\gamma}_2^{\frac{-\alpha_2}{2}}\big)^{\mu_2}}{\mu_2}\int_0^{\infty}\frac{\gamma^{\frac{\alpha_2\mu_2}{2}}}{1+\gamma}\Gamma\big(\mu_1, C_1\bar{\gamma}_1^{\frac{-\alpha_1}{2}}\gamma^{\frac{\alpha_1}{2}}\big)d\gamma \tag{4.104}$$

The first integral of (4.104) can be solved similar to the first integral of (4.103). The second integral can be solved by representing $\frac{1}{1+\gamma}$ and incomplete gamma function in terms of Meijer's G and applying the identity [171, 07.34.21.0013.01]. Capitalizing these, we get the ergodic capacity of THz-RF relay system in (4.39) of Theorem 4.3. It should be noted that the use of simple approximations in the third and fourth integrals of (4.103) results the derived approximation of the ergodic capacity into very close agreement with the exact.

To prove the asymptotic ergodic capacity in (4.40), we use [171, 07.34.21.0013.01] to solve the first three integrals in (4.103) and the second integral in (4.104) in terms of Fox's H- function. The first integral in (4.104) is solved by applying the series expansion $\Gamma(a, bx)$ $=(a-1)!e^{(-bx)}\sum_{k=0}^{a-1}\frac{(bx)^k}{k!}$. Finally, we apply the asymptotic result of the Fox-H function [166, Theorem (1.11)] to get (4.40) of Theorem 4.3.

4.11.5 Appendix 4.5: Proof of Theorem 4.4

Using (4.14) in (2.16), we get the average BER of the THz link as

$$\bar{P}_{e1} = \frac{A_1 C_1^{-\frac{\phi}{\alpha_1}} q^p}{2\Gamma(p)\phi} \Bigg[\int_0^\infty \gamma^{p-1} e^{-q\gamma} \Gamma(\mu_1) d\gamma + C_1^{\frac{\phi}{\alpha_1}} \bar{\gamma}_1^{\frac{-\phi}{2}} \times \int_0^\infty \gamma^{\frac{\phi}{2}} \gamma^{p-1} e^{-q\gamma} \Gamma\Big(B_1, C_1 \bar{\gamma}_1^{\frac{-\alpha_1}{2}} \gamma^{\frac{\alpha_1}{2}}\Big) d\gamma - \int_0^\infty \gamma^{p-1} e^{-q\gamma} \Gamma\Big(\mu_1, C_1 \bar{\gamma}_1^{\frac{-\alpha_1}{2}} \gamma^{\frac{\alpha_1}{2}}\Big) d\gamma \Bigg] \tag{4.105}$$

Representing the incomplete gamma function into its Meijer's G equivalent, (4.105) can be rewritten as

$$\bar{P}_{e1} = \frac{A_1 C_1^{-\frac{\phi}{\alpha_1}} q^p}{2\Gamma(p)\phi} \Bigg[\int_0^\infty \gamma^{p-1} e^{-q\gamma} \Gamma(\mu_1) d\gamma + C_1^{\frac{\phi}{\alpha_1}} \bar{\gamma}_1^{\frac{-\phi}{2}} \int_0^\infty \gamma^{\frac{\phi+2p}{2}-1} e^{-q\gamma} \times G_{1,2}^{2,0}\left(\begin{matrix} 1 \\ B_1, 0 \end{matrix} \middle| C_1 \bar{\gamma}_1^{\frac{-\alpha_1}{2}} \gamma^{\frac{\alpha_1}{2}} \right) d\gamma - \int_0^\infty \gamma^{p-1} e^{-q\gamma} G_{1,2}^{2,0}\left(\begin{matrix} 1 \\ \mu_1, 0 \end{matrix} \middle| C_1 \bar{\gamma}_1^{\frac{-\alpha_1}{2}} \gamma^{\frac{\alpha_1}{2}} \right) d\gamma \Bigg] \tag{4.106}$$

The first integral in (4.105) contains a simple algebraic expression. For the second and third integrals, we apply the identity of definite integration of the Meijer G function [171, 07.34.21.0088.01]. Thus, we get (4.47).

Similarly, using (4.11) in (2.16), we get the average BER of the RF link as

$$\bar{P}_{e2} = \frac{q^p}{2\Gamma(p)} \Bigg[\int_0^\infty \gamma^{p-1} e^{-q\gamma} d\gamma - \frac{1}{\mu_2} \int_0^\infty \gamma^{p-1} e^{-q\gamma} \Gamma\Big(\mu_2, B_2 \bar{\gamma}_2^{\frac{-\alpha_2}{2}} \gamma^{\frac{\alpha_2}{2}}\Big) d\gamma \Bigg] \tag{4.107}$$

We use the similar procedure in deriving (4.47) to solve (4.107) in terms of Meijer's G function and obtain (4.48) of Theorem 4.4.

To prove the asymptotic expression in (4.50), we use [171, 07.34.21.0013.01] to solve the integrals in (4.106) and (4.107) in terms of Fox's H- function. Then, we apply the asymptotic result of the Fox-H function [166, Theorem (1.11)] to get $\bar{P}_e^\infty = \bar{P}_{e1}^\infty + \bar{P}_{e2}^\infty$ in terms of Gamma function, as given in (4.50). Note that we can also obtain the asymptotic BER of the THz-RF link in the low SNR region by applying the corresponding asymptotic result in [166, Theorem (1.7)].

4.11.6 Appendix 4.6: Proof of Theorem 4.5

First, we express the PDF and CDF of the RF link in a compatible form so that statistical results of the combined channel can be obtained in a simplified form. Substituting (4.71) in

(4.77) we can get the CDF of the first link as

$$F_{\gamma_{RF}}(\gamma) = \left[1 - \left(\frac{\Gamma\Big(\mu_i, B_i\big(\sqrt{\gamma/\bar{\gamma}_{\mathrm{RF}}}\big)^{\alpha_i}\Big)}{\Gamma(\mu_i)}\right)\right]^N \tag{4.108}$$

Applying the binomial expansion and using the series expansion of incomplete Gamma function $\Gamma(\mu_i, at) = (\mu_i - 1)!\exp(-at)\sum_{j=0}^{\mu_i-1}\frac{(at)^j}{j!}$, we express (4.108) as

$$F_{\gamma_{\mathrm{RF}}}(\gamma) = (-1)^k \sum_{k=0}^{N}\binom{N}{k}\exp\Big(-kB_i\sqrt{\frac{\gamma}{\bar{\gamma}_{\mathrm{RF}}}}^{\alpha_i}\Big)\left(\sum_{j=0}^{\mu_i-1}\frac{B_i\Big(\sqrt{\frac{\gamma}{\bar{\gamma}_{\mathrm{RF}}}}\Big)^{j\alpha_i}}{j!}\right)^k \tag{4.109}$$

Applying the multinomial expansion $(x_1+x_2+\cdots+x_m)^n = \sum_{k_1+k_2+\cdots+k_m=n}\binom{n}{k_1, k_2, \cdots, k_m}$ $\prod_{t=1}^{m} x_t^{k_t}$, where $\binom{n}{k_1, k_2, \cdots, k_m} = \frac{n!}{k_1!k_2!\cdots k_m!}$ on the last term of (4.109), we get the CDF of the first link as

$$\begin{aligned} F_{\gamma_{\mathrm{RF}}}(\gamma) =& (-1)^k \sum_{k=0}^{N}\binom{N}{k}\sum_{k_0+k_1+\cdots+k_{\mu_i-1}=k}\binom{k}{k_0+k_1+\cdots+k_{\mu_i-1}}\exp\Big(-kB_i\Big(\frac{\gamma}{\bar{\gamma}_{\mathrm{RF}}}\Big)^{\frac{\alpha_i}{2}}\Big) \\ &\times\prod_{t=o}^{\mu_i-1}\frac{B_i^{k_t}\gamma^{(\sum_{t=0}^{\mu_i-1}\frac{t\alpha_i k_t}{2})}}{(t!)^{k_t}\bar{\gamma}_{\mathrm{RF}}^{(\frac{t\alpha_i k_t}{2})}} \end{aligned} \tag{4.110}$$

We use (4.70) and (4.71) in $f_{\gamma_{\mathrm{RF}}}(\gamma) = N(1-F_{\gamma_i}(\gamma))^{N-1}f_{\gamma_i}(\gamma)$ to get the PDF of the first link:

$$f_{\gamma_{\mathrm{RF}}}(\gamma) = \left[\left(\frac{\Gamma\Big(\mu_i, B_i\big(\sqrt{\frac{\gamma}{\bar{\gamma}_{\mathrm{RF}}}}\big)^{\alpha_i}\Big)}{\Gamma(\mu_i)}\right)\right]^{N-1}\frac{NA_i\gamma^{\frac{\alpha_i\mu_i}{2}-1}}{2\bar{\gamma}_{\mathrm{RF}}^{\frac{\alpha_i\mu_i}{2}}}\exp\Big(-\frac{\mu_i}{\Omega^{\alpha_i}}\Big(\sqrt{\frac{\gamma}{\bar{\gamma}_{\mathrm{RF}}}}\Big)^{\alpha_i}\Big) \tag{4.111}$$

Thus, we use the series expansion of incomplete Gamma function and multinomial expansion in (4.108) to get the PDF of the RF link as

$$\begin{aligned} f_{\gamma_{\mathrm{RF}}}(\gamma) =& \frac{NA_i}{2\bar{\gamma}_{\mathrm{RF}}^{\frac{\alpha_i\mu_i}{2}}}\sum_{k_0+k_1+\cdots+k_{\mu_i-1}=N-1}\binom{N-1}{k_0+k_1+\cdots+k_{\mu_i-1}}\exp\Big(-\frac{N\gamma^{\frac{\alpha_i}{2}}B_i}{\bar{\gamma}_{\mathrm{RF}}^{\frac{\alpha_i}{2}}}\Big) \\ &\times\prod_{t=o}^{\mu_i-1}\frac{B_i^{k_t}\gamma^{(\sum_{t=0}^{\mu_i-1}\frac{t\alpha_i k_t}{2}+\frac{\alpha_i\mu_i}{2}-1)}}{(t!)^{k_t}\bar{\gamma}_{\mathrm{RF}}^{(\frac{t\alpha_i k_t}{2})}} \end{aligned} \tag{4.112}$$

Next, we derive the PDF of the mixed link by substituting (4.73) and (4.112) in (4.75) using the integral representation of Meijer's-G function [170]:

$$f_{\gamma}^{\mathrm{SC}}(z)=\frac{NAA_i\phi S_0^{-\alpha\mu}}{2\alpha^2\bar{\gamma}_{\mathrm{RF}}^{\frac{\alpha_i\mu_i}{2}}\bar{\gamma}_{\mathrm{THz}}^{\frac{\alpha\mu}{2}}}\sum_{k_0+k_1+\cdots+k_{\mu_i-1}=N-1}\binom{N-1}{k_0+k_1+\cdots+k_{\mu_i-1}}\prod_{t=o}^{\mu_i-1}\frac{B^{k_t}(z)^{(\sum_{t=0}^{\mu_i-1}\frac{t\alpha_ik_t}{2}+\frac{\alpha_i\mu_i}{2}-1)}}{(t!)^{k_t}\bar{\gamma}_{\mathrm{RF}}^{(\frac{t\alpha_ik_t}{2})}}$$
$$\times\frac{1}{2\pi\jmath}\int_{\mathcal{L}_1}\Gamma(0-S_1)\left(\frac{Nz^{\frac{\alpha_i}{2}}B_i}{\bar{\gamma}_{\mathrm{RF}}^{\frac{\alpha_i}{2}}}\right)^{S_1}dS_1\frac{1}{2\pi\jmath}\int_{\mathcal{L}_2}\frac{\Gamma(-\mu+\frac{\phi}{\alpha}-S_2)\Gamma(-S_2)\Gamma(\mu+S_2)}{\Gamma(1-\mu+\frac{\phi}{\alpha}-S_2)\Gamma(1+\mu+S_2)}\left(\frac{B}{S_o^{\alpha}\bar{\gamma}_{\mathrm{THz}}^{\frac{\alpha}{2}}}\right)^{S_2}dS_2I_1 \tag{4.113}$$

where $\mathcal{L}_1$ and $\mathcal{L}_2$ are the contours of line integrals. The inner integral I_1 is solved by applying [168, 3.194/3] and [168, 8.384/1]:

$$I_1=\int_0^{\infty}x^{(\frac{\alpha\mu}{2}+\frac{\alpha S_2}{2}-1)}\big(\frac{x+C}{x}\big)^{\sum_{t=0}^{\mu_i-1}\frac{t\alpha_ik_t}{2}+\frac{\alpha_i\mu_i}{2}+\frac{\alpha_iS_1}{2}}dx=$$
$$\frac{C^{(\frac{\alpha\mu+\alpha S_2}{2})}\Gamma\big(\frac{-\alpha\mu-\alpha S_2}{2}\big)\Gamma\big(\frac{\alpha\mu-\sum_{t=0}^{\mu_i-1}t\alpha_ik_t-\alpha_i\mu_i-\alpha_iS_1+\alpha S_2}{2}\big)}{\Gamma\big(-\sum_{t=0}^{\mu_i-1}\frac{t\alpha_ik_t}{2}-\frac{\alpha_i\mu_i}{2}-\frac{\alpha_iS_1}{2}\big)} \tag{4.114}$$

Substituting I_1 back into (4.113), converting $S_1\rightarrow -S_1$ and applying the definition of Fox's H-function [178, 1.1], we get the PDF of multiantenna RF mixed with THz employing MRC in (4.78). The CDF can be derived using $F_{\gamma}^{\mathrm{SC}}(z)=\int_0^{\gamma}f_{\gamma}^{\mathrm{SC}}(z)dz$

$$F_{\gamma}^{\mathrm{SC}}(z)=\frac{NAA_i\phi S_0^{-\alpha\mu}C^{\frac{\alpha\mu}{2}}}{2\alpha^2\bar{\gamma}_{\mathrm{RF}}^{\frac{\alpha_i\mu_i}{2}}\bar{\gamma}_{\mathrm{THz}}^{\frac{\alpha\mu}{2}}}\sum_{k_0+k_1+\cdots+k_{\mu_i-1}=N-1}\binom{N-1}{k_0+k_1+\cdots+k_{\mu_i-1}}\prod_{t=o}^{\mu_i-1}\frac{B^{k_t}}{(t!)^{k_t}\bar{\gamma}_{\mathrm{RF}}^{(\frac{t\alpha_ik_t}{2})}}$$
$$\frac{1}{2\pi\jmath}\int_{\mathcal{L}_1}\Gamma(0+S_1)\left(\frac{\bar{\gamma}_{\mathrm{RF}}^{\frac{\alpha_i}{2}}}{NB_i}\right)^{S_1}dS_1\frac{1}{2\pi\jmath}\int_{\mathcal{L}_2}\frac{\Gamma(-\mu+\frac{\phi}{\alpha}-S_2)\Gamma(-S_2)\Gamma(\mu+S_2)}{\Gamma(1-\mu+\frac{\phi}{\alpha}-S_2)\Gamma(1+\mu+S_2)}\left(\frac{BC^{\frac{\alpha}{2}}}{S_o^{\alpha}\bar{\gamma}_{\mathrm{THz}}^{\frac{\alpha}{2}}}\right)^{S_2}dS_2$$
$$\frac{\Gamma\big(\frac{-\alpha\mu-\alpha S_2}{2}\big)\Gamma\big(\frac{\alpha\mu}{2}-\sum_{t=0}^{\mu_i-1}\frac{t\alpha_ik_t}{2}-\frac{\alpha_i\mu_i}{2}+\frac{\alpha_iS_1}{2}+\frac{\alpha S_2}{2}\big)}{\Gamma\big(-\sum_{t=0}^{\mu_i-1}\frac{t\alpha_ik_t}{2}-\frac{\alpha_i\mu_i}{2}+\frac{\alpha_iS_1}{2}\big)}$$
$$\int_0^{\gamma}(z)^{(\sum_{t=0}^{\mu_i-1}\frac{t\alpha_ik_t}{2}+\frac{\alpha_i\mu_i}{2}-\frac{\alpha_iS_1}{2}-1)}dz \tag{4.115}$$

We can simplify the inner integral $\int_0^{\gamma}(z)^{(\sum_{t=0}^{\mu_i-1}\frac{t\alpha_ik_t}{2}+\frac{\alpha_i\mu_i}{2}-\frac{\alpha_iS_1}{2}-1)}dz$ in terms of Gamma function and applying the definition of Fox's H-function [178, 1.1] we obtain the CDF of multiantenna RF mixed with THz employing MRC in (4.79), which proves Theorem 4.5.

4.11.7 Appendix 4.7: Proof of Theorem 4.6

First, we derive the PDF of $\gamma_{\mathrm{RF}}=\sum_{i=1}^{N}\gamma_{r_i}$ using the moment generating function (MGF) based approach. We apply inverse Laplace transform to get the PDF $f_{\gamma_{\mathrm{RF}}}(\gamma)=\mathcal{L}^{-1}\mathcal{M}_{\gamma}(s)$, where $\mathcal{M}(s)$ is defined as $\mathcal{M}_{\gamma}(s)=\prod_{i=1}^{N}\mathcal{M}_{\gamma_i}(s)$ with $\mathcal{M}_{\gamma_i}(s)=\int_0^{\infty}e^{-s\gamma_i}f_{\gamma_i}(\gamma)d\gamma$. Representing (4.70) in its Meijer's G equivalent and simplifying, we get

$$\mathcal{M}_{\gamma}(s)=\prod_{i=1}^{N}\left[\frac{A_i\bar{\gamma}_{\mathrm{RF}}^{\frac{-\alpha_i\mu_i}{2}}}{2s^{\frac{\alpha_i\mu_i}{2}}}\frac{1}{2\pi i}\int_{\mathcal{L}}\Gamma(0-S_1)\Gamma\Big(\frac{\alpha_i\mu_i+\alpha_iS_1}{2}\Big)\Big(\frac{B_i}{s^{\frac{\alpha_i}{2}}\bar{\gamma}_{\mathrm{RF}}^{\frac{\alpha_i}{2}}}\Big)^{S_1}dS_1\right] \tag{4.116}$$

Applying the inverse Laplace transform in (4.116) with standard Mathematical procedure, and using the definition of multivariate Fox's H-function, we get the PDF of MRC-RF:

$$f_{\gamma_{\mathrm{RF}}}(\gamma)=\prod_{i=1}^{N}\frac{A_i}{2\bar{\gamma}_{\mathrm{RF}}^{\frac{\alpha_i\mu_i}{2}}}\left(\frac{1}{\gamma}\right)^{\left(\sum_{i=1}^{N}\frac{-\alpha_i\mu_i}{2}+1\right)}H_{0,1;1,1;\cdots;1,1}^{0,0;1,1;\cdots;1,1}\left[\left\{\frac{B_i\gamma^{\frac{\alpha_i}{2}}}{\bar{\gamma}_{\mathrm{RF}}^{\frac{\alpha_i}{2}}}\right\}_{i=1}^{N}\middle|\begin{array}{c}U_9\\V_9\end{array}\right] \tag{4.117}$$

where $U_9=\big\{-\big\}:\Big\{\Big(1-\frac{\alpha_1\mu_1}{2},\frac{\alpha_1}{2}\Big),\cdots,\Big(1-\frac{\alpha_i\mu_i}{2},\frac{\alpha_i}{2}\Big)\Big\}$ and $V_9=\Big\{\Big(1-\sum_{i=1}^{N}\frac{\alpha_i\mu_i}{2};\frac{\alpha_1}{2},\cdots,\frac{\alpha_{r_N}}{2}\Big)\Big\}:\Big\{(0,1),\cdots,(0,1)_N\Big\}$.

Next, we use (4.117) and (4.73) in (4.75) with the inner integral $\int_0^{\infty}\left(\frac{(x+C)}{x}\right)^{\left(\sum_{i=1}^{N}\frac{\alpha_i\mu_i+\alpha_{r_i}S_i}{2}\right)}x^{\frac{\alpha\mu+\alpha\zeta}{2}-1}dx=\frac{C^{\frac{\alpha\mu+\alpha\zeta}{2}}\Gamma\left(\frac{-\alpha\mu-\alpha\zeta}{2}\right)\Gamma\left(\sum_{i=1}^{N}\frac{-\alpha_i\mu_i-\alpha_{r_i}S_i}{2}+\frac{\alpha\mu+\alpha\zeta}{2}\right)}{\Gamma\left(\sum_{i=1}^{N}\frac{-\alpha_i\mu_i-\alpha_{r_i}S_i}{2}\right)}$, and changing the sign of integral contour S_1, we get

$$f_{\gamma}^{\mathrm{MRC}}(\gamma)=\prod_{i=1}^{N}\frac{A_{r_i}\gamma^{\left(\sum_{i=1}^{N}\frac{\alpha_i\mu_i}{2}-1\right)}A\phi S_0^{-\alpha\mu}C^{\frac{\alpha\mu}{2}}}{2\bar{\gamma}_{\mathrm{RF}}^{\frac{\alpha_i\mu_i}{2}}\alpha^2\tilde{\gamma}_{\mathrm{THz}}^{\frac{\alpha\mu}{2}}}\Bigg[\Big(\frac{1}{2\pi\jmath}\Big)^{N}\prod_{i=1}^{N}\int_{\mathcal{L}}\Gamma(0+S_i)\Gamma\Big(\frac{\alpha_i\mu_i-\alpha_iS_i}{2}\Big)$$
$$\Big(\prod_{i=1}^{N}\frac{\bar{\gamma}_{\mathrm{RF}}^{\frac{\alpha_i}{2}}}{B_i\gamma^{\frac{\alpha_i}{2}}}\Big)^{S_i}\frac{2\pi i}{\Gamma\left(\sum_{i=1}^{N}\frac{\alpha_i\mu_i-\alpha_iS_1}{2}\right)}dS_i\Bigg]\frac{1}{2\pi\jmath}\int_{L_2}\frac{\Gamma(-\mu+\frac{\phi}{\alpha}-\zeta)\Gamma(0-\zeta)\Gamma(\mu+\zeta)}{\Gamma(1-\mu+\frac{\phi}{\alpha}-\zeta)\Gamma(1+\mu+\zeta)}\Big(\frac{BC^{\frac{\alpha}{2}}}{S_o^{\alpha}\bar{\gamma}_{\mathrm{THz}}^{\frac{\alpha}{2}}}\Big)^{\zeta}d\zeta$$
$$\frac{\Gamma\left(\frac{-\alpha\mu-\alpha\zeta}{2}\right)\Gamma\left(\sum_{i=1}^{N}\frac{-\alpha_i\mu_i+\alpha_{r_i}S_i}{2}+\frac{\alpha\mu+\alpha\zeta}{2}\right)}{\Gamma\left(\sum_{i=1}^{N}\frac{-\alpha_i\mu_i+\alpha_{r_i}S_i}{2}\right)} \tag{4.118}$$

We apply the definition of multivariate Fox's H-function [170, A.1] to get the PDF of the RF link with the MRC mixed with THz in (4.82).

Finally, we derive the CDF $F_{\gamma_{\mathrm{RF}}}^{\mathrm{MRC}}(\gamma)=\int_0^{\gamma}f_{\gamma_{\mathrm{RF}}}^{\mathrm{MRC}}(\gamma)d\gamma$ using the inner integral $\int_0^{\gamma}\gamma^{\left(\sum_{i=1}^{N}\frac{-\alpha_{r_i}S_i+\alpha_i\mu_i}{2}-1\right)}d\gamma=\frac{\gamma^{\left(\sum_{i=1}^{N}\frac{-\alpha_{r_i}S_i+\alpha_i\mu_i}{2}\right)}}{\Gamma\left(\sum_{i=1}^{N}\frac{-\alpha_{r_i}S_i+\alpha_i\mu_i}{2}\right)}$, and applying [170, A.1] in terms of $N+1$-variate Fox's H-function in (4.83), which concludes the proof of Theorem 4.6.

Chapter 5

THz-Assisted Backhaul for Data Collection from IoT Network: Distributed Protocol and Performance Analysis

5.1 Introduction

IoT networks are capable of collecting critical information in remote and hard-to-reach areas. However, due to the infeasibility of wireline backhaul, there may be connectivity issues between the IoT network and the core network. Moreover, the limited power of IoT devices necessitates consideration of the network's lifetime when connected to the AP, making it challenging to collect data and process it on time for optimal decision-making. With the proliferation of connected devices, data collection has become a crucial aspect of IoT networks. Extensive research has been carried out in this area, with numerous studies focusing on various aspects of IoT data collection [105–111]. Once the data is collected, it needs to be transmitted to a core network for further processing and analysis.

Collecting data in IoT networks poses challenges due to factors like data volume, terrain difficulties, and energy constraints on IoT devices. In recent years, researchers have been dedicated to addressing this challenge efficiently [105–111]. For example, in [106], an information-centric data collection algorithm is proposed, focusing on gathering multimedia sensor data over short ranges between mobile devices and wireless sensors based on their movement speeds.

The research contributions in this chapter have been reported in these publications:

1. **P. Bhardwaj**, V. Bansal, N. Biyani, S. Shukla, and S. M. Zafaruddin, "Performance of Integrated IoT Network with Hybrid mmWave/FSO/THz Backhaul Link," in **IEEE Internet of Things Journal**, vol. 11, no. 2, pp. 3639-3652, Jan. 2024.
2. **P. Bhardwaj** and S. M. Zafaruddin, "Performance Analysis of Outdoor THz Wireless Transmission over Mixed Gaussian Fading with Pointing Errors," **2022 International Conference on Next Generation Systems and Networks: (BITS EEE CON)**, BITS Pilani, India, 2023, pp.187-196.
3. A. A. Joshi, **P. Bhardwaj**, and S. M. Zafaruddin, "Terahertz Wireless Transmissions with Maximal Ratio Combining over Fluctuating Two-Ray Fading," **2022 IEEE Wireless Communications and Networking Conference (WCNC), Austin**, TX, USA, 2022, pp. 1575-1580.

Similarly, the work presented in [107] emphasizes a secure data collection scheme for an IoT-based healthcare system, employing FPGA hardware-based ciphers and secret cipher shared algorithms. Additionally, [109] offers a comprehensive survey of UAV-assisted data collection technologies, covering sensor node clustering, UAV data collection modes, and resource allocation. Moreover, [110] tackles the challenge of maximizing data collection with energy-constrained UAVs in IoT networks, while [111] explores the efficient use of UAVs for collecting sensed data in wireless rechargeable sensor clusters situated in challenging terrains.

There are two potential approaches for transmitting data from each device to the UAV: (i) direct transmission from each device to the UAV, or (ii) the devices send their data to a chosen aggregate node (AN), which then transmits the aggregated data to the UAV. The choice of AN can be made using either a centralized procedure, in which the UAV measures the SNR of each device and selects the device with the highest SNR as the AN. However, under a distributed approach, each device undergoes a self-configuring process to become an AN. Current research primarily focuses on collecting data from IoT devices to an AP or an UAV using centralized approach with little emphasis on further transmitting it to the core network through a backhaul link. The algorithms used for data collection must be optimized, considering the energy constraints of IoT devices. Moreover, the backhaul link must be capable of handling the amounts of data generated by IoT devices while also providing high reliability. Thus, developing low-complexity data collection algorithm for IoT networks, coupled with a robust backhaul link, is essential to ensure seamless connectivity with the core network. Based on the preceding discussion, it is necessary to develop efficient algorithms for data collection in challenging terrain for IoT networks. Further, ensuring the reliable data transmission from the UAV to the core network is crucial for information processing, necessitating a robust backhaul link.

5.2 Motivation and Contributions

Current research primarily focuses on collecting data from IoT devices to an AP or an UAV using centralized approach with little emphasis on further transmitting it to the core network through a backhaul link. The algorithms used for data collection must be optimized, considering the energy constraints of IoT devices. Moreover, the backhaul link must be capable of handling the amounts of data generated by IoT devices while also providing high reliability. Thus, developing low-complexity data collection algorithm for IoT networks, coupled with a robust backhaul link, is essential to ensure seamless connectivity with the core network. The use of triple-technology hybrid wireless backhaul integrated for data collection from an IoT network with distributed selection of AN is not available in the literature.

In this chapter, we investigate end-to-end performance of data collection from an IoT network in hard-to-access terrains transferred to the core network via an intermediate UAV and a high-speed wireless backhaul link. The major contributions are as follows:

- We develop a self-configuring protocol for AN selection, which sends a data packet collected from the IoT network to a UAV. Selecting a single AN requires local communication from each device to the AN, thereby eliminating independent transmission from each device to the UAV.

- We utilize a hybrid triple-technology wireless backhaul, which simultaneously transmits the collected data from the UAV to the core network using mmWave, FSO, and THz links. The inclusion of THz connectivity into the current hybrid mmWave/FSO system brings about system diversity, resulting in improved performance, increased reliability, and superior QoS in different scenarios, particularly in challenging weather conditions.

- We also integrate the IoT network and backhaul link employing the DF protocol at the UAV and analyze the physical layer performance using the outage probability and average BER.

5.3 System Description and Channel Models

The system model illustrated in Fig. 5.1 shows a network of n IoT devices in hard-to-reach terrain. These devices transmit and receive critical sensing data to and from a backhaul network through a UAV. In challenging terrain, installing traditional base stations may be impractical or difficult due to physical or geographical limitations. The use of UAVs as relays between the IoT devices and the core network offers several advantages, such as mobility, flexibility, rapid deployment capabilities, and coverage extension potential.

Instead of transmitting the data from every IoT device directly to the UAV, the other devices in the network send their data to the n^* device, termed as the AN (selected through a self-configuring protocol discussed in the next section) with an SNR $\gamma_n^{\mathrm{local}}$ at the AN, where $n = 1, 2, 3, \cdots N$ excluding the AN device n^*. The AN further transmits the collected data from all the other devices to the UAV for efficient transmission. We define the SNR for the i-th IoT device at the UAV as $\gamma_i = \bar{\gamma}^{\mathrm{IoT}}|h_f|^2$, where h_f denotes the channel gain coefficient, and $\bar{\gamma}^{\mathrm{IoT}}$ denotes the average SNR. Assuming Rayleigh fading, γ_i is random variable with the PDF $f_{\gamma_i}^{\mathrm{IoT}}(\gamma) = \frac{1}{\bar{\gamma}^{\mathrm{IoT}}}\exp(-\frac{\gamma}{\bar{\gamma}^{\mathrm{IoT}}})$ and CDF $F_{\gamma_i}^{\mathrm{IoT}}(\gamma) = 1 - e^{-\lambda\frac{\gamma}{\bar{\gamma}^{\mathrm{IoT}}}}$.

We employ a DF-assisted UAV to integrate the IoT link with a wireless backhaul. We use a hybrid transmission approach that employs three high-bandwidth wireless technologies, namely mmWave, FSO, and THz, simultaneously from the UAV to the core network.

In the following, we describe the fading channel models of the backhaul link involving mmWave, FSO, and THz. We define the SNR for mmWave, FSO, and THz channels as $\gamma^{\mathrm{mW}} = \bar{\gamma}^{\mathrm{mW}}|h_{fp}^{\mathrm{FTR}}|^2$, $\gamma^{\mathrm{FSO}} = \bar{\gamma}^{\mathrm{FSO}}|h_f^{\mathcal{F}}|^2$, and $\gamma^{\mathrm{THz}} = \bar{\gamma}^{\mathrm{THz}}|h_{fp}^{\mathrm{THz}}|^2$, where $\bar{\gamma}^{\mathrm{mW}}$, $\bar{\gamma}^{\mathrm{FSO}}$, and $\bar{\gamma}^{\mathrm{THz}}$ denotes the average SNR of the respective transmission technologies.

To model the small-scale fading in the mmWave band, we use the FTR fading channel. The FTR channel model is specifically designed to capture the statistical properties of a received signal that consists of dominant specular components along with random fluctuations. It has

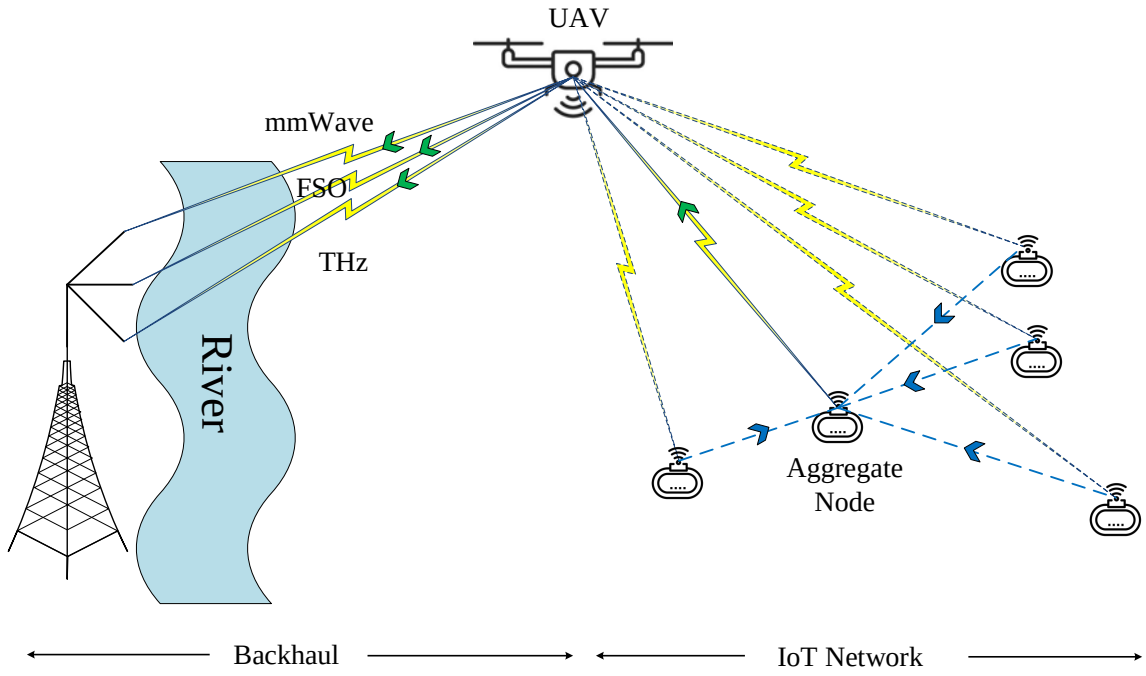

Figure 5.1: System model consisting of data collection from IoT network and triple-technology hybrid backhaul.

been shown to provide a more accurate representation of small-scale fading measurements in mmWave communications compared to other fading models [154]. The PDF and CDF of the FTR fading channel can be expressed as follows :

$$f_{\gamma}^{\mathrm{mW}}(\gamma) = \frac{m^m}{\Gamma(m)} \sum_{j=0}^{\infty} \frac{K^j d_j \gamma^j}{(\Gamma(j+1))^2 (2\zeta^2)^{j+1} (\bar{\gamma}^{\mathrm{mW}})^{j+1}} G_{0,1}^{1,0}\left(\frac{\gamma}{2\zeta^2 \bar{\gamma}^{\mathrm{mW}}} \middle| \begin{matrix} - \\ 0 \end{matrix} \right) \tag{5.1}$$

$$F_{\gamma}^{\mathrm{mW}}(\gamma) = \frac{m^m}{\Gamma(m)} \sum_{j=0}^{\infty} \frac{K^j d_j \gamma^j}{(\Gamma(j+1))^2 (\bar{\gamma}^{\mathrm{mW}})^{j}} G_{1,2}^{1,1}\left(\frac{\gamma}{2\zeta^2 \bar{\gamma}^{\mathrm{mW}}} \middle| \begin{matrix} 1 \\ 1+j, 0 \end{matrix} \right) \tag{5.2}$$

where K denotes the ratio between the average power of the dominant component and that of the multi-path, m represents the index of fading severity, and Δ signifies the similarity between the two dominant waves. The term ζ^2 corresponds to the variance of diffused components, which satisfies $\zeta^2 = \frac{1}{2(1+K)}$ for the normalized averaged SNR. Additionally, the factor d_j was initially defined in [154] and updated in [155] with an additional factor.

The misalignment of antennas between the IoT device and the UAV, as well as the disorientation of the UAV, can lead to antenna misalignment errors in the FSO link. Thus, the PDF of

the antenna misalignment error is given by [194] [195]:

$$f_{h_p}(h_p) = \frac{\phi}{S_0}\left(\frac{h_p}{S_0}\right)^{\phi-1}; \quad 0 \leq h_p \leq S_0 \tag{5.3}$$

Here, S_0 is defined as $\mathrm{erf}(v_{\min})\mathrm{erf}(v_{\max})$, with $v_i = \frac{\zeta}{w(L_2)}\sqrt{\frac{\pi}{2\chi_i}}$ for $i \in \{\min, \max\}$. We define $\chi_{\min} = \frac{2}{\chi_y+\chi_z+\sqrt{(\chi_y-\chi_z)^2+4\chi_{yz}^2}}$ and $\chi_{\max} = \frac{2}{\chi_y+\chi_z-\sqrt{(\chi_y-\chi_z)^2+4\chi_{yz}^2}}$, where $\chi_y = \cos^2(\theta)+\sin^2(\theta)\cos^2(\delta)$, $\chi_z = \sin^2(\theta)$, and $\chi_{yz} = -\cos(\theta)\sin(\theta)\sin(\delta)$ with θ and δ are defined in [194]. The radius of the effective area of the UAV antenna is denoted by ζ. The beam-width at distance L_2, given by $w(L_2)$, is given by $w(L_2) = w_0\sqrt{1+\left(1+\frac{2w_0^2}{\chi^2(L_2)}\right)\left(\frac{cL_2}{\pi f w_0^2}\right)^2}$, where w_0 represents the beam-waist radius, c is the speed of light, f is the transmission frequency, and $\chi(L_2) = (0.55C_n^2k^2L_2)^{-\frac{3}{5}}$. Here, C_n^2 denotes the index of the refraction structure parameter, and $k = \frac{2\pi f}{c}$ represents the wave number. The value of ϕ in (5.3) is defined as $\phi = \frac{k_m(w(L_2))^2}{4\sigma_p^2+4d_x^2\sigma_0^2}$, where $k_m = \frac{k_{\min}+k_{\max}}{2}$ and $k_i = \frac{\sqrt{\pi}\chi_i\mathrm{erf}(v_i)}{2v_i\exp(-v_i^2)}$ for $i \in \min, \max$.

We utilize $\mathcal{F}$-turbulence channel to model the turbulence in the FSO link. The $\mathcal{F}$-turbulence channel is a suitable choice for modeling FSO wireless channels exhibiting weak and strong irradiance fluctuations. It offers a more accurate fit to experimental and computer simulation data than other models. Additionally, the density and distribution functions of the $\mathcal{F}$-turbulence channel can be represented in a simplified form, making it convenient for modeling and analysis purposes[118]. The PDF and CDF of the FSO channel experiencing turbulence in the presence of the zero-boresight antenna misalignment error are given by [118]

$$f_\gamma^{\mathrm{FSO}}(\gamma) = \frac{\alpha\phi\gamma^{-\frac{1}{2}}G_{2,2}^{2,1}\left[\frac{\alpha\gamma^{\frac{1}{2}}}{\psi(\bar{\gamma}^{\mathrm{FSO}})^{\frac{1}{2}}}\middle|\begin{matrix}-\beta,\phi\\ \beta-1,\phi-1\end{matrix}\right]}{(\bar{\gamma}^{\mathrm{FSO}})^{\frac{1}{2}}\psi\Gamma(\alpha)\Gamma(\beta)} \tag{5.4}$$

$$F_\gamma^{\mathrm{FSO}}(\gamma) = \frac{\alpha_F\phi\gamma^{\frac{1}{2}}G_{3,3}^{2,2}\left[\frac{\alpha\gamma^{\frac{1}{2}}}{\psi(\bar{\gamma}^{\mathrm{FSO}})^{\frac{1}{2}}}\middle|\begin{matrix}-\beta,0,\phi\\ \beta-1,\phi-1,-1\end{matrix}\right]}{(\bar{\gamma}^{\mathrm{FSO}})^{\frac{1}{2}}\psi\Gamma(\alpha)\Gamma(\beta)} \tag{5.5}$$

where $\alpha = \frac{1}{\exp(\sigma_{\ln S}^2)-1}$, $\beta = \frac{1}{\exp(\sigma_{\ln \mathcal{L}}^2)-1}$, and $\psi = (\beta-1)S_0$. The terms $\sigma_{\ln S}^2$ and $\sigma_{\ln \mathcal{L}}^2$ represent the variances of small and large scale log-irradiance, respectively [118].

For the THz link, recently, the authors in [160] have demonstrated through experiments that short-term fading in outdoor THz environments can be precisely modeled using a Gaussian mixture fading model. The PDF of the Gaussian mixture distribution is given by:

$$f_{|h_f|}^{\mathrm{THz}}(x) = \sum_{i=1}^{K} w_i \frac{\exp\left(-\frac{(x-\mu_i)^2}{2\sigma_i^2}\right)}{\sqrt{2\pi}\sigma_i} \tag{5.6}$$

where the mean and standard deviation of the i-th Gaussian mixture component are denoted by μ_i and σ_i, respectively. The number of GM components is represented by K, and the weight of the i-th mixture component is given by $w_i \in [0, 1]$ such that $\sum_{i=1}^{K} w_i = 1$.

Previous research studies have used the FSO antenna misalignment error model for the THz band to analyze performance. We use a new antenna misalignment error model designed specifically for the THz band as proposed by the authors in [152]. The model is suitable for aerial mobile communication, with the PDF given as:

$$f_{h_p}^{\mathrm{THz}}(y) = -\rho^2 \ln(y) y^{\rho-1} \tag{5.7}$$

where $0 < y < 1$ and ρ is the antenna misalignment error parameter. Higher values of ρ correspond to the lower antenna misalignment errors and vice versa.

5.4 Protocol Description for Aggregate-Node Selection

Consider a scenario where an IoT network consists of N devices, and each device has an independent data packet that needs to be transmitted to a core network. To facilitate this transmission, we employ a UAV as a relay. There are two potential approaches for transmitting data from each device to the UAV: (i) direct transmission from each device to the UAV, or (ii) the devices send their data to a chosen AN, which then transmits the aggregated data to the UAV. We opt for the second method, wherein N-1 devices locally transfer their data to the AN selected to minimize power consumption and reduce transmission overhead.

The choice of AN can be made using either a centralized procedure, in which the UAV measures the SNR of each device and selects the device with the highest SNR as the AN. However, under a distributed approach, each device undergoes a self-configuring process to become an AN. In order to simplify the centralized control complexity at the UAV, we employ a distributed algorithm to select AN from a set of N IoT devices [196]. Our study assumes that each IoT device measures its own SNR and can become the AN based on a back-off time. A common function based on the PDF of the SNR $f_{\gamma}^{\mathrm{IoT}}(\gamma) = \frac{1}{\bar{\gamma}^{\mathrm{IoT}}} e^{-\frac{\gamma}{\bar{\gamma}^{\mathrm{IoT}}}}$ is taken to compute the back-off time τ_i by mapping $\tau_i = f_{\gamma}^{\mathrm{IoT}}(\gamma_i)$, where γ_i is the SNR of the i-th device. The device with the minimum $\tau_i < \tau_j, \forall i, j, i \neq j$ establishes communication with all other devices by announcing itself as the AN over a control channel. Note that the distributed protocol introduces latency corresponding to the back-off time of the AN device.

Subsequently, other IoT devices share their respective data packets with the AN at an SNR $\gamma_n^{\mathrm{local}}$, where $n = 1, 2, 3, \cdots, N$ excluding the AN device index. The AN transmits the combined data from all the devices to the UAV. Upon receiving the data, the UAV applies the DF protocol and forwards the data to the backhaul link using mmWave, FSO, and THz technologies by applying a frequency up-converter for the mmWave and the THz and a RF to optical converter for the FSO. A schematic implementation approach to the protocol is described in

Algorithm 1 Distributed Data Collection from IoT Network

Initialization:

1. **PDF Estimation**—Find the PDF of SNR $f_{\gamma}^{\mathrm{IoT}}(\gamma) = \frac{1}{\bar{\gamma}^{\mathrm{IoT}}} e^{-\frac{\gamma}{\bar{\gamma}^{\mathrm{IoT}}}}$ by fitting instantaneous SNR from IoT devices to the UAV.

2. **Coherence Time**— Estimate the coherence time t^{IoT} of the channel between the UAV and IoT devices.

3. **Throughput Estimation**— Estimate the throughput of the transmission as $R = \min(R^{\mathrm{BHL}}, R^{\mathrm{IoT}})$, where R^{BHL}, and R^{IoT} is the throughput of backhaul link and IoT network, respectively.

4. **Data Packet Size**— Estimate the data packet size for the i-th device as $L_i = (R \times t^{\mathrm{IoT}})/N$ such that the packet size of the AN becomes $L = NL_i$,

For each new packet L do
A. Selection of AN — For each IoT device $i = 1$ to N

1. The i-th device measures its own SNR γ_i and computes back-off time τ_i by mapping $\tau_i = f_{\gamma}^{\mathrm{IoT}}(\gamma_i)$

2. The device with minimum $\tau_i < \tau_j, \forall i, j, i \neq j$ communication with all other devices announcing being the AN.

3. All the devices send their sensing information to the AN.

B. Transmission —

1. The AN transmits the training data to the UAV. The UAV estimates the channel using the training data.

2. The AN transmits the information data to the UAV

3. The UAV applies the DF protocol to decode the data.

4. The UAV forwards the data to the backhaul link using mW, FSO, and THz technologies by applying a frequency up-converter for mW and THz and RF to optical converted for FSO.

B. Data Collection —

1. The signals from the backhaul link are received at a base station.

2. The base station applies MRC or OSC to decode the data from the UAV.

3. The decoded data is sent to the central unit for post-processing.

End

Algorithm 1. The average communication resources (such as transmit power) needed for transmitting data from the IoT devices to the AN through local communication will be significantly lower than the direct transmission from each device to the UAV at a similar QoS. Thus, we assume $\gamma_n^{\text{local}} >> \gamma_i$ such that the performance is limited by the link between the AN (selected from N IoT devices) and UAV. It is important to consider that the proposed approach of utilizing multiple high-frequency bands in the backhaul link comes with the trade-off of improved performance. While it offers potential benefits regarding increased reliability and QoS, it also introduces the challenge of managing the computational demands required for signal processing.

5.5 Statistical Results for Triple Technology

In this section, we derive the PDF and CDF for the hybrid backhaul using MRC and OSC diversity schemes. To obtain the statistical analysis of the hybrid backhaul, first, we require the PDF and CDF of the SNR of the outdoor THz channel combined with the new statistical model for antenna misalignment errors. To understand the derivation process, we outline the steps involved before delving into the specific details. The derivation begins by developing the PDF and CDF for the Gaussian outdoor THz channel model with THz antenna misalignment errors by utilizing the Mellin Barnes type integral and generalized Fox's H-function. Next, we derive the PDF and CDF for the hybrid backhaul system employing the MRC and OSC diversity schemes. To obtain the statistical results for MRC, we employ the MGF approach to calculate the sum of random variables. However, for the OSC, we utilize the order statistics to determine the signal with the maximum SNR.

Lemma 5.1. *The PDF and CDF of the SNR for the Gaussian outdoor THz channel combined with the statistical model for THz antenna misalignment error is given by*

$$f_{\gamma}^{\text{THz}}(\gamma) = \sum_{i=1}^{K} \frac{\rho^2 w_i \exp\left(\frac{-\mu_i^2}{2\sigma_i^2}\right)\gamma^{-\frac{1}{2}}}{2\sqrt{2\pi}\sigma_i(\bar{\gamma}^{\text{THz}})^{\frac{1}{2}}} H_{2,2:0,1;0,1}^{0,2:1,0;1,0}\left[\frac{\gamma}{\bar{\gamma}^{\text{THz}}}, \frac{-2\mu_i\gamma^{\frac{1}{2}}}{(\bar{\gamma}^{\text{THz}})^{\frac{1}{2}}}\middle| \begin{matrix} T_1 \\ T_2 \end{matrix}\right] \tag{5.8}$$

$$F_{\gamma}^{\text{THz}}(\gamma) = \sum_{i=1}^{K} \frac{\rho^2 w_i \exp\left(\frac{-\mu_i^2}{2\sigma_i^2}\right)\gamma^{\frac{1}{2}}}{2\sqrt{2\pi}\sigma_i(\bar{\gamma}^{\text{THz}})^{\frac{1}{2}}} H_{3,3:0,1;0,1}^{0,3:1,0;1,0}\left[\frac{\gamma}{\bar{\gamma}^{\text{THz}}}, \frac{-2\mu_i\gamma^{\frac{1}{2}}}{(\bar{\gamma}^{\text{THz}})^{\frac{1}{2}}}\middle| \begin{matrix} T_3 \\ T_4 \end{matrix}\right] \tag{5.9}$$

where $T_1 = \{(\rho-1;2,1)^2\} : \{-\};\{-\}$, $T_2 = \{(\rho-2;2,1)^2\} : \{(0,1)\};\{(0,1)\}$, $T_3 = \{(\rho-1;2,1)^2,(0;2,1)\} : \{-\};\{-\}$, *and* $T_4 = \{(\rho-2;2,1)^2,(-1;2,1)\} : \{(0,1)\};\{(0,1)\}$.

Proof. Proof is given in Appendix 5.1. ■

Next, we apply the diversity schemes (MRC and OSC) to improve the performance of the backhaul link. For the BHL-MRC, the received signals from the UAV are combined to

maximize the SNR. Thus, the combiner output SNR is the sum of the SNRs of each wireless link:

$$\gamma^{\mathrm{MRC}} = \gamma^{\mathrm{mW}} + \gamma^{\mathrm{FSO}} + \gamma^{\mathrm{THz}} \tag{5.10}$$

Here, we use the MGF based approach to develop a statistical analysis for the MRC system. The PDF of the SNR for the BHL-MRC can be derived using the inverse Laplace transform as

$$f_{\gamma}^{\mathrm{MRC}} = \frac{1}{2\pi \jmath} \int_{\mathcal{L}} \mathcal{M}_{\gamma}^{\mathrm{MRC}}(s) e^{s\gamma} ds \tag{5.11}$$

where $\mathcal{L}$ denotes the contour, and $\mathcal{M}_{\gamma}^{\mathrm{MRC}}(s)$ denotes the MGF of γ^{MRC}, which is defined as

$$\mathcal{M}_{\gamma}^{\mathrm{MRC}}(s) = \mathcal{M}_{\gamma}^{\mathrm{mW}}(s) \mathcal{M}_{\gamma}^{\mathrm{FSO}}(s) \mathcal{M}_{\gamma}^{\mathrm{THz}}(s) \tag{5.12}$$

with MGF of the individual link given as

$$\mathcal{M}_{\gamma}(s) = \int_{0}^{\infty} e^{-s\gamma} f_{\gamma}(\gamma) d\gamma \tag{5.13}$$

In the following theorem, we develop the statistical analysis of the SNR for the BHL-MRC:

Theorem 5.1. *The PDF and CDF of the SNR for BHL-MRC with triple technology using mmWave, FSO, and THz are given by*

$$\begin{aligned} f_{\gamma}^{\mathrm{MRC}}(\gamma) =& \frac{m^m}{\Gamma(m)} \sum_{j=0}^{\infty} \frac{K^j d_j \gamma^{1+j}}{(\Gamma(j+1))^2 (2\zeta^2)^{j+1} (\bar{\gamma}^{\mathrm{mW}})^{j+1}} \sum_{i=1}^{K} \frac{\rho^2 w_i \exp\left(\frac{-\mu_i^2}{2\sigma_i^2}\right)}{2\sqrt{2\pi}\sigma_i (\bar{\gamma}^{\mathrm{THz}})^{\frac{1}{2}}} \frac{\alpha\phi}{\psi\Gamma(\alpha)\Gamma(\beta)} \\ & \times H_{3,3:1,1;2,2;1,0;1,0}^{0,3:1,1;2,2;1,0;1,0} \left[\frac{\gamma}{2\zeta^2 \bar{\gamma}^{\mathrm{mW}}}, \frac{\alpha\gamma^{\frac{1}{2}}}{\psi(\bar{\gamma}^{\mathrm{FSO}})^{\frac{1}{2}}}, \frac{\gamma}{\bar{\gamma}^{\mathrm{THz}}}, \frac{-2\mu_i\gamma^{\frac{1}{2}}}{(\bar{\gamma}^{\mathrm{THz}})^{\frac{1}{2}}} \middle| \begin{matrix} T_3 \\ T_4 \end{matrix} \right] \end{aligned} \tag{5.14}$$

where $T_3 = \left\{(\rho-1;0,0,2,1)^2, (\frac{1}{2};0,0,1,\frac{1}{2})\right\} : \left\{(-j,1)\right\}; \left\{(-\beta,1),(\frac{1}{2},\frac{1}{2})(\phi,1)\right\}; \left\{-\right\}; \left\{-\right\}$ *and* $T_4 = \left\{(\rho-2;0,0,2,1)^2, (-j;1,\frac{1}{2},1,\frac{1}{2})\right\} : \left\{(0,1)\right\}; \left\{(\beta-1,1),(\phi,1)\right\}; \left\{(0,1)\right\}; \left\{(0,1)\right\}$.

$$\begin{aligned} F_{\gamma}^{\mathrm{MRC}}(\gamma) =& \frac{m^m}{\Gamma(m)} \sum_{j=0}^{\infty} \frac{K^j d_j \gamma^{2+j}}{(\Gamma(j+1))^2 (2\zeta^2)^{j+1} (\bar{\gamma}^{\mathrm{mW}})^{j+1}} \sum_{i=1}^{K} \frac{\rho^2 w_i \exp\left(\frac{-\mu_i^2}{2\sigma_i^2}\right)}{2\sqrt{2\pi}\sigma_i (\bar{\gamma}^{\mathrm{THz}})^{\frac{1}{2}}} \frac{\alpha\phi}{\psi\Gamma(\alpha)\Gamma(\beta)} \\ & \times H_{4,4:1,1;3,2;0,1;0,1}^{0,4:1,1;2,2;1,0;1,0} \left[\frac{\gamma}{2\zeta^2 \bar{\gamma}^{\mathrm{mW}}}, \frac{\alpha\gamma^{\frac{1}{2}}}{\psi(\bar{\gamma}^{\mathrm{FSO}})^{\frac{1}{2}}} \frac{\gamma}{\bar{\gamma}^{\mathrm{THz}}}, \frac{-2\mu_i\gamma^{\frac{1}{2}}}{(\bar{\gamma}^{\mathrm{THz}})^{\frac{1}{2}}} \middle| \begin{matrix} T_5 \\ T_6 \end{matrix} \right] \end{aligned} \tag{5.15}$$

where $T_5 = \left\{(\rho-1;0,0,2,1)^2, (\frac{1}{2};0,0,1,\frac{1}{2}), (-1-j;1,\frac{1}{2},1,\frac{1}{2})\right\} : \left\{(-j,1)\right\}; \left\{(-\beta,1),(\frac{1}{2},\frac{1}{2}),(\phi,1)\right\}; \left\{-\right\}; \left\{-\right\}$; *and* $T_6 = \left\{(\rho-2;0,0,2,1)^2, (-j;1,\frac{1}{2},1,\frac{1}{2}), (-2-j;1,\frac{1}{2},1,\frac{1}{2})\right\} : \left\{(0,1)\right\}; \left\{(\beta-1,1),(\phi,1)\right\}; \left\{(0,1)\right\}; \left\{(0,1)\right\}$.

Proof. See Appendix 5.2. ■

In BHL-OSC, the SNR of each link (i.e., mmWave, FSO, and THz links) is measured, and the link with the maximum SNR value is selected. The resulting SNR, in this case, will be

$$\gamma^{\mathrm{OSC}} = \max\{\gamma^{\mathrm{mW}}, \gamma^{\mathrm{THz}}, \gamma^{\mathrm{FSO}}\} \tag{5.16}$$

Substituting the CDFs of the individual links from (5.2), (5.5), and (5.9) into (5.17), we get the CDF of the BHL-OSC, as compiled in the following proposition:.

Proposition 5.1. *The CDF is given by [174]*

$$F_{\gamma}^{\mathrm{OSC}}(\gamma) = F_{\gamma}^{\mathrm{mW}}(\gamma) F_{\gamma}^{\mathrm{FSO}}(\gamma) F_{\gamma}^{\mathrm{THz}}(\gamma) \tag{5.17}$$

Proof. The proof is a straightforward application of the maximum of 3 random variables. ■

Fox's H representation for statistical analysis is increasingly prevalent in the research community. This allows researchers to obtain insights into the behavior of complex systems and processes, which would have been difficult to obtain otherwise. Moreover, it provides asymptotic expressions in terms of the simpler Gamma function for a better understanding of the performance and identifying key system parameters.

5.6 Data Collection Performance

In this section, we will use the statistical results obtained in the previous section to analyze physical layer performance metrics such as the outage probability and average BER for the considered system. Additionally, we derive an asymptotic expression for the outage probability in high SNR regions to determine the diversity order of the integrated system for better engineering insight.

Using the DF relay scheme at the UAV, the resulting SNR of the integrated link can be expressed as follows:

$$\gamma^{\mathrm{IL}} = \min\{\gamma^{\mathrm{IoT}}, \gamma^{\mathrm{BHL}}\} \tag{5.18}$$

where the SNR of the AN at the UAV is given by [174]

$$\gamma^{\mathrm{IoT}} = \max\left\{\gamma_1, \gamma_2, \cdots, \gamma_N\right\} \tag{5.19}$$

where γ_1, γ_2, $\cdots$ γ_N are individual SNRs of the N IoT devices at the UAV under Rayleigh fading channel. The CDF of the device with maximum SNR is given by [174]

$$F_{\gamma}^{\mathrm{IoT}}(\gamma) = \prod_{i=1}^{N} F_{\gamma_i}(\gamma) \tag{5.20}$$

Considering identical fading characteristics, the resultant CDF can be given as

$$F_{\gamma}^{\mathrm{IoT}}(\gamma) = (F_{\gamma_i}(\gamma))^N = \left(1 - e^{-\lambda \frac{\gamma}{\bar{\gamma}^{\mathrm{IoT}}}}\right)^N \tag{5.21}$$

We use the binomial expansion as $(x+y)^n = \sum_{k=0}^{n} \binom{n}{k} x^{n-k} y^k$: $(1-x)^n = \sum_{k=0}^{n} \binom{n}{k} (-x)^k$ to get (5.21) as:

$$F_{\gamma}^{\mathrm{IoT}}(\gamma) = \sum_{k=0}^{N} \binom{N}{k} \left(-e^{-\frac{\lambda\gamma}{\bar{\gamma}^{\mathrm{IoT}}}}\right)^k \tag{5.22}$$

5.6.1 Outage Probability

Outage probability refers to the probability that the SNR of a communication system falls below a certain threshold level γ_{th}, i.e., $P(\gamma < \gamma_{\mathrm{th}})$. The outage probability of the integrated link is given in the following lemma.

Lemma 5.2. *The outage probability of the integrated link $P_{\mathrm{out}}^{\mathrm{IL}}$ is given by*

$$P_{\mathrm{out}}^{\mathrm{IL}} = P_{\mathrm{out}}^{\mathrm{IoT}} + P_{\mathrm{out}}^{\mathrm{BHL}} - P_{\mathrm{out}}^{\mathrm{IoT}} P_{\mathrm{out}}^{\mathrm{BHL}} \tag{5.23}$$

where $P_{\mathrm{out}}^{\mathrm{IoT}}$ is the outage probability of the IoT network and $P_{\mathrm{out}}^{\mathrm{BHL}}$ is the outage probability of the backhaul link.

Proof. Using (5.18), a simple application of the theory of random variables leads to the CDF of the integrated link:

$$F_{\gamma}^{\mathrm{IL}}(\gamma) = F_{\gamma}^{\mathrm{IoT}}(\gamma) + F_{\gamma}^{\mathrm{BHL}}(\gamma) - F_{\gamma}^{\mathrm{IoT}}(\gamma) F_{\gamma}^{\mathrm{BHL}}(\gamma) \tag{5.24}$$

Thus, the outage probability of the IoT link $P_{\mathrm{out}}^{\mathrm{IoT}}$ can be derived by substituting $\gamma = \gamma_{\mathrm{th}}$ in (5.22). To derive $P_{\mathrm{out}}^{\mathrm{BHL}}$, we substitute $\gamma = \gamma_{\mathrm{th}}$ in the CDF of the backhaul link, as given in (5.15) for MRC or in (5.17) for OSC. Compiling the outage probabilities of individual links, we get the outage probability of the integrated system in (5.23). ■

In order to determine the diversity order of the system, we express the outage probability in high SNR region using asymptotic expressions for both the backhaul and IoT links. To obtain the asymptotic outage probability for the BHL-MRC, we calculate the residue on the dominant poles, resulting in the following expression:

$$P_{\mathrm{out}}^{\mathrm{MRC}^{\infty}}(\gamma) = C_1 \left(\frac{\gamma}{\bar{\gamma}^{\mathrm{THz}}}\right)^{\frac{1}{2}} + C_2 \left(\frac{\gamma}{\bar{\gamma}^{\mathrm{THz}}}\right)^{\frac{\rho}{2}} + C_3 \left(\frac{\gamma}{\bar{\gamma}^{\mathrm{FSO}}}\right)^{\frac{\beta}{2}} + C_4 \left(\frac{\gamma}{\bar{\gamma}^{\mathrm{FSO}}}\right)^{\frac{\phi}{2}} + C_5 \left(\frac{\gamma}{\bar{\gamma}^{\mathrm{mW}}}\right)^{1} \tag{5.25}$$

where C_1, C_2, C_3, C_4 and C_5 are constants. It is evident by observing the exponents of average SNR in (5.25) that the diversity order of the BHL-MRC is $\min\left\{1, \frac{\beta}{2}, \frac{\phi}{2}, \frac{1}{2}, \frac{\rho}{2}\right\}$. Similarly, the

diversity order for the BHL-OSC can be obtained by individually calculating the diversity order for each of the three links in the backhaul, which turns out to be the same as that of the BHL-MRC. The diversity order for the N Rayleigh faded links equals to N. Hence, the diversity order of the outage probability for the integrated system is given:

$$DO^{\mathrm{OP}} = \min\Big\{1, \frac{\beta}{2}, \frac{\phi}{2}, \frac{1}{2}, \frac{\rho}{2}, N\Big\}. \tag{5.26}$$

The diversity order in (5.26) depicts design and deployment scenarios using various channel and system parameters. It should be noted that the factor of 1 is due to the FTR channel model for the mmWave propagation.

5.6.2 Average BER

The average BER refers to the average rate of bit errors in a communication system and is given by [165]

$$\bar{P}_e = \frac{q^p}{2\Gamma(p)} \int_0^\infty e^{-q\gamma} \gamma^{p-1} F_\gamma(\gamma) d\gamma \tag{5.27}$$

The modulation scheme selection is represented by the values of p and q, while $F_\gamma(\gamma)$ refers to the CDF of the communication system. Denote $\bar{P}_e^{\mathrm{IoT}}$ and $\bar{P}_e^{\mathrm{IoT}}$ as the average BER of the individual links: IoT and backhaul link (either using MRC or OSC), respectively.

Lemma 5.3. *The average BER of the integrated link is given by*

$$\bar{P}_e^{\mathrm{IL}} = \bar{P}_e^{\mathrm{IoT}} + \bar{P}_e^{\mathrm{BHL}} - \bar{P}_e^{\mathrm{IoT}} \bar{P}_e^{\mathrm{BHL}} \tag{5.28}$$

where

$$\bar{P}_e^{\mathrm{IoT}} = \frac{q^p}{2} \sum_{k=0}^{N} \binom{N}{k} (-1)^k \left(\frac{k\lambda\gamma}{\bar{\gamma}^{\mathrm{RF}}} + q \right)^{-p} \tag{5.29}$$

and

$$\begin{aligned} \bar{P}_e^{\mathrm{BHL}} =& \frac{m^m}{2\Gamma(m)\Gamma(p)} \sum_{j=0}^{\infty} \frac{K^j d_j q^{-j}}{(\Gamma(j+1))^2 (2\zeta^2)^{j+1} (\bar{\gamma}^{\mathrm{mW}})^{j+1}} \sum_{i=1}^{K} \frac{\rho^2 w_i \exp\left(\frac{-\mu_i^2}{2\sigma_i^2}\right)}{2\sqrt{2\pi}\sigma_i (\bar{\gamma}^{\mathrm{THz}})^{\frac{1}{2}}} \frac{\alpha\phi}{\psi\Gamma(\alpha)\Gamma(\beta)} \\ & \times H_{5,4:1,1;3,2;0,1;0,1}^{0,5:1,1;2,2;1,0;1,0} \left[\frac{\gamma\zeta^{-2}}{2q\bar{\gamma}^{\mathrm{mW}}}, \frac{\alpha\gamma^{\frac{1}{2}}}{\psi(q\bar{\gamma}^{\mathrm{FSO}})^{\frac{1}{2}}}, \frac{\gamma q^{-1}}{\bar{\gamma}^{\mathrm{THz}}}, \frac{-2\mu_i\gamma^{\frac{1}{2}}}{(q\bar{\gamma}^{\mathrm{THz}})^{\frac{1}{2}}} \middle| \begin{matrix} T_7 \\ T_8 \end{matrix} \right] \end{aligned} \tag{5.30}$$

where $T_7 = \big\{(\rho-1;0,0,2,1)^2, (\frac{1}{2};0,0,1,\frac{1}{2}), (-1-j;1,\frac{1}{2},1,\frac{1}{2}), (-1-p-j;1,\frac{1}{2},1,\frac{1}{2})\big\} : \big\{(-j,1)\big\}; \big\{(-\beta,1), (\frac{1}{2},\frac{1}{2})(\phi,1)\big\}; \big\{-\big\}; \big\{-\big\}$; *and* $T_8 = \big\{(\rho-2;0,0,2,1)^2, (-j;1,\frac{1}{2},1,\frac{1}{2}), (-2-j;1,\frac{1}{2},1,\frac{1}{2})\big\} : \big\{(0,1)\big\}; \big\{(\beta-1,1), (\phi,1)\big\}; \big\{(0,1)\big\}; \big\{(0,1)\big\}$.

Proof. The average BER of DF relaying using Gray coding can be represented as follows:

Table 5.1: List of Simulation Parameters

Parameter	**Value**	**Parameter**	**Value**
Carrier frequency - mmWave	50 GHz	Transmit power	0 dBm
Carrier frequency - THz	300 GHz	Noise Power (mmWave, FSO, THz)	-131 dBm
Carrier frequency - RF	800 MHz	Noise Power (RF)	-144 dBm
Operating Wavelength - FSO	750 nm	θ	$-\frac{\pi}{4}$
Transmitting Antenna Gain (mmWave)	10 dBi	δ	$\frac{3\pi}{4}$
Receiving Antenna Gain (mmWave)	26 & 27 dBi	σ_0	0.1 rad
Transmitting Antenna Gain (THz)	10 dBi	σ_p	0.05 rad
Receiving Antenna Gain (THz)	51 dBi	d_x	0.1
Transmitting Antenna Gain (RF)	0 dBi	w_0	1 mm
Receiving Antenna Gain (RF)	0 dBi	ρ	27.94
Backhaul link Distance	500 & 1 km	IoT Link Distance	100 m

[184]:

$$\bar{P}_e^{\mathrm{IL}} = \bar{P}_e^{\mathrm{IoT}} + \bar{P}_e^{\mathrm{BHL}} - \bar{P}_e^{\mathrm{IoT}} \bar{P}_e^{\mathrm{BHL}} \tag{5.31}$$

The derivation of the average BER for individual links are presented in Appendix 5.3. ■

Likewise, the ergodic capacity of the integrated link can also be derived by following a similar procedure but omitted to avoid redundancy.

5.7 Simulation and Numerical Results

In this section, we demonstrate the performance of the considered system by assessing the performance of the hybrid backhaul link and its integration with the IoT. We verify the accuracy of our derived analytical expressions through Monte Carlo simulations. We consider 50 terms for the convergence of the infinite series for the FTR channel in the mmWave band. We assume perfect channel knowledge at the base station to implement the BHL-MRC. To ensure consistency in our comparison, we maintained the same average SNR for all three links in the backhaul, i.e., $\bar{\gamma}^{\mathrm{mW}} = \bar{\gamma}^{\mathrm{FSO}} = \bar{\gamma}^{\mathrm{THz}} = \bar{\gamma}$. As a result, the system's performance is determined by the level of randomness rather than the path-gain of each channel. Our evaluation of the IoT network includes a channel coherence time of 1 ms and a data packet size of 1 kB for each device. We will showcase the backhaul link's effectiveness in different situations and then examine the integrated link's performance between the IoT and backhaul link. Table 5.1 provides the simulation parameter list.

First, in Fig. 5.2, we demonstrate the outage probability performance of the hybrid BHL-MRC and BHL-OSC with specific parameters ($m = 0.5, \Delta = 0.9, k = 1, \mu_i = 0, \sigma = 0.6$). In particular, Fig. 5.2(a) compares the proposed backhaul link's performance with an individual

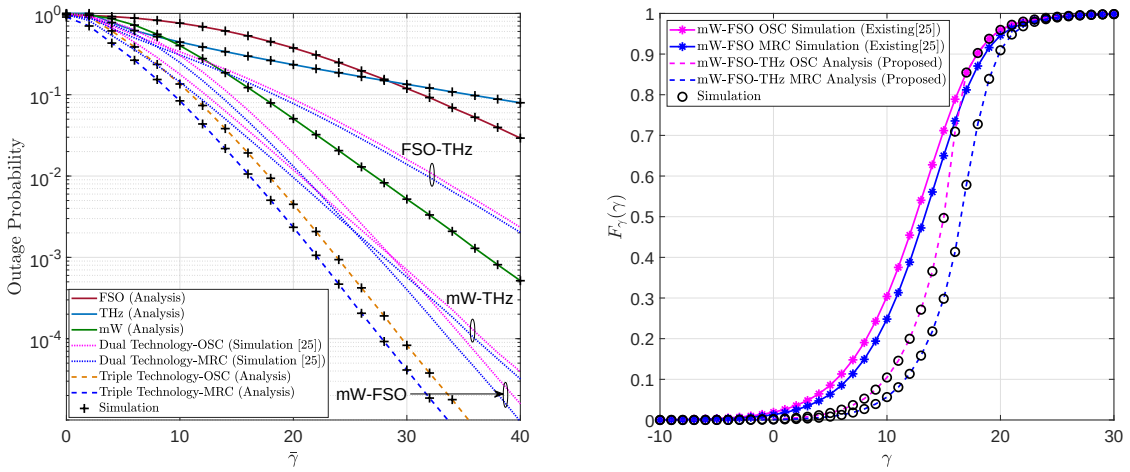

(a) Outage probability with $\gamma_{\text{th}} = 7$dB

(b) Outage probability Comparison with existing literature results

Figure 5.2: Outage probability performance of the Hybrid backhaul link with $m = 0.5, \Delta = 0.9, k = 1, \mu_i = 0, \sigma_i = 0.6$ and strong atmospheric turbulence.

link and any dual-technology backhaul, demonstrating that the proposed backhaul link outperforms both options. It can be observed from the figure that the system's outage performance improves almost 10 times for the triple-technology BHL-MRC than the existing dual-technology (mmWave-FSO) for an average SNR of 30 dB. Fig. 5.2(b) compares the outage probability of the proposed backhaul schemes with an existing mmWave-FSO backhaul link[118], highlighting that the dual-technology backhaul has a higher outage probability for a given value of average SNR.

Next, Fig. 5.3 shows the average BER of the proposed backhaul schemes compared to the existing mmWave-FSO backhaul link. The figures demonstrate that the proposed scheme has a better average BER than the existing dual-technology backhaul counterpart for a wide range of average SNR. The plots indicate that employing a triple-technology backhaul instead of an existing dual-technology backhaul can result in a saving of 5 dB of the transmitted power to achieve an average BER in the range of 10^{-3}-10^{-5}.

In Fig. 5.4, we demonstrate how the number of IoT devices impacts the outage probability and average BER performance of the integrated link. Fig. 5.4 displays the effect of outage probability and average BER performance of the mixed hybrid BHL-MRC and the IoT access link. As shown in Fig. 5.4(a), increasing the number of IoT devices improves the outage performance of the integrated system. At first, increasing the number of devices from 1 to 5 does not have a significant impact on the performance. However, as the number of devices increases, the average BER performance improves considerably. This suggests that having more devices can mitigate the randomness of the wireless channel, leading to a more reliable communication link. Similarly, Fig. 5.4(b) depicts a similar trend in the average BER performance as the number of IoT devices in the access link increases.

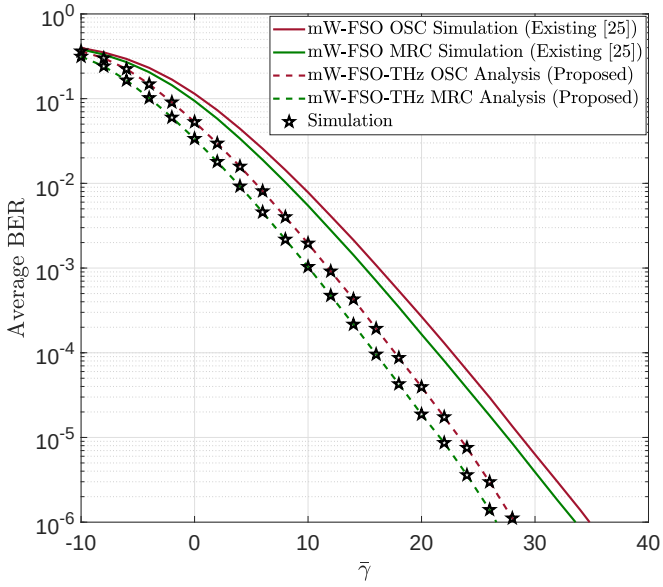

Figure 5.3: Average BER performance of the hybrid backhaul link with $m = 0.5, \Delta = 0.9, k = 1, \mu_i = 0, \sigma_i = 0.8$ and strong atmospheric turbulence.

In Fig. 5.5, we present the average BER performance of the integrated link using realistic simulation parameters, as specified in Table 5.1. We investigate the system performance with different distances for the backhaul and varying numbers of devices in the IoT network. Specifically, the distance between the IoT devices and the UAV is set at 100 m, while two distances are considered for the backhaul link, i.e., 500 m and 1 km. For the mmWave link, we employ the 3GPP path-loss model given by $H_{l_{\text{mW}}} = 32.4 + 17.3\log_{10}(d) + 20\log_{10}(10^{-9}f)$. This results in path-loss values of 113 dB at 500 m and 118.27 dB for the mmWave backhaul at a carrier frequency 50 GHz. The visibility range of the FSO link is adjusted to 370 m and 620 m, corresponding to the backhaul link distances of 500 m and 1 km, respectively. We consider both weak and strong turbulence scenarios for the FSO link. The path-loss for the FSO link is determined using $H_{l_{\text{FSO}}} = \exp(-\psi d)$, where ψ is the attenuation coefficient [118], resulting in path-loss values of 45.89 dB for 500 m and 52.78 dB for 1 km. For the THz link, the path loss due to the atmospheric absorption $H_{l_{\text{THz}}} = \exp\left(-\frac{1}{2}\kappa d\right)$, where κ is the absorption coefficient [34], yields path-loss values of 136.65 dB for 500 m and 143.36 dB for 1 km. For the AN to the UAV link, the 3GPP path-loss model results in a path-loss value of 65 dB for an average IoT link distance of 100 m. We fix the transmit power at 0 dBm, and utilizing the parameters provided in Table 5.1, we obtain an average SNR of 20 dB (500 m) and 13 dB (1 km) for all three links in the backhaul. In order to keep the average SNR of the RF link unchanged, it is necessary to decrease the transmitted power of the IoT devices. This would lead to a power savings of 23 dBm for a distance of 500 m and 30 dBm for a distance of 1 km. Note that we ignore the local communication between the IoT devices and the AN.

The plots in Fig. 5 demonstrate that the average BER performance of the integrated link improves as the number of devices in the IoT network increases. However, after approximately

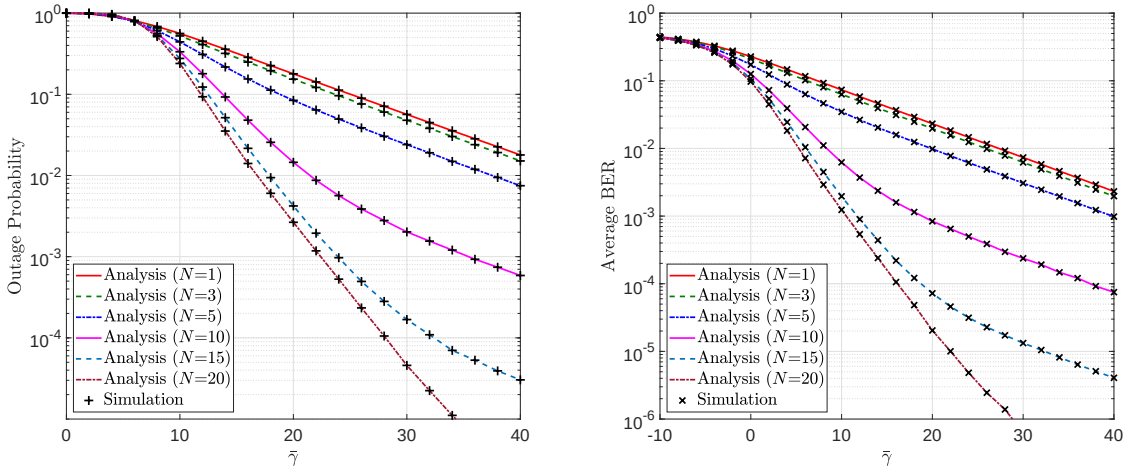

(a) Outage probability (b) Average BER

Figure 5.4: Outage probability and average BER performance of integrated link with $m = 0.5, \Delta = 0.9, k = 1, \mu_i = 0, \sigma_i = 0.6$ and strong turbulence with varying number of IoT devices in the access link.

20 devices, the average BER reaches a saturation point (a characteristic of the OSC technique). It is evident from the plots that the average BER increases as we increase the distance of the backhaul owing to higher atmospheric attenuation and path loss in the backhaul link. Further, we can illustrate the achievable data rate using the simulation scenario in Fig. 5. In Fig. 5, an average SNR of 20 dB gives a spectral efficiency of 8.28 bits/sec/Hz for the MRC and 7.71 bits/sec/Hz for the OSC. Similarly, setting parameters for the IoT network such that an average SNR of the AN is 20 dB (the same average SNR is required for dual-hop DF system to have more meaningful results of the relay-assisted system), giving an achievable spectral efficiency of 6.65 bits/sec/Hz. Thus, the backhaul link is sufficient to support the data collection from N=20 devices in the IoT network, each device having a packet size of 332 kb of data if 1 MHz of channel bandwidth is assumed for the AN.

The hybrid backhaul-based data collection network has the capability of delivering superior performance. However, a trade-off exists between performance and complexity in exchange for this benefit, which varies across operating conditions. Therefore, we have conducted comprehensive simulations to capture the behavior of the integrated link and presented a comparison between the proposed wireless backhaul and other existing technologies in Table 5.2 on page 114. We have created various use cases to identify the most suitable choice between single, dual, and triple-technology backhaul for different listed scenarios. We consider two types of channel conditions, namely Type-1 (poor) and Type-2 (good), for each of the mmWave (Type-1: $m = 0.5, \Delta = 0.9$; Type-2: $m = 20, \Delta = 0.1$), FSO (Type-1: strong turbulence; Type-2: weak turbulence), and THz (Type-1: $\sigma_i = 0.6$; Type-2: $\sigma_i = 1.1$) links, individually, as well as all possible combinations for low, moderate, and high SNR regions. The last column of each row shows the outage probability of the integrated link with the triple-technology BHL-MRC,

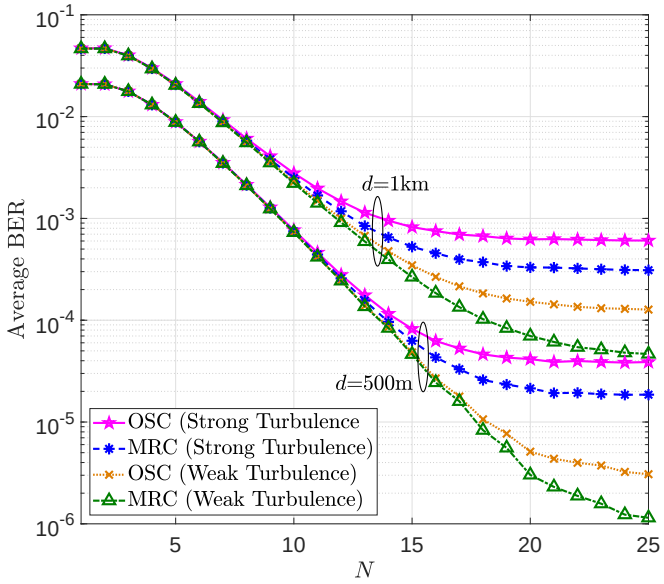

Figure 5.5: Effect of the number of IoT devices on the average BER performance of the integrated link.

while the other columns in that row indicate the outage probability of the particular scenario as the factor of the triple-technology BHL-MRC. This allows us to identify the best alternative to the triple-technology BHL-MRC based on the lowest factor in a single row for a given SNR range. The minimum factor for each row is highlighted for both single-technology and dual-technology BHL-MRC combinations. For instance, if we consider the Type-1 channel for all the individual links, the mmWave link alone provides a better outage probability at moderate and high SNR. However, the THz link performs better at low SNR for single-technology backhaul link. The mmWave-THz backhaul link outperforms the mmWave-FSO in low and moderate SNR, while the mmWave-FSO performs better in high SNR for the dual-technology backhaul link. However, choosing a backhaul technology depends on the specific network configuration and the acceptable level of outage probability, with a trade-off between network complexity and performance. Choosing a single, dual, or triple-technology backhaul based on the desired outage probability can reduce network complexity and power requirements. Nevertheless, the triple-technology backhaul consistently delivers superior performance regardless of the channel and SNR scenarios.

Our study provides a comprehensive investigation of the selection of hybrid schemes in different channel and SNR scenarios based on the trade-off between acceptable outage probability and the complexity of the hybrid backhaul. In particular, we found that the mmWave-THz backhaul link outperforms the mmWave-FSO in low and moderate SNR scenarios, while the mmWave-FSO performs better in high SNR for the dual-technology backhaul link. The triple-technology backhaul consistently delivers superior performance regardless of the channel and SNR scenarios.

Table 5.2: Comparison of outage probability for the integrated link using triple, dual, and single-technology based backhaul with $N = 5$ devices in the IoT network.

The Table can be read as follows: the outage probability of the triple-technology backhaul (given in the last column) is denoted by P_{out}, while X is the factor by which the outage probability of a single or dual-technology backhaul exceeds that of the triple-technology backhaul. Thus, the outage probability of different configurations P_{out} should be multiplied by the corresponding factor X, depicted in rows. For example, P_{out} (for mmWave at 5dB SNR with Type-1 channel) is $2.34 \times 0.34 = 0.79$.

Link / SNR	**nmWave** $X \times P_{\text{out}}$	**FSO** $X \times P_{\text{out}}$	**THz** $X \times P_{\text{out}}$	**nmWave-FSO** $X \times P_{\text{out}}$	**nmWave-THz** $X \times P_{\text{out}}$	**FSO-THz** $X \times P_{\text{out}}$	**nmWave-FSO-THz** P_{out}
Low (5dB)	2.34 (Type-1)	2.64 (Type-1)	2.00 (Type-1)	1.91	1.27	1.67	0.34
Low (5dB)	2.94 (Type-1)	3.10 (Type-1)	3.15 (Type-2)	2.41	1.42	2.30	0.27
Low (5dB)	2.92 (Type-1)	3.10 (Type-2)	2.49 (Type-1)	2.02	1.58	1.81	0.27
Low (5dB)	4.42 (Type-1)	4.67 (Type-2)	4.73 (Type-2)	3.1	2.12	2.63	0.18
Low (5dB)	2.42 (Type-2)	2.73 (Type-1)	2.10 (Type-1)	1.96	1.3	1.72	0.33
Low (5dB)	3.19 (Type-2)	3.59 (Type-1)	3.40 (Type-2)	2.58	1.43	2.48	0.25
Low (5dB)	3.00 (Type-2)	3.23 (Type-2)	2.62 (Type-1)	2.21	1.65	1.89	0.26
Low (5dB)	4.40 (Type-2)	4.62 (Type-2)	4.68 (Type-2)	3.15	1.96	2.60	0.18
Moderate (15dB)	9.94 (Type-1)	35.31 (Type-1)	20.00 (Type-1)	4.00	2.48	10.06	0.016
Moderate (15dB)	53.00 (Type-1)	188.33 (Type-1)	31.00 (Type-2)	21.33	2.77	13.77	0.003
Moderate (15dB)	31.80 (Type-1)	54.00 (Type-2)	64.00 (Type-1)	4.49	7.8	13.82	0.005
Moderate (15dB)	169.15 (Type-1)	287.23 (Type-2)	98.94 (Type-2)	23.89	8.83	16.28	9.4×10^{-4}
Moderate (15dB)	10.00 (Type-2)	48.46 (Type-1)	27.45 (Type-1)	4.18	2.56	13.81	11.6×10^{-3}
Moderate (15dB)	50.87 (Type-2)	245.65 (Type-1)	40.43 (Type-2)	21.17	2.78	17.96	2.3×10^{-3}
Moderate (15dB)	31.62 (Type-2)	72.97 (Type-2)	86.49 (Type-1)	4.54	8.05	18.68	3.7×10^{-3}
Moderate (15dB)	169.57 (Type-2)	391.30 (Type-2)	134.78 (Type-2)	24.35	9.28	22.17	6.9×10^{-4}
High (30dB)	139.47 (Type-1)	3157.90 (Type-1)	3526.30 (Type-1)	11.13	14.74	368.42	3.8×10^{-5}
High (30dB)	5300 (Type-1)	120000 (Type-1)	8000 (Type-2)	423	23.00	700	1×10^{-6}
High (30dB)	2650 (Type-1)	4080 (Type-2)	67000 (Type-1)	8.00	280	421	2×10^{-6}
High (30dB)	26500 (Type-1)	40800 (Type-2)	40000 (Type-2)	80	115	235	2×10^{-7}
High (30dB)	119.35 (Type-2)	3871 (Type-1)	4322.6 (Type-1)	8.94	13.23	451.61	3.1×10^{-5}
High (30dB)	9250 (Type-2)	300000 (Type-1)	20000 (Type-2)	692.50	40.00	1750	4×10^{-7}
High (30dB)	1850 (Type-2)	4080 (Type-2)	67000 (Type-1)	5.00	205	421	2×10^{-6}
High (30dB)	37000 (Type-2)	81600 (Type-2)	8000 (Type-2)	100	160	470	1×10^{-7}

5.8 Chapter Summary

In this chapter, we analyzed the end-to-end performance of data collection from an IoT network located in hard-to-reach areas, which is transferred to the core network through an intermediate UAV and a high-speed wireless backhaul link. We designed a self-configuring algorithm for AN selection from IoT devices in the network. Further, we utilized a novel hybrid transmission technique for wireless backhaul, which transmitted data packets simultaneously over mmWave, FSO, and THz channels using OSC and MRC. We assessed the outage probability and average BER performance of the integrated link that comprises the IoT and backhaul link. Moreover, we derived a simpler asymptotic expression for the outage probability in the high SNR region and determined the diversity order for the integrated link.

By leveraging the collective strength of a triple-technology backhaul and multiple IoT devices, it may be possible to enhance the overall performance and reliability of the communication link for data collection. This could have a wide range of potential applications, such as in environmental monitoring, disaster response, military communication, and other scenarios where reliable communication is essential. Our proposed solution and statistical analysis provide valuable insights into the performance of IoT networks and can be helpful for the future design and optimization of similar networks. Further, it can potentially steer the development of more practical and robust solutions, addressing beam alignment issues and the increased computational demands for the UAV in real-world situations.

5.9 Appendix

5.9.1 Appendix 5.1: Proof of Lemma 5.1

Substituting the limits of (5.6) and (5.7), the joint PDF of $|h_{fp}| = |h_f|h_p$ can be expressed as [174]

$$f_{h_{fp}}(z) = \int_0^1 \frac{1}{y} f_{h_p}(y) f_{h_f}\left(\frac{z}{y}\right) \mathrm{d}y. \tag{5.32}$$

substituting the PDFs from (5.6) and (5.7) in (5.32) and simplifying, we get

$$f_{h_{fp}}(z) = -\sum_{i=1}^{K} \frac{\rho^2 w_i \exp\left(\frac{-\mu_i^2}{2\sigma_i^2}\right)}{\sqrt{2\pi}\sigma_i} \int_0^1 y^{\rho-2} \ln(y) \exp\left(\frac{(-\frac{z}{y})^2}{2\sigma_i^2}\right) \exp\left(\frac{(\frac{2z\mu_i}{y})}{2\sigma_i^2}\right) \mathrm{d}y. \tag{5.33}$$

The closed form solution of the above integral with powers on the exponential is not possible. Thus, using Meijer's G representation of both the exponential functions, we can rewrite the

equation as

$$f_{h_{fp}}(z) = -\sum_{i=1}^{K} \frac{\rho^2 w_i \exp\left(\frac{-\mu_i^2}{2\sigma_i^2}\right)}{\sqrt{2\pi}\sigma_i} \left(\frac{1}{2\pi\jmath}\right)^2 \int_{\mathcal{L}_1}\int_{\mathcal{L}_2} \Gamma(0-s_1)(z^2)^{s_1}\Gamma(0-s_2)(-2z\mu_i)^{s_2} ds_1 ds_2 \times I_1 \tag{5.34}$$

The inner integral I_1 can be solved to

$$I_1 = \int_0^1 y^{\rho-2-2s_1-s_2} \ln(y) \mathrm{d}y = -\frac{(\Gamma(-\rho+2+2s_1+s_2))^2}{(\Gamma(-\rho+3+2s_1+s_2))^2} \tag{5.35}$$

Substituting back (5.35) in (5.34), and using the definition of bivariate Fox's H-function [178], we can write the PDF of THz outdoor channel combined with THz antenna misalignment error in (5.8). The CDF can be derived using the PDF in $F_{h_{fp}}^{\mathrm{THz}}(z) = \int_0^z f_{h_{fp}}^{\mathrm{THz}}(z)dz$. Using (5.8), we can write CDF as

$$\begin{aligned} F_{h_{fp}}(z) = &\sum_{i=1}^{K} \frac{\rho^2 w_i \exp\left(\frac{-\mu_i^2}{2\sigma_i^2}\right)}{\sqrt{2\pi}\sigma_i} \left(\frac{1}{2\pi\jmath}\right)^2 \int_{\mathcal{L}_1}\int_{\mathcal{L}_2} \Gamma(0-s_1)(z^2)^{s_1} \\ &\times\Gamma(0-s_2)(-2z\mu_i)^{s_2} \frac{(\Gamma(-\rho+2+2s_1+s_2))^2}{(\Gamma(-\rho+3+2s_1+s_2))^2} ds_1 ds_2 \times I_2 \end{aligned} \tag{5.36}$$

The inner integral is straightforward and is simplified to

$$I_2 = \int_0^z z^{2s_1+s_2} dz = \frac{z^{2s_1+s_2+1}\Gamma(2s_1+s_2+1)}{\Gamma(2s_1+s_2+2)} \tag{5.37}$$

Substituting I_2 in (5.36), and applying the definition of bivariate Fox's H-function, we get the CDF in (5.9). Using the standard transforms of the random variables for the SNR [174], we get the PDF and CDF of the SNR to conclude the proof of Lemma 5.1.

5.9.2 Appendix 5.2: Proof of Theorem 5.1

To begin with the proof, we compute the MGF for each of the three technologies used in the backhaul link. To achieve this, we substitute the PDF of (5.4) into (5.13), employ the Mellin Barnes type representation of the exponential function, and change the order of integration to obtain the MGF of the mmWave link as

$$\begin{aligned} \mathcal{M}_{\gamma}^{\mathrm{mW}}(s) = &\frac{m^m}{\Gamma(m)} \sum_{j=0}^{\infty} \frac{K^j d_j}{(\Gamma(j+1))^2 (2\zeta^2)^{j+1} (\bar{\gamma}^{\mathrm{mW}})^{j+1}} \\ &\times \frac{1}{2\pi\jmath} \int_{L_3} \Gamma(0-s_3) \Big(\frac{1}{2\zeta^2\bar{\gamma}^{\mathrm{mW}}}\Big)^{s_3} ds_3 \int_0^{\infty} e^{-s\gamma} \gamma^{j+s_3} d\gamma \end{aligned} \tag{5.38}$$

which, using the identity [168, 3.381/4] can be simplified to

$$\mathcal{M}_{\gamma}^{\mathrm{mW}}(s) = \frac{m^m}{\Gamma(m)} \sum_{j=0}^{\infty} \frac{K^j d_j}{(\Gamma(j+1))^2 (2\zeta^2)^{j+1} (\bar{\gamma}^{\mathrm{mW}})^{j+1}} \times \frac{1}{2\pi\jmath} \int_{L_3} \Gamma(0-s_3) \Big(\frac{1}{2\zeta^2 \bar{\gamma}^{\mathrm{mW}}} \Big)^{s_3} s^{-1-j-s_3} \Gamma(1+j+s_3) ds_3 \tag{5.39}$$

Similarly, the MGFs of the FSO and THZ links can be obtained as

$$\mathcal{M}_{\gamma}^{\mathrm{FSO}}(s) = \frac{\alpha_{_F} \phi}{\psi \Gamma(\alpha) \Gamma(\beta)} \frac{1}{2\pi\jmath} \int_{L_4} \frac{\Gamma(\beta_{_F} - 1 - s_4) \Gamma(\phi - 1 - s_4) \Gamma(1 + \beta_{_F} + s_4)}{\Gamma(\phi - s_4)} \times \left(\frac{\alpha}{\psi (\bar{\gamma}^{\mathrm{FSO}})^{\frac{1}{2}}} \right)^{s_4} ds_4 \times s^{-\frac{1}{2} - \frac{s_4}{2}} \Gamma\left(\frac{1}{2} + \frac{s_4}{2} \right) \tag{5.40}$$

$$\mathcal{M}_{\gamma}^{\mathrm{THz}}(s) = \sum_{i=1}^{K} \frac{\rho^2 w_i \exp\left(\frac{-\mu_i^2}{2\sigma_i^2} \right)}{2\sqrt{2\pi} \sigma_i (\bar{\gamma}^{\mathrm{THz}})^{\frac{1}{2}}} \left(\frac{1}{2\pi\jmath} \right)^2 \int_{\mathcal{L}_5} \int_{\mathcal{L}_6} \Gamma(0-s_5) \Big(\frac{1}{\bar{\gamma}^{\mathrm{THz}}} \Big)^{s_5} \Gamma(0-s_6) \left(\frac{-2\mu_i}{(\bar{\gamma}^{\mathrm{THz}})^{\frac{1}{2}}} \right)^{s_6} \times \frac{(\Gamma(-\rho+2+2s_5+s_6))^2}{(\Gamma(-\rho+3+2s_5+s_6))^2} s^{-\frac{1}{2} - s_5 - \frac{s_6}{2}} \Gamma(\frac{1}{2} + s_5 + \frac{s_6}{2}) ds_5 ds_6 \tag{5.41}$$

Substituting the MGFs of (5.39), (5.40), and (5.41) into (5.12) and applying the inverse Laplace transform, we get the PDF of the hybrid system for MRC diversity combining as

$$\begin{aligned} f_{\gamma}^{\mathrm{MRC}}(\gamma) = {} & \frac{m^m}{\Gamma(m)} \sum_{j=0}^{\infty} \frac{K^j d_j}{(\Gamma(j+1))^2 (2\zeta^2)^{j+1} (\bar{\gamma}^{\mathrm{mW}})^{j+1}} \frac{1}{2\pi\jmath} \int_{L_3} \Gamma(0-s_3) \Big(\frac{1}{2\zeta^2 \bar{\gamma}^{\mathrm{mW}}} \Big)^{s_3} ds_3 \\ & \times \Gamma(1+j+s_3) \frac{\alpha\phi}{\psi \Gamma(\alpha) \Gamma(\beta)} \frac{1}{2\pi\jmath} \int_{L_4} \frac{\Gamma(\beta_{_F} - 1 - s_4) \Gamma(\phi - 1 - s_4) \Gamma(1 + \beta_{_F} + s_4)}{\Gamma(\phi - s_4)} \\ & \times \left(\frac{\alpha}{\psi (\bar{\gamma}^{\mathrm{FSO}})^{\frac{1}{2}}} \right)^{s_4} ds_4 \Gamma(\frac{1}{2} + \frac{s_4}{2}) \sum_{i=1}^{K} \frac{\rho^2 w_i \exp\left(\frac{-\mu_i^2}{2\sigma_i^2} \right)}{2\sqrt{2\pi} \sigma_i (\bar{\gamma}^{\mathrm{THz}})^{\frac{1}{2}}} \left(\frac{1}{2\pi\jmath} \right)^2 \int_{\mathcal{L}_5} \int_{\mathcal{L}_6} \Gamma(0-s_5) \Big(\frac{1}{\bar{\gamma}^{\mathrm{THz}}} \Big)^{s_5} \\ & \times \Gamma(0-s_6) \left(\frac{-2\mu_i}{(\bar{\gamma}^{\mathrm{THz}})^{\frac{1}{2}}} \right)^{s_6} \frac{(\Gamma(-\rho+2+2s_5+s_6))^2}{(\Gamma(-\rho+3+2s_5+s_6))^2} ds_5 ds_6 \times I_3 \end{aligned} \tag{5.42}$$

The inner integral I_3 can be simplified by substituting $s\gamma = -t$ to get [168, 8.315]

$$I_3 = \int_{L_5} e^{s\gamma} s^{-1-j-s_3} s^{-\frac{1}{2} - \frac{s_4}{2}} s^{-\frac{1}{2} - s_5 - \frac{s_6}{2}} = \Big(\frac{1}{\gamma} \Big)^{(-1-j-s_3-\frac{s_4}{2}-s_5-\frac{s_6}{2})} \frac{2\pi\jmath}{\Gamma(1+j+s_3+\frac{s_4}{2}+s_5+\frac{s_6}{2})} \tag{5.43}$$

Substituting (5.43) into (5.42) and using the definition of multivariate Fox's H-function [170], we get the PDF of hybrid BHL-MRC in (5.14). The CDF can be derived using (5.14) in $F_{\gamma}^{\mathrm{MRC}}(\gamma) = \int_0^{\gamma} f_{\gamma}^{\mathrm{MRC}}(\gamma) d\gamma$. Applying the similar procedure as that of PDF, we get the inner

integral as

$$\int_0^{\gamma} \gamma^{(1+j+s_3+\frac{s_4}{2}+s_5+\frac{s_6}{2})} d\gamma = \frac{\gamma^{(2+j+s_3+\frac{s_4}{2}+s_5+\frac{s_6}{2})}\Gamma\big(2+j+s_3+\frac{s_4}{2}+s_5+\frac{s_6}{2}\big)}{\Gamma\big(3+j+s_3+\frac{s_4}{2}+s_5+\frac{s_6}{2}\big)} \tag{5.44}$$

Applying the definition of multivariate Fox's H-function, we get the CDF of hybrid BHL-MRC in (5.15) to finish the proof of Theorem 5.1.

5.9.3 Appendix 5.3: Proof of Lemma 5.3

The average BER of hybrid BHL-MRC can be derived by substituting the CDF of (5.15) in (5.27) to get

$$\begin{aligned}
\bar{P}_e^{\mathrm{MRC}} &= \frac{m^m q^p}{2\Gamma(m)\Gamma(p)} \sum_{j=0}^{\infty} \frac{K^j d_j}{(\Gamma(j+1))^2 (2\zeta^2)^{j+1} (\bar{\gamma}^{\mathrm{mW}})^{j+1}} \frac{1}{2\pi\jmath} \int_{L_3} \Gamma(0-s_3) \Big(\frac{1}{2\zeta^2 \bar{\gamma}^{\mathrm{mW}}}\Big)^{s_3} ds_3 \\
&\times \Gamma(1+j+s_3) \frac{\alpha\phi}{\psi\Gamma(\alpha)\Gamma(\beta)} \frac{1}{2\pi\jmath} \int_{L_4} \frac{\Gamma(\beta_{_F}-1-s_4)\Gamma(\phi-1-s_4)\Gamma(1+\beta_{_F}+s_4)}{\Gamma(\phi-s_4)} \\
&\times \left(\frac{\alpha}{\psi(\bar{\gamma}^{\mathrm{FSO}})^{\frac{1}{2}}}\right)^{s_4} ds_4 \Gamma\big(\frac{1}{2}+\frac{s_4}{2}\big) \sum_{i=1}^{K} \frac{\rho^2 w_i \exp\left(\frac{-\mu_i^2}{2\sigma_i^2}\right)}{2\sqrt{2\pi}\sigma_i (\bar{\gamma}^{\mathrm{THz}})^{\frac{1}{2}}} \left(\frac{1}{2\pi\jmath}\right)^2 \int_{\mathcal{L}_5}\int_{\mathcal{L}_6} \Gamma(0-s_5) \left(\frac{1}{\bar{\gamma}^{\mathrm{THz}}}\right)^{s_5} \\
&\times \Gamma(0-s_6) \left(\frac{-2\mu_i}{(\bar{\gamma}^{\mathrm{THz}})^{\frac{1}{2}}}\right)^{s_6} \frac{(\Gamma(-\rho+2+2s_5+s_6))^2}{(\Gamma(-\rho+3+2s_5+s_6))^2} \Gamma\big(\frac{1}{2}+s_5+\frac{s_6}{2}\big) \\
&\times \frac{1}{\Gamma(1+j+s_3+\frac{s_4}{2}+s_5+\frac{s_6}{2})} \frac{\Gamma\big(2+j+s_3+\frac{s_4}{2}+s_5+\frac{s_6}{2}\big)}{\Gamma\big(3+j+s_3+\frac{s_4}{2}+s_5+\frac{s_6}{2}\big)} ds_5 ds_6 \times I_4
\end{aligned} \tag{5.45}$$

The inner integral I_4 can be solved to [168, 3.381/4]

$$I_4 = \int_0^{\infty} e^{-q\gamma} \gamma^{(1+p+j+s_3+\frac{s_4}{2}+s_5+\frac{s_6}{2})} d\gamma = q^{(-p-j-s_3-\frac{s_4}{2}-s_5-\frac{s_6}{2})} \Gamma(2+p+j+s_3+\frac{s_4}{2}+s_5+\frac{s_6}{2}) \tag{5.46}$$

substituting the inner integral (5.46) in (5.45), and applying the definition of Fox's H-function, we get the average BER of the BHL-MRC in (5.30). To derive the average BER of the IoT device with maximum SNR in the access link, we substitute (5.22) in (5.27) to get

$$\bar{P}_e^{\mathrm{IoT}} = \frac{q^p}{2\Gamma(p)} \sum_{k=0}^{n} \binom{n}{k} \int_0^{\infty} e^{-q\gamma} \gamma^{p-1} \Big(- e^{-\frac{\lambda\gamma}{\bar{\gamma}^{\mathrm{RF}}}} \Big)^k d\gamma \tag{5.47}$$

Using the identity [168, 3.381/4], we get the average BER of the IoT network in (5.29). Finally, plugging (5.30) and (5.29) into (5.28), we get the average BER of the relayed system to finish the proof.

To derive the average BER of BHL-OSC, we substitute (5.17) in (5.27) to get

$$\bar{P}_e^{\mathrm{OSC}} = \frac{q^p}{2\Gamma(p)}\frac{m^m}{\Gamma(m)}\sum_{j=0}^{\infty}\frac{K^j d_j}{(\Gamma(j+1))^2(\bar{\gamma}^{\mathrm{mW}})^j}\frac{1}{2\pi\jmath}\int_{L_3}\frac{\Gamma(1+j-s_3)\Gamma(0+s_3)}{\Gamma(1+s_3)}\left(\frac{1}{2\zeta^2\bar{\gamma}^{\mathrm{mW}}}\right)^{s_3}ds_3$$
$$\times\frac{\alpha_{_F}\phi}{(\bar{\gamma}^{\mathrm{FSO}})^{\frac{1}{2}}\psi\Gamma(\alpha)\Gamma(\beta)}\frac{1}{2\pi\jmath}\int_{L_4}\frac{\Gamma(\beta-1-s_4)\Gamma(\phi-1-s_4)\Gamma(1+\beta+s_4)}{\Gamma(\phi-s_4)\Gamma(2+s_4)}\Gamma(1+s_4)$$
$$\times\left(\frac{\alpha}{\psi(\bar{\gamma}^{\mathrm{FSO}})^{\frac{1}{2}}}\right)^{s_4}ds_4\sum_{i=1}^{K}\frac{\rho^2 w_i\exp\left(\frac{-\mu_i^2}{2\sigma_i^2}\right)}{2\sqrt{2\pi}\sigma_i(\bar{\gamma}^{\mathrm{THz}})^{\frac{1}{2}}}\left(\frac{1}{2\pi\jmath}\right)^2\int_{\mathcal{L}_5}\int_{\mathcal{L}_6}\Gamma(0-s_5)\left(\frac{1}{\bar{\gamma}^{\mathrm{THz}}}\right)^{s_5}\Gamma(0-s_6)$$
$$\times\left(\frac{-2\mu_i}{(\bar{\gamma}^{\mathrm{THz}})^{\frac{1}{2}}}\right)^{s_6}\frac{(\Gamma(-\rho+2+2s_5+s_6))^2}{(\Gamma(-\rho+3+2s_5+s_6))^2}\frac{\Gamma(2s_5+s_6+1)}{\Gamma(2s_5+s_6+2)}ds_5ds_6\times I_5 \tag{5.48}$$

where I_5 is the inner integral, which is simplified to

$$I_5 = \int_0^{\infty} e^{-q\gamma}\gamma^{s_3+\frac{s_4}{2}+s_5+\frac{s_6}{2}+j+p}d\gamma = q^{-1-s_3-\frac{s_4}{2}-s_5-\frac{s_6}{2}-j-p}\Gamma\big(1+s_3+\frac{s_4}{2}+s_5+\frac{s_6}{2}+j+p\big) \tag{5.49}$$

substituting (5.49) into (5.48), and applying the definition of multivariate Fox's H-function, we get the average BER of BHL-OSC as

$$\bar{P}_e^{\mathrm{OSC}} = \frac{m^m q^{-1}}{2\Gamma(m)\Gamma(p)}\sum_{j=0}^{\infty}\frac{K^j d_j}{(\Gamma(j+1))^2(\bar{\gamma}^{\mathrm{mW}})^j}\sum_{i=1}^{K}\frac{\rho^2 w_i\exp\left(\frac{-\mu_i^2}{2\sigma_i^2}\right)}{2\sqrt{2\pi}\sigma_i(\bar{\gamma}^{\mathrm{THz}})^{\frac{1}{2}}}\frac{\alpha_{_F}\phi}{(\bar{\gamma}^{\mathrm{FSO}})^{\frac{1}{2}}\psi\Gamma(\alpha)\Gamma(\beta)}$$
$$\times H^{0,4:1,1;2,2;0,1;0,1}_{4,3:1,2;3,3;1,0;1,0}\left[\begin{matrix}\frac{\zeta^{-2}\gamma}{2q\bar{\gamma}^{\mathrm{mW}}},\frac{\alpha\gamma^{\frac{1}{2}}}{\psi(q\bar{\gamma}^{\mathrm{FSO}})^{\frac{1}{2}}},\frac{q^{-1}\gamma}{\bar{\gamma}^{\mathrm{THz}}},\frac{-2\mu_i\gamma^{\frac{1}{2}}}{(q\bar{\gamma}^{\mathrm{THz}})^{\frac{1}{2}}}\end{matrix}\middle|\begin{matrix}T_9\\T_{10}\end{matrix}\right] \tag{5.50}$$

where $T_9 = \big\{(\rho{-}1;0,0,2,1)^2,(0;0,0,2,1),(-p{-}j;1,\frac{1}{2},1,\frac{1}{2})\big\}:\big\{(1,1)\big\};\big\{(-\beta,1),(0,1),(\phi,1)\big\};\big\{-\big\};\big\{-\big\}$ and $T_{10} = \big\{(\rho{-}2;0,0,2,1)^2,(-1;0,0,2,1),(0;0,02,1),\big\}:\big\{(1{+}j,1),(0,1)\big\};\big\{(\beta{-}1,1),(\phi-1),(-1,1)\big\};\big\{(0,1)\big\};\big\{(0,1)\big\}$.

Chapter 6

Low Complexity Algorithms for Multi-User Cell-Free Wireless Networks Exploiting THz Channel Characteristics

6.1 Introduction

THz wireless technology has the potential to play a crucial role in access networks, particularly in dense network deployments with limited coverage range like cell-free networks [125–128]. In particular, cell-free networks are envisioned as a key network architecture in wireless communication, where multiple APs are strategically deployed within a specific area, serving multiple users in close proximity. As a consequence, the distance between users and the APs is significantly reduced compared to traditional cellular systems. This inherent characteristic makes the THz band an ideal candidate for integration into multiuser cell-free networks [129–132].

The research contributions in this chapter have been reported in these publications:

1. **P. Bhardwaj** S. M. Zafaruddin, and Amir Leshem, "Random Access Protocols for Cell-Free Wireless Network Exploiting Statistical Behavior of THz Signal Propagation", arXiv:2311.06.06166, under review in **IEEE Transactions on Wireless Communications**, Nov. 2023.

2. **P. Bhardwaj**, Raghav Khanna, and S. M. Zafaruddin, " A Generalized Statistical Channel Model for THz Wireless Communication," " arXiv:2310.18616v1, Oct. 2023, accepted for presentation, **2024 IEEE Wireless Communications and Networking Conference: (IEEE WCNC 2024 Workshops)** , Dubai, UAE, 21-24 April, 2024.

3. **P. Bhardwaj**, Eesha K. Santosh, and S. M. Zafaruddin, " An Exact Statistical Representation of α-η-κ-μ Fading Model for THz Wireless Communication," in press, **2023 IEEE Globecom Workshops (IEEE GC 2023 Workshop - HCWC)**, Kuala Lumpur, Malaysia, Dec. 2023, pp.1-6.

4. **P. Bhardwaj** and S. M. Zafaruddin, "Exact Performance Analysis of THz Link under Transceiver Hardware Impairments," in **IEEE Communications Letters**, vol. 27, no. 8, pp. 2197-2201, Aug. 2023.

5. S. M. Zafaruddin and **P. Bhardwaj**, " Interference Cancellation in Wireless Communications: Past, Present, and Future" in **IETE Journal of Education**, Vol 63, no. 1, pp. 5-13, Oct. 2021. (**Best paper award in IETE Students' Journal Award category, 2023**).

THz wireless backhaul/fronthaul networks have been investigated specifically in the context of single-user transmission [75, 119, 124, 197, 198], limited research have focused on the multi-user THz wireless communications [133–137].

The use of THz band for cell-free wireless communication is studied in [129–132]. The authors in [129] and [130] list qualitative research directions for the use of THz in the cell-free mMIMO systems. The work presented in [131] proposes employing the THz spectrum for wireless backhaul connections connecting UAV base stations to central-processing unit (CPU). The authors in [132] explores the vulnerability of THz wireless technology to physical-layer jamming in the framework of cell-free mMIMO systems.

Multiuser interference cancellation has been studied extensively for cell-free wireless network [138–142]. The interference cancellation requires complex signal processing at the CPU and significant overheads. In this context, random access protocol can be a potential alternative [91, 143–147]. The work in [147] proposes an adaptive random access protocol for massive IoT networks that exploits nonorthogonal multiple access (NOMA) with short-packet transmissions and automatic request and repeat (ARQ) strategy with a limited number of retransmissions.

6.2 Motivation and Contributions

THz wireless transmission encounters several challenges, including high path-loss resulting from atmospheric absorption, misalignment errors, short-term fading, and hardware impairments. Current statistical channel models for THz wireless communication primarily concentrate on the sub-THz band, mostly with α-μ and Gaussian mixture fading distributions for short-term fading and deterministic modeling for atmospheric absorption.

The effectiveness of a random access protocol is contingent upon the number of users attempting to access the channel. In contrast to RF, THz signal propagation involves greater complexity, including losses attributed to molecular absorption, short-term fading, antenna misalignment errors, and transceiver hardware impairments. There is currently no existing research on a random access protocol designed for a cell-free wireless network that leverages the unique characteristics of THz signal propagation.

In this chapter, we develop random access protocols for efficient communication in a multi-user cell-free network over the THz band. The main contributions of this chapter are as follows:

- We develop a generalized statistical model for THz signal propagation, incorporating random path-loss with a Gamma distribution for the molecular absorption coefficient, short-term fading characterized by the α-η-κ-μ distribution, as well as accounting for antenna misalignment errors and transceiver hardware impairments. Note that existing literature assumed a deterministic path-loss model, which is suitable for stable channel environments like backhaul/fronthaul scenarios. However, in the access link, where obstruction (such as human movement and others) between the transmitter and receiver is prevalent, a deterministic path-loss model may not be appropriate.

- We propose random access protocols designed for a cell-free wireless network, ensuring successful transmissions for multiple users with minimal delay and energy loss by leveraging the collective impact of random atmospheric absorption, the non-linearity of fading, hardware impairments, and antenna misalignment errors. We assume that each user is assigned a single packet to transmit during data transmission requiring novel approach for the analysis compared to the conventional analysis of the ALOHA protocol [199].

- We consider two schemes: a fixed transmission probability (FTP) scheme where the transmission probability (TP) of each user is updated at the beginning of the data transmission and an adaptive transmission probability (ATP) scheme where the TP is updated with each successful reception of the data. The FTP implementation is characterized by simplicity, while the ATP scheme demonstrates superior performance, scaling linearly with the number of active users.

- We analyze the performance of both protocols using delay, energy consumption, and outage probability with scaling laws for the transmission of a data frame consisting of a single packet from users at a predefined quality of service (QoS). Computer simulations demonstrate the efficacy of the proposed random access schemes and accuracy in performance assessment with the statistical effect of THz propagation for a cell-free network.

6.3 System Model

As depicted in Fig. 6.1, we consider a multiuser network consisting of a L APs that supports K users, all operating on same time-frequency resources within the THz band, emulating a typical cell-free architecture. Consequently, there are $K-1$ interference signals that contribute to the degradation of signal quality for the i-th user. In this situation, random access methods can provide potential benefits. When utilizing a random access protocol, if the transmission is successful, the signal received at the AP is expressed as [42]:

$$y = h(s + w_t) + w_r + w \tag{6.1}$$

where h represents the channel coefficient, comprising of the path gain h_l due to signal propagation and atmospheric absorption, short-term fading h_f, and antenna misalignment errors h_p. Here, s denotes the desired signal, and w stands for the additive white Gaussian noise (AWGN) with variance σ_ω^2.

The terms w_t and w_r refer to components representing residual hardware impairment, which are statistically modeled using a Gaussian distribution [34, 42]. Specifically, $w_t \sim \mathcal{CN}(0, k_t^2 P)$, and $w_r \sim \mathcal{CN}(0, k_r^2 P|h|^2)$, where k_t and k_r quantify the extent of hardware imperfections in the transmitter and receiver, respectively. In the THz band, typical values of k_t and k_r fall within the range of $(0\text{-}0.4)$, as suggested in [34]. A value of $k_t = k_r = 0$ corresponds

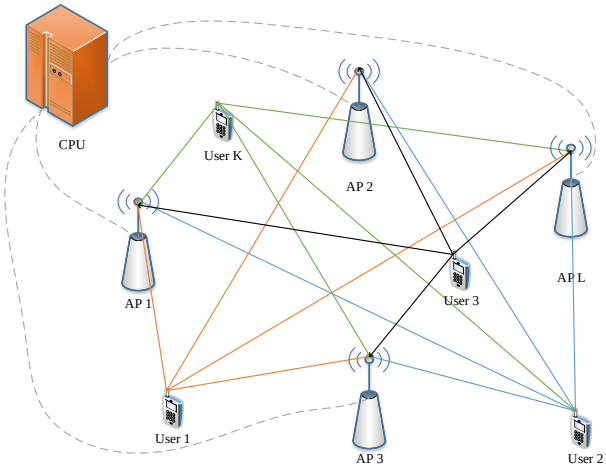

Figure 6.1: System model for a typical cell-free network.

to an ideal front-end, representing no hardware imperfections. The achievable performance is limited by transceiver hardware impairment at higher frequencies [34, 75].

The path gain, denoted as h_l, relies on various factors such as antenna gains, frequency, and molecular absorption coefficient, as defined in [34]:

$$h_l = \frac{c\sqrt{G_t G_r}}{4\pi f d} \exp(-\frac{1}{2}\kappa(f, T, \psi, p)d) \tag{6.2}$$

Here, c represents the speed of light, f denotes the transmission frequency, and d represents the distance. G_t and G_r are the antenna gains of the transmitting and receiving antennas, respectively. The term $\kappa(f, T, \psi, p)$ corresponds to the molecular absorption coefficient, which is influenced by temperature T, relative humidity ψ, and atmospheric pressure p. It can be expressed as:

$$\begin{aligned}\kappa(f, T, \psi, p) = &\frac{q_1 v(q_2 v + q_3)}{(q_4 v + q_5)^2 + (\frac{f}{100c} - p_1)^2} \\ &+ \frac{q_6 v(q_7 v + q_8)}{(q_9 v + q_{10})^2 + (\frac{f}{100c} - p_2)^2} + c_1 f^3 + c_2 f^2 + c_3 f + c_4\end{aligned} \tag{6.3}$$

In the above equation, $v = \frac{\psi}{100}\frac{p_w(T,p)}{p}$, where $p_w(T, p)$ represents the saturated water vapor partial pressure at temperature T. The value of $p_w(T, p)$ can be evaluated using Buck's equation.

As is for many wireless communications, short-term fading is inevitable at THz frequencies. Several studies have suggested various distributions to model the short-term fading in the THz band, like α-μ, fluctuating two-ray (FTR), and Gaussian mixture distributions at sub-THz frequencies [149][160]. The α-η-κ-μ model is a comprehensive representation that embodies a wide range of fading characteristics, including the number of multi-path clusters, power

of dominant components, nonlinearity of the propagation medium, and scattering level. This flexibility allows the model to effectively capture and fit measurement data in various propagation scenarios, making it an ideal choice for a more generalized and diverse channel model at high frequencies. To model the short-term fading in the THz band for outdoor environment, we adopt the α-η-κ-μ fading model [158]. The authors in [200] demonstrated that the α-η-κ-μ is the best fading model fitting over a wide range of propagation environments for higher frequency mmWave and THz systems.

The effect of antenna misalignment errors is also detrimental to THz performance, which occurs when transmit and receive antennas fail to adequately align for line-of-sight (LOS) transmissions, significantly limiting the physical communication range [51]. The antenna misalignment errors in the THz band for aerial/mobile communication [51, 152] are statistically modeled using the PDF

$$f_{h_p}(h_p) = -\rho^2 \ln(h_p) h_p^{\rho-1} \tag{6.4}$$

where $0 < x < 1$. $\rho = \sqrt{\frac{w_B^2}{\sigma_\theta^2}}$ determines the severity of the misalignment errors, where w_B is the angular beamwidth (beam divergence) of the signal and σ_θ is the variance of the angular fluctuation, which models the effect of angular fluctuations at both the transmitter and receiver.

We define the instantaneous SNR of the THz link at the receiver as $\gamma = |h|^2\bar{\gamma}$, where $h = h_l h_f h_p$ and $\bar{\gamma}$ is the average SNR of the link and is defined as $\bar{\gamma} = \frac{P_t}{\sigma_\omega^2}$ with P_t as the transmit power. From (6.1), the resultant SNR with transceiver hardware impairment parameters $k_h = \sqrt{k_t^2 + k_r^2}$ is given by

$$\gamma = \frac{\bar{\gamma}|h_l h_f h_p|^2}{k_h^2 \bar{\gamma}|h_l h_f h_p|^2 + 1} \tag{6.5}$$

It can be seen that SNR γ for THz transmission exhibit significant randomness due to the combined effect of h_l, h_f, and h_p. In previous studies, $\kappa(f, T, \psi, p)$ (which determines h_l) has been considered deterministic. This assumption holds for backhaul/fronthaul applications where the environment remains relatively stable. However, in cluttered urban environments where factors like human blockage come into play, $\kappa(f, T, \psi, p)$ can exhibit randomness. Further, modeling for h_f becomes more intricate to characterize short-term fading of THz signals. Moreover, there is a randomness in the signal quality due to antenna misalignment parameter h_p.

It is crucial to recognize that when implemented in large multiuser networks, random access protocols can experience drawbacks in terms of latency and inefficient utilization of communication resources. However, unique channel characteristics of THz propagation can enable efficient implementation of the random access protocol.

In what follows, we develop a statistical model for signal propagation in THz frequencies. This model encompasses random path loss, short-term fading, antenna misalignment errors, and transceiver hardware impairments. Subsequently, we introduce random access protocols

designed for a cell-free wireless network. These protocols aim to facilitate successful transmissions for multiple users with minimal delay and energy loss, leveraging the combined impact of random atmospheric absorption, the non-linearity of fading, hardware impairments, and antenna misalignment errors.

6.4 A Generalized Channel Model for THz Transmission

In this section, we develop a generalized channel model for the THz transmission which includes several random components for its statistical analysis resulting from atmospheric absorption, misalignment errors, short-term fading, and hardware impairments.

6.4.1 Exact Statistical Derivation of α-η-κ-μ Model

The α-η-κ-μ model includes almost all short-term propagation phenomena to generalize the fading model for a wireless channel. The envelope R of the α-η-κ-μ is given by [158][159]

$$R^{\alpha} = \sum_{i=1}^{\mu_x} (X_i + \lambda_{x_i})^2 + \sum_{i=1}^{\mu_y} (Y_i + \lambda_{y_i})^2 \tag{6.6}$$

where α denotes the non-linearity of the channel, μ_x and μ_y denote the number of multi-path clusters of in-phase component and quadrature component, respectively, λ_{x_i} and λ_{y_i} are the average values of the in-phase and quadrature components of the multi-path waves of the i-th cluster, respectively, and $X_i \sim \mathcal{N}(0, \sigma_x^2)$ and $Y_i \sim \mathcal{N}(0, \sigma_y^2)$ are mutually independent Gaussian processes, where σ_x^2 and σ_y^2 are variances of in-phase and quadrature components of the multi-path waves, respectively. In general, the α-η-κ-μ model is quantified by seven different parameters, namely α, η, κ, μ, p, q, and $\hat{r}$. To define these parameter, denote the power of in-phase (x) and quadrature-phase (y) components of dominant (d) waves and scattered (s) waves as P_{ab}, where $a \in \{d, s\}$ and $b \in \{x, y\}$. Thus, we define the parameters as $\eta = \frac{P_{sx}}{P_{sy}}$, $\kappa = \frac{P_{dx}+P_{dy}}{P_{sx}+P_{sy}}$, $\mu = \frac{\mu_x+\mu_y}{2}$, $p = \frac{\mu_x}{\mu_y}$, $q = \frac{P_{dx}}{P_{dy}} / \frac{P_{sx}}{P_{sy}}$, and $\hat{r} = \sqrt[\alpha]{\mathbb{E}[R^{\alpha}]}$.

For statistical analysis of the wireless systems, the density and distribution functions of the channel envelope are required. Using (6.6), the authors in [159] presented the PDF $f_R(r)$ of the envelope R in terms of the generalized Laguerre polynomial (L_n) and the regularized hypergeometric function $({}_0\tilde{F}_1)$:

$$\begin{aligned} f_R(r) = {} & \frac{\alpha(\xi\mu)^{\mu}}{\exp\left(\frac{(1+pq)\kappa\mu}{\delta}\right)} \left(\frac{p}{\eta}\right)^{\frac{p\mu}{1+p}} \frac{r^{\alpha\mu-1}}{\hat{r}^{\alpha\mu}} \exp\Big(-\frac{r^{\alpha} p\xi\mu}{\hat{r}^{\alpha}\eta}\Big) \\ & \times \sum_{n=0}^{\infty} \Big(\frac{r^{\alpha}\xi\mu(p-\eta)}{\hat{r}^{\alpha}\eta}\Big)^{n} L_n^{\frac{\mu}{1+p}-1}\Big(\frac{\eta\kappa\mu}{\delta(\eta-p)}\Big) \\ & \times {}_0\tilde{F}_1\Big(;\mu+n;\frac{p^2 q r^{\alpha}\kappa\xi\mu^2}{\hat{r}^{\alpha}\delta\eta}\Big) \end{aligned} \tag{6.7}$$

where $\xi = \frac{(1+\eta)(1+\kappa)}{(1+p)}$ and $\delta = \frac{(1+q\eta)(1+p)}{(1+\eta)}$. It can be seen that the PDF $f_R(r)$ contains an infinite

series representation, which approximates the system performance when a finite number of terms are used for the convergence of the distribution function. It is always desirable to express the statistics of the channel envelope in an exact form using tractable mathematical functions for efficient performance analysis and numerical computations.

We derive exact expressions of the PDF of the channel envelope distributed according to the α-η-κ-μ model using a single Fox's H-function. We denote the multi-variate Fox's H-function as given in [170, A.1]. We define $\psi_1 = \frac{p\alpha\mu^2\xi^{1+\frac{\mu}{2}}\delta^{\frac{\mu}{2}-1}q^{\frac{1+p-p\mu}{2+2p}}\eta^{-\frac{1+p+p\mu}{2+2p}}}{\kappa^{\frac{\mu}{2}-1}\exp\left(\frac{(1+pq)\kappa\mu}{\delta}\right)}$, $\psi_2 = \alpha - 1$, $\psi_3 = \frac{p\xi\mu}{\eta\hat{r}^{\alpha}}$, $A_1 = \frac{p\mu}{1+p}$-1, $A_2 = \frac{\mu}{1+p}$-1, $A_3 = \frac{(\eta-p)\xi\mu}{\eta\hat{r}^{\alpha}}$, $A_4 = 2p\mu\sqrt{\frac{q\kappa\xi}{\eta\delta\hat{r}^{\alpha}}}$, and $A_5 = 2\mu\sqrt{\frac{\kappa\xi}{\delta\hat{r}^{\alpha}}}$.

First, we use (6.6) to present the PDF of the channel envelope in the following theorem:

Theorem 6.1. *The PDF of the channel envelope for the α-η-κ-μ fading model is given by*

$$f_R(r) = \frac{\psi_1\pi^2 2^{(2-\mu)}A_4^{A_1}A_5^{A_2}r^{\alpha\mu-1}e^{-\psi_3 r^{\alpha}}}{(\hat{r}^{\alpha})^{1+\frac{\mu}{2}}}H_{1,1;0,1;2,3;1,3}^{0,1;1,0;1,1;1,0}\left[\begin{matrix}V_1\\V_2\end{matrix}\middle| A_3r^{\alpha}, \frac{A_4^2}{4}r^{\alpha}, \frac{A_5^2}{4}r^{\alpha}\right], \tag{6.8}$$

where $V_1 = \{(-A_2;1,0,1)\} : \{(-,-)\};\{(-A_1,1)(\frac{1}{2},1)\};\{(\frac{1}{2},1)\}$ and $V_2 = \{(-1-A_1-A_2;1,1,1)\} : \{(0,1)\};\{(0,1),(-A_1,1),(\frac{1}{2},1)\};\{(0,1),(-A_2,1),(\frac{1}{2},1)\}$.

Proof. See Appendix 6.1. ■

6.4.2 Statistical Model for Atmospheric Absorption

The THz band experiences higher path-loss due to signal absorption by molecules at extremely small wavelengths [29–31]. The path gain as depicted in (6.2) depends on molecular absorption coefficient $\zeta(f,T,\psi,p)$. At sub-THz frequencies, $\zeta(f,T,\psi,p)$ has been considered deterministic. However, at higher frequencies, the interaction of THz signals with the atmosphere can become intricate at the molecular level, making it essential to employ complex modeling for the molecular absorption coefficient $\zeta(f,T,\psi,p)$. As measurement data beyond a few hundred GHz is unavailable for parameterizing $\zeta(f,T,\psi,p)$ at THz frequencies, we resort to a statistical approach. We adopt the Gamma distribution $f_{\zeta(f,T,\psi,p)}(x) = \frac{x^{k-1}}{\beta^k\Gamma(k)}e^{-\frac{x}{\beta}}$ with parameters k and β in dB to model $\zeta(f,T,\psi,p)$. This statistical model allows for a diverse range of support for $\zeta(f,T,\psi,p)$ between 0 and ∞, with an average value of $k\beta$ dB/km selected from existing measurement data. In a recent study, the Gamma distribution has been utilized to model the attenuation coefficient in free-space optics (FSO) transmission under foggy weather conditions [201]. Indeed, experimental data is crucial to validate the use of the Gamma distribution for the absorption coefficient observed in practical scenarios, which presents an excellent opportunity for further research.

Proposition 6.1. *If the molecular absorption coefficient $\zeta(f,T,\psi,p)$ is Gamma distributed with parameters k and β in dB, then the PDF of the path-gain h_l is given by*

$$f_{h_l}(h_l) = \frac{z^k a_l^{-z}}{\Gamma(k)}\left[ln\left(\frac{a_l}{h_l}\right)\right]^{k-1}h_l^{z-1} \tag{6.9}$$

where $a_l = \frac{c\sqrt{G_t G_r}}{4\pi f d}$, $0 < h_l \leq a_l$, *and* $z = 8.686/(\beta d)$.

Proof. Converting ζ in dB, (6.2) can be represented by

$$h_l = \frac{c\sqrt{G_t G_r}}{4\pi f d} \exp\left(-\frac{1}{2}\zeta^{\text{dB}}(f, T, \psi, p) d^{\text{km}}/4.343 \right) \tag{6.10}$$

where d^{km} is the distance in km. Using $f_{\zeta(f,T,\psi,p)}(x) = \frac{x^{k-1}}{\beta^k \Gamma(k)} e^{-\frac{x}{\beta}}$ and applying standard transformation of random variables, the PDF of h_l is given (6.9). ■

6.4.3 A General THz Model with Combined Channel Effects

Finally, we present the PDF and CDF of a single link THz transmission, which includes the combined effect of random path loss, antenna misalignment errors, the generalized α-η-κ-μ short-term fading, and transceiver hardware impairments. We define $\gamma_h = \sqrt{\frac{\gamma}{\bar{\gamma}(1-\gamma k_h^2)}}$ for the subsequent analysis.

Theorem 6.2. *The PDF and CDF of SNR combining the effects of random path loss, antenna misalignment errors, and short-term fading with transceiver hardware impairments for a THz link is given by*

$$f_\gamma(\gamma) = \frac{(-1)^{-k}\psi_1 \rho^2 z^k}{(\hat{r}^\alpha)^{1+\frac{\mu}{2}}} \left(\frac{1}{a_l}\right)^{\alpha(1+A_1+A_2)+1} \frac{1}{2\big(1-\gamma k_h^2\big)\sqrt{\frac{\bar{\gamma}\gamma}{1-\gamma k_h^2}}} \left(\frac{\gamma_h}{\bar{\gamma}}\right)^{\frac{\alpha(1+A_1+A_2)}{2}}$$
$$\times H^{0,2+k;1,0;1,1;1,0;1,0}_{2+k,2+k;0,1;2,3;1,3;0,1}\left[\begin{matrix} V_5 \\ V_6 \end{matrix} \middle| \frac{A_3\gamma_h^{\frac{\alpha}{2}}}{a_l^\alpha \bar{\gamma}^{\frac{\alpha}{2}}}, \frac{A_4^2\gamma_h^{\frac{\alpha}{2}}}{4a_l^\alpha \bar{\gamma}^{\frac{\alpha}{2}}}, \frac{A_5^2\gamma_h^{\frac{\alpha}{2}}}{4a_l^\alpha \bar{\gamma}^{\frac{\alpha}{2}}}, \frac{\psi_3\gamma_h^{\frac{\alpha}{2}}}{a_l^\alpha \bar{\gamma}^{\frac{\alpha}{2}}} \right], \tag{6.11}$$

where $V_5 = \big\{(-A_2; 1, 0, 1, 0)\big\}, \big\{\rho - \alpha - \alpha A_1 - \alpha A_2; \alpha, \alpha, \alpha, \alpha\big\}, \big\{z - \alpha - \alpha A_1 - \alpha A_2; \alpha, \alpha, \alpha, \alpha\big\}_k : \big\{(-, -)\big\}; \big\{(-A_1, 1)(\frac{1}{2}, 1)\big\}; \big\{(\frac{1}{2}, 1)\big\}; \big\{-, -\big\}$ *and* $V_6 = \big\{(-1 - A_1 - A_2; 1, 1, 1, 0)\big\}, \big\{\rho - 1 - \alpha - \alpha A_1 - \alpha A_2; \alpha, \alpha, \alpha, \alpha\big\}, \big\{z - 1 - \alpha - \alpha A_1 - \alpha A_2; \alpha, \alpha, \alpha, \alpha\big\}_k : \big\{(0, 1)\big\}; \big\{(0, 1), (-A_1, 1), (\frac{1}{2}, 1)\big\}; \big\{(0, 1), (-A_2, 1), (\frac{1}{2}, 1)\big\};$
$\big\{(0, 1)\big\}.$

$$F_{h_{fpl}}(x) = \frac{\psi_1 \rho^2 z^k}{(\hat{r}^\alpha)^{1+\frac{\mu}{2}}} \left(\frac{1}{a_l}\right)^{\alpha(1+A_1+A_2)+1} \left(\frac{\gamma}{\bar{\gamma}}\right)^{\frac{\alpha(1+A_1+A_2)+1}{2}}$$
$$H^{0,3+k;1,0;1,1;1,0;1,0}_{3+k,3+k;0,1;2,3;1,3;0,1}\left[\begin{matrix} V_7 \\ V_8 \end{matrix} \middle| \frac{A_3\gamma_h^{\frac{\alpha}{2}}}{a_l^\alpha \bar{\gamma}^{\frac{\alpha}{2}}}, \frac{A_4^2\gamma_h^{\frac{\alpha}{2}}}{4a_l^\alpha \bar{\gamma}^{\frac{\alpha}{2}}}, \frac{A_5^2\gamma_h^{\frac{\alpha}{2}}}{4a_l^\alpha \bar{\gamma}^{\frac{\alpha}{2}}}, \frac{\psi_3\gamma_h^{\frac{\alpha}{2}}}{a_l^\alpha \bar{\gamma}^{\frac{\alpha}{2}}} \right], \tag{6.12}$$

where $V_7 = \big\{(-A_2; 1, 0, 1, 0)\big\}, \big\{\rho - \alpha - \alpha A_1 - \alpha A_2; \alpha, \alpha, \alpha, \alpha\big\}, \big\{z - \alpha - \alpha A_1 - \alpha A_2; \alpha, \alpha, \alpha, \alpha\big\}_k, \big\{-\alpha - \alpha A_1 - \alpha A_2; \alpha, \alpha, \alpha, \alpha\big\} : \big\{(-, -)\big\}; \big\{(-A_1, 1)(\frac{1}{2}, 1)\big\}; \big\{(\frac{1}{2}, 1)\big\}; \big\{-, -\big\}$
and $V_8 = \big\{(-1 - A_1 - A_2; 1, 1, 1, 0)\big\}, \big\{\rho - 1 - \alpha - \alpha A_1 - \alpha A_2; \alpha, \alpha, \alpha, \alpha\big\}, \big\{z - 1 - \alpha - \alpha A_1 - \alpha A_2; \alpha, \alpha, \alpha, \alpha\big\}_k, \big\{-1 - \alpha - \alpha A_1 - \alpha A_2; \alpha, \alpha, \alpha, \alpha\big\} : \big\{(0, 1)\big\}; \big\{(0, 1), (-A_1, 1), (\frac{1}{2}, 1)\big\}; \big\{(0, 1), (-A_2, 1)$
$\big\{(0, 1)\big\}.$

Proof. The proof is presented in Appendix 6.2. ■

It can be seen that Theorem 6.1 results into a 4-variate Fox's H-function. Note that multivariate Fox's H- function is extensively used to analyze wireless systems for complicated fading channels [202]. However, to simplify further, as a specific instance of Theorem 6.1, we consider the special case where $\eta = 1$ and $\kappa = 0$, which leads to the α-μ model [149]. In this context, we provide statistical results in terms of single-variate Fox's H-function:

Corollary 6.1. *The PDF and CDF of the THz link with random path loss, antenna misalignment errors, and transceiver hardware impairments with α-μ short-term fading are given by*

$$f_\gamma(\gamma) = \frac{\alpha\mu^\mu\rho^2 z^k}{\Omega^{\alpha\mu}\Gamma(\mu)a_l^{\alpha\mu-z}} \frac{1}{2\big(1-\gamma k_h^2\big)\sqrt{\frac{\bar{\gamma}\gamma}{1-\gamma k_h^2}}} \left(\sqrt{\frac{\gamma_h}{\bar{\gamma}}}\right)^{\alpha\mu-1} H_{2+k,3+k}^{3+k,0}\left[\frac{\mu\gamma_h^{\frac{\alpha}{2}}}{\Omega^{\alpha\mu}a_l^{\alpha}\bar{\gamma}^{\frac{\alpha}{2}}}\middle|\begin{matrix}(1-\alpha\mu+\rho,\alpha)_2,(-\alpha\mu+z+1,\alpha)_k\\(0,1),(-\alpha\mu+\rho,\alpha)_2,(-\alpha\mu+z,\alpha)_k\end{matrix}\right] \tag{6.13}$$

$$F_\gamma(\gamma) = \frac{\alpha\mu^\mu\rho^2 z^k}{\Omega^{\alpha\mu}\Gamma(\mu)a_l^{\alpha\mu-z}} \left(\sqrt{\frac{\gamma_h}{\bar{\gamma}}}\right)^{\alpha\mu} H_{3+k,4+k}^{3+k,1} \left[\frac{\mu\gamma_h^{\frac{\alpha}{2}}}{\Omega^{\alpha\mu}a_l^{\alpha}\bar{\gamma}^{\frac{\alpha}{2}}}\middle|\begin{matrix}(1-\alpha\mu,\alpha),(1-\alpha\mu+\rho,\alpha)_2,(-\alpha\mu+z+1,\alpha)_k\\(0,1),(-\alpha\mu+\rho,\alpha)_2,(-\alpha\mu+z,\alpha)_k,(-\alpha\mu,\alpha)\end{matrix}\right] \tag{6.14}$$

Proof. The proof follows similar steps as that of Theorem 6.1. ■

In the following corollary, we simplify the statistical outcomes by assuming that short-term fading can be disregarded. This scenario might arise in specific situations, such as when dealing with a shorter link. This assumption allows the representation of PDF and CDF in terms of incomplete Gamma functions.

Corollary 6.2. *The PDF and CDF of SNR with the effect of random path loss and antenna misalignment errors with transceiver hardware impairments for the THz link are given by*

$$f_\gamma(\gamma) = -\frac{z^k\rho^2 a_l^{z-\rho}\gamma^{\frac{\rho-1}{2}}(z-\rho)^{-k}}{\Gamma(k)\bar{\gamma_h}^{\frac{\rho-1}{2}}} \frac{1}{2\big(1-\gamma k_h^2\big)\sqrt{\frac{\bar{\gamma}\gamma}{1-\gamma k_h^2}}} \left[\frac{1}{z-\rho}\Big[\Gamma(k+1)-\Gamma\Big(k+1,(z-\rho)\ln\Big(\frac{a_l\bar{\gamma}}{\gamma_h}\Big)\Big)\Big] - \Big[\Gamma(k)-\Gamma\Big(k,(z-\rho)\ln\Big(\frac{a_l\bar{\gamma}}{\gamma_h}\Big)\Big)\Big]\right] \tag{6.15}$$

$$F_{\gamma}(\gamma) = -z^{k}\rho^{2}a_{l}^{z}(z-\rho)^{-k}\Bigg[\frac{k}{z-\rho}\Bigg[\frac{1}{\rho}\Big(\ln\Big(\frac{a_{l}\bar{\gamma}}{\gamma_{h}}\Big)\Big)^{-\rho} + \sum_{j=0}^{k}\frac{\Big((z-\rho)\Big)^{j}}{j!}(z+2\rho)^{-j-1}\Gamma\Big(j+1,(z+2\rho)\ln\Big(\frac{a_{l}\bar{\gamma}}{\gamma_{h}}\Big)\Big)\Bigg] + \Bigg[\frac{1}{\rho}\Big(\ln\Big(\frac{a_{l}\bar{\gamma}}{\gamma_{h}}\Big)\Big)^{-\rho} + \sum_{j=0}^{k-1}\frac{\Big((z-\rho)\Big)^{j}}{j!}(z+2\rho)^{-j-1} \times \Gamma\Big(j+1,(z+2\rho)\ln\Big(\frac{a_{l}\bar{\gamma}}{\gamma_{h}}\Big)\Big)\Bigg]\Bigg] \tag{6.16}$$

Proof. The proof is presented in Appendix 6.3. ■

By utilizing the statistical findings presented in Theorem 6.1, Corollary 6.1, and Corollary 6.2, we can derive analytical expressions for various performance metrics in THz wireless systems. Moreover, the proposed statistical model facilitates the development of channel-aware random access protocols, as described in the following section.

6.5 Random Access Protocols for multiuser THz transmission

This section introduces channel-aware random access protocols to optimize communication in a THz multi-user network. The randomness is present at low frequencies mainly due to the shadowing effect or short-term fading. On the other hand, at higher frequency bands, various factors could cause randomness in the propagation environment. In the THz link, we consider the random effects of path loss, short-term fading, and antenna misalignment errors, along with the effects of transceiver hardware impairment. Since there are so many random effects in the THz link, a number of users might have a signal strength lower than the predefined quality of service (QoS). As a result, the number of users accessing the channel becomes limited. Thus, we capitalize on the inherent variability in channel conditions to formulate a random access protocol specifically tailored for multi-user THz transmission.

6.5.1 Description of the Protocol

In our approach, we adopt a random access protocol that enables users to access the multi-access channel, without the need for centralized control. Our model assigns each user a single data packet for transmission. The chosen random access scheme is based on the well-known ALOHA protocol due to its simplicity of implementation and straightforward operation. However, we assume that each user is designated a single packet for transmission during a data frame, necessitating a novel approach to the analysis in contrast to the conventional approach of

the slotted ALOHA protocol [199]. Here, a packet refers to the data from a single active user, while a frame denotes the aggregation of data from all active users.

Prior to data transmission, the protocol necessitates knowledge of the number of active users K who are participating in the process. This information is typically available for the operation and maintenance of the network, and therefore does not add any extra complexity. AP assigns a unique identity (ID) to each active user.

We adopt a collision channel model, where a successful transmission is only guaranteed when a single user transmits at a given time. In this case, the AP receives a unique packet and sends an "ACK" message to the successful user. Once acknowledged, the user clears its buffer and remains non-operative until the transmission of the current frame is completed. However, if more than one user transmits simultaneously, a collision occurs. In such cases, the users involved in the collision wait for a another slot and then resume their transmission attempts until successful transmission conditions are met. There may be instances when no user transmits at a given time, resulting in an idle multi-access channel for that duration. Thus, channel idle time increases the latency of data transmission, while collisions increase both latency and energy consumption for users.

The occurrence of successful transmission, which primarily depends on the TP of each user, is highly desirable. We propose two schemes: the FTP scheme and the ATP scheme. The FTP scheme offers a simple procedure for assigning the TP, while the ATP scheme aims to achieve optimal performance in each transmission. For a given network of K transmitting users, a stable transmission is ensured if the probability of transmission for each user is set as $p = \frac{1}{K}$ [203]. This probability of transmission is assigned to each user at the beginning of the data collection process in both schemes. In the FTP scheme, once assigned, the probability of transmission remains constant for the entire duration of the frame. On the other hand, in the ATP scheme, the TP is dynamically adapted with each successful transmission of a packet, utilizing ACK/NACK messages, to ensure stable transmission for each packet during the frame. The algorithm is described in Algorithm 2.

In what follows next, we evaluate delay and energy consumption using FTP and ATP protocols. We also analyze outage performance following successful transmission, utilizing the derived generalized channel model from the previous section.

6.5.2 Performance Analysis for Delay and Scaling Laws

Taking into account the probabilities of multiple transmissions (collisions) and no transmission (idle channel), we can express the expected delay for a successful transmission as $\mathbb{E}D_k = \sum_{k=1}^{\infty} kP_s(1-P_s)^{k-1} = \frac{1}{P_s}$, where $P_s = kp(1-p)^{(k-1)}$ represents the probability of successful transmission in a network of k users. Consequently, the expected D_K required to

Algorithm 2 FTP and ATP Protocols

procedure DATA TRANSMISSION FOR FRAME i
    AP performs network discovery to compute number of users N with a data packet.
    AP considers a threshold SNR γ_{QoS} based on quality of service.
    AP estimates SNR γ_i, $i = 1, 2, \cdots, N$ from each user.
    AP selects K active users only if the SNR $\gamma_i > \gamma_{\mathrm{QoS}}$, $i = 1, 2, \cdots, N$. The THz propagation may ensure $K \ll N$.
loop 1
    AP assigns a transmission probability to each user $p = \frac{1}{K}$
loop 2
    All K active users transmits with probability p
    if multiple users transmit **then** AP **return** "NACK" failure messages: **goto** *loop 2* (for both FTP and ATP)
    else AP **return** "ACK" success message and $K \leftarrow K - 1$: **goto** *loop 1*(ATP), **goto** *loop 2* (FTP)
    if $K = 0$ **then** $i \leftarrow i + 1$
    goto *top*.

successfully collect data from K users can be expressed as:

$$D_K = \sum_{k=1}^{K} \frac{1}{kp(1-p)^{(k-1)}}. \tag{6.17}$$

The equation (6.17) demonstrates that the number of transmissions is predominantly influenced by the number of active users, denoted as K, and their respective transmission probabilities, represented by p.

In the FTP scheme, we substitute $p = \frac{1}{K}$ in (6.17) to compute the number of transmissions required by the FTP scheme. We denote by $r = 1 - \frac{1}{K} < 1$, and $r^{k-1} = \exp\big((k-1)\log r\big)$ to simplify (6.17):

$$D_{\mathrm{FTP}} = (K-1)\sum_{k=1}^{K} \frac{1}{k \cdot \exp(k \log r)}. \tag{6.18}$$

Lemma 6.1. *The expected number of transmissions required by the random access FTP scheme to transmit data from K active users can be bounded by*

$$\begin{aligned} &(K-1)\Big(\log K + \frac{1}{1+2K} + \gamma + 1\Big) < D_{\mathrm{FTP}} \\ &< (K-1)\Big(\log K + \frac{1}{K(K-1)} + \frac{K}{K-1}\mathrm{e} + 1\Big), \end{aligned} \tag{6.19}$$

and thus scales as $M_{\mathrm{FTP}} = \mathcal{O}(K \log K)$.

Proof. The proof is presented in Appendix 6.4. ■

When the number of active users decreases, the constant transmission probability in the FTP scheme results in a reduction in collisions but an increase in delay for subsequent successful transmissions. This delay is primarily due to longer periods of channel idle time without any transmissions. While this increase in delay has a minimal impact on energy consumption for users, it introduces latency in data collection. To address this latency issue, the ATP scheme can be implemented.

The ATP scheme is more stable as it continually updates the transmission probability with each successful transmission. Thus, we substitute $p = 1/k$ in 6.17) to obtain:

$$D_{\mathrm{ATP}} = \sum_{k=1}^{K} \left(\frac{k}{k-1} \right)^{(k-1)}. \tag{6.20}$$

Lemma 6.2. *The expected number of transmissions required by the random access ATP scheme to transmit data from K active users can be bounded by*

$$K\mathrm{e} - \mathrm{e}(\gamma + \log K + \frac{1}{2K}) \leq D_{\mathrm{ATP}} \leq K\mathrm{e}, \tag{6.21}$$

and thus scales as $D_{\mathrm{ATP}} = \mathcal{O}(K\mathrm{e})$.

Proof. The expression (6.20) can be rewritten as $D_{\mathrm{ATP}} = \sum_{k=1}^{K} \exp\left((k-1)\log\left(1+\frac{1}{k-1}\right)\right)$. By applying the logarithm inequality $\log\left(1+\frac{1}{k-1}\right) < \frac{1}{k-1}$, we establish the upper bound stated in (6.21).

For the lower bound, we can utilize the inequalities $\log\left(1+\frac{1}{k-1}\right) > \frac{1}{k}$ and $\exp\left(-\frac{1}{k}\right) > 1 - \frac{1}{k}$ to obtain $D_{\mathrm{ATP}} > \mathrm{e}K - \mathrm{e}\mathcal{H}_K$. By using an upper bound on the harmonic number, $\mathcal{H}_K < \gamma + \log K + \frac{1}{2K}$ [204], we derive the lower bound as stated in (6.21). Furthermore, it is evident that the scaling law holds true as $K \to \infty$ in (6.21). ■

It is worth highlighting that the ATP scheme requires only approximately e times more transmissions compared to optimal scheduling, where centralized control is necessary to enable sequential transmissions from selected users.

Finally, we utilize Hoeffding's concentration inequality to illustrate the tightness of the proposed average delay analysis. This is achieved by examining the deviation (represented by ϵ) of the probability of the sample delay from all users:

$$\Pr[|\bar{D}_K - D_K| > \epsilon] \leq 2\exp\left(-\frac{2\epsilon^2}{n}\right) \leq 2\exp\left(-\frac{2\epsilon^2}{n}\right) \tag{6.22}$$

where $\bar{D}_K$ is the sample delay (obtained with n samples) and D_K is the average delay. It can be seen that the sample delay can provide higher accuracy for a moderate value of n for real-time simulations.

6.5.3 Analysis for Energy Consumption Performance

In this subsection, we examine the expected energy required to collect the data as a parameter to analyze the energy consumption of the protocol. We derive analytical bounds on the expected energy of both ATP and FTP with scaling laws.

In the p-persistent slotted ALOHA protocol each node transmits with probability p. Therefore, when we have m users that have data to transmit, the distribution of the number of users accessing the channel is binomial: $P[Z = m] = \binom{k}{m} p^m (1-p)^{k-m}$, where $k \leq K$ and K is the total number of active users. Hence the expected number of colliding packets in each transmission given that the transmission was unsuccessful is denoted by $\mathbb{E}[N_c]$ (i.e. number of collisions per transmission event given that it failed):

$$\mathbb{E}[N_c] = \sum_{m=2}^{k} mP[Z = m] = kp - kp(1-p)^{k-1}. \tag{6.23}$$

The expected number of transmission attempts between two successful consecutive data transmissions is given by

$$\mathbb{E}[N_{\text{tx}}] = \sum_{k=1}^{\infty} kP_s(1-P_s)^{k-1} = 1/P_s, \tag{6.24}$$

where $P_s = kp(1-p)^{(k-1)}$ is the probability of success. Using (6.23) and (6.24), the expected energy consumed until a single successful transmission of a single packet out of k users that still need to transmit is given by:

$$\mathbb{E}[E_k] = \mathbb{E}[N_{tx}]\mathbb{E}[N_c]E_{\text{tx}} + E_{\text{tx}} = \frac{E_{\text{tx}}}{(1-p)^{(k-1)}}, \tag{6.25}$$

where plus E_{tx} corresponds to the final successful user transmission. The constant E_{tx} represents the energy consumption per single packet transmission. We assume $E_{\text{tx}} = 1$ for the following analysis. The expected energy consumed to collect data from K users is given by:

$$\mathbb{E}[E_K] = \sum_{k=1}^{K} \Big[\frac{1}{(1-p)^{(k-1)}}\Big]. \tag{6.26}$$

In what follows, we derive performance bounds on the consumed energy by the FTP and ATP schemes.

We substitute $p = 1/K$ in (6.26) to compute the expected energy E_{FTP} required by the FTP scheme. We denote by $r = 1 - 1/K < 1$, and $r^{k-1} = \exp\big((k-1)\log r\big)$ to simplify (6.26):

$$E_{\text{FTP}} = \frac{K-1}{K} \sum_{k=1}^{K} \Big[\frac{1}{\exp\big(k \log r\big)}\Big]. \tag{6.27}$$

Lemma 6.3. *The expected energy consumption by the random access FTP scheme with K active users can be bounded by*

$$\frac{3K}{2} - \frac{1}{2K} - 1 < \eta_{\text{FTP}} < \frac{\mathrm{e}(\mathrm{K}-1)^2}{K(K-2)} - 1 + 1/K. \tag{6.28}$$

and thus does not scale with the number of users.

Proof. Applying upper bound $\log r < -1/K$ and then lower bound $\exp(k/K) > 1 + k/K$ in (6.27), we get the lower bound in (6.28). For the upper bound, we use geometric series to sum (6.27) as $(K-1)[\exp(-K\log(r))-1]$. Using $\log(1-1/K) > 1/(1-K)$ and $\exp(1/(K-1)) < (K-1)/(K-2)$, the expression is simplified as $(K-1)[\mathrm{e}(\mathrm{K}-1)/(\mathrm{K}-2)-1]$ and thus we get the upper bound in (6.28). The lower and upper bounds in (6.19) reveal that the scaling law holds true as $K \to \infty$. ■

Since the transmission probability is held constant even with a decrease in the number of active users, there is a decrease in the number of collisions but an increase in the delay for subsequent successful transmissions. This delay is due to the increase in the channel idle time with no transmissions, and thus has a negligible effect on the energy consumption of the users. It is emphasized that the expected energy consumption in the FTP scheme is merely $\mathrm{e}-1$ times more than the optimal scheduling where a centralized control is required to allow sequential transmissions from the selected users.

To compute the expected energy with the ATP scheme, we substitute $p = 1/k$ in (6.26) to get

$$E_{\text{ATP}} = \sum_{k=1}^{K} \left(\frac{k}{k-1}\right)^{(k-1)}. \tag{6.29}$$

Lemma 6.4. *The expected energy consumption by the random access ATP scheme to collect data from K active users can be bounded by*

$$\mathrm{e} - \frac{\mathrm{e}}{K}(\gamma + \log K + \frac{1}{2K}) \leq E_{\text{ATP}} \leq \mathrm{e}, \tag{6.30}$$

and thus does not scale with number of users.

Proof. We can represent (6.29) as $E_{\text{ATP}} = \sum_{k=1}^{K} \exp\big((k-1)\log(1+1/(k-1))\big)$. By applying the logarithm inequality $\log\big(1+1/(k-1)\big) < 1/(k-1)$, we prove the upper bound in (6.30). For the lower bound, we can use the inequalities $\log\big(1+1/(k-1)\big) > 1/k$ and $\exp(-1/k) > 1-1/k$ to get $E_{\text{ATP}} > \mathrm{e}K - \mathrm{e}\mathcal{H}_K$, where $\mathcal{H}_K$ is K-th harmonic number. Using an upper bound on the harmonic number $\mathcal{H}_K < \gamma + \log K + 1/2K$ [204], we get the lower bound in (6.30). Further, it can be seen that the scaling law holds true as $K \to \infty$ in (6.30). ■

Using (6.28) and (6.30), the energy difference ΔE_k between the ATP and FTP can be bounded as

$$(\mathrm{e}-1)\mathcal{H}_{\mathrm{K}}+\mathrm{K}-\frac{\mathrm{e}(\mathrm{K}-1)^2}{(\mathrm{K}-2)}-1<\Delta\mathrm{E_k}<\mathrm{Ke}-\frac{3\mathrm{K}}{2}+\frac{1}{2\mathrm{K}}+1. \tag{6.31}$$

It is important to note that the expected energy consumption of the ATP scheme is larger than the FTP scheme. This can be easily verified by analyzing the energy function in (6.27) and (6.29). This function increases monotonically with p and thus the lower transmission probability in the FTP requires less expected energy consumption. Essentially, the ATP scheme consumes e times more than the optimal scheduling whereas the energy consumption in the FTP scheme is $\mathrm{e}-1$ times more than the same.

Similar to average delay, we utilize Hoeffding's concentration inequality to illustrate the tightness of the proposed average energy analysis:

$$\Pr[|\bar{E}_K-E_K|>\epsilon]\leq 2\exp\left(-\frac{2\epsilon^2}{n(n-1)^2}\right) \tag{6.32}$$

where $\bar{E}_K$ is the sample value and E_K is the average value.

6.5.4 Outage Performance for ATP and FTP Protocols

In this section, we analyze the outage probability for both ATP and FTP Protocols in the event of successful transmission. In this case, the analysis remains the same for the protocols.

The outage probability of a THz system is the probability that the wireless link quality falls below a specified threshold of SNR γ_{th}. The outage probability is an important performance metric, which can be obtained using the CDF function $F_\gamma(\gamma)=P(\gamma<\gamma_{\mathrm{th}})$. We can substitute $\gamma=\gamma_{\mathrm{th}}$ in (6.12), (6.14), and (6.16) to get the outage probability for the THz transmission link under different propagation scenarios.

An asymptotic expression for the outage probability can be obtained by invoking $\bar{\gamma}\to\infty$ (6.12), (6.14), and (6.16). As an illustration, the asymptotic outage probability in high SNR region for (6.12) can be derived using the method of residues as described in [172], while the asymptotic outage probability for (6.14) can be obtained using the approach described in [166, Th. 1.11]. A general expression for the asymptotic outage probability for both the cases is given by

$$P_{\mathrm{out}}^{\infty}(\gamma_{\mathrm{th}})=C_1\left(\frac{\gamma_{h_{\mathrm{th}}}}{\bar{\gamma}}\right)^{\frac{\alpha\mu}{2}}+C_2\left(\frac{\gamma_{h_{\mathrm{th}}}}{\bar{\gamma}}\right)^{\frac{\rho}{2}}+C_3\left(\frac{\gamma_{h_{\mathrm{th}}}}{\bar{\gamma}}\right)^{\frac{z}{2}} \tag{6.33}$$

where C_1, C_2, and C_3 are constants. Analyzing the exponents of the average SNR in (6.33), the

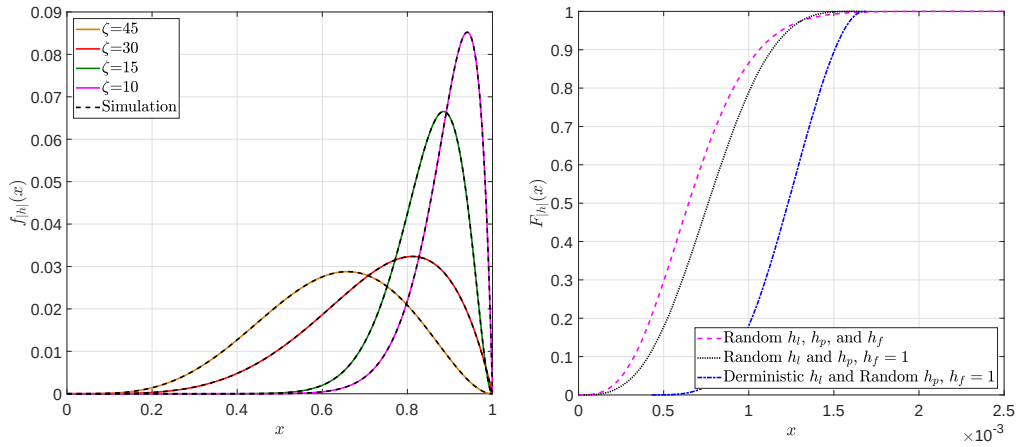

(a) PDF of channel gain $|h|$. (b) CDF of channel gain $|h|$.

Figure 6.2: Generalized channel model for THz propagation with $\alpha = 2$, $\mu = 1$, $\eta = 1$, $\kappa = 1$, $\rho = 4$.

diversity order of the considered system can be obtained as

$$DO = \left\{ \frac{\alpha\mu}{2}, \frac{\rho}{2}, \frac{z}{2} \right\}. \tag{6.34}$$

The diversity order offers multiple options to mitigate the effects of antenna misalignment errors and atmospheric absorption. By understanding the diversity order, we can establish guidelines for effectively utilizing the beam width and link distance to counteract the impact of antenna misalignment errors and random atmospheric absorption. Consequently, the appropriate selection of beam width (to address pointing errors) and link distance (to deal with atmospheric absorption) can help overcome the signal fading.

6.6 Simulation and Numerical Analysis

In this section, we employ Monte Carlo simulations and numerical computations to illustrate the generalized channel model for THz transmission, considering random path loss. We also assess the effectiveness of suggested random access protocols in a cell-free network by leveraging the statistical characterization of THz propagation.

6.6.1 Generalized Channel Model for THz Transmission with Random Path Loss

In this subsection, we assess the accuracy of the generalized channel model compared with the existing model through simulations and numerical analysis conducted using MATLAB. We utilize Monte Carlo simulations to validate our statistical analysis in random path loss. Our study investigates the THz link performance for numerous channel conditions by adopting different absorption coefficient values ζ. The product of shape and scale parameters for the random path-loss ($k\beta$) in (6.9) provides the average value of the absorption coefficient ζ [201].

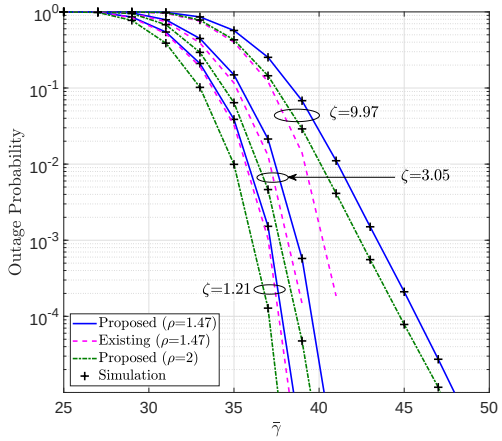

Figure 6.3: Outage probability for generalized channel model for THz propagation with different ζ and $\alpha = 2$, $\mu = 1$, $\eta = 1$, $\kappa = 1$, $\rho = 4$ at d=100 m..

In Fig. 6.2(a), we illustrate the PDF of generalized model, as derived in (6.9) across a wide range of ζ values, representing different propagation scenarios by considering the impact of random path-loss and antenna misalignment errors. Observing the plots, it is evident that for smaller absorption coefficient values (ζ), the random variable tends to cluster around the value of 1. Conversely, with higher ζ values, the variable attenuates and shows a greater tendency to be situated in regions with lower amplitudes. In Fig. 6.2(b), we simulate the generalized THz statistical model under the combined effect of random atmospheric absorption, non-linearity of fading, hardware impairments, and antenna misalignment errors. The figure shows that the probability of getting a higher threshold value of channel gain decreases with an increase in random characteristics of the channel, motivating for the development of random access protocols over THz band.

Further, we utilize the simulation environment to demonstrate and verify the effect of the derived random path-loss on the outage probability of the THz link. In Fig. 6.3, we analyze the outage probability by considering random path-loss and antenna misalignment errors. For this analysis, we exclude the effect of short-term fading and transceiver hardware impairments on the THz link's performance. The plots clearly demonstrate that with increases in ζ value, the outage probability increases. Additionally, we demonstrate the impact of antenna misalignment errors on the outage probability performance. The system's outage performance improves as the antenna misalignment error parameter ρ increases. We compare our proposed results with existing ones employing a deterministic ζ. Figure 6.3 clearly shows that using the deterministic model of ζ sets an upper bound on the performance of the THz link. At an SNR of 45 dB, the outage probability is nearly four times lower when employing the random path-loss model compared to the deterministic path-loss model used in previous works. This highlights the importance of considering the random path-loss model to accurately capture the behavior of the actual system.

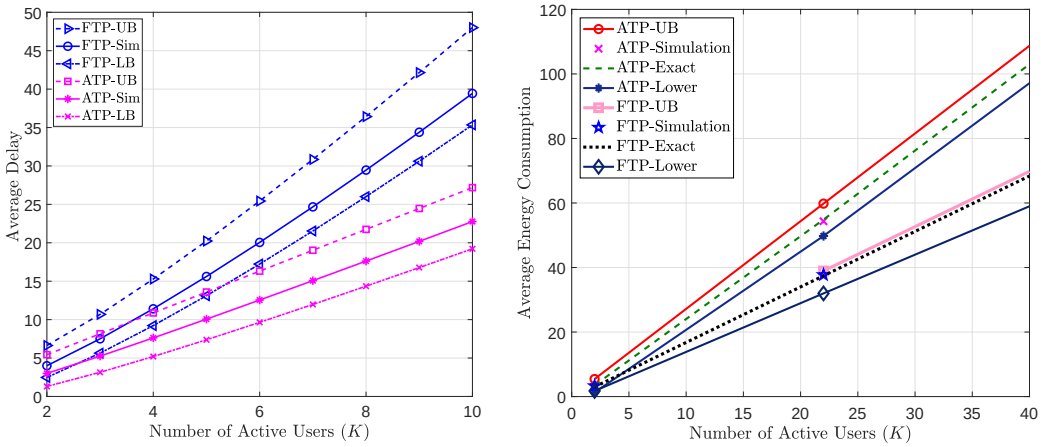

(a) Expected number of transmissions (D_K). (b) Energy consumption (E_K).

Figure 6.4: Delay and energy consumption performance of random access protocols.

6.6.2 Random Access Protocols for Cell-Free Network

In this section we analyze the efficacy of the proposed random access protocols with respect to delay and energy consumption in a multiuser environment. We simulate random access protocols transmitting randomly with assigned transmission probabilities based on the FTP and ATP schemes. The simulation results of the number of transmissions (which also includes multiple transmissions due to the collision) required for each successful transmission were averaged over 5000 trials. For delay analysis, we assign unit time for each unsuccessful data collection event, which includes either the collision or the idle state each consuming a single unit time. For energy consumption, first, we assign unit energy for each transmission from users (including number of collisions) and neglect the energy consumed during the reception of ACK messages and in the event of idle condition of the users. Later, we use actual energy consumed during data transmission and other overheads.

In Fig. 6.4, we analyze the expected delay and energy consumption by the proposed scheme by considering a fixed number of active users (K = 1 to 10) in a network. As shown in Fig. 6.4(a), the adaptive scheme always performs better and incurs less delay than the FTP scheme for data collection. It can be observed form the Fig. 6.4(a) that there occurs more delay for the FTP scheme and number of transmission attempts almost doubles for FTP scheme as compared with the ATP scheme for 10 active users. Further, simulation results can be seen to be in excellent agreement with the exact expressions and derived bounds, as depicted in Fig. 6.4(a).

Fig. 6.4(b) shows that the energy consumption is almost 1.5 times more for ATP scheme at 40 active users since FTP incurs more idle slots than the ATP. It can be seen that the relative gain in the energy by the ATP scheme approaches to $1/\mathrm{e}$ with an increase in the number of active users. The plots in Fig. 6.4(b) show that the an increase in the delay in the FTP scheme has a negligible effect on its energy consumption; in fact the FTP consumes less energy than the ATP scheme due to reduced collisions. We also compare the derived analytical bounds with

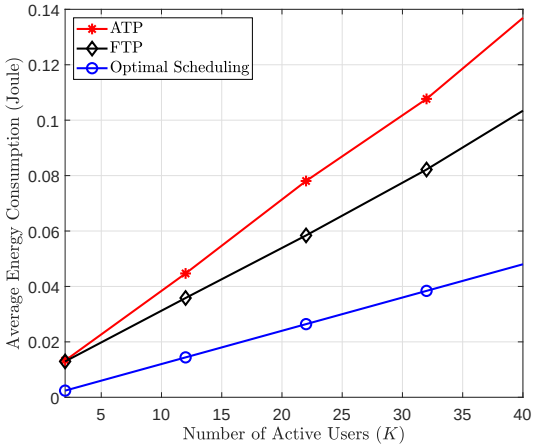

(a)

Figure 6.5: Energy consumption (E_K) of random access protocol using realistic parameters.

the simulation and numerical results in Fig. 6.4(b). The derived bounds for energy consumption are shown to be an excellent match with the exact results except the lower bound of the FTP scheme.

Further, we demonstrate energy consumption using realistic parameters, which includes energy consumption during the reception of ACK messages and energy consumed in the idle state of users with a packet of data. We use transmission energy for data packet 1200 μJ, energy for ACK message 120 μJ, and idle energy consumption per user 40 μJ [205]. The performance is compared with the optimal scheduling. It is shown in Fig. 6.5 that the simple FTP scheme (without collision control and adaptation of TP during data collection) requires less energy than the ATP scheme, and can be effective to prolong the life time of network. However, the advantage of reduced energy consumption in the FTP scheme comes with an increased delay in collecting the data, as demonstrated in Fig. 6.4(a). Although the optimal scheduling requires less energy than the proposed random access protocols, it requires centralized processing or more time/frequency resources.

Finally, Fig. 6.6 demonstrates the outage performance for successful transmission by considering random path-loss, antenna misalignment error, α-η-κ-μ short-term fading, and transceiver hardware impairments. In Fig. 6.6(a), we present the outage performance of the THz link with the channel fading parameter μ and the antenna misalignment error parameter ρ. The outage probability decreases as the number of multi-path clusters increases. Further, the outage performance improves with an increase in ρ, indicating a decrease in antenna misalignment error. It can be observed from the plots that the outage performance improves by approximately 30 times when μ is increased from 1.5 to 2.5 at an SNR of 60 dB for $\rho = 4.1$. Fig. 6.6(b) shows that the THz link's outage performance improves with higher values of the fading parameters α and κ. Further, the impact of transceiver hardware impairment is evident in the outage probability. As the hardware impairment coefficient k_h increases, the outage probability also increases. When α increases from 1.2 to 2 for $\kappa = 0.2$ and $k_h = 0.4$ at an SNR of 55

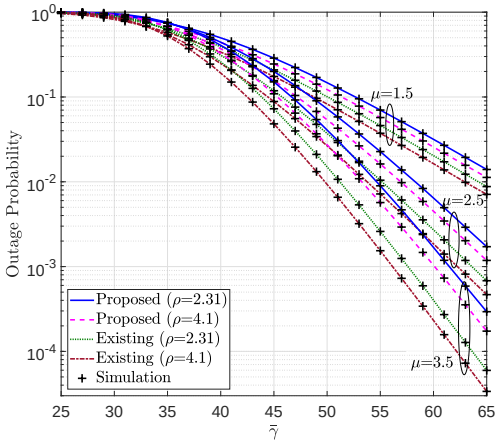

(a) Channel parameters $k = 1$ and $\alpha = 1$ for various ρ and μ.

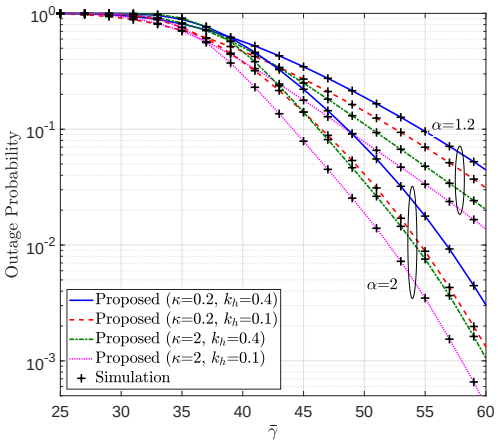

(b) Channel parameters with $k = 3$, $\mu = 2$, $\eta = 1$, and $\rho = 4.1$ for various α, κ, and k_h.

Figure 6.6: Outage probability performance for FTP/ATP protocol over generalized THz channel model at $d = 100$ m.

dB, the outage probability is reduced by nearly 9 times. The figure demonstrates that the slope of the plots remains constant when ρ and k ($z = 8.686/(\beta d)$) values change but changes only with α and μ, thereby confirming our diversity order analysis.

6.7 Chapter Summary

In this chapter, we developed a generalized THz transmission model, including random path-loss, antenna misalignment errors, short-term fading, and transceiver hardware impairments. By accounting for the random path loss, generalized short-term fading, and transceiver hardware impairment, the proposed channel model can better capture the actual behavior and performance of the system at THz frequencies. Leveraging the statistical model, we proposed random access protocols for a cell-free wireless network to ensure transmission for multiple users while minimizing delay and energy consumption. The protocols adapt the transmission probability using a-priori estimates of the number of active users with data to transmit. We derived tight bounds on the performance of both schemes and showed that the simple FTP scheme incurs reduced energy consumption compared to the ATP at the cost of an increased expected delay. Computer simulations demonstrated the efficacy of the proposed random access schemes and accuracy in performance assessment with the statistical effect of THz propagation for a cell-free network.

The next chapter concludes this thesis by presenting a summary and suggesting potential avenues for future research.

Appendix 6.1: Proof of Theorem 6.1

Defining $U = \sum_{i=1}^{\mu_x}(X_i + \lambda_{x_i})^2$ and $V = \sum_{i=1}^{\mu_y}(X_i + \lambda_{y_i})^2$, i.e. $R^\alpha = U + V$. By means of transformation of variables, the PDF $f_R(r)$ of R is found as [159]

$$f_R(r) = \alpha r^{\alpha-1} \int_0^{r^\alpha} f_U(r^\alpha - v) f_V(v) dv \tag{6.35}$$

Using $f_U(u)$ and $f_V(v)$ from [159] in (6.35) and after some algebraic manipulation, we get

$$f_R(r) = \frac{\psi_1 r^{\psi_2}}{(\hat{r}^\alpha)^{1+\frac{\mu}{2}}} \times e^{-\psi_3 r^\alpha} \int_0^{r^\alpha} \frac{(r^\alpha - v)^{\frac{A_1}{2}}}{v^{-\frac{A_2}{2}}} e^{-A_3 v} I_{A_1}(A_4 (r^\alpha - v)^{\frac{1}{2}}) I_{A_2}(A_5 v^{\frac{1}{2}}) dv \tag{6.36}$$

where I_{A_1} and I_{A_2} are the modified Bessel function of the first kind. Using Meijer's G representation of the Bessel functions [206], (6.36) can be rewritten as

$$\begin{aligned} f_R(r) = \frac{\psi_1 r^{\psi_2}}{(\hat{r}^\alpha)^{1+\frac{\mu}{2}}} e^{-\psi_3 r^\alpha} \pi 2^{-A_1} (A_4 (r^\alpha - v)^{\frac{1}{2}})^{A_1} \pi 2^{-A_2} (A_5 v^{\frac{1}{2}})^{A_2} \int_0^{r^\alpha} \frac{(r^\alpha - v)^{\frac{A_1}{2}}}{v^{-\frac{A_2}{2}}} G_{0,1}^{1,0}\left(\begin{matrix} - \\ 0 \end{matrix} \middle| A_3 \right) \\ \times G_{1,3}^{1,0}\left(\begin{matrix} \frac{1}{2} \\ 0, -A_1, \frac{1}{2} \end{matrix} \middle| \frac{A_4^2 (r^\alpha - v)}{4} \right) G_{1,3}^{1,0}\left(\begin{matrix} \frac{1}{2} \\ 0, -A_2, \frac{1}{2} \end{matrix} \middle| \frac{A_5^2 v}{4} \right) dv \end{aligned} \tag{6.37}$$

Utilizing the integral representation of Meijer's G-function [170], we can represent (6.37) as

$$\begin{aligned} f_R(r) = \frac{\psi_1}{(\hat{r}^\alpha)^{1+\frac{\mu}{2}}} \pi^2 2^{(2-\mu)} A_4^{A_1} A_5^{A_2} r^{\psi_2} e^{-\psi_3 r^\alpha} \frac{1}{(2\pi i)^3} \int_{\mathcal{L}_1} \int_{\mathcal{L}_2} \int_{\mathcal{L}_3} \Gamma(-s_1) {A_3}^{s_1} ds_1 \\ \times \frac{\Gamma(-s_2)}{\Gamma(1 + A_1 + s_2)\Gamma(\frac{1}{2} + s_2)\Gamma(\frac{1}{2} - s_2)} \left(\frac{A_4^2}{4}\right)^{s_2} ds_2 \frac{\Gamma(-s_3)}{\Gamma(1 + A_2 + s_3)\Gamma(\frac{1}{2} + s_3)\Gamma(\frac{1}{2} - s_3)} \left(\frac{A_5^2}{4}\right)^{s_3} I_1 ds_3 \end{aligned} \tag{6.38}$$

where $\mathcal{L}_1$, $\mathcal{L}_2$, and $\mathcal{L}_3$, denote the contour integrals. The inner integral I_1 can be represented and simplified using the identity [168, 3.191.1] as

$$\begin{aligned} I_1 = \int_0^{r^\alpha} v^{A_2 + s_1 + s_3} (r^\alpha - v)^{A_1 + s_2} dv = \\ \frac{\Gamma(1 + A_2 + s_1 + s_3)\Gamma(1 + A_1 + s_2)}{\Gamma(2 + A_2 + s_1 + s_3 + A_1 + s_2)} r^{\alpha(1 + A_2 + s_1 + s_3 + A_1 + s_2)} \end{aligned} \tag{6.39}$$

Finally, substituting (6.39) in (6.38), rearranging the terms, and applying the definition of multivariate Fox's H-function [170], we get the PDF of Theorem 6.1 in (6.8), which concludes the proof.

Appendix 6.2: Proof of Theorem 6.2

To derive the combined PDF of random path-loss, antenna misalignment error, and short-term fading, we first derive the joint PDF of short-term fading and antenna misalignment error

$f_{h_{\rm fp}}(x)$, which is given by [174]

$$f_{h_{fp}}(z) = \int_z^{\infty} \frac{1}{x} f_{h_f}(x) f_{h_p}\left(\frac{z}{x}\right) \mathrm{d}x. \tag{6.40}$$

Substituting the respective PDFs of short-term fading and antenna misalignment error from (6.8) and (6.4) in (6.40), utilizing the Mellin Barnes type integral form of the exponential function and substituting $\ln\left(\frac{z}{x}\right) = t$, we rewrite the integration and get the inner integral $\int_0^{\infty} (e^{-t})^{\alpha(1+A_1+A_2+s_1+s_2+s_3+s_4)-\rho+1} t\mathrm{d}t$. We solve the inner integral by applying the identity [168, (3.381/4)] and after some mathematical manipulation and utilizing the definition of multivariate Fox's H-function, we get the joint PDF of short-term fading and antenna misalignment error as

$$f_{h_{fp}}(z) = \frac{\psi_1 \rho^2 (z)^{\alpha(1+A_1+A_2)}}{(\hat{r}^{\alpha})^{1+\frac{\mu}{2}}} H^{0,2;1,0;1,1;1,0;1,0}_{2,2;0,1;2,3;1,3;0,1}\left[\begin{matrix} V_3 \\ V_4 \end{matrix} \middle| A_3 z^{\alpha}, \frac{A_4^2}{4} z^{\alpha}, \frac{A_5^2}{4} z^{\alpha}, \psi_3 z^{\alpha} \right], \tag{6.41}$$

where $V_3 = \big\{(-A_2; 1, 0, 1, 0)\big\}, \big\{\rho - \alpha - \alpha A_1 - \alpha A_2; \alpha, \alpha, \alpha, \alpha\big\} : \big\{(-,-)\big\}; \big\{(-A_1, 1)(\frac{1}{2}, 1)\big\}; \big\{(\frac{1}{2}, 1)\big\}; \big\{-,-\big\}$ and $V_4 = \big\{(-1 - A_1 - A_2; 1, 1, 1, 0)\big\}, \big\{\rho - 1 - \alpha - \alpha A_1 - \alpha A_2; \alpha, \alpha, \alpha, \alpha\big\} : \big\{(0, 1)\big\}; \big\{(0, 1), (-A_1, 1), (\frac{1}{2}, 1)\big\}; \big\{(0, 1), (-A_2, 1), (\frac{1}{2}, 1)\big\}; \big\{(0, 1)\big\}$.

Now, we need to multiply the joint PDF derived in (6.41), with the PDF of random path-loss in (6.9) to derive the combined PDF of short-term fading, antenna misalignment error, and random path-loss. The combined PDF equation is given by [174]

$$f_{h_{fpl}}(y) = \int_{\frac{y}{a}}^{\infty} \frac{1}{x} f_{h_{fp}}(x) f_{h_l}\left(\frac{y}{x}\right) \mathrm{d}x. \tag{6.42}$$

Similarly, plugging the PDFs of (6.9) and (6.41) in (6.42) and substituting $\ln\left(\frac{ax}{y}\right) = t$, and following the similar procedure, we get the combined PDF of fading, antenna misalignment error and random path-loss in (6.11). The PDF of SNR can be derived by simple transformation of random variable [174] as $f_{\gamma}(\gamma) = \frac{1}{2\sqrt{\gamma\gamma_0}} f_{h_{fpl}}\left(\sqrt{\frac{\gamma}{\gamma_0}}\right)$. To derive the CDF, we integrate the PDF $F_{h_{fpl}}(y) = \int_0^y f_{h_{fpl}}(y) dy$, to get the inner integral as $\int_0^y y^{\alpha(1+A_1+A_2+s_1+s_2+s_3+s_4)} dy$. Solving the inner integral and applying the definition of Fox's H-function, the CDF is given in (6.12). Similar to the PDF, the CDF of the SNR can be derived by simple transformation of a random variable as $F_{\gamma}(\gamma) = \left(\sqrt{\frac{\gamma}{\gamma_0}}\right)$ to conclude the proof.

Appendix 6.3: Proof of Corollary 6.2

The combined PDF of random path loss and antenna misalignment error $f_{h_{\rm lp}}(x)$ is given by [174]

$$f_{h_{\rm lp}}(x) = \int_x^a \frac{1}{h_l} f_{h_l}(h_l) f_{h_p}\left(\frac{x}{h_l}\right) \mathrm{d}h_l. \tag{6.43}$$

Substituting the PDFs of the random path-loss and antenna misalignment error from (6.9) and (6.4), respectively, in (6.43), to get the PDF as

$$f_{h_{lp}}(x) = -\frac{z^k \rho^2 x^{\rho-1}}{\Gamma(k)} \int_x^{a_l} h_l^{z-\rho-1} \left[ln\left(\frac{a_l}{h_l}\right)\right]^{k-1} \ln\left(\frac{x}{h_l}\right) \mathrm{d}h_l \tag{6.44}$$

substituting $\ln(\frac{a_l}{h_l}) = t$ in (6.44), and applying the identity $\int_0^u x^{\nu-1} e^{-\mu x} dx = \mu^{-\nu}\big[\Gamma(\nu) - \Gamma(\nu, \mu u)\big]$ in (6.44), we get the combined PDF of random path-loss and antenna misalignment error in (6.15). The PDF of SNR can be derived by simple transformation of a random variable [174] as $f_\gamma(\gamma) = \frac{1}{2\sqrt{\gamma\gamma_0}} f_{h_{fpl}}\left(\sqrt{\frac{\gamma}{\gamma_0}}\right)$. To derive the CDF, we will integrate the PDF $F_{h_{lpl}}(y) = \int_0^y f_{h_{lpl}}(x)dx$ and use the series expansion of the upper incomplete Gamma function $\Gamma(a, z) = (a-1)! e^{-z} \sum_{j=0}^{a-1} \frac{z^j}{j!}$, to get

$$\begin{aligned} F_{h_{lp}}(y) = &-\frac{z^k \rho^2 a_l^{z-\rho} (z-\rho)^{-k}}{\Gamma(k)} \Bigg[\frac{1}{z-\rho} \Big[\int_0^y x^{\rho-1} \Gamma(k+1) dx \\ &- k! \sum_{j=0}^{k} \frac{\Big((z-\rho)\Big)^j}{j!} \int_0^y x^{\rho-1} \Big(\frac{a_l}{x}\Big)^{-(z-\rho)} \Big(\ln\big(\frac{a_l}{x}\big)\Big)^j dx \Big] \\ &- \Bigg[\int_0^y x^{\rho-1} \Gamma(k) dx - (k-1)! \sum_{j=0}^{k-1} \frac{\Big((z-\rho)\Big)^j}{j!} \int_0^y x^{\rho-1} \Big(\frac{a_l}{x}\Big)^{-(z-\rho)} \Big(\ln\big(\frac{a_l}{x}\big)\Big)^j dx \Bigg] \Bigg] \end{aligned} \tag{6.45}$$

substituting $\ln(\frac{a_l}{x}) = t$ and applying the identity [168, 3.351,2] $\int_u^\infty x^n e^{-\mu x} dx = \mu^{-n-1} \Gamma(n+1, \mu u)$, we get the combined CDF of random path-loss and antenna misalignment error in (6.16). The CDF of the SNR can be derived by transforming the random variable as $F_\gamma(\gamma) = \left(\sqrt{\frac{\gamma}{\gamma_0}}\right)$ to finish the proof.

Appendix 6.4: Upper Bound of Lemma 6.1

Since $f(k) = 1/(k \cdot \exp(k \log r))$ satisfies the integral inequality $\sum_{k=1}^{K} f(k) \leq f(1) + \int_1^{K-1} f(x)dx$ in the interval of $1 \leq k \leq K-1$, D_{FTP} in (6.18) can be upper bounded

$$D_{\mathrm{FTP}} \leq (K-1)\Big(\frac{K}{K-1} + I_{K-1} + f(K)\Big), \tag{6.46}$$

where $I_{K-1} = \int_1^{K-1} \frac{dx}{x \cdot \exp(x \log r)}$. Substituting $z = x \log r$, we can express I_{K-1}:

$$I_{K-1} = \Big(E_1(\log r) - E_1\big((K-1)\log r\big)\Big). \tag{6.47}$$

Using series expansion of the exponential integral $E_1(z) = -\gamma - \log z - \sum_{m=1}^{\infty} (-1)^m z^m/(m \cdot m!)$ [204, 5.1.11], we can represent (6.47):

$$I_{K-1} = \log(K-1) + \sum_{m=1}^{\infty} \frac{\big((K-1)\log r\big)^{2m}}{2m \cdot 2m!} - \frac{(\log r)^{2m}}{2m \cdot 2m!} + \sum_{m=1}^{\infty} \frac{\big(\log r\big)^{2m+1}}{2m+1 \cdot 2m+1!} - \frac{((K-1)\log r)^{2m+1}}{2m+1 \cdot 2m+1!} \tag{6.48}$$

We use $\log(r) < -1/K$ and $\log(r) > -1/(K-1)$ in (6.48) appropriately to simplify:

$$I_{K-1} \leq \log(K-1) + I_1 - I_2 \tag{6.49}$$

where $I_1 = \sum_{m=1}^{\infty} 1/(m \cdot m!)$ and $I_2 = \sum_{m=0}^{\infty} \big(1/K\big)^m/(m \cdot m!)$. Using the definition of the exponential integral $E_1(z)$, we obtain $I_1 = -(E_1(-1) + \gamma + i\pi)$. We also derive an upper bound $I_1 \leq \sum_{m=1}^{\infty} 1/m! = \mathrm{e} - 1$ with an error bound $\epsilon(I_1) < \mathrm{e} - J_0(2)$, where $J_0(\cdot)$ is the zeroth order Bessel function of the first kind. After a simple algebraic manipulation, we get a lower bound on $I_2 > J_0\big(2/\sqrt{K}\big) - 1$. Using these bounds in (6.49) with $\log(K-1) = \log K + \log(1 - 1/K) < \log K - 1/K$:

$$I_{K-1} \leq \log K - \frac{1}{K} + \mathrm{e} - J_0(2/\sqrt{K}) \tag{6.50}$$

Further, we represent $f(K) = 1/(K-1).\exp\big((K-1)\log(1 + 1/(K-1)\big)$ and use $\log(1 + 1/(K-1) > 1/(K-1)$ to bound $f(K)$:

$$f(K) < \frac{\mathrm{e}}{K-1} \tag{6.51}$$

Thus, using (6.50) and (6.51) in (6.46), we get the upper bound of Lemma 6.1.

Chapter 7

Conclusions and Future Directions

This dissertation examined the statistical performance analysis of THz wireless communication and developed algorithms to seamlessly incorporate THz wireless systems into access, IoT, and cell-free networks. The study focused on the THz spectrum as a high-speed wireless link and backhaul support for access, IoT, and cell-free networks. The first introductory chapter dealt with the basic concepts of the thesis, providing related research, research gaps, and motivation for the proposed research work. The second chapter provided an overview of the THz systems with applications, statistical models for various channel impairments, and performance metrics used.

In the third chapter, a general analysis for multihop transmission was presented to extend the coverage range for the THz wireless backhaul. The proposed analysis involved a novel approach of Mellin-Barnes integral to develop statistical results for FG and CA based multihop techniques. By considering generalized fading channels, antenna misalignment errors, and dynamic shadowing caused by human movement, a more comprehensive performance evaluation for multihop THz propagation was conducted. The conventional iterative approach used for analytically deriving RF and FSO multihop systems was found to be special cases within the framework of this proposed analysis. The research presented in this chapter demonstrated the advantages of multihop transmission in extending the transmission range of the THz system.

In Chapter 4, an in-depth performance analysis was provided for the integration of THz and RF systems, illustrating how the current RF access networks could be seamlessly incorporated into the core network by employing THz wireless backhaul as a viable substitute for traditional wired fiber connections. The proposed analysis incorporated practical scenarios such as asymmetrical channel conditions for THz and RF links, multiple antennas at the APs, and a low complexity relaying approach, albeit providing exact analysis for a better performance evaluation of the integrated system. Analytical results in terms of simple mathematical functions under some special cases of THz and RF transmission was presented to demonstrate an efficient integration of the THz backhaul with the RF access network.

Chapter 5 introduced a distributed algorithm to select AN to collect data from an IoT network to a UAV. This simple, self-configuring AN selection algorithm for IoT devices within the

network reduces the overhead typically associated with centralized methods, thereby improving the efficiency of IoT devices. To leverage the diversity of fading channels when transmitting collected data to the core network, a triple-technology wireless backhaul was proposed. This backhaul incorporated mmWave, FSO, and THz technologies. The study conducted a thorough exploration of hybrid scheme selection in various channel and SNR scenarios, considering the trade-off between achieving acceptable performance and managing the complexity of the hybrid backhaul.

Chapter 6 focused on developing low-complexity receivers for multiuser transmission in cell-free wireless networks operating in the THz spectrum. The cell-free network had the access link operating in the sub-GHz range and the fronthaul link operating in the sub-THz spectrum. The combined effects of random atmospheric absorption, nonlinear fading, hardware limitations, and antenna misalignment errors in THz transmission facilitated the development of random access protocols, ensuring successful data transmission for multiple users with minimal delay and energy loss. These protocols provided a potential alternative to address the complexity of signal processing required for interference cancellation at the CPU when dealing with data collected from many APs.

In conclusion, this thesis has provided a thorough examination of the statistical performance analysis of THz wireless communication and has developed algorithms for seamlessly integrating THz wireless systems into access, IoT, and cell-free networks. The study addresses critical fundamental research gaps and offers practical insights into deploying THz technology by exploring how THz spectrum can serve as a high-speed wireless link and support network backhaul for diverse network architectures. By presenting novel approaches and methodologies, such as the use of Mellin-Barnes integrals for multihop transmission analysis and distributed algorithms for IoT device coordination, the research presents the potential benefits of utilizing THz systems across various network scenarios. Moreover, the investigation into the integration of THz and RF systems and utilizing the THz spectrum for cell-free networks operating have demonstrated promising areas for enhancing wireless communication efficiency in future 6G networks. Overall, this work contributes to the advancement of THz technology and lays the groundwork for its effective deployment in next-generation wireless communication systems.

The proposed research presents several avenues for expansion. While the current findings are based on sub-THz frequencies up to 300 GHz, there is potential for further exploration into true THz frequencies, allowing for more efficient utilization of a broader spectrum. An intriguing avenue for study lies in investigating channel modeling, encompassing factors such as path-loss, fading, hardware limitations, and antenna misalignment, and using real measurement data.

In addition to extending the range of THz communication through relay technology, it is worth considering integrating emerging technologies like RIS and RHS to enhance THz wireless systems. There is also a need for more in-depth research into multiuser and multi-antenna transmission over THz.

Integrated sensing and communication (ISAC) over the THz spectrum presents a promising area for research activities. Furthermore, in the future, THz communication research could explore applications in satellite and underwater communication, providing an alternative to light-based systems. A deeper exploration of the THz spectrum for in-vivo applications and nano-communications is essential for better use cases of THz communications. Validating the proposed models and developing protocols with experimental data would be a possible avenue for future research. The standardization of THz communication should be an integral part of the 6G communication framework.

Bibliography

[1] Tapan K. Sarkar, Robert J. Mailloux, Arthur A. Oliner, Magdalena Salazar-Palma, and Dipak L. Sengupta. *History of Wireless*. Wiley-IEEE Press, 2006.

[2] Theodore Rappaport. *Wireless Communications: Principles and Practice*. Prentice Hall PTR, 2001.

[3] Andreas F. Molisch. *Wireless Communications*. Wiley-IEEE Press, 2011.

[4] Andrea Goldsmith. *Wireless Communications*. Cambridge University Press, 2012.

[5] H. Nyquist. Certain topics in telegraph transmission theory. *Transactions of the American Institute of Electrical Engineers*, 47(2):617–644, 1928.

[6] C. E. Shannon. A mathematical theory of communication. *The Bell System Technical Journal*, 27(3):379–423, 1948.

[7] V. H. Mac Donald. Advanced mobile phone service: The cellular concept. *Bell System Technical Journal*, 58(1):15–41, 1979.

[8] Robert C. Daniels, James N. Murdock, Theodore S. Rappaport, and Robert W. Heath. 60 GHz wireless: Up close and personal. *IEEE Microwave Magazine*, 11(7):44–50, 2010.

[9] Kao-Cheng Huang and Zhaocheng Wang. *Millimeter Wave Communication Systems*. Wiley-IEEE Press, 2011.

[10] Theodore S. Rappaport, George R. MacCartney, Mathew K. Samimi, and Shu Sun. Wideband Millimeter-Wave propagation measurements and channel models for future wireless communication system design. *IEEE Transactions on Communications*, 63(9):3029–3056, 2015.

[11] Erik G. Larsson, Ove Edfors, Fredrik Tufvesson, and Thomas L. Marzetta. Massive mimo for next generation wireless systems. *IEEE Communications Magazine*, 52(2): 186–195, 2014.

[12] S. Dang et al. What should 6G be? *Nature Electron*, (3):20–29, 2020.

[13] Ziwei Wan, Zhen Gao, Feifei Gao, Marco Di Renzo, and Mohamed-Slim Alouini. Terahertz massive MIMO with holographic reconfigurable intelligent surfaces. *IEEE Transactions on Communications*, 69(7):4732–4750, 2021.

[14] Haobo Zhang, Hongliang Zhang, Boya Di, and Lingyang Song. Holographic integrated sensing and communications: Principles, technology, and implementation. *IEEE Communications Magazine*, 61(5):83–89, 2023.

[15] Tierui Gong, Panagiotis Gavriilidis, Ran Ji, Chongwen Huang, George C. Alexandropoulos, Li Wei, Zhaoyang Zhang, Mérouane Debbah, H. Vincent Poor, and Chau Yuen. Holographic MIMO communications: Theoretical foundations, enabling technologies, and future directions. *IEEE Communications Surveys & Tutorials*, pages 1–1, 2023.

[16] Martin Koch. Terahertz communications: A 2020 vision, terahertz frequency detection and identification of materials and objects, springer netherlands 2007.

[17] Radoslaw Piesiewicz, Thomas Kleine-Ostmann, Norman Krumbholz, Daniel Mittleman, Martin Koch, Joerg Schoebel, and Thomas Kurner. Short-range ultra-broadband terahertz communications: Concepts and perspectives. *IEEE Antennas and Propagation Magazine*, 49(6):24–39, 2007.

[18] Ho-Jin Song and Tadao Nagatsuma. Present and future of Terahertz communications. *IEEE Transactions on Terahertz Science and Technology*, 1(1):256–263, 2011.

[19] Ian F. Akyildiz, Josep Miquel Jornet, and Chong Han. Terahertz band: Next frontier for wireless communications. *Physical Communication*, 12:16–32, 2014. ISSN 1874-4907.

[20] S. Koenig, D.Lopez-Diaz, and J.Antes et al. Wireless sub-THz communication system with high data rate. *Nature Photon*, 7:977–981, 2013.

[21] H. Elayan, O. Amin, B. Shihada, R. M. Shubair, and M. Alouini. Terahertz band: The last piece of RF spectrum puzzle for communication systems. *IEEE Open Journal of the Communications Society*, 1:1–32, 2020.

[22] Theodore S. Rappaport et al. Wireless communications and applications above 100 GHz: Opportunities and challenges for 6G and beyond. *IEEE Access*, 7:78729–78757, 2019.

[23] Ian F. Akyildiz et al. 6G and beyond: The future of wireless communications systems. *IEEE Access*, 8:133995–134030, 2020.

[24] Hadi Sarieddeen et al. Next generation Terahertz communications: A rendezvous of sensing, imaging, and localization. *IEEE communicatons Magazine*, 58(5):69–75, 2020.

[25] A. Faisal, H. Sarieddeen, H. Dahrouj, T. Y. Al-Naffouri, and M. S. Alouini. Ultramassive MIMO systems at Terahertz bands: Prospects and challenges. *IEEE Vehicular Technology Magazine*, 15(4):33–42, 2020.

[26] A. A. Boulogeorgos, A. Alexiou, T. Merkle, C. Schubert, R. Elschner, A. Katsiotis, P. Stavrianos, D. Kritharidis, P. Chartsias, J. Kokkoniemi, M. Juntti, J. Lehtomaki, A. Teixeira, and F. Rodrigues. Terahertz technologies to deliver optical network quality of experience in wireless systems beyond 5G. *IEEE Communications Magazine*, 56 (6):144–151, 2018.

[27] Mohammad Ali Khalighi and Murat Uysal. Survey on free space optical communication: A communication theory perspective. *IEEE Communications Surveys & Tutorials*, 16(4): 2231–2258, 2014.

[28] N. Wang, E. Hossain, and V. K. Bhargava. Backhauling 5G small cells: A radio resource management perspective. *IEEE Wireless Communications*, 22(5):41–49, 2015.

[29] S. Kim and A. G. Zajić. Statistical characterization of 300-GHz propagation on a desktop.

IEEE Transactions on Vehicular Technology, 64(8):3330–3338, 2015.

[30] J. Kokkoniemi, J. Lehtomäki, and M. Juntti. Simplified molecular absorption loss model for 275–400 Gigahertz frequency band. In *12th European Conference on Antennas and Propagation (EuCAP 2018)*, pages 1–5, 2018.

[31] Y. Wu, J. Kokkoniemi, C. Han, and M. Juntti. Interference and coverage analysis for Terahertz networks with indoor blockage effects and line-of-sight access point association. *IEEE Transactions on Wireless Communications*, 20(3):1472–1486, 2021.

[32] H. Sarieddeen, M. Alouini, and T. Y. Al-Naffouri. Terahertz-band ultra-massive spatial modulation MIMO. *IEEE Journal on Selected Areas in Communications*, 37(9):2040–2052, 2019.

[33] A. A. Boulogeorgos and A. Alexiou. Error analysis of mixed THz-RF wireless systems. *IEEE Communications Letters*, 24(2):277–281, 2020.

[34] A. A. Boulogeorgos and A. Alexiou. Analytical performance assessment of THz wireless systems. *IEEE Access*, 7:11436–11453, 2019.

[35] R. Boluda-Ruiz, A. García-Zambrana, C. Castillo-Vázquez, B. Castillo-Vázquez, and S. Hranilovic. Outage performance of exponentiated Weibull FSO links under generalized pointing errors. *Journal of Lightwave Technology*, 35(9):1605–1613, 2017.

[36] J. Kokkoniemi, A. Boulogeorgos, M. Aminu, J. Lehtomäki, A. Alexiou, and M. Juntti. Impact of beam misalignment on THz wireless systems. *Nano Communication Networks*, 24:100302, 2020. ISSN 1878-7789.

[37] J. M. Jornet and I. F. Akyildiz. Channel modeling and capacity analysis for electromagnetic wireless nanonetworks in the Terahertz band. *IEEE Transactions on Wireless Communications*, 10(10):3211–3221, 2011.

[38] S. Priebe, C. Jastrow, M. Jacob, T. Kleine-Ostmann, T. Schrader, and T. Kürner. Channel and propagation measurements at 300 GHz. *IEEE Transactions on Antennas and Propagation*, 59(5):1688–1698, 2011.

[39] C. Cheng, S. Sangodoyin, and A. Zajić. Terahertz MIMO fading analysis and doppler modeling in a data center environment. In *2020 14th European Conference on Antennas and Propagation (EuCAP)*, pages 1–5, 2020.

[40] A. Olutayo, J. Cheng, and J. F. Holzman. A new statistical channel model for emerging wireless communication systems. *IEEE Open Journal of the Communications Society*, 1:916–926, 2020.

[41] J. Bian, C. X. Wang, X. Gao, X. You, and M. Zhang. A general 3D non-stationary wireless channel model for 5G and beyond. *IEEE Transactions on Wireless Communications*, pages 1–1, 2021.

[42] T. Schenk. *RF Imperfections in High-rate Wireless Systems Impact and Digital Compensation*. Dordrecht, The Netherlands: Springer, 2008.

[43] Lothar Moeller John Federici. Review of terahertz and subterahertz wireless communications. *J. Appl. Phys*, 107(11):24–39, 2010.

[44] Kao-cheng Huang and Zhaocheng Wang. Terahertz terabit wireless communication. *IEEE Microwave Magazine*, 12(4):108–116, 2011.

[45] Hongyang Du, Jiayi Zhang, Ke Guan, Dusit Niyato, Huiying Jiao, Zhiqin Wang, and Thomas Kürner. Performance and optimization of reconfigurable intelligent surface aided THz communications. *IEEE Transactions on Communications*, 70(5):3575–3593, 2022.

[46] P. Boronin, D. Moltchanov, and Y. Koucheryavy. A molecular noise model for THz channels. In *2015 IEEE International Conference on Communications (ICC)*, pages 1286–1291, 2015.

[47] V. Petrov, D. Moltchanov, and Y. Koucheryavy. Interference and SINR in dense Terahertz networks. In *2015 IEEE 82nd Vehicular Technology Conference (VTC2015-Fall)*, pages 1–5, 2015.

[48] R. Zhang, K. Yang, A. Alomainy, Q. H. Abbasi, K. Qaraqe, and R. M. Shubair. Modelling of the Terahertz communication channel for in-vivo nano-networks in the presence of noise. In *2016 16th Mediterranean Microwave Symposium (MMS)*, pages 1–4, 2016.

[49] H. Elayan, C. Stefanini, R. M. Shubair, and J. M. Jornet. End-to-end noise model for intra-body Terahertz nanoscale communication. *IEEE Transactions on NanoBioscience*, 17(4):464–473, 2018.

[50] Evangelos N. Papasotiriou, Alexandros-Apostolos A. Boulogeorgos, and Angeliki Alexiou. Performance analysis of THz wireless systems in the presence of antenna misalignment and phase noise. *IEEE Communications Letters*, 24(6):1211–1215, 2020.

[51] Mohammad Taghi Dabiri and Mazen Hasna. Pointing error modeling of mmWave to THz high-directional antenna arrays. *IEEE Wireless Communications Letters*, 11(11): 2435–2439, 2022.

[52] A. Nosratinia, T. E. Hunter, and A. Hedayat. Cooperative communication in wireless networks. *IEEE Communications Magazine*, 42(10):74–80, 2004.

[53] M.O. Hasna and M.-S. Alouini. A performance study of dual-hop transmissions with fixed gain relays. *IEEE Transactions on Wireless Communications*, 3(6):1963–1968, 2004.

[54] E. Bjornson, M. Matthaiou, and M. Debbah. A new look at dual-hop relaying: Performance limits with hardware impairments. *IEEE Transactions on Communications*, 61 (11):4512–4525, 2013.

[55] M.O. Hasna and M.-S. Alouini. Outage probability of multihop transmission over Nakagami fading channels. *IEEE communicatons Letters*, 7(5):216–218, 2003.

[56] G.K. Karagiannidis et al. Bounds for multihop relayed communications in nakagami-m fading. *IEEE Transactions on communicatons*, 54(1):18–22, 2006.

[57] G.K. Karagiannidis. Performance bounds of multihop wireless communications with blind relays over generalized fading channels. *IEEE Transactions on Wireless communicatons*, 5(3):498–503, 2006.

[58] Eduardo Morgado et al. End-to-end average BER in multihop wireless networks over fading channels. *IEEE Transactions on Wireless communicatons*, 9(8):2478–2487, 2010.

[59] Hafiz Yasar Lateef et al. Performance analysis of multi-user, multi-hop cooperative relay networks over Nakagami-m fading channels. *IEEE communicatons Letters*, 15(7):776–778, 2011.

[60] Imene Trigui et al. Closed-form error analysis of variable-gain multihop systems in Nakagami-m fading channels. *IEEE Transactions on communicatons*, 59(8):2285–2295, 2011.

[61] Xingqin Lin and Jeffrey G. Andrews. Connectivity of Millimeter Wave networks with multi-hop relaying. *IEEE Wireless communicatons Letters*, 4(2):209–212, 2015.

[62] Theodoros A. Tsiftsis et al. Multihop free-space optical communications over strong turbulence channels. In *2006 IEEE International Conferenece on Communications*, volume 6, pages 2755–2759, 2006.

[63] Xuan Tang et al. Multihop free-space optical communications over turbulence channels with pointing errors using heterodyne detection. *Journal of Lightwave Technology*, 32 (15):2597–2604, 2014.

[64] Emna Zedini and Mohamed-Slim Alouini. Multihop relaying over IM/DD FSO systems with pointing errors. *Journal of Lightwave Technology*, 33(23):5007–5015, 2015.

[65] Behnam Ashrafzadeh et al. Unified performance analysis of multi-hop FSO systems over double generalized gamma turbulence channels with pointing errors. *IEEE Transactions on Wireless communicatons*, 19(11):7732–7746, 2020.

[66] Chaouki Ben Issaid et al. A generic simulation approach for the fast and accurate estimation of the outage probability of single hop and multihop FSO links subject to generalized pointing errors. *IEEE Transactions on Wireless communicatons*, 16(10):6822–6837, 2017.

[67] Wael G. Alheadary et al. BER analysis of multi-hop heterodyne FSO systems with fixed gain relays over general Malaga turbulence channels. In *2017 13th International Wireless communicatons and Mobile Computing Conference (IWCMC)*, pages 1172–1177, 2017.

[68] Jianfei Cao et al. Performance of multihop wireless links over generalized-K fading channels. In *2010 IEEE 72nd Vehicular Technology Conference - Fall*, pages 1–5, 2010.

[69] Osamah S. Badarneh and Fares S. Almehmadi. Performance of multihop wireless networks in α-μ fading channels perturbed by an additive generalized gaussian noise. *IEEE communicatons Letters*, 20(5):986–989, 2016.

[70] Dharmendra Dixit and P. R. Sahu. Exact closed-form ABER for multi-hop regenerative relay systems over $\kappa - \mu$ fading. *IEEE Wireless communicatons Letters*, 6(2):246–249, 2017.

[71] Ping Wang et al. Multihop FSO over exponentiated Weibull fading channels with nonzero boresight pointing errors. *IEEE Photonics Technology Letters*, 28(16):1747–1750, 2016.

[72] Xiang Yi et al. Performance analysis for a mixed RF and multihop FSO communication

system in 5G C-RAN. *IEEE/OSA Journal of Optical communicatons and Networking*, 11(8):452–464, 2019.

[73] Talha Mir, Muhammad Waqas, Usama Mir, Syed Mudassir Hussain, Ahmet M. Elbir, and Shanshan Tu. Hybrid precoding design for two-way relay-assisted Terahertz massive MIMO systems. *IEEE Access*, 8:222660–222671, 2020.

[74] Alexandros-Apostolos A. Boulogeorgos and Angeliki Alexiou. Outage probability analysis of THz relaying systems. In *2020 IEEE 31st Annual International Symposium on Personal, Indoor and Mobile Radio Communications*, pages 1–7, 2020.

[75] Sai Li and Liang Yang. Performance analysis of dual-hop THz transmission systems over α-μ fading channels with pointing errors. *IEEE Internet of Things Journal*, pages 1–1, 2021.

[76] Q. Xia and J. M. Jornet. Cross-layer analysis of optimal relaying strategies for Terahertz-band communication networks. In *2017 IEEE 13th International Conference on Wireless and Mobile Computing, Networking and Communications (WiMob)*, pages 1–8, 2017.

[77] Giorgos Stratidakis et al. Relay-based blockage and antenna misalignment mitigation in THz wireless communications. In *2020 2nd 6G Wireless Summit (6G SUMMIT)*, pages 1–4, 2020.

[78] Z. Rong, M. S. Leeson, and M. D. Higgins. Relay-assisted nanoscale communication in the THz band. *Micro Nano Letters*, 12(6):373–376, 2017.

[79] Q. H. Abbasi, A. A. Nasir, K. Yang, K. A. Qaraqe, and A. Alomainy. Cooperative In-Vivo nano-network communication at Terahertz frequencies. *IEEE Access*, 5:8642–8647, 2017.

[80] T. Mir, M. Waqas, U. Mir, S. M. Hussain, A. M. Elbir, and S. Tu. Hybrid precoding design for two-way relay-assisted Terahertz massive MIMO systems. *IEEE Access*, 8: 222660–222671, 2020.

[81] A. A. Boulogeorgos, E. N. Papasotiriou, and A. Alexiou. Outage probability analysis of THz relaying systems. *arXiv:2007.07186*, 2020.

[82] Juan Xu et al. An energy efficient multi-hop routing protocol for Terahertz wireless nanosensor networks. In *Wireless Algorithms, Systems, and Applications*, pages 367–376. Springer International Publishing, 2016.

[83] Chongwen Huang, Zhaohui Yang, George C. Alexandropoulos, Kai Xiong, Li Wei, Chau Yuen, Zhaoyang Zhang, and Mérouane Debbah. Multi-hop RIS-empowered Terahertz communications: A DRL-based hybrid beamforming design. *IEEE Journal on Selected Areas in Communications*, 39(6):1663–1677, 2021.

[84] E. Lee, J. Park, D. Han, and G. Yoon. Performance analysis of the asymmetric dual-hop relay transmission with mixed RF/FSO links. *IEEE Photonics Technology Letters*, 23 (21):1642–1644, 2011.

[85] I. S. Ansari, F. Yilmaz, and M. Alouini. Impact of pointing errors on the performance of mixed RF/FSO dual-hop transmission systems. *IEEE Wireless Communications Letters*,

2(3):351–354, 2013.

[86] H. Samimi and M. Uysal. End-to-end performance of mixed RF/FSO transmission systems. *IEEE/OSA Journal of Optical Communications and Networking*, 5(11):1139–1144, 2013.

[87] S. Anees and M. R. Bhatnagar. Performance of an amplify and forward dual hop asymmetric RF FSO communication system. *IEEE/OSA Journal of Optical Communications and Networking*, 7(2):124–135, February 2015.

[88] L. Kong, W. Xu, L. Hanzo, H. Zhang, and C. Zhao. Performance of a free-space-optical relay-assisted hybrid RF/FSO system in generalized M-distributed channels. *IEEE Photonics Journal*, 7(5):1–19, Oct 2015.

[89] E. Zedini, H. Soury, and M. Alouini. On the performance analysis of dual-hop mixed FSO/RF systems. *IEEE Transactions on Wireless Communications*, 15(5):3679–3689, May 2016.

[90] B. Bag, A. Das, I. S. Ansari, A. Prokeš, C. Bose, and A. Chandra. Performance analysis of hybrid FSO systems using FSO/RF-FSO link adaptation. *IEEE Photonics Journal*, 10 (3):1–17, 2018.

[91] Y. Zhang, J. Zhang, L. Yang, B. Ai, and M. Alouini. On the performance of dual-hop systems over mixed FSO/mmWave fading channels. *IEEE Open Journal of the Communications Society*, 1:477–489, 2020.

[92] Liang Yang, Mazen O. Hasna, and Xiqi Gao. Performance of mixed RF/FSO with variable gain over generalized atmospheric turbulence channels. *IEEE Journal on Selected Areas in Communications*, 33(9):1913–1924, 2015.

[93] Ahmed H. Abd El-Malek, Anas M. Salhab, Salam A. Zummo, and Mohamed-Slim Alouini. Security-reliability trade-off analysis for multiuser SIMO mixed RF/FSO relay networks with opportunistic user scheduling. *IEEE Transactions on Wireless Communications*, 15(9):5904–5918, 2016.

[94] Liang Yang, Mazen O. Hasna, and Imran Shafique Ansari. Unified performance analysis for multiuser mixed η - μ and $\mathcal{M}$ - distribution dual-hop rf/fso systems. *IEEE Transactions on Communications*, 65(8):3601–3613, 2017.

[95] Imène Trigui, Sofiène Affes, Anas M. Salhab, and Mohamed-Slim Alouini. Multi-user mixed FSO-RF systems with aperture selection under Poisson field interference. *IEEE Access*, 7:73764–73781, 2019.

[96] Nesrine Cherif, Imène Trigui, and Sofiène Affes. On the performance analysis of mixed multi-aperture FSO/multiuser RF relay systems with interference. In *2017 IEEE 18th International Workshop on Signal Processing Advances in Wireless Communications (SPAWC)*, pages 1–5, 2017.

[97] Behnam Ashrafzadeh, Ehsan Soleimani-Nasab, Mehdi Kamandar, and Murat Uysal. A framework on the performance analysis of dual-hop mixed FSO-RF cooperative systems. *IEEE Transactions on Communications*, 67(7):4939–4954, 2019.

[98] Jiliang Zhang, Xiaojun Pan, Gaofeng Pan, and Yiyuan Xie. Secrecy analysis for multi-relaying RF-FSO systems with a multi-aperture destination. *IEEE Photonics Journal*, 12 (2):1–11, 2020.

[99] Liang Yang, Xiaoqin Yan, Sai Li, Daniel Benevides da Costa, and Mohamed-Slim Alouini. Performance analysis of dual-hop mixed PLC/RF communication systems. *IEEE Systems Journal*, 16(2):2867–2878, 2022.

[100] Imène Trigui, Panagiotis D. Diamantoulakis, Sofiène Affes, and George K. Karagiannidis. Shadowed FSO/mmWave systems with interference. *IEEE Transactions on Communications*, 67(9):6256–6267, 2019.

[101] Yan Zhang, Jiayi Zhang, Liang Yang, Bo Ai, and Mohamed-Slim Alouini. On the performance of dual-hop systems over mixed FSO/mmWave fading channels. *IEEE Open Journal of the Communications Society*, 1:477–489, 2020.

[102] Waled Gheth, Khaled M. Rabie, Bamidele Adebisi, Muhammad Ijaz, and Georgina Harris. Performance analysis of integrated power-line/visible-light communication systems with AF relaying. In *2018 IEEE Global Communications Conference (GLOBECOM)*, pages 1–6, 2018.

[103] Sai Li, Liang Yang, Daniel Benevides da Costa, Jiayi Zhang, and Mohamed-Slim Alouini. Performance analysis of mixed RF-UWOC dual-hop transmission systems. *IEEE Transactions on Vehicular Technology*, 69(11):14043–14048, 2020.

[104] M. D. Yacoub. The α-μ distribution: A physical fading model for the stacy distribution. *IEEE Transactions on Vehicular Technology*, 56(1):27–34, 2007.

[105] Nguyen Cong Luong, Dinh Thai Hoang, Ping Wang, Dusit Niyato, Dong In Kim, and Zhu Han. Data collection and wireless communication in internet of things (IoT) using economic analysis and pricing models: A survey. *IEEE Communications Surveys & Tutorials*, 18(4):2546–2590, 2016.

[106] Gang Xu, Edith C.-H. Ngai, and Jiangchuan Liu. Ubiquitous transmission of multimedia sensor data in internet of things. *IEEE Internet of Things Journal*, 5(1):403–414, 2018.

[107] Hai Tao, Md Zakirul Alam Bhuiyan, Ahmed N. Abdalla, Mohammad Mehedi Hassan, Jasni Mohamad Zain, and Thaier Hayajneh. Secured data collection with hardware-based ciphers for IoT-based healthcare. *IEEE Internet of Things Journal*, 6(1):410–420, 2019.

[108] Shuhang Liu, Zhiqing Wei, Zijun Guo, Xin Yuan, and Zhiyong Feng. Performance analysis of UAVs assisted data collection in wireless sensor network. In *2018 IEEE 87th Vehicular Technology Conference (VTC Spring)*, pages 1–5, 2018.

[109] Zhiqing Wei, Mingyue Zhu, Ning Zhang, Lin Wang, Yingying Zou, Zeyang Meng, Huici Wu, and Zhiyong Feng. UAV-assisted data collection for internet of things: A survey. *IEEE Internet of Things Journal*, 9(17):15460–15483, 2022.

[110] Yuchen Li, Weifa Liang, Wenzheng Xu, Zichuan Xu, Xiaohua Jia, Yinlong Xu, and Haibin Kan. Data collection maximization in IoT-sensor networks via an energy-constrained UAV. *IEEE Transactions on Mobile Computing*, 22(1):159–174, 2023.

[111] Yawei Pang, Yanru Zhang, Yunan Gu, Miao Pan, Zhu Han, and Pan Li. Efficient data collection for wireless rechargeable sensor clusters in harsh terrains using UAVs. In *2014 IEEE Global Communications Conference*, pages 234–239, 2014.

[112] Li Chen, Weidong Wang, and Chi Zhang. Multiuser diversity over parallel and hybrid FSO/RF links and its performance analysis. *IEEE Photonics Journal*, 8(3):1–9, 2016.

[113] Behrooz Makki, Tommy Svensson, Thomas Eriksson, and Mohamed-Slim Alouini. On the performance of RF-FSO links with and without hybrid ARQ. *IEEE Transactions on Wireless Communications*, 15(7):4928–4943, 2016.

[114] Hayssam Dahrouj, Ahmed Douik, Frank Rayal, Tareq Y. Al-Naffouri, and Mohamed-Slim Alouini. Cost-effective hybrid RF/FSO backhaul solution for next generation wireless systems. *IEEE Wireless Communications*, 22(5):98–104, 2015.

[115] Saeede Enayati and Hamid Saeedi. Deployment of hybrid FSO/RF links in backhaul of relay-based rural area cellular networks: Advantages and performance analysis. *IEEE Communications Letters*, 20(9):1824–1827, 2016.

[116] Yasser F. Al-Eryani, Anas M. Salhab, Salam A. Zummo, and Mohamed-Slim Alouini. Protocol design and performance analysis of multiuser mixed RF and hybrid FSO/RF relaying with buffers. *Journal of Optical Communications and Networking*, 10(4):309–321, 2018.

[117] Shubha Sharma, A. S. Madhukumar, and R. Swaminathan. Switching-based cooperative decode-and-forward relaying for hybrid FSO/RF networks. *Journal of Optical Communications and Networking*, 11(6):267–281, 2019.

[118] Osamah S. Badarneh and Raed Mesleh. Diversity analysis of simultaneous mmwave and free-space-optical transmission over $\mathcal{F}$-distribution channel models. *Journal of Optical Communications and Networking*, 12(11):324–334, 2020.

[119] Praveen Kumar Singya, Behrooz Makki, Antonio D'Errico, and Mohamed-Slim Alouini. Hybrid FSO/THz-based backhaul network for mmWave terrestrial communication. *IEEE Transactions on Wireless Communications*, pages 1–1, 2022.

[120] Phuc V. Trinh, Truong Cong Thang, and Anh T. Pham. Mixed mmWave RF/FSO relaying systems over generalized fading channels with pointing errors. *IEEE Photonics Journal*, 9(1):1–14, 2017.

[121] Ruijie Li, Te Chen, Luhai Fan, and Anhong Dang. Performance analysis of a multiuser dual-hop amplify-and-forward relay system with FSO/RF links. *Journal of Optical Communications and Networking*, 11(7):362–370, 2019.

[122] Elyes Balti and Mohsen Guizani. Mixed RF/FSO cooperative relaying systems with co-channel interference. *IEEE Transactions on Communications*, PP:1–1, 03 2018.

[123] Yan Zhang, Jiayi Zhang, Liang Yang, Bo Ai, and Mohamed-Slim Alouini. On the performance of dual-hop systems over mixed FSO/mmWave fading channels. *IEEE Open Journal of the Communications Society*, 1:477–489, 2020.

[124] Sai Li, Liang Yang, Jiayi Zhang, Petros Bithas, Theodoros Tsiftsis, and Mohamed-Slim

Alouini. Mixed THz/FSO relaying systems: Statistical analysis and performance evaluation. *IEEE Transactions on Wireless Communications*, PP:1–1, 12 2022.

[125] Hien Quoc Ngo, Alexei Ashikhmin, Hong Yang, Erik G. Larsson, and Thomas L. Marzetta. Cell-Free massive MIMO versus small cells. *IEEE Transactions on Wireless Communications*, 16(3):1834–1850, 2017.

[126] Bjornson E. Quoc Ngo H. et al. Interdonato, G. Ubiquitous cell-free massive MIMO communications. *Journal of Wireless Communication and Networking*, 197, 2019.

[127] Jiayi Zhang, Shuaifei Chen, Yan Lin, Jiakang Zheng, Bo Ai, and Lajos Hanzo. Cell-free massive MIMO: A new next-generation paradigm. *IEEE Access*, 7:99878–99888, 2019.

[128] Salah Elhoushy, Mohamed Ibrahim, and Walaa Hamouda. Cell-Free massive MIMO: A survey. *IEEE Communications Surveys & Tutorials*, 24(1):492–523, 2022.

[129] Alice Faisal, Hadi Sarieddeen, Hayssam Dahrouj, Tareq Y. Al-Naffouri, and Mohamed-Slim Alouini. Ultramassive MIMO systems at Terahertz bands: Prospects and challenges. *IEEE Vehicular Technology Magazine*, 15(4):33–42, 2020.

[130] Reza Sayyari, Jafar Pourrostam, and Mir Javad Musevi Niya. Cell-free massive MIMO system with an adaptive switching algorithm between cooperative NOMA, non-cooperative NOMA, and OMA modes. *IEEE Access*, 9:149227–149239, 2021.

[131] Omid Abbasi and Halim Yanikomeroglu. A cell-free scheme for UAV base stations with HAPS-assisted backhauling in Terahertz band. In *ICC 2022 - IEEE International Conference on Communications*, pages 249–254, 2022.

[132] Amitav Mukherjee. Jamming vulnerability of Terahertz wireless networks. In *MILCOM 2022 - 2022 IEEE Military Communications Conference (MILCOM)*, pages 426–430, 2022.

[133] Boyu Ning, Zhi Chen, Wenrong Chen, Yiming Du, and Jun Fang. Terahertz multi-user massive MIMO with intelligent reflecting surface: Beam training and hybrid beamforming. *IEEE Transactions on Vehicular Technology*, 70(2):1376–1393, 2021.

[134] Rui Chen, Min Chen, Xiao Xiao, Wei Zhang, and Jiandong Li. Multi-user orbital angular momentum based Terahertz communications. *IEEE Transactions on Wireless Communications*, pages 1–1, 2023.

[135] Yang Wang, Chuang Yang, and Mugen Peng. Sensing-aided hybrid precoding for efficient Terahertz wideband communications in multi-user high-data-rate IoT. 6 2023.

[136] Chen Wenjie, Chen Zhiand, and Ma Xinying. Channel estimation for intelligent reflecting surface aided multi-user MISO Terahertz system. *Terahertz Science & Technology*, 13(2):51–60, 2020.

[137] Seunghyun Lee, Woojae Jeong, Jungsoo Jung, Juho Lee, and Sunghyun Choi. A new preamble signal design for random access in sub-Terahertz 6G cellular systems. In *2022 IEEE International Conference on Communications Workshops (ICC Workshops)*, pages 1147–1152, 2022.

[138] Emil Björnson and Luca Sanguinetti. Scalable Cell-Free massive MIMO systems. *IEEE*

Transactions on Communications, 68(7):4247–4261, 2020.

[139] Pei Liu, Kai Luo, Da Chen, and Tao Jiang. Spectral efficiency analysis of Cell-Free massive MIMO systems with zero-forcing detector. *IEEE Transactions on Wireless Communications*, 19(2):795–807, 2020.

[140] Emil Björnson and Luca Sanguinetti. Making Cell-Free massive MIMO competitive with MMSE processing and centralized implementation. *IEEE Transactions on Wireless Communications*, 19(1):77–90, 2020.

[141] Jiayi Zhang, Jing Zhang, Emil Björnson, and Bo Ai. Local partial zero-forcing combining for Cell-Free massive MIMO systems. *IEEE Transactions on Communications*, 69 (12):8459–8473, 2021.

[142] Mohamed Ibrahim, Salah Elhoushy, and Walaa Hamouda. Uplink performance of MmWave-fronthaul Cell-Free massive MIMO systems. *IEEE Transactions on Vehicular Technology*, 71(2):1536–1548, 2022.

[143] M.E. Rivero-Angeles, D. Lara-Rodriguez, and F.A. Cruz-Perez. Random-access control mechanisms using adaptive traffic load in ALOHA and CSMA strategies for EDGE. *IEEE Transactions on Vehicular Technology*, 54(3):1160–1186, 2005.

[144] Francois Baccelli and Chandramani Singh. Adaptive spatial ALOHA, fairness and stochastic geometry. In *2013 11th International Symposium and Workshops on Modeling and Optimization in Mobile, Ad Hoc and Wireless Networks (WiOpt)*, pages 7–14, 2013.

[145] Ling Wang, Hanshang Li, and Yingtao Jiang. Adaptive-opportunistic aloha: A media access control protocol for unmanned aerial vehicle–wireless sensor network systems. *International Jornal of Distributed Sensor Networks*, 12(8):1550147716662785, 2016.

[146] Dejan Vukobratovic and Francisco J. Escribano. Adaptive multi-receiver coded slotted ALOHA for indoor optical wireless communications. *IEEE Communications Letters*, 24 (6):1308–1312, 2020. doi: 10.1109/LCOMM.2020.2981070.

[147] Mohammad Moed Ebrahimi, Keyhan Khamforoosh, MohammadReza Amini, Amir Sheikhahmadi, and Hana Khamfroush. Adaptive–persistent nonorthogonal random access scheme for URLL massive IoT networks. *IEEE Systems Journal*, 17(1):1660–1671, 2023.

[148] Pablo Ramirez-Espinosa et al. The alpha-k-μ shadowed fading distribution: Statistical characterization and applications. In *2019 IEEE Global communicatons Conference (GLOBECOM)*, pages 1–6, 2019.

[149] E.N. Papasotiriou et al. An experimentally validated fading model for THz wireless systems. *Scientific report*, 11, 2021.

[150] A. A. Farid and S. Hranilovic. Outage capacity optimization for free-space optical links with pointing errors. *Journal of Lightwave Technology*, 25(7):1702–1710, 2007.

[151] Fan Yang, Julian Cheng, and Theodoros A. Tsiftsis. Free-space optical communication with nonzero boresight pointing errors. *IEEE Transactions on Communications*, 62(2):

713–725, 2014.

[152] Osamah S. Badarneh, Mohammad T. Dabiri, and Mazen Hasna. Channel modeling and performance analysis of directional THz links under pointing errors and α-μ distribution. *IEEE Communications Letters*, pages 1–1, 2023.

[153] Evangelos N. Papasotiriou et al. A new look to THz wireless links: Fading modeling and capacity assessment. In *2021 IEEE 32nd Annual International Symposium on Personal, Indoor and Mobile Radio Communications*, pages 1–6, 2021.

[154] Jiayi Zhang et al. Performance analysis of 5G mobile relay systems for high-speed trains. *IEEE Journal on Selected Areas in Communications*, 38(12):2760–2772, 2020.

[155] Miguel López-Benítez and Jiayi Zhang. Comments and corrections to "new results on the fluctuating two-ray model with arbitrary fading parameters and its applications". *IEEE Transactions on Vehicular Technology*, 70(2):1938–1940, 2021.

[156] Jia Ye et al. Modeling co-channel interference in the THz band. *IEEE Transactions on Vehicular Technology*, 70(7):6319–6334, 2021.

[157] P. Shankar. Error rates in generalized shadowed fading channels. *Wireless Personal communicatons*, 28(3):233–238, 2004.

[158] Michel Daoud Yacoub. The α - η - κ - μ fading model. *IEEE Transactions on Antennas and Propagation*, 64(8):3597–3610, 2016.

[159] Carlos Rafael Nogueira da Silva et al. The α - η - κ - μ fading model: New fundamental results. *IEEE Transactions on Antenna and Propagation*, 68(1):443–454, 2020.

[160] E.N. Papasotiriou, AA.A. Boulogeorgos, and A. Alexiou. Outdoor THz fading modeling by means of gaussian and gamma mixture distributions. *Scientific Reports*, 13(6385), 2023.

[161] Christoph Studer, Markus Wenk, and Andreas Burg. MIMO transmission with residual transmit-RF impairments. In *2010 International ITG Workshop on Smart Antennas (WSA)*, pages 189–196, 2010.

[162] Emil Bjornson, Michail Matthaiou, and Merouane Debbah. A new look at dual-hop relaying: Performance limits with hardware impairments. *IEEE Transactions on Communications*, 61(11):4512–4525, 2013.

[163] Alexandros-Apostolos A. Boulogeorgos, José Manuel Riera, and Angeliki Alexiou. On the joint effect of rain and beam misalignment in terahertz wireless systems. *IEEE Access*, 10:58997–59012, 2022.

[164] Yassine Mouchtak et al. Performance analysis of I/Q imbalance with hardware impairments over hyper Fox's H-fading channels. *IEEE Transactions on Wireless Communications*, 21(11):9519–9536, 2022.

[165] I. S. Ansari, S. Al-Ahmadi, F. Yilmaz, M. Alouini, and H. Yanikomeroglu. A new formula for the BER of binary modulations with dual-branch selection over generalized-k composite fading channels. *IEEE Transactions on Communications*, 59(10):2654–2658, 2011.

[166] A. A. Kilbas. *H-Transforms: Theory and Applications*, volume First edition. CRC Press, 2004.

[167] M.O. Hasna and M.-S. Alouini. End-to-end performance of transmission systems with relays over Rayleigh-fading channels. *IEEE Transactions on Wireless Communications*, 2(6):1126–1131, 2003.

[168] I. S. Gradshteyn and I. M. Ryzhik . *Table of Integrals, Series, and Products*. Academic press, San Diego, CA, 6th edition, 2000.

[169] Husam R. Alhennawi et al. Closed-form exact and asymptotic expressions for the symbol error rate and capacity of the H-Function fading channel. *IEEE Transactions on Vehicular Technology*, 65(4):1957–1974, 2016.

[170] A. M. Mathai, R. K. Saxena, and H. J. Haubold. The H-function: Theory and applications. New York, NY, USA, Springer, 2010.

[171] *The Wolfram function Site*, https://functions.wolfram.com/HypergeometricFunctions/MeijerG/, (Accessed: May 06, 2021).

[172] Yousuf Abo Rahama, Mahmoud H. Ismail, and Mohamed S. Hassan. On the sum of independent Fox's H -function variates with applications. *IEEE Transactions on Vehicular Technology*, 67(8):6752–6760, 2018.

[173] Emna Zedini et al. Dual-hop FSO transmission systems over Gamma–Gamma turbulence with pointing errors. *IEEE Transactions on Wireless communicatons*, 16(2):784–796, 2017.

[174] A. Papoulis and S. Pillai. *Probability, Random Variables, and Stochastic Processes*. McGraw Hill, Boston, Fourth Edition, 2002.

[175] Priyangshu Sen, D. A. Pados, S. N. Batalama, E. Einarsson, J. P. Bird, and J. M. Jornet. The TeraNova platform: An integrated testbed for ultra-broadband wireless communications at true Terahertz frequencies. *Computer Networks, Elsevier*, 2020.

[176] Elmehdi Illi, Faissal El Bouanani, and Fouad Ayoub. A performance study of a hybrid 5G RF/FSO transmission system. In *2017 International Conference on Wireless Networks and Mobile Communications (WINCOM)*, pages 1–7, 2017.

[177] V.S. Adamchik and O.I. Marichev. *The algorithm for calculating integrals of hypergeometric type functions and its realization in reduce system*. John Wiley and Sons, 3rd Edition, 1990.

[178] P.K. Mittal and K.C. Gupta. An integral involving generalized function of two variables. *Proc. Indian Acad. Sci.*, 75(9):117–123, 1972.

[179] Sajid Hussain Alvi, Shurjeel Wyne, and Daniel B. da Costa. Performance analysis of dual-hop AF relaying over α-μ fading channels. *AEU - International Journal of Electronics and Communications*, 108:221–225, 2019. ISSN 1434-8411.

[180] Eunju Lee, Jaedon Park, Dongsoo Han, and Giwan Yoon. Performance analysis of the asymmetric dual-hop relay transmission with mixed RF/FSO links. *IEEE Photonics Technology Letters*, 23(21):1642–1644, 2011.

[181] A. A. Boulogeorgos, E. N. Papasotiriou, J. Kokkoniemi, J. Lehtomaeki, A. Alexiou, and M. Juntti. Performance evaluation of THz wireless systems operating in 275-400 GHz band. In *2018 IEEE 87th Vehicular Technology Conference (VTC Spring)*, pages 1–5, 2018.

[182] G. J. O. Jameson. The incomplete gamma functions. *The Mathematical Gazette*, 100, Iss. 548:298–306, Jul 2016.

[183] A. Annamalai, R. C. Palat, and J. Matyjas. Estimating ergodic capacity of cooperative analog relaying under different adaptive source transmission techniques. In *2010 IEEE Sarnoff Symposium*, pages 1–5, 2010.

[184] Theodoros A. Tsiftsis, Harilaos G. Sandalidis, George K. Karagiannidis, and Nikos C. Sagias. Multihop free-space optical communications over strong turbulence channels. In *2006 IEEE International Conference on Communications*, volume 6, pages 2755–2759, 2006.

[185] C.A. Balanis. *Antenna Theory: Analysis and Design*. John Wiley and Sons, 3rd Edition, 2016.

[186] Pranay Bhardwaj and Syed Mohammad Zafaruddin. Performance analysis of dual-hop relaying for THz-RF wireless link over asymmetrical - fading. *IEEE Transactions on Vehicular Technology*, pages 1–1, 2021.

[187] Emna Zedini, Hamza Soury, and Mohamed-Slim Alouini. On the performance analysis of dual-hop mixed FSO/RF systems. *IEEE Transactions on Wireless Communications*, 15(5):3679–3689, 2016.

[188] Daniel Benevides Da Costa, Michel Daoud Yacoub, and Jose Filho. Highly accurate closed-form approximations to the sum of α-μ variates and applications. *IEEE Transactions on Wireless Communications*, 7(9):3301–3306, 2008.

[189] Alexandre C. Moraes, Daniel B. da Costa, and Michel D. Yacoub. A simple, accurate approximation for the outage probability of equal-gain receivers with cochannel interference in an α-μ fading scenario. In *2008 IEEE Wireless Communications and Networking Conference*, pages 54–58, 2008.

[190] Moataz M. H. El Ayadi and Mahmoud H. Ismail. Novel closed-form exact expressions and asymptotic analysis for the symbol error rate of single- and multiple-branch MRC and EGC receivers over α– μ fading. *IEEE Transactions on Vehicular Technology*, 63 (9):4277–4291, 2014.

[191] Kezhi Wang, Tian Wang, Yunfei Chen, and Mohamed-Slim Alouini. Statistics of $\alpha - \mu$ random variables and their applications in wireless multihop relaying and multiple scattering channels. *IEEE Transactions on Vehicular Technology*, 64(6):2754–2759, 2015.

[192] Long Kong, Georges Kaddoum, and Zouheir Rezki. Highly accurate and asymptotic analysis on the SOP over SIMO α – μ fading channels. *IEEE Communications Letters*, 22(10):2088–2091, 2018.

[193] Incomplete Gamma and realted functions. *http://dlmf.nist.gov/8.14, (Accessed: Sept. 26,*

2020).

[194] Marzieh Najafi, Hedieh Ajam, Vahid Jamali, Panagiotis D. Diamantoulakis, George K. Karagiannidis, and Robert Schober. Statistical modeling of the FSO fronthaul channel for UAV-based communications. *IEEE Transactions on Communications*, 68(6):3720–3736, 2020.

[195] Alexandros-Apostolos A. Boulogeorgos et al. Outage performance analysis of RIS-assisted UAV wireless systems under disorientation and misalignment. *IEEE Transactions on Vehicular Technology*, 71(10):10712–10728, 2022.

[196] A. Bletsas, A. Khisti, D.P. Reed, and A. Lippman. A simple cooperative diversity method based on network path selection. *IEEE Journal on Selected Areas in Communications*, 24(3):659–672, 2006.

[197] Vinay U. Pai, Pranay Bhardwaj, and S. M. Zafaruddin. Performance analysis of dual-hop THz wireless transmission for backhaul applications. In *2021 IEEE International Conference on Advanced Networks and Telecommunications Systems (ANTS)*, pages 438–443, 2021.

[198] Pranay Bhardwaj and S. M. Zafaruddin. On the performance of multihop THz wireless system over mixed channel fading with shadowing and antenna misalignment. *IEEE Transactions on Communications*, pages 1–1, 2022.

[199] R. Rom and M. Sidi. *Multiple Access Protocols: Performance and Analysis*. Springer-Verlag, 1990.

[200] Tiago Reis Rufino Marins, André Antônio dos Anjos, Vicent Miquel Rodrigo Peñarrocha, Lorenzo Rubio, Juan Reig, Rausley Adriano Amaral de Souza, and Michel Daoud Yacoub. Fading evaluation in the mmWave band. *IEEE Transactions on Communications*, 67(12):8725–8738, 2019.

[201] Maged Abdullah Esmail, Habib Fathallah, and Mohamed-Slim Alouini. On the performance of optical wireless links over random foggy channels. *IEEE Access*, 5:2894–2903, 2017.

[202] Hongyang Du, Jiayi Zhang, Ke Guan, Dusit Niyato, Huiying Jiao, Zhiqin Wang, and Thomas Kürner. Performance and optimization of reconfigurable intelligent surface aided THz communications. *IEEE Transactions on Communications*, 70(5):3575–3593, 2022.

[203] N. Abramson. The ALOHA system: Another alternative for computer communications. In *Proceedings of Fall Joint Computer Conference*, 1970.

[204] M. Abramowitz and I. A. Stegun. *Handbook of Mathematical Functions with Formulas, Graphs, and Mathematical Tables*. Academic, 10th priniting edition, 1972.

[205] K. Biswas, V. Muthukkumarasamy, X. W. Wu, and K. Singh. An analytical model for lifetime estimation of wireless sensor networks. *IEEE Communications Letters*, 19(9): 1584–1587, 2015.

[206] *The Wolfram function Site*, https://functions.wolfram.com/Bessel-TypeFunctions/BesselY/introductions/Bessels/, (Accessed: Sept. 26, 2022).

Brief Biography of the Supervisor

Prof. Syed Mohammad Zafaruddin received his Ph.D. degree in electrical engineering from IIT Delhi, New Delhi, India, in 2013. From 2012 to 2015, he was with Ikanos Communications (now Qualcomm), Bengaluru, India, working directly with the CTO Office, Red Bank, NJ, USA, where he was involved in research and development for xDSL systems. From 2015 to 2018, he was a Post-Doctoral Researcher with the Faculty of Engineering, Bar-Ilan University, Ramat Gan, Israel, where he was involved in signal processing for wireline and wireless communications. He is currently an Associate Professor with the Department of Electrical and Electronics Engineering, Birla Institute of Technology and Science at Pilani, Pilani, India. His current research interests include signal processing and machine learning for wireless and wireline communications, THz wireless technology, optical wireless communications, reconfigurable intelligent surface, distributed signal processing, and resource allocation algorithms. He received the Planning and Budgeting Commission Fellowship for Outstanding Post-Doctoral Researchers from China and India by the Council for Higher Education, Israel (2016–2018). He is also an Associate Editor of the IEEE ACCESS.

Brief Biography of the Candidate

Pranay Bhardwaj, received the M.E. in electronics and communication engineering from Birla Institute of Technology and Science (BITS) Pilani, Pilani Campus, India, in 2012. He is currently pursuing the Ph.D. degree in the area of wireless communications with the Department of Electrical and Electronics Engineering, Birla Institute of Technology and Science at Pilani, Pilani, India. His current research interests include Terahertz wireless systems and interference cancellation for wireless networks. In 2022, he was awarded International Travel Support (ITS) from Science and Research Board (SERB), Department of Science and Technology (DST), Govt of India, to present a research paper in Helsinki, Finland. He was also awarded IEEE ComSoc's student travel grant from IEEE Communication Society to present a research paper in Austin, Texas, USA, in 2022. He won the Best paper award in IETE Students' Journal Award category, 2023.

List of Publications

Journal Articles

1. **P. Bhardwaj**, S. M. Zafaruddin, and Amir Leshem, "Random Access Protocols for Cell-Free Wireless Network Exploiting Statistical Behavior of THz Signal Propagation," arXiv:2311.06.06166, under review in *IEEE Transactions on Wireless Communications* (SCI IF 10.4), Nov. 2023.

2. **P. Bhardwaj**, V. Bansal, N. Biyani, S. Shukla, and S. M. Zafaruddin, "Performance of Integrated IoT Network with Hybrid mmWave/FSO/THz Backhaul Link," in *IEEE Internet of Things Journal* (SCI IF 10.6), vol. 11, no. 2, pp. 3639-3652, Jan. 2024.

3. **P. Bhardwaj** and S. M. Zafaruddin, "Exact Performance Analysis of THz Link under Transceiver Hardware Impairments," in *IEEE Communications Letters* (SCI IF 4.1), vol. 27, no. 8, pp. 2197-2201, Aug. 2023.

4. **P. Bhardwaj** and S. M. Zafaruddin, "Performance of Hybrid THz and Multiantenna RF System With Diversity Combining," in *IEEE Systems Journal* (SCI IF 4.4), vol. 17, no. 2, pp. 2546-2557, June 2023.

5. **P. Bhardwaj** and S. M. Zafaruddin, "On the Performance of Multihop THz Wireless System Over Mixed Channel Fading with Shadowing and Antenna Misalignment," in *IEEE Transactions on Communications* (SCI IF 8.3), vol. 70, no. 11, pp. 7748-7763, Nov. 2022.

6. **P. Bhardwaj** and S. M. Zafaruddin, "Fixed-Gain AF Relaying for RF-THz Wireless System over α-κ-μ Shadowed and α-μ Channels," in *IEEE Communications Letters* (SCI IF 4.1), vol. 26, no. 5, pp. 999-1003, May 2022.

7. **P. Bhardwaj** and S. M. Zafaruddin, "Performance Analysis of Dual-Hop Relaying for THz-RF Wireless Link over Asymmetrical α-μ Fading" in *IEEE Transactions on Vehicular Technology* (SCI IF 6.8), vol. 70, no. 10, pp. 10031-10047, Oct. 2021.

8. S. M. Zafaruddin and **P. Bhardwaj**, " Interference Cancellation in Wireless Communications: Past, Present, and Future" in *IETE Journal of Education*, Vol 63, no. 1, pp. 5-13, Oct. 2021. (**Best paper award in IETE Students' Journal Award category, 2023**).

Conference Proceedings

1. **P. Bhardwaj**, Raghav Khanna, and S. M. Zafaruddin, "A Generalized Statistical Model for THz Wireless Channel with Random Atmospheric Absorption," accepted for presentation, *2024 IEEE Wireless Communications and Networking Conference: (IEEE WCNC 2024 Workshops)*, 21-24 April, 2024, Dubai, UAE.

2. **P. Bhardwaj**, Eesha K. Santosh, and S. M. Zafaruddin, " An Exact Statistical Representation of α-η-κ-μ Fading Model for THz Wireless Communication," in press, *2023 IEEE Globecom Workshops (IEEE GC 2023 Workshop - HCWC)*, Kuala Lumpur, Malaysia, Dec. 2023, pp.1-6.

3. **P. Bhardwaj** and S. M. Zafaruddin, "Performance Analysis of Outdoor THz Wireless Transmission over Mixed Gaussian Fading with Pointing Errors," *2022 International Conference on Next Generation Systems and Networks: (BITS EEE CON)*, BITS Pilani, India, 2023, pp.187-196.

4. **P. Bhardwaj** and S. M. Zafaruddin, "Performance Analysis of Cooperative Relaying for Multi-Antenna RF Transmissions over THz Wireless Link," 2022 *IEEE 95th Vehicular Technology Conference: (VTC2022-Spring)*, Helsinki, Finland, 2022, pp. 1-5.

5. A. A. Joshi, **P. Bhardwaj**, and S. M. Zafaruddin, "Terahertz Wireless Transmissions with Maximal Ratio Combining over Fluctuating Two-Ray Fading," 2022 *IEEE Wireless Communications and Networking Conference (WCNC)*, Austin, Texas, USA, 2022, pp. 1575-1580.

6. V. U. Pai, **P. Bhardwaj**, and S. M. Zafaruddin, "Performance Analysis of Dual-Hop THz Wireless Transmission for Backhaul Applications," *2021 IEEE International Conference on Advanced Networks and Telecommunications Systems (ANTS)*, Hyderabad, India, 2021, pp. 438-443.

7. **P. Bhardwaj** and S. M. Zafaruddin, "Performance of Dual-Hop Relaying for THz-RF Wireless Link," 2021 *IEEE 93rd Vehicular Technology Conference (IEEE VTC2021-Spring)*, Helsinki, Finland, 2021, pp. 1-5.